

THE UNIVERSITY OF MANITOBA

THE STRUCTURE OF TURBULENT FLOW IN  
TRIANGULAR ARRAY ROD BUNDLES

by

Allan Charles Trupp

A THESIS

SUBMITTED TO THE FACULTY OF GRADUATE STUDIES  
IN PARTIAL FULFILLMENT OF THE REQUIREMENTS FOR THE DEGREE  
OF DOCTOR OF PHILOSOPHY

DEPARTMENT OF MECHANICAL ENGINEERING

WINNIPEG, MANITOBA

October 1973



THE STRUCTURE OF TURBULENT FLOW IN  
TRIANGULAR ARRAY ROD BUNDLES

By: Allan Charles Trupp

A dissertation submitted to the Faculty of Graduate Studies of  
the University of Manitoba in partial fulfillment of the requirements  
of the degree of

DOCTOR OF PHILOSOPHY

© 1973

Permission has been granted to the LIBRARY OF THE UNIVER-  
SITY OF MANITOBA to lend or sell copies of this dissertation, to  
the NATIONAL LIBRARY OF CANADA to microfilm this  
dissertation and to lend or sell copies of the film, and UNIVERSITY  
MICROFILMS to publish an abstract of this dissertation.

The author reserves other publication rights, and neither the  
dissertation nor extensive extracts from it may be printed or other-  
wise reproduced without the author's written permission.

ABSTRACT

An experimental study of fully developed uniform-density turbulent flow through triangular array rod bundles is described. The pitch-to-rod diameter ( $P/D$ ) ratios were 1.20, 1.35 and 1.50, and the Reynolds number range was 12,000 to 84,000. Based on the equivalent hydraulic diameter concept, friction factors were found to be functions of both Reynolds number and  $P/D$  ratio. Local wall shear stress variations were much smaller than predictions ignoring secondary flow, and the maxima did not occur at the positions facing the sub-channel centerline. Spatial distributions of the mean axial velocity when scaled on the bulk average axial velocity, were substantially independent of Reynolds number and  $P/D$  ratio, but the radial distributions were modified forms of the universal logarithmic laws. Attempts at direct measurement of the secondary velocities were unsuccessful, however the secondary flow pattern (common to the three  $P/D$  ratios) was inferred from the available evidence. The order of magnitude of the secondary velocities were indicated to be probably less than  $\frac{1}{2}\%$  of the bulk average axial velocity.

The turbulence data were found to scale only fairly well on the average friction velocity. The normalized radial distributions of the normal stresses and the primary shear stress ( $\rho \bar{u} \bar{v}$ ) were fairly similar to the distributions for fully developed pipe flow. The experimental data also include the shear stress  $\rho \bar{u} \bar{w}$ , one-dimensional (axial) power

spectra and the Taylor microscale. Using the experimental data, calculations were made for the mean turbulent kinetic energy, eddy diffusivities, and the approximate mean energy balance. A literature review and developments of the fluid-mechanical equations are also included.



## TABLE OF CONTENTS

	Page
Abstract . . . . .	I
Table of Contents . . . . .	III
List of Tables . . . . .	V
List of Figures . . . . .	VI
Nomenclature . . . . .	X
1.0 INTRODUCTION . . . . .	1
1.1 Motivation . . . . .	1
1.2 Scope . . . . .	2
1.3 Objectives . . . . .	4
2.0 LITERATURE REVIEW . . . . .	5
3.0 THEORETICAL CONSIDERATIONS . . . . .	14
3.1 Continuity and Reynolds Equations . . . . .	14
3.2 Vorticity Equation . . . . .	25
3.3 Mechanical Dissipation Function . . . . .	27
3.4 Mean Energy Equation . . . . .	29
3.5 Turbulent Energy Equation . . . . .	38
3.6 Mean Total Energy Equation . . . . .	41
4.0 EXPERIMENTAL FACILITY AND EQUIPMENT . . . . .	43
4.1 Wind Tunnel . . . . .	43
4.2 Test-Sections . . . . .	44
4.3 Traversing Mechanisms . . . . .	45
4.4 Pitot and Static Pressure Probes . . . . .	47
4.5 Hot-Wire Equipment . . . . .	48

5.0	EXPERIMENTAL RESULTS AND DISCUSSION . . . . .	51
5.1	Proof of Developed Flow . . . . .	51
5.2	Flow Symmetry . . . . .	54
5.3	Friction Factors . . . . .	60
5.4	Local Wall Shear Stress Distributions . . . . .	63
5.5	Mean Axial Velocity Distributions . . . . .	69
5.6	Normal Stresses and Turbulent Kinetic Energy . . . . .	76
5.7	Shear Stresses and Correlation Coefficients . . . . .	86
5.8	Axial Turbulence Power Spectra and Microscale . . . . .	92
5.9	Secondary Flows . . . . .	96
6.0	CONCLUDING REMARKS . . . . .	104
7.0	ACKNOWLEDGEMENTS . . . . .	111
8.0	REFERENCES . . . . .	112
APPENDIX A -	Description of Wind Tunnel Design and Construction . . . . .	120
APPENDIX B -	Friction Velocity Correction . . . . .	127
APPENDIX C -	Wall Shear Stress Probe . . . . .	131
APPENDIX D -	Approximate Mean Energy Equation Calculations . . . . .	134
TABLES	. . . . .	139 - 142
FIGURES	. . . . .	143 - 251

## LIST OF TABLES

<u>Table</u>		<u>Page</u>
I	Summary of Test Conditions - Triangular Array Rod Bundles - Fully Developed Flow. . . . .	139
II	Summary of Least-Squares-Fit Results for Mean Axial Velocity Variations in the Radial Direction. . . . .	140
III	Some Three-Wire Probe Results - Test A1 . . . . .	142

## LIST OF FIGURES

<u>Figure</u>		<u>Page</u>
1	Cross-section of typical nineteen element fuel bundle showing the various sub-channels	143
2	Cross-sections of test-sections used by previous investigators	144
3	Cross-section of test-section IA - $P/D = 1.50$	145
4	Cylindrical coordinate system and velocity directions	146
5	Variation of fluid shear stress at radial boundaries of primary flow cell	147
6	Plan view of wind tunnel for rod bundle turbulence studies	148
7	Wind tunnel flow calibration	149
8	Probe/traversing mechanism-assembly	150
9	Pitot and static pressure probes	151
10	Schematic of wire orientation for u-v X-probe	152
11	Schematic of wire orientation for u-w X-probe	153
12	Sub-division of flow cell geometry for rod bundle of $P/D = 1.50$	154
13	Sub-division of flow cell geometry for rod bundle of $P/D = 1.35$	155
14	Sub-division of flow cell geometry for rod bundle of $P/D = 1.20$	156
15	Mean velocities along sub-channel center-line for test-section IA ( $P/D = 1.50$ )	157

<u>Figure</u>		<u>Page</u>
16	Static pressure along sub-channel center-line for test-section IA ( $P/D = 1.50$ )	158
17	Relative axial turbulence intensities along sub-channel center-line for test-section IA ( $P/D = 1.50$ )	159-159a
18	Identification of primary flow cells for symmetry studies	160
19	Some turbulence distributions along $\hat{y}_{\max}$ boundaries - Test section IC	161
20	Some turbulence distributions along $\hat{y}_{\max}$ boundaries - Test-section IB	162
21	Variations of $R_{uw}$ at fixed distances from central rod surface	163
22	Variations of $R_{uw}$ across primary flow cell 1 and its radial boundaries	164
23	Plot of static pressure vs axial distance along test-section - Test B4	165
24	Experimental friction factor data	166
25	Local wall shear stress variations - $P/D = 1.20$	167
26	Comparison of wall shear stress distribution with other studies	168
27	Local wall shear stress variations - $P/D = 1.35$	169
28	Wall shear stress fluctuations	170
29	Normalized spectrum of wall shear stress for pipe flow ( $Re = 86,000$ )	171
30	Wall shear stress power spectra	172

<u>Figure</u>		<u>Page</u>
31	Isovel plots ~ $P/D = 1.50$	173 - 175
32	Isovel plots ~ $P/D = 1.35$	176 - 178
33	Isovel plots ~ $P/D = 1.20$	179 - 181
34	Distributions of mean axial velocity in the peripheral direction	182 - 184
35	Least-squares-fit lines ~ $P/D = 1.50$ - All tests - $Re = 24,000$ to $84,000$	185
36	Distribution of mean axial velocity in the radial direction ~ $P/D = 1.50$ , Test A1	186
37	Velocity defect plots ~ Test Cond. 5 - $Re = 36,000$	187
38	Turbulence intensities measured by different probes ~ $P/D = 1.35$ , Test B4, $\theta = 30^\circ$	188
39	Axial turbulence distributions	189 - 194
40	Radial turbulence distributions	195 - 200
41	Peripheral turbulence distributions	201 - 206
42	Mean turbulent kinetic energy distributions	207 - 212
43	Distributions of mean turbulent kinetic energy on $y = \bar{y}$ boundary - Test Cond. 5, $Re = 36,000$	213
44	Plot of $u'$ at center of half gap as function of tube spacing and Reynolds number	214
45	Distributions of $R_{uv}$	215 - 220
46	Distributions of Reynolds shear stress $\overline{uv}$	221 - 226
47	Correlation between turbulent shear stress and mean turbulent kinetic energy for rod bundle flows	227

<u>Figure</u>		<u>Page</u>
48	Distributions of $R_{uw}$	228 - 233
49	Distributions of Reynolds shear stress $\overline{uw}$	234 - 239
50	Distributions of eddy diffusivities in the radial direction	240
51	Power spectra of axial turbulence	241 - 246
52	Microscale distributions	247
53	Microscale distributions - $P/D = 1.20$	248
54	Inferred Secondary Flow Pattern - $P/D = 1.50$	249
55	Inferred Secondary Flow Pattern - $P/D = 1.35$	250
56	Inferred Secondary Flow Pattern - $P/D = 1.20$	251

## NOMENCLATURE

$D$	tube diameter
$D_h$	equivalent hydraulic diameter
$E$	energy spectrum function
$f$	friction factor defined by equation (26)
$g_c$	dimensional universal constant
$k$	wavenumber
$L$	axial distance from start of test-section
$\ln$	natural logarithm
$n$	frequency
$P$	pitch (distance between rod centers)
$p^*$	instantaneous static pressure
$\bar{p}$	mean static pressure
$\bar{Q}$	mean flow kinetic energy per unit mass
$Q'$	instantaneous total kinetic energy per unit mass
$\bar{q}$	mean turbulent kinetic energy per unit mass
$q'$	defined by equation (41)
$R$	tube radius
$\hat{R}$	radial length = $\hat{y} + R$
$r$	radial distance from center of tube (radial coordinate)
$Re$	Reynolds number based on $U_b$ and $D_h$
$R_{uv}$	Correlation coefficient = $\overline{uv}/(u'v')$
$R_{uw}$	correlation coefficient = $\overline{uw}/(u'w')$
$S$	normalized power spectral density
$t$	time
$u, v, w$	fluctuating components of the velocities in the axial, radial and peripheral directions respectively
$u', v', w'$	root-mean-square values (rod bundle)
$u'_p, v'_p, w'_p$	root-mean-square values for comparable pipe flow



$u^*$	friction velocity (rod bundle)
$u_p^*$	friction velocity for comparable pipe flow
$u^+$	dimensionless mean axial velocity = $\bar{U}/\bar{u}^*$
$U$	instantaneous axial velocity
$\bar{U}$	axial mean velocity (time-average)
$U_b$	average mean axial velocity over primary flow cell cross-section (bulk velocity)
$U_c$	average mean axial velocity at contraction cone exit
$v^+$	dimensionless mean radial velocity = $\bar{V}/\bar{u}^*$
$V, W$	instantaneous velocities in the radial and peripheral directions respectively
$\bar{V}, \bar{W}$	Radial and peripheral mean velocities (secondary velocities)
$x$	axial coordinate
$y$	radial distance from tube wall
$\hat{y}$	radial distance from wall to primary flow cell boundary
$y^+$	dimensionless radial distance from wall = $y \bar{u}^*/\nu$
$\alpha$	proportional
$\epsilon$	eddy diffusivity for momentum
$\theta$	angular location = $\pi - \phi$
$\lambda$	microscale = $\bar{U} u' / \left[ \overline{(du/dt)^2} \right]^{1/2}$
$\mu$	laminar dynamic viscosity
$\nu$	kinematic viscosity = $\mu/\rho$
$\rho$	air density (rod bundle)
$\rho_c$	air density at contraction cone
$T_{rx}$	shear stress acting on fluid element on surface perpendicular to $r$ in the direction $x$
$T_w$	wall shear stress
$\phi$	angular coordinate
$\Phi$	dissipation rate

$\psi$	stream function defined by equation (30)
$\bar{\omega}$	mean axial vorticity component defined by equation (29)
$\omega^+$	defined in Figure 29 where $\omega = 2 \pi n$
$\nabla^2$	Laplacian operator

### Subscripts

dd	direct dissipation
max	maximum
min	minimum
r	radial
td	turbulent dissipation
$\phi$	peripheral

— overbar designates time-averaging in general, but  $\bar{u}^*$  and  $\bar{\tau}_w$ , called the average friction velocity and average wall shear stress respectively, are the means of the local time-average values obtained by averaging over the rod perimeter of the primary flow cell.

## THE STRUCTURE OF TURBULENT FLOW IN TRIANGULAR ARRAY ROD BUNDLES

### 1.0 INTRODUCTION

#### 1.1 Motivation

Nuclear reactor fuel channels generally consist of a cluster of fuel rods arranged in a flow tube with the coolant moving axially through the sub-channels formed between neighbouring fuel rods and between the peripheral fuel rods and the flow tube. The cross-section of a typical nineteen element fuel bundle channel is shown in Figure 1 which illustrates the various sub-channel shapes. It may be noted that of the 18 interior sub-channels, 12 are triangular array and 6 are square array. There exists little fundamental knowledge of the turbulent flow structure in these sub-channels. Fuel channel designs are currently based largely on heat transfer and sub-channel mixing technology derived from a multitude of full scale ad hoc experiments.

It is well known that increasing reactor coolant outlet temperatures will increase Carnot cycle and actual cycle efficiencies. Advances in material science are gradually allowing for higher fuel sheath and pressure tube temperatures. In order to fully capitalize on improved high temperature materials, it is imperative that fuel be designed at the optimum heat transfer consistent with hydraulic, neutron and fabrication cost considerations. Single-phase coolant candidates for advanced heavy water moderated reactors range from liquid metals

(low Prandtl numbers) to molten salts (high Prandtl numbers). This wide variety of heat transfer conditions makes it even more important that a firm foundation for the heat transfer work be laid by a thorough investigation of the flow structure in rod bundles. As a minimum, turbulence research provides valuable insight into fuel design and the interpretation of heat transfer test results. It is even feasible in the limit, that new fuel-coolant designs could be based entirely on numerical solutions of the momentum and thermal energy equations by using turbulence data and the momentum-heat transfer analogy with respect to the eddy diffusivities.

## 1.2 Scope

The experimental study described herein concerns the fully developed flow structure in rod bundles arranged to simulate infinite equilateral triangular arrays. As alluded to above, the triangular geometry is the most common encountered in current fuel designs. For infinite arrays, each sub-channel consists of six symmetric flow cells. Secondary flows are also confined by symmetry to individual flow cells, hence there are no complicating effects due to secondary flows between heterogeneous sub-channels or induced by finite array effects. For triangular arrays, pitch ( $P$ , distance between rod centers) to rod diameter ( $D$ ) ratios of interest for the potential coolants, range

from  $P/D = 1.06$  to  $1.50$ . The present work has dealt with three test-sections having  $P/D$  ratios of  $1.50$ ,  $1.35$  and  $1.20$ , the latter being a lower practical limit corresponding to the rod size involved.

Aluminum alloy tubes of  $5.08$  cm O.D. were used as rods for all test-sections, hence the geometric variable was  $P/D$  in the form of rod spacing. A complementary program in which the pitch is held constant while the rod diameter is varied (preferable down to  $P/D$  ratios of at least  $1.10$ ), may be necessary in order to confidently extrapolate to reactor fuel rod sizes.

Each of the three test-sections was installed in turn in a closed return wind tunnel, and mean flow and turbulence measurements were made under steady flow isothermal conditions. The Reynolds number range under investigation was  $12,000$  to  $84,000$ ; being limited by the wind tunnel capacity. For the same geometric scale and fully developed flow, in view of the pressure drop characteristics of the rod bundle channels, higher Reynolds numbers would be best accomplished using a liquid facility.

The research project was sponsored by Atomic Energy of Canada Limited. The project history is contained in a series of annual progress reports<sup>(1) (2) (3)</sup>.

### 1.3. Objectives

The primary experimental objectives were to obtain data on the spatial distributions (within central sub-channels of triangular array rod bundles) of mean velocities and Reynolds stresses as functions of Reynolds number and tube spacing for fully developed flow. These objectives were largely met, however only very limited information was obtained on the shear stress  $\rho \overline{v'w'}$  and on the secondary velocities. Although evidence of secondary flows was observed experimentally, it was not possible to obtain reliable measurements of the secondary velocities via X-probe or three-wire probe<sup>(4)</sup>. The problem was simply that the very small secondary velocities were continually being swamped by errors incurred by imperfect matching of anemometer channels, relative drift and signal processing. Nonetheless, by using several techniques employing the experimental data, it was possible to deduce certain general features of the secondary flow patterns and to establish the order of magnitude of the secondary velocities.

## 2.0 LITERATURE REVIEW

The only known publications on turbulence characteristics in triangular array rod bundles are those due to Kjellstrom et al originating from AB Atomenergi, Sweden, where a project on fundamental studies of turbulent transport phenomena in rod bundle flows has been underway for several years. It is highly probable that some hot-wire research on rod bundles is in progress in the U.S.A., U.S.S.R. and Great Britian, however there are apparently no publications in the open literature. Only the literature of direct relevance to the current work is reviewed. This includes the literature on secondary flows in other asymmetric geometries. This mechanism has been found to play a key role in rod bundle flows.

In contrast to the lack of fundamental work, a survey of the fluid mechanical and thermal aspects of nuclear fuel design technology, readily shows that a large number of experimental and analytical studies on velocity distributions, friction factors, heat transfer coefficients and sub-channel mixing for rod bundles, have been carried out starting about 1955. Comprehensive reviews of the major contributions in these areas up to 1968 are contained in Reference 5. Although of obvious peripheral relevance, no attempt is made here to review the current technology. However, it is interesting to note that the need for fundamental work has been widely recognized. Rogers and Todreas<sup>(5)</sup>,

in their survey on coolant interchannel mixing, specifically recommend turbulence measurements in large-scale models of fuel bundle geometries as a useful step towards eventually arriving at a reliable generalized correlation for natural mixing by turbulent interchange\*. Rosehart and Rogers in a later report<sup>(6)</sup> continued to advocate turbulence research, and obtained inferred relationships between  $P/D$  and the ratio of the Lagrangian integral scale of turbulence to a 'mixing distance'. Their empirical mixing equation for turbulent interchange entails a pseudo mass cross-flow between neighbouring sub-channels which is expressed as a function of sub-channel geometries, eddy diffusivity for heat and a 'mixing distance' between sub-channels. For infinite triangular arrays, or homogeneous sub-channels in general, this turbulent mixing flow rate represents energy transport between sub-channels due to pressure and velocity fluctuations, and there is, of course, no net flow across a sub-channel boundary. Singh and St. Pierre<sup>(7)</sup> have recently qualitatively explained their turbulent mixing results for square-square sub-channels on the basis of secondary flows and their ability, depending on gap size and flow Reynolds number, to penetrate into the gap region

---

\*Defined as natural eddy diffusion between the sub-channels of a bundle of smooth, bare rods. Other recognized mixing effects are 'diversion cross-flow' resulting from flow redistribution caused by rod bowing, non-uniform heat flux distributions, etc., and 'flow scattering' and 'flow sweeping' as the result of forced mixing induced by end plates, spacers, wire wrap, etc.



and thus influence turbulent mixing rates. For heterogeneous sub-channels, there is still no net flow across the common boundary, however, due to secondary flows there may be a net flow along one portion of a boundary and an opposite net flow along another portion of the same boundary. Skinner et al<sup>(8)</sup> found experimental mixing rates between heterogeneous sub-channels to be greater than could be explained by turbulent diffusion theory, and properly attributed the large mixing rates to secondary flows. This prompted Rowe<sup>(9) (10)</sup> to modify the eddy diffusion model of turbulent interchange mixing by altering the 'mixing distance' criteria. Rowe also has noted that much more fundamental work must be done to identify the mixing mechanisms in order that meaningful correlations can be developed.

A number of analytical studies have been conducted to predict velocity distributions in rod bundles for various rod spacings and Reynolds numbers. This information is prerequisite to the solution of the thermal energy equation which contains velocity in the convective terms. For triangular array rod bundles in laminar flow, solutions are available for the velocity fields<sup>(11) (12)</sup> and for the heat transfer for the case of uniform peripheral surface temperature<sup>(13)</sup>. For turbulent flow, the pioneering work was by Deissler and Taylor<sup>(14)</sup> in 1956. Other prediction methods followed; notably Buleev<sup>(15)</sup> (1964), Rapier and Redman<sup>(16)</sup> (1964), Nijssing et al<sup>(17)</sup> (1966), Dwyer<sup>(18)</sup> (1966),

Bender and Switick<sup>(19)</sup> (1968) and Cook<sup>(20)</sup> (1969). These methods have been reviewed and compared by Kjellstrom and Stenback<sup>(21)</sup>. All neglect secondary flows, and hence typically predict local wall shear stress to increase monotonically from the position facing the gap to the position facing the sub-channel axial centerline. In principle, the method of Gosman et al<sup>(22)</sup> is capable of solving this secondary flow problem by using experimental data for the source terms. This method has been successfully applied to the square duct problem<sup>(23)</sup>, but Kjellstrom<sup>(24)</sup> could not obtain a convergent solution for the rod bundle sub-channel problem.

At turbulent Reynolds numbers, the time-averaged longitudinal flow in a straight duct of non-circular cross-section, consists of helical streamlines. The lateral spiral motion, classified as secondary flow of the second kind, is usually described by the distributions of the mean velocity components in the plane normal to the longitudinal flow. Here the secondary velocities form closed contour streamlines in certain regions of the cross-section. Usually one cell of secondary flow exists in each symmetric part of the cross-section, with the circulation being opposite-handed in neighbouring cells; however, more than one cell may exist in a symmetric part<sup>(25)</sup>. Secondary flows, by convecting main flow momentum and energy towards the walls in some regions and away from the walls in other regions, act to equalize the wall shear stresses and

and maintain the primary flow isovels (contours of constant velocity) parallel to the nearest wall.

For rectangular shaped ducts, the effects of secondary flow on the axial velocity distribution (bulging of isovels towards the duct corners and away from the mid-wall) were first reported by Nikuradse<sup>(26)</sup> in 1926. Prandtl<sup>(27)</sup>, at the time, postulated that velocity fluctuations along the isovel lines, caused a transverse mean flow to develop in regions of isovel curvature which was directed from the concave towards the convex side of the isovel. This meant a secondary flow from the center of the duct along the corner bisector towards the corner, and a return flow along the wall and then back to the center from the mid-wall. This pattern was not confirmed until 1960 when Hoagland<sup>(28)</sup> succeeding in measuring the secondary velocities using a very sensitive hot-wire system. Maximum secondary velocities of about 1 to 1½ percent of the axial centerline velocity were recorded near the wall in the corner region. Later, Brundrett and Baines<sup>(29)</sup> measured the components of the Reynolds stress tensor, and evaluated the point density of the production, diffusion and convection of the axial vorticity. They found that vorticity production was predominately due to gradients of the normal stresses in the plane of the cross-section. Gessner and Jones<sup>(30)</sup> reported on a number of interesting aspects of turbulent flow in rectangular channels, including the cause of secondary flow from a

momentum standpoint by evaluating the terms (except pressure) in the equation along a secondary flow streamline in streamline coordinates. The driving force for secondary flow was traced tentatively to small differences in magnitude of opposing forces exerted by the Reynolds stresses and static pressure gradients in the plane normal to the axial flow direction. Gessner and Jones also found that secondary velocities, when non-dimensionalized by either the bulk velocity or the axial centerline velocity, decreased with increasing Reynolds number. However, Launder and Ying<sup>(31)</sup> established that secondary velocities normalized with friction velocity are effectively independent of Reynolds number. Recent studies by Gessner<sup>(32)</sup> have shown that secondary flow is generated by turbulent shear stress gradients normal to the corner bisector. In regard to the various roles played by secondary flow as a convective transport mechanism, Gessner categorized convection of momentum and total energy of the mean motion as first-order effects, whereas convective transport of streamwise vorticity and turbulence kinetic energy are second-order effects. Concerning the latter, Hinze<sup>(33)</sup> has suggested a simple rule for deducing the existence and direction of secondary flow. When, in a localized region, the production of turbulence kinetic energy is much greater (smaller) than the dissipation, energy conservation requires there to be a secondary current that transports turbulence-poor fluid into (out of) this region

and turbulence-rich fluid out of (into) the region. This rule caters to situations where production and dissipation rates differ by amounts which exceed normal rates of convection of turbulent kinetic energy by turbulence.

Experimental data on secondary flows in other geometries is sparse. Lyall<sup>(34)</sup> has reported on a geometry consisting of two square interconnected sub-channels, 76.2 mm and 50.8 mm square. Two configurations were tested; the interconnecting gap fully open, and half closed by dividing plates. For both configurations, peak secondary velocities of about 3½% of the local axial mean velocity were recorded near the gap region. The distribution of the flow between the two sub-channels was unexpectedly uniform, indicating a significant momentum transfer from the larger to the smaller sub-channel via the interconnecting gap. Since the secondary velocity data were inadequate to confidently infer the secondary flow patterns, Lyall proceeded to model the secondary flows and was reasonably successful in quantizing the momentum transfer required to provide the observed degree of primary flow uniformity in the two sub-channels. Concerning the relative importance of momentum transports by turbulence and by secondary flows, Lyall estimated that secondary flow convection becomes greater than turbulent diffusion when the ratio of secondary velocity to primary velocity exceeds about  $10^{-3}$ , a level which of course is readily surpassed in practise. Kjellstrom<sup>(24)</sup> arrived at a

similar conclusion.

Kacker<sup>(25)</sup> recently conducted an experimental study of fully developed turbulent flow in a circular pipe (14.43 cm I.D.) containing one or two rods (2.54 cm O.D.) located off-center. The measurements included mean velocity, wall shear stress and peripheral secondary velocity distributions. For the single-pin geometry (eccentric annulus), one flow cell was found to exist in each symmetric half of the geometry. The secondary flow pattern was such as to convect fluid momentum from the region of high velocity (largest gap) to the region of low velocity (smallest gap). Secondary velocities were of the order of 1% of the local axial mean velocities. For the two-pin geometry, a very interesting result emerged. Each of the four symmetric quadrants contained two counter-rotating flow cells--a large cell similar to the single-pin geometry, and a small cell sandwiched between the central region of the pipe and the half pin. The total flow in the small cell was nearly 60% of the flow in the large cell. The magnitudes of secondary velocity were similar to the single-pin geometry.

Turning finally to the available experimental results on mean velocity distributions, local wall shear stress variations and turbulence characteristics for triangular array rod bundle sub-channels, only the scopes of the various studies are outlined. Further details of the published data are given in conjunction with discussion of the present

experimental results. Palmer and Swanson<sup>(35)</sup> (1961) measured mean axial velocity distributions for air flow through a tricuspid channel of  $P/D = 1.015$  at a Reynolds number of 20,000 using a fine Pitot tube near the wall and in the narrow gap region and a Kiel probe elsewhere. Eifler and Nijssing<sup>(36)</sup> (1967), using an adjustable test-section and water flow, systematically explored mean axial velocity distributions via Pitot tube for  $P/D$  ratios of 1.05, 1.10 and 1.15 at Reynolds numbers of 15,000, 30,000 and 50,000. Subbotin et al<sup>(37)</sup> (~1968), using a test-section similar to Eifler and Nijssing but involving air flow, investigated mean axial velocity distributions (Pitot tube) and wall shear stress distributions (Preston tube) for  $P/D$  ratios of 1.05, 1.10 and 1.20 at Reynolds numbers of about 40,000. Kjellstrom and Stenback<sup>(21)</sup> (1970) measured mean axial velocity distributions (Pitot tube), wall shear stress distributions (Preston tube) and the distributions of five Reynolds stresses (constant temperature hot-wire anemometry-single wire and  $45^\circ$  slanting wire) for air flow through a tricuspid channel of  $P/D = 1.217$  at Reynolds numbers of 149,000, 271,000 and 355,000. Hall and Svenningsson<sup>(38)</sup> (1971) used the same experimental facility as Kjellstrom and Stenback ( $P/D = 1.217$ ), and measured wall shear stress distributions (Preston tube) and peripheral secondary velocities (rotatable hot-wire) at a Reynolds number of 270,000. Cross-sections of the test-sections used by the above investigators are shown in Figure 2. Finite array effects have been discussed by the various authors.

### 3.0 THEORETICAL CONSIDERATIONS

The three test-sections involved in the present study were of similar design; each having 5.08 cm O.D. tubes but different spacing between tubes. A cross-sectional view of one of the test-sections (typical of all) is shown in Figure 3. Each tricuspid sub-channel is symmetric in six parts, each part constituting a 'primary flow cell'. The primary flow cell under study was one adjacent to the central tube as indicated in Figure 3. In the following paragraphs, the various fluid-mechanical equations are developed and discussed as applicable to turbulent, fully-developed, steady flow of an incompressible, isothermal fluid ( $\rho = \text{const.}$ ,  $\mu = \text{const.}$ ) through a primary flow cell of an infinite array. Special attention is given to deriving analytical techniques for obtaining information on the secondary flows. Since the array is infinite, due to symmetry, there is no momentum transfer across the boundaries of the primary flow cell, and this is reflected in formulating the boundary conditions.

#### 3.1 Continuity and Reynolds Equations

The cylindrical polar coordinate system  $(r, \phi, x)$  is shown in Figure 4. The primary flow is in the positive  $x$ -direction. Due to the fully developed flow conditions,  $\partial \bar{P} / \partial x = \text{constant}$  and  $\partial (\bar{u}) / \partial x = 0$ . The boundary conditions are: At the wall, due to the no-slip condition:

- 1)  $\bar{U} = \bar{V} = \bar{W} = 0 = u = v = w$  at  $y = 0$ , all  $\theta$  or  $\phi$ .



Due to symmetry with neighbouring cells:

$$2) \frac{\partial (\bar{\psi})}{\partial \theta} = 0 = - \frac{\partial (\bar{\psi})}{\partial \phi} \text{ at } \theta = 0 \text{ and } \pi/6, \text{ all } y;$$

$$3) \cos \theta \frac{\partial (\bar{\psi})}{\partial r} - \frac{\sin \theta}{r} \frac{\partial (\bar{\psi})}{\partial \theta} = 0 \text{ at } y = \hat{y}, \text{ all } \theta,$$

i.e. at  $r = P/2 \cos \theta$ ; and

$$4) \frac{\partial (\bar{\psi})}{\partial r} = 0 \text{ at the singular point } r = P/2; \text{ and, at least}$$

$$\frac{\partial \bar{U}}{\partial r} = 0 \text{ at } r = P/2 \cos (\pi/6) \text{ since here } \bar{U} \text{ is a maximum.}$$

In addition, since the secondary flow is bounded by lines of symmetry:

$$5) \bar{W} = 0 \text{ at } \theta = 0 \text{ and } \pi/6, \text{ all } y; \text{ and}$$

$$6) \bar{W} = 0 = \bar{V} \text{ at the singular points defined by } r = P/2 \\ \text{and } r = P/2 \cos (\pi/6).$$

The continuity equations representing conservation of mass are:

$$\frac{\partial U}{\partial x} + \frac{1}{r} \frac{\partial rV}{\partial r} + \frac{1}{r} \frac{\partial W}{\partial \phi} = 0 \quad \dots \dots \dots (1)$$

$$\frac{1}{r} \frac{\partial r\bar{V}}{\partial r} + \frac{1}{r} \frac{\partial \bar{W}}{\partial \phi} = 0 \quad \dots \dots \dots (2)$$

$$\frac{\partial u}{\partial x} + \frac{1}{r} \frac{\partial rv}{\partial r} + \frac{1}{r} \frac{\partial w}{\partial \phi} = 0 \quad \dots \dots \dots (3)$$

At the two radial boundaries defined by  $\theta = 0$  and  $\Pi/6$ , due to B.C. 2, equation (2) reduces to:

$$\frac{1}{r} \frac{\partial r\bar{V}}{\partial r} = 0 \quad \text{or } r\bar{V} = \text{constant} \quad \dots \dots \dots (4)$$

Since  $\bar{V} = 0$  at each end of these boundaries (B.C. 1 and 6), the only solution is  $r\bar{V} = 0$ , i.e.  $\bar{V} = 0$  everywhere. This is consistent with the fact that the secondary flow is confined within the primary flow cell, and in fact the primary flow cell boundaries define the secondary flow streamline  $\bar{\psi} = 0$ . (The stream function  $\bar{\psi}$  is defined in Section 3.2 and satisfies continuity.)

The Reynolds equations representing conservation of momentum are:

For the x-direction:

$$\bar{V} \frac{\partial \bar{U}}{\partial r} + \frac{\bar{W}}{r} \frac{\partial \bar{U}}{\partial \phi} = - \frac{1}{\rho} \frac{\partial \bar{P}}{\partial x} - \left[ \frac{1}{r} \frac{\partial r\bar{U}\bar{V}}{\partial r} + \frac{1}{r} \frac{\partial \bar{U}\bar{W}}{\partial \phi} \right] + \nu \left[ \frac{\partial^2 \bar{U}}{\partial r^2} + \frac{1}{r} \frac{\partial \bar{U}}{\partial r} + \frac{1}{r^2} \frac{\partial^2 \bar{U}}{\partial \phi^2} \right] \quad (5)$$

For the r-direction:

$$\bar{V} \frac{\partial \bar{V}}{\partial r} + \frac{\bar{W}}{r} \frac{\partial \bar{V}}{\partial \phi} - \frac{\bar{W}^2}{r} = - \frac{1}{\rho} \frac{\partial \bar{P}}{\partial r} - \left[ \frac{1}{r} \frac{\partial}{\partial r} r\bar{V}^2 + \frac{1}{r} \frac{\partial \bar{V}\bar{W}}{\partial \phi} - \frac{\bar{W}^2}{r} \right] + \dots \dots \dots (6)^*$$

$$+ \nu \left[ \frac{\partial^2 \bar{V}}{\partial r^2} + \frac{1}{r} \frac{\partial \bar{V}}{\partial r} + \frac{1}{r^2} \frac{\partial^2 \bar{V}}{\partial \phi^2} - \frac{\bar{V}}{r^2} - \frac{2}{r^2} \frac{\partial \bar{W}}{\partial \phi} \right]$$

---

\*Due to the fully developed flow condition, by differentiating equations (6) and (7) with respect to x, it follows that  $\partial \bar{P} / \partial x$  is independent of both r and  $\phi$ .

For the  $\phi$ -direction:

$$\bar{V} \frac{\partial \bar{W}}{\partial r} + \frac{\bar{W}}{r} \frac{\partial \bar{W}}{\partial \phi} + \frac{\bar{V}\bar{W}}{r} = -\frac{1}{\rho r} \frac{\partial \bar{P}}{\partial \phi} - \left[ \frac{\partial}{\partial r} \bar{v}\bar{w} + \frac{1}{r} \frac{\partial \bar{w}^2}{\partial \phi} + \frac{2\bar{v}\bar{w}}{r} \right] +$$

$$+ \nu \left[ \frac{\partial^2 \bar{W}}{\partial r^2} + \frac{1}{r} \frac{\partial \bar{W}}{\partial r} + \frac{1}{r^2} \frac{\partial^2 \bar{W}}{\partial \phi^2} + \frac{2}{r^2} \frac{\partial \bar{V}}{\partial \phi} - \frac{\bar{W}}{r^2} \right] \quad (7)$$

By defining the eddy diffusivities for momentum (eddy viscosities) in the radial and peripheral directions by:

$$-\bar{u}\bar{v} = \epsilon_r \frac{\partial \bar{U}}{\partial r} \quad \dots \dots \dots (8)$$

and

$$-\bar{u}\bar{w} = \frac{\epsilon_\phi}{r} \frac{\partial \bar{U}}{\partial \phi} \quad \dots \dots \dots (9)$$

respectively, equation (5) may be rewritten as:

$$\bar{V} \frac{\partial \bar{U}}{\partial r} + \frac{\bar{W}}{r} \frac{\partial \bar{U}}{\partial \phi} = -\frac{1}{\rho} \frac{\partial \bar{P}}{\partial x} + \frac{1}{r} \frac{\partial}{\partial r} r \left[ (\epsilon_r + \nu) \frac{\partial \bar{U}}{\partial r} \right] +$$

$$+ \frac{1}{r} \frac{\partial}{\partial \phi} \left[ (\epsilon_\phi + \nu) \frac{1}{r} \frac{\partial \bar{U}}{\partial \phi} \right] \quad \dots \dots \dots (10)$$

At the two cell boundaries defined by  $\phi = 0$  and  $\Pi/6$ , since

$\bar{W} = 0 = \bar{V}$  and in view of B.C. 2, the Reynolds equations reduce to:

$$0 = -\frac{1}{\rho} \frac{\partial \bar{P}}{\partial x} - \frac{1}{r} \frac{\partial}{\partial r} r \bar{u}\bar{v} + \frac{\nu}{r} \frac{\partial}{\partial r} \left[ r \frac{\partial \bar{U}}{\partial r} \right] \quad \dots \dots \dots (11)$$

$$0 = -\frac{1}{\rho} \frac{\partial \bar{P}}{\partial r} - \frac{1}{r} \frac{\partial}{\partial r} r \bar{v}^2 + \frac{\bar{w}^2}{r} \quad \dots \dots \dots (12)$$

$$0 = -\frac{\partial \bar{v}\bar{w}}{\partial r} - \frac{2\bar{v}\bar{w}}{r} \quad \dots \dots \dots (13)$$

By using B.C. 4 in equation (12), it can be shown that  $v' = w'$  at the singular point  $r = P/2$  and perhaps at  $r = P/2 \cos(\Pi/6)$ . Equations (11), (12) and (13) are the same as for fully developed pipe flow.

Regarding equation (13), as a result of peripheral symmetry (B.C. 2), by employing the same argument used by Laufer<sup>(39)</sup>, it may be shown that  $\bar{w} = 0$  over these radial boundaries. Having thus formally established that there is no peripheral momentum transfer across the boundaries\* defined by  $\theta = 0$  and  $\Pi/6$ , it may be further shown, by simple force balance involving pressure and fluid shear stress, that:

$$\frac{T_{rx}}{T_w} = \frac{R}{r} \left[ \frac{\hat{R}^2 - r^2}{\hat{R}^2 - R^2} \right] \dots \dots \dots (14)$$

where  $T_{rx}$  is the shear stress acting on a fluid element over the surface perpendicular to  $r$  in the  $x$ -direction,  $T_w$  is the local wall shear stress, and  $\hat{R} = \hat{y} + R$ . Thus  $T_{rx}$  varies monotonically from  $T_{rx} = T_w$  at  $r = R$  to  $T_{rx} = 0$  at  $r = \hat{R}$ . The non-linear variation has been calculated for each of the six radial boundaries associated with  $P/D = 1.50, 1.35$  and  $1.20$ .

The envelope of the distributions is shown in Figure 5. For each distribution, the maximum deviation from the linear (pipe flow)

---

\*A convenient proof for the  $y = \hat{y}$  boundary is obtained by locating the origin of a cylindrical coordinate system at the mid-gap, and treating the sub-channel as symmetric in two parts. The procedure is parallel to the one given here, and like the present proof, is predicated on a boundary condition of  $\partial(\bar{w})/\partial\phi = 0$  which stems from symmetry for an infinite array.

distribution occurs at:

$$\frac{r}{\hat{R}} = \sqrt{\frac{R}{\hat{R}}}, \text{ or equivalently, at } \frac{y}{\hat{y}} = \sqrt{\frac{R}{\hat{R}}} \left[ 1 + \frac{R}{\hat{y}} \right] - \frac{R}{\hat{y}}.$$

For  $P/D = 1.20$  and  $\Theta = 0^\circ$ , the maximum deviation occurs at  $y/\hat{y} = 0.4772$  where the shear stress is 4.75% lower than in pipe flow at the same dimensionless position. For  $P/D = 1.50$  and  $\Theta = 30^\circ$ , the corresponding figures are  $y/\hat{y} = 0.4318$  and 15.23% lower.

Equation (11) may be rewritten as:

$$r \frac{\partial \bar{P}}{\partial x} = - \rho \frac{\partial}{\partial r} r \bar{u} \bar{v} + \mu \frac{\partial}{\partial r} \left[ r \frac{\partial \bar{U}}{\partial r} \right]$$

Integration with respect to  $r$  over the limits  $r$  to  $\hat{R}$  yields:

$$\left[ \frac{\hat{R}^2 - r^2}{2} \right] \frac{\partial \bar{P}}{\partial x} = \rho r \bar{u} \bar{v} - \mu r \frac{\partial \bar{U}}{\partial r} \quad \dots \dots \dots (15)$$

where at  $r = \hat{R}$ ,  $\partial \bar{U} / \partial r = 0$  via B.C. 4 and  $\bar{u} \bar{v}$  has been assumed equal to zero.

At  $r = R$ , in view of B.C. 1, the equation is:

$$\left[ \frac{\hat{R}^2 - R^2}{2} \right] \frac{\partial \bar{P}}{\partial x} = - \mu R \left[ \frac{\partial \bar{U}}{\partial r} \right]_w = - R \rho (u^*)^2 \quad \dots \dots \dots (16)$$

$$\text{where } \mu \left[ \frac{\partial \bar{U}}{\partial r} \right]_w = g_c T_w = \rho (u^*)^2 \quad \dots \dots \dots (17)$$

Dividing equation (15) by (16) yields:

$$\frac{\hat{R}^2 - r^2}{\hat{R}^2 - R^2} = -\frac{r}{R} \left[ \frac{\overline{uv}}{(u^*)^2} - \frac{v}{(u^*)^2} \frac{\partial \bar{U}}{\partial r} \right] \dots \dots \dots (18)$$

By comparing equations (18) and (14), it follows that:

$$\frac{R}{r} \left[ \frac{\hat{R}^2 - r^2}{\hat{R}^2 - R^2} \right] = \frac{T_{rx}}{T_w} = -\frac{\overline{uv}}{(u^*)^2} + \frac{v}{(u^*)^2} \frac{\partial \bar{U}}{\partial r} \dots \dots \dots (19)$$

or

$$T_{rx} = -(\rho \overline{uv} + \mu \frac{\partial \bar{U}}{\partial r})/g_c \dots \dots \dots (20)$$

At  $r = \hat{R}$ ,  $T_{rx} = 0 = \partial \bar{U} / \partial r$ , hence  $\overline{uv} = 0$  which validates the earlier assumption. This fact was also confirmed experimentally.

Equation (20) shows that the local total fluid shearing stress at the radial boundaries, is composed only of the usual turbulent and viscous shear stresses. This however is not the general case. Mean flow shear stresses exist in the interior fluid. This may be demonstrated in an approximate manner as follows.

For a given radial boundary, the secondary flow streamlines are distributed symmetrically about the boundary. These streamlines would

tend to be parallel to the boundary ( $\bar{V} \neq 0$ ,  $\bar{W} = 0$ ) over its central portion. Suppose, for this region, that quantities averaged over a small area segment,  $d\theta$  wide and centered on the boundary, are used in equation (5). This would correspond roughly to the data recorded by X-probes straddling the boundary. Since the secondary flow cells on each side of the boundary are counter-rotating,  $\bar{V} \neq 0$  while  $\bar{W} = 0$ . By assuming  $\partial(\bar{\quad})/\partial\theta = 0$  (a good assumption except with respect to  $\bar{u}\bar{w}$  which, as shown later, has an antisymmetric character linked to the counter-rotation), equation (5) becomes:

$$\bar{V} \frac{\partial \bar{U}}{\partial r} = - \frac{1}{\rho} \frac{\partial \bar{P}}{\partial x} - \frac{1}{r} \frac{\partial r \bar{u}\bar{v}}{\partial r} + \frac{\nu}{r} \frac{\partial}{\partial r} r \frac{\partial \bar{U}}{\partial r}$$

or

$$r \frac{\partial \bar{P}}{\partial x} = - \rho \frac{\partial r \bar{u}\bar{v}}{\partial r} - \rho r \bar{V} \frac{\partial \bar{U}}{\partial r} + \mu \frac{\partial}{\partial r} r \frac{\partial \bar{U}}{\partial r}.$$

Since equation (4) now applies with  $r \bar{V} = \text{non-zero constant}$ , integration with respect to  $r$  gives:

$$\frac{r^2}{2} \frac{\partial \bar{P}}{\partial x} = - \rho r \bar{u}\bar{v} - \rho r \bar{V} \bar{U} + \mu r \frac{\partial \bar{U}}{\partial r} + C$$

or

$$\frac{r}{2} \frac{\partial \bar{P}}{\partial x} - \frac{C}{r} = - \rho (\bar{u}\bar{v} + \bar{U}\bar{V}) + \mu \frac{\partial \bar{U}}{\partial r} \quad \dots \dots \dots (21)$$

The LHS which includes the integration constant (C) represents  $T_{rx}$ . The RHS shows a mean flow shear stress. The above exercise also illustrates the experimental difficulty associated with evaluating equation (19).

It is also of interest to pursue the above approach with respect to equation (6) which becomes:

$$\bar{V} \frac{\partial \bar{V}}{\partial r} = - \frac{1}{\rho} \frac{\partial \bar{P}}{\partial r} - \frac{1}{r} \frac{\partial}{\partial r} r \bar{v}^2 + \frac{\bar{w}^2}{r}$$

The viscous term vanishes since

$$\frac{\partial^2 \bar{V}}{\partial r^2} + \frac{1}{r} \frac{\partial \bar{V}}{\partial r} - \frac{\bar{V}}{r^2} = 0$$

due to equation (4). Substituting  $\partial \bar{V} / \partial r = - \bar{V} / r$  from continuity gives:

$$\bar{V}^2 = \frac{r}{\rho} \frac{\partial \bar{P}}{\partial r} + r \frac{\partial \bar{v}^2}{\partial r} - (\bar{w}^2 - \bar{v}^2) \quad \dots \dots \dots (22)$$

In the absence of secondary flow (eg, fully developed pipe flow), the RHS = 0. For finite  $\bar{V}$ , the RHS > 0, which suggests that  $\bar{V}$  owes its existence here to small imbalances between the three terms. The magnitude of  $\bar{V}$  would also appear to be no greater than the order of magnitude of the root-mean-square fluctuating velocities.



Turning now to the interior flow, the Reynolds number for the primary flow has been defined by:

$$Re = \rho U_b D_h / \mu \quad \dots \dots \dots (23)$$

where  $U_b$  is the average mean axial velocity over the primary flow cell cross-section (bulk velocity) and  $D_h$  is the equivalent hydraulic diameter of the primary flow cell (same value as for the entire sub-channel), defined as four times the cross-sectional area divided by the actual wetted perimeter. The hydraulic diameter may be calculated from:

$$D_h = 2R \left[ \frac{2\sqrt{3}}{\pi} \left\{ \frac{P}{D} \right\}^2 - 1 \right] \quad \dots \dots \dots (24)$$

It may also be shown that the average friction velocity is:

$$(\bar{u}^*)^2 = \frac{g_c \bar{T}_w}{\rho} = - \frac{g_c}{\rho} \frac{D_h}{4} \frac{\partial \bar{P}}{\partial x} \quad \dots \dots \dots (25)$$

which permits direct evaluation of  $\bar{u}^*$  based on experimental pressure drop data. Equation (25) is identical to pipe flow where the term  $(D_h/4)$  reduces simply to half the pipe radius. By defining the friction factor (f) by:

$$- \frac{\partial \bar{P}}{\partial x} = \frac{f \rho U_b^2}{2 g_c D_h} \quad \dots \dots \dots (26)$$

the relationship between  $\bar{u}^*$  and  $f$  becomes:

$$\bar{u}^* = \left[ \frac{f U_b^2}{8} \right]^{1/2} \dots \dots \dots (27)$$

which is again the same as for pipe flow.

If  $\partial \bar{U} / \partial \phi = 0$ , equation (5) becomes:

$$\bar{V} \frac{\partial \bar{U}}{\partial r} = -\frac{1}{\rho} \frac{\partial \bar{P}}{\partial x} - \left[ \frac{1}{r} \frac{\partial r \bar{u} \bar{v}}{\partial r} + \frac{1}{r} \frac{\partial \bar{u} \bar{w}}{\partial \phi} \right] + \nu \left[ \frac{\partial^2 \bar{U}}{\partial r^2} + \frac{1}{r} \frac{\partial \bar{U}}{\partial r} \right]$$

If the wall shear stress variation is negligible, i.e.  $u^* = \bar{u}^*$ , this equation may be rewritten (using equation (25)) as:

$$v^+ \frac{\partial u^+}{\partial y} = \frac{4}{D_h} - \frac{\partial (\bar{u} \bar{v} / (\bar{u}^*)^2)}{\partial y} - \frac{\bar{u} \bar{v} / (\bar{u}^*)^2}{(y + R)} - \frac{1}{(y + R)} \frac{\partial (\bar{u} \bar{w} / (\bar{u}^*)^2)}{\partial \phi} +$$

$$+ \frac{y}{y^+} \left[ \frac{\partial^2 u^+}{\partial y^2} + \frac{1}{(y + R)} \frac{\partial u^+}{\partial y} \right] \quad (28)$$

The required conditions for equation (28) were found to be approximately met in the near-wall region, hence this equation provided a means for estimating  $\bar{V}$  in the near-wall region. Compared to pipe flow, the equation contains two additional terms, namely those involving  $v^+$  and  $\bar{u} \bar{w}$ . Since the secondary flow vectors in the near-wall region should consist mainly of the  $\bar{W}$  component, the above association suggests that  $\partial \bar{u} \bar{w} / \partial \phi$

provides the turning effect as the secondary flow approaches and leaves its path(s) parallel to the wall.

### 3.2 Vorticity Equation

The equation for conservation of the streamwise (axial) vorticity component may be derived by multiplying equation (6) by  $\rho$  and differentiating with respect to  $\phi$ , multiplying equation (7) by  $\rho r$  and differentiating with respect to  $r$ , and finally subtracting one from the other (which eliminates the pressure). The mean axial vorticity component ( $\bar{\omega}$ ) is:

$$\bar{\omega} = \frac{1}{r} \left[ \frac{\partial r \bar{W}}{\partial r} - \frac{\partial \bar{V}}{\partial \phi} \right] \dots \dots \dots (29)$$

By defining a stream function  $\bar{\psi}$  as:

$$\rho \bar{V} = \frac{1}{r} \frac{\partial \bar{\psi}}{\partial \phi} \text{ and } \rho \bar{W} = - \frac{\partial \bar{\psi}}{\partial r} \dots \dots \dots (30)$$

the final equation (after multiplying through by  $1/r$ ) may be written in compact form as:

$$\frac{1}{r} \frac{\partial}{\partial r} \left[ \bar{\omega} \frac{\partial \bar{\psi}}{\partial \phi} \right] - \frac{1}{r} \frac{\partial}{\partial \phi} \left[ \bar{\omega} \frac{\partial \bar{\psi}}{\partial r} \right] + Z - \mu \nabla^2 \bar{\omega} = 0 \dots \dots \dots (31)$$

where  $\nabla^2 = \frac{1}{r} \frac{\partial}{\partial r} \left[ r \frac{\partial}{\partial r} \right] + \frac{1}{r^2} \frac{\partial^2}{\partial \phi^2}$ , for fully developed flow and cylindrical coordinates. The last term obviously represents diffusion of vorticity. The first two terms represent convection of vorticity by the secondary velocities as may be seen by writing them in the form

$\rho \left[ \frac{1}{r} \frac{\partial}{\partial r} r \bar{v} (\bar{\omega}) + \frac{1}{r} \frac{\partial}{\partial \phi} \bar{w} (\bar{\omega}) \right]$ . The term  $Z$  is:

$$Z = \rho \left\{ \frac{1}{r} \frac{\partial^2}{\partial \phi \partial r} (\bar{w}^2 - \bar{v}^2) + \left[ \frac{\partial^2}{\partial r^2} - \frac{1}{r^2} \frac{\partial^2}{\partial \phi^2} \right] [\bar{v}\bar{w}] + \frac{1}{r^2} \frac{\partial}{\partial \phi} (\bar{w}^2 - \bar{v}^2) + \frac{3}{r} \frac{\partial \bar{v}\bar{w}}{\partial r} \right\} \dots (32)$$

and is usually referred to as the vorticity production term, however its effect may be either production or destruction of vorticity depending on whether or not the terms are directed in the same sense as the vorticity vector (29).

A detailed knowledge of the secondary flow field is required to compute distributions of  $\bar{\omega}$ ,  $\bar{\psi}$ , convection and diffusion. However the distribution of vorticity production in the flow field requires no knowledge of the secondary flow, but rather is solely dependent on the distributions of three of the Reynolds stresses. For the case of the square duct, Brundrett and Baines (29) found that the term involving  $(\bar{w}^2 - \bar{v}^2)$  (in Cartesian coordinates) dominated over the term involving  $\bar{v}\bar{w}$ . Assuming the same situation for the rod bundle case, distributions

of  $v'$  and  $w'$  are sufficient to compute the vorticity production field within a primary flow cell. The vorticity production field, even with low accuracy, would then serve to identify the number of secondary flow cells within a primary flow cell, and the secondary flow direction for each secondary flow cell. This technique was explored in the present work.

### 3.3 Mechanical Dissipation Function

The mechanical or viscous dissipation function which gives the rate per unit mass at which flow energy is transformed into internal energy via viscous action, is given by:

$$\begin{aligned} \Phi = \nu & \left[ 2 \left( \frac{\partial V}{\partial r} \right)^2 + 2 \left( \frac{1}{r} \frac{\partial W}{\partial \phi} \right)^2 + \frac{4V}{r} \left( \frac{1}{r} \frac{\partial W}{\partial \phi} \right) + 2 \left( \frac{V}{r} \right)^2 + 2 \left( \frac{\partial U}{\partial x} \right)^2 + \right. \\ & + \left( \frac{1}{r} \frac{\partial U}{\partial \phi} \right)^2 + 2 \left( \frac{1}{r} \frac{\partial U}{\partial \phi} \right) \left( \frac{\partial W}{\partial x} \right) + \left( \frac{\partial W}{\partial x} \right)^2 + \left( \frac{\partial V}{\partial x} \right)^2 + 2 \left( \frac{\partial V}{\partial x} \right) \left( \frac{\partial U}{\partial r} \right) + \\ & + \left( \frac{\partial U}{\partial r} \right)^2 + \left( \frac{1}{r} \frac{\partial V}{\partial \phi} \right)^2 + 2 \left( \frac{1}{r} \frac{\partial V}{\partial \phi} \right) \left( \frac{\partial W}{\partial r} \right) - 2 \left( \frac{1}{r} \frac{\partial V}{\partial \phi} \right) \left( \frac{W}{r} \right) + \\ & \left. + \left( \frac{\partial W}{\partial r} \right)^2 - 2 \left( \frac{\partial W}{\partial r} \right) \left( \frac{W}{r} \right) + \left( \frac{W}{r} \right)^2 \right] \dots \dots \dots (33) \end{aligned}$$

Substituting  $U = \bar{U}$ , etc., the direct dissipation for fully developed flow becomes (after some rearrangement):

$$\begin{aligned} \Phi_{dd} = & \nu \left[ \left( \frac{\partial \bar{U}}{\partial r} \right)^2 + 3 \left( \frac{\partial \bar{V}}{\partial r} \right)^2 + \left( \frac{\partial \bar{W}}{\partial r} \right)^2 + \left( \frac{1}{r} \frac{\partial \bar{U}}{\partial \phi} \right)^2 + \left( \frac{1}{r} \frac{\partial \bar{V}}{\partial \phi} \right)^2 + \left( \frac{1}{r} \frac{\partial \bar{W}}{\partial \phi} \right)^2 + \right. \\ & \left. + \left( \frac{\bar{W}^2 - \bar{V}^2}{r^2} \right) - \frac{2}{r} \left( \bar{V} \frac{\partial \bar{V}}{\partial r} + \bar{W} \frac{\partial \bar{V}}{\partial \phi} + \bar{W} \frac{\partial \bar{W}}{\partial r} - \frac{\partial \bar{V}}{\partial \phi} \frac{\partial \bar{W}}{\partial r} \right) \right] \dots (34) \end{aligned}$$

At the two boundaries of the primary flow cell defined by  $\theta = 0$  and  $\pi/6$ , equation (34) reduces to:

$$\Phi_{dd} = \nu \left( \frac{\partial \bar{U}}{\partial r} \right)^2 \dots (35)$$

which is the same as for fully developed pipe flow. Under conditions of weak secondary flow such that

$$\frac{\partial \bar{U}}{\partial r} \text{ and } \frac{1}{r} \frac{\partial \bar{U}}{\partial \phi} \gg \left[ \frac{1}{r} \left( \frac{\partial \bar{V}}{\partial \phi}, \frac{\partial \bar{W}}{\partial \phi} \right), \frac{\partial \bar{V}}{\partial r} \text{ and } \frac{\partial \bar{W}}{\partial r} \right],$$

equation (34) may be approximated as:

$$\Phi_{dd} \approx \nu \left( \frac{\partial \bar{U}}{\partial r} \right)^2 + \nu \left( \frac{1}{r} \frac{\partial \bar{U}}{\partial \phi} \right)^2 \dots (36)$$

The turbulent energy dissipation is obtained by substituting  $U = \bar{U} + u$ , etc., in equation (33), time-averaging, and finally subtracting equation (34) from the result. After some rearrangement, the equation is:

$$\begin{aligned}
\Phi_{td} = v \left[ 2 \overline{\left( \frac{\partial u}{\partial x} \right)^2} + 2 \overline{\left( \frac{\partial v}{\partial r} \right)^2} + 2 \overline{\left( \frac{1}{r} \frac{\partial w}{\partial \phi} \right)^2} + \right. \\
\left. + \overline{\left( \frac{\partial u}{\partial r} + \frac{\partial v}{\partial x} \right)^2} + \overline{\left( \frac{1}{r} \frac{\partial u}{\partial \phi} + \frac{\partial w}{\partial x} \right)^2} + \overline{\left( \frac{1}{r} \frac{\partial v}{\partial \phi} + \frac{\partial w}{\partial r} \right)^2} + \right. \\
\left. + \frac{2}{r^2} \left( 2 v \frac{\partial w}{\partial \phi} - w \frac{\partial v}{\partial \phi} \right) + \frac{2}{r^2} (\overline{w^2} + \overline{v^2}) - \frac{1}{r^2} \frac{\partial}{\partial r} r w^2 \right] \dots \dots \dots (37)
\end{aligned}$$

### 3.4 Mean Energy Equation

The following definitions are used in writing the mean energy and turbulent energy equations.

The mean flow kinetic energy,  $\bar{Q}$ , is:

$$\bar{Q} \equiv \frac{1}{2} (\bar{U}^2 + \bar{V}^2 + \bar{W}^2) \dots \dots \dots (38)$$

The mean turbulent kinetic energy,  $\bar{q}$ , is:

$$\bar{q} \equiv \frac{1}{2} (\overline{u^2} + \overline{v^2} + \overline{w^2}) \dots \dots \dots (39)$$

The instantaneous total kinetic energy,  $Q'$ , is:

$$Q' \equiv \frac{1}{2} (U^2 + V^2 + W^2) = \bar{Q} + q + q' \dots \dots \dots (40)$$

where  $q$  is the instantaneous turbulent kinetic energy, and

$$q' = \bar{U}u + \bar{V}v + \bar{W}w \quad . . . . . (41)$$

Both  $q$  and  $q'$  are fluctuating quantities; their instantaneous sum, according to equation (40), is the difference between the instantaneous total kinetic energy and the mean flow kinetic energy. The mean total kinetic energy is given by:

$$\bar{Q}' = \bar{Q} + \bar{q} \quad . . . . . (42)$$

since  $\bar{q}' = 0$ , hence it represents the sum of the mean flow kinetic energy and the mean turbulent kinetic energy.

The equation for conservation of the mean energy may be obtained by multiplying equation (5) by  $\bar{U}$ , multiplying equation (6) by  $\bar{V}$ , multiplying equation (7) by  $\bar{W}$ , and finally adding the three resultant equations together. After considerable rearrangement, the mean energy equation may be written in the form:

$$I + II + III + IV + V + \bar{\Phi}_{dd} = 0 \quad . . . . . (43)$$

where  $\bar{\Phi}_{dd}$  is the direct dissipation as given by equation (34).

$$a) \text{ Term I} = \frac{\bar{U}}{\rho} \frac{\partial \bar{P}}{\partial x} \quad . . . . . (44)$$



is the energy input per unit mass and time due to the axial pressure drop, i.e. the specific power equivalent to the loss in thermodynamic flow energy as it becomes degraded into internal energy by viscous effects either by direct dissipation or (via the turbulence mechanism) by turbulent dissipation.

$$\text{b) Term II} = \frac{1}{r} \frac{\partial}{\partial r} r \bar{V} \left( \bar{Q} + \frac{\bar{P}}{\rho} \right) + \frac{1}{r} \frac{\partial}{\partial \phi} \bar{W} \left( \bar{Q} + \frac{\bar{P}}{\rho} \right) \dots \dots \dots (45)$$

represents convection of the total mean energy by the secondary velocities. Decomposed, it becomes:

$$\begin{aligned} \text{Term II} = & \overline{UV} \frac{\partial \bar{U}}{\partial r} + \bar{V}^2 \frac{\partial \bar{V}}{\partial r} + \overline{VW} \frac{\partial \bar{W}}{\partial r} + \frac{\overline{UW}}{r} \frac{\partial \bar{U}}{\partial \phi} + \frac{\overline{VW}}{r} \frac{\partial \bar{V}}{\partial \phi} + \\ & + \frac{\overline{W^2}}{r} \frac{\partial \bar{W}}{\partial \phi} + \frac{\bar{V}}{\rho} \frac{\partial \bar{P}}{\partial r} + \frac{\bar{W}}{\rho r} \frac{\partial \bar{P}}{\partial \phi} \dots \dots \dots (45a) \end{aligned}$$

Parallel to equation (36), under conditions of weak secondary flow, Term II may be approximated as:

$$\text{Term II} \approx \overline{UV} \frac{\partial \bar{U}}{\partial r} + \frac{\overline{UW}}{r} \frac{\partial \bar{U}}{\partial \phi} \dots \dots \dots (45b)$$

$$\text{c) Term III} = \frac{1}{r} \frac{\partial}{\partial r} r \overline{v q'} + \frac{1}{r} \frac{\partial}{\partial \phi} \overline{w q'} \dots \dots \dots (46)$$

represents the convection of  $q'$  by the turbulence. The correlations  $\overline{v q'}$  and  $\overline{w q'}$  might be obtained by evaluating  $q'$  from equation (40) or,

perhaps more accurately, by the form  $q' = Q' - \bar{Q}' = (q - \bar{q})$ . The experimental complexity involved, however, need not be encountered since Term III decomposes to:

$$\begin{aligned} \text{Term III} = & \frac{\bar{U}}{r} \left( \frac{\partial r \bar{u} \bar{v}}{\partial r} + \frac{\partial \bar{u} \bar{w}}{\partial \phi} \right) + \frac{\bar{V}}{r} \left( \frac{\partial r \bar{v}^2}{\partial r} + \frac{\partial \bar{v} \bar{w}}{\partial \phi} - \bar{w}^2 \right) + \\ & + \frac{\bar{W}}{r} \left( \frac{\partial r \bar{v} \bar{w}}{\partial r} + \frac{\partial \bar{w}^2}{\partial \phi} + \bar{v} \bar{w} \right) - \text{Term IV} \quad \dots \dots \dots (46a) \end{aligned}$$

Parallel to equation (45b), Term III may be approximated as:

$$\text{Term III} \approx \frac{\bar{U}}{r} \left( \frac{\partial r \bar{u} \bar{v}}{\partial r} + \frac{\partial \bar{u} \bar{w}}{\partial \phi} \right) + \bar{u} \bar{v} \frac{\partial \bar{U}}{\partial r} + \frac{\bar{u} \bar{w}}{r} \frac{\partial \bar{U}}{\partial \phi} \quad \dots \dots \dots (46b)$$

$$\begin{aligned} \text{d) Term IV} = & - \left[ \bar{u} \bar{v} \frac{\partial \bar{U}}{\partial r} + \frac{\bar{u} \bar{w}}{r} \frac{\partial \bar{U}}{\partial \phi} + (\bar{v}^2 - \bar{w}^2) \frac{\partial \bar{V}}{\partial r} + \right. \\ & \left. + \bar{v} \bar{w} \left( \frac{\partial \bar{W}}{\partial r} - \frac{\bar{W}}{r} + \frac{1}{r} \frac{\partial \bar{V}}{\partial \phi} \right) \right] \quad \dots \dots \dots (47) \end{aligned}$$

is the rate of production of turbulent energy. Parallel to equation (45b), Term IV may be approximated as:

$$\text{Term IV} \approx - \bar{u} \bar{v} \frac{\partial \bar{U}}{\partial r} - \frac{\bar{u} \bar{w}}{r} \frac{\partial \bar{U}}{\partial \phi} \quad \dots \dots \dots (47a)$$

$$\begin{aligned} \text{e) Term V} = & - \frac{\nu}{r} \frac{\partial}{\partial r} \left( r \frac{\partial \bar{Q}}{\partial r} \right) - \frac{\nu}{r^2} \frac{\partial^2 \bar{Q}}{\partial \phi^2} + 2 \nu \left( \frac{\bar{V}}{r} \frac{\partial \bar{V}}{\partial r} + \frac{\bar{W}}{r} \frac{\partial \bar{W}}{\partial r} \right) - \\ & - 2 \nu \left( \frac{1}{r} \frac{\partial \bar{V}}{\partial \phi} \frac{\partial \bar{W}}{\partial r} - \frac{1}{r} \frac{\partial \bar{W}}{\partial \phi} \frac{\partial \bar{V}}{\partial r} \right) \quad \dots \dots \dots (48) \end{aligned}$$

represents energy diffusion by viscous effects. This term may also be written as:

$$\begin{aligned} \text{Term } V = -\nu \left\{ \frac{\bar{U}}{r} \left[ \frac{\partial}{\partial r} \left( r \frac{\partial \bar{U}}{\partial r} \right) + \frac{1}{r} \frac{\partial^2 \bar{U}}{\partial \phi^2} \right] + \frac{\bar{V}}{r} \left[ \frac{\partial}{\partial r} \left( r \frac{\partial \bar{V}}{\partial r} \right) + \frac{1}{r} \frac{\partial^2 \bar{V}}{\partial \phi^2} \right] + \right. \\ \left. + \frac{\bar{W}}{r} \left[ \frac{\partial}{\partial r} \left( r \frac{\partial \bar{W}}{\partial r} \right) + \frac{1}{r} \frac{\partial^2 \bar{W}}{\partial \phi^2} \right] - \frac{2}{r} \left( \frac{\partial \bar{W}}{\partial \phi} \frac{\partial \bar{V}}{\partial r} - \bar{W} \frac{\partial \bar{V}}{\partial \phi} \right) - \right. \\ \left. - \left( \frac{\bar{W}^2}{r^2} - \bar{V}^2 \right) - 2 \left( \frac{\partial \bar{V}}{\partial r} \right)^2 \right\} - \Phi_{dd} \dots \dots \dots (48a) \end{aligned}$$

Parallel to equation (45b), Term V may be approximated as:

$$\text{Term } V \approx -\nu \frac{\bar{U}}{r} \left[ \frac{\partial}{\partial r} \left( r \frac{\partial \bar{U}}{\partial r} \right) + \frac{1}{r} \frac{\partial^2 \bar{U}}{\partial \phi^2} \right] - \Phi_{dd} \dots \dots \dots (48b)$$

where  $\Phi_{dd}$  is approximated by equation (36).

In general, according to equation (43), for any given point in the primary flow cell cross-section, the available energy due to the pressure drop is partly converted into turbulent energy and partly directly dissipated into internal energy, while any surplus (or deficit) is diffused by viscous action and/or convected away (or in) by the secondary flow and by the turbulence. Since no net energy crosses the boundaries of the primary flow cell, the area integrals of convection

and diffusion are zero. The mean energy which is converted into turbulent energy is ultimately also dissipated into internal energy by turbulent dissipation as shown later by the turbulent energy equation.

By substituting equations (44), (45b), (46b), (47a), (48b) and (36) into equation (43), an approximate mean energy equation is obtained as follows:

$$\begin{aligned}
 & \frac{\bar{U}}{\rho} \frac{\partial P}{\partial x} + \left\{ \overline{UV} \frac{\partial \bar{U}}{\partial r} + \frac{\overline{UW}}{r} \frac{\partial \bar{U}}{\partial \phi} \right\} + \left\{ \frac{\bar{U}}{r} \left( \frac{\partial r \overline{uv}}{\partial r} + \frac{\partial \overline{uw}}{\partial \phi} \right) + \overline{uv} \frac{\partial \bar{U}}{\partial r} + \frac{\overline{uw}}{r} \frac{\partial \bar{U}}{\partial \phi} \right\} - \\
 & - \left\{ \overline{uv} \frac{\partial \bar{U}}{\partial r} + \frac{\overline{uw}}{r} \frac{\partial \bar{U}}{\partial \phi} \right\} - \left\{ \nu \frac{\bar{U}}{r} \left[ \frac{\partial}{\partial r} \left( r \frac{\partial \bar{U}}{\partial r} \right) + \frac{1}{r} \frac{\partial^2 \bar{U}}{\partial \phi^2} \right] + \nu \left( \frac{\partial \bar{U}}{\partial r} \right)^2 + \nu \left( \frac{1}{r} \frac{\partial \bar{U}}{\partial \phi} \right)^2 \right\} + \\
 & + \left\{ \nu \left( \frac{\partial \bar{U}}{\partial r} \right)^2 + \nu \left( \frac{1}{r} \frac{\partial \bar{U}}{\partial \phi} \right)^2 \right\} \approx 0 \quad \dots \dots \dots (49)
 \end{aligned}$$

All of the above terms except  $(\overline{UV} \partial \bar{U} / \partial r + \overline{UW} \partial \bar{U} / r \partial \phi)$  could be evaluated from the present experimental data. By treating the unknown terms as the closure term for the energy budget, the approximate magnitude of the convection of mean energy by the secondary velocities, could be deduced.

It is also of interest to examine equation (49) in "net" form. The "net" approximate mean energy equation reads;

$$\begin{aligned} \frac{\bar{U}}{\rho} \frac{\partial \bar{P}}{\partial x} + \overline{UV} \frac{\partial \bar{U}}{\partial r} + \frac{\overline{UW}}{r} \frac{\partial \bar{U}}{\partial \phi} + \frac{\bar{U}}{r} \left( \frac{\partial r \overline{UV}}{\partial r} + \frac{\partial \overline{UW}}{\partial \phi} \right) - \\ - \frac{\bar{U}}{r} \left[ \frac{\partial}{\partial r} \left( r \frac{\partial \bar{U}}{\partial r} \right) + \frac{1}{r} \frac{\partial^2 \bar{U}}{\partial \phi^2} \right] \approx 0 \quad \dots (50) \end{aligned}$$

where the "net" production and "net" direct dissipation are both zero. The energy input due to the pressure drop is balanced (approximately) by the secondary flow convection, the "net" turbulence convection and the "net" viscous diffusion. The area integrals of the "net" convection and the "net" diffusion are no longer zero. In fact, the area integral of equation (46b) is zero (approximately), hence:

$$\begin{aligned} \int_A \frac{\bar{U}}{r} \left( \frac{\partial r \overline{UV}}{\partial r} + \frac{\partial \overline{UW}}{\partial \phi} \right) &= \int_A - \overline{UV} \frac{\partial \bar{U}}{\partial r} - \frac{\overline{UW}}{r} \frac{\partial \bar{U}}{\partial \phi} = \\ &= \int_A (\text{Production terms in (47a)}) \quad \dots (51) \end{aligned}$$

The fourth term in equation (50) may, in the above sense, be interpreted as "production". Similarly, the last term in equation (50) may be interpreted as "direct dissipation". In effect, then, the energy input splits into convection by secondary flow, "production" and "direct dissipation".

It is also noted that equation (50) amounts (as an equality) to equation (5) multiplied through by  $\bar{U}$ . This is consistent with the fact that if the secondary velocities are very small compared to  $\bar{U}$ , the total mean velocity vector is only slightly inclined to the x-axis at all locations, hence its magnitude is approximately the local value of  $\bar{U}$ .

An exact mean energy equation is developed next for the two boundaries of the primary flow cell defined by  $\theta = 0$  and  $\pi/6$ . Here equation (43) reduces to:

$$\frac{\bar{U}}{\rho} \frac{\partial \bar{P}}{\partial x} + \frac{1}{r} \frac{\partial}{\partial r} r \overline{vq'} - \overline{uv} \frac{\partial \bar{U}}{\partial r} - \frac{v}{r} \frac{\partial}{\partial r} \left( r \frac{\partial \bar{Q}}{\partial r} \right) + \Phi_{dd} = 0 \dots \dots (52)$$

where  $\Phi_{dd}$  is now given by equation (35), and it is noted that  $\bar{Q} = \bar{U}^2/2$  and  $q' = \bar{U}u$ .

The second term may be decomposed to:

$$\frac{1}{r} \frac{\partial}{\partial r} r \overline{vq'} = \overline{uv} \frac{\partial \bar{U}}{\partial r} + \frac{\bar{U}}{r} \frac{\partial}{\partial r} (r \overline{uv}) \dots \dots \dots (53)$$

Similarly, the fourth term may be written as:

$$-\frac{v}{r} \frac{\partial}{\partial r} \left( r \frac{\partial \bar{Q}}{\partial r} \right) = -\frac{\bar{U}}{r} \frac{\partial}{\partial r} \left( r \frac{\partial \bar{U}}{\partial r} \right) - \Phi_{dd} \dots \dots \dots (54)$$

where again  $\Phi_{dd}$  is as given by equation (35).

Substituting equation (53), (54) and (35) into equation (52) gives:

$$\frac{\bar{U}}{\rho} \frac{\partial \bar{P}}{\partial x} + \left\{ \bar{u}v \frac{\partial \bar{U}}{\partial r} + \frac{\bar{U}}{r} \frac{\partial}{\partial r} (r\bar{u}v) \right\} - \bar{u}v \frac{\partial \bar{U}}{\partial r} - \left\{ v \frac{\bar{U}}{r} \frac{\partial}{\partial r} \left( r \frac{\partial \bar{U}}{\partial r} \right) + v \left( \frac{\partial \bar{U}}{\partial r} \right)^2 \right\} + v \left( \frac{\partial \bar{U}}{\partial r} \right)^2 = 0 \quad \dots \dots (55)$$

or

$$\frac{\bar{U}}{\rho} \frac{\partial \bar{P}}{\partial x} + \frac{\bar{U}}{r} \frac{\partial}{\partial r} r (\bar{u}v - v \frac{\partial \bar{U}}{\partial r}) = 0$$

which is equation (11) (applicable to the boundaries under consideration) multiplied through by  $\bar{U}$ . This equation may also be written as:

$$\frac{\bar{U}}{\rho} \frac{\partial \bar{P}}{\partial x} + \frac{1}{r} \frac{\partial}{\partial r} \bar{U} r (\bar{u}v - v \frac{\partial \bar{U}}{\partial r}) - (\bar{u}v - v \frac{\partial \bar{U}}{\partial r}) \frac{\partial \bar{U}}{\partial r} = 0$$

Substituting equation (15) into the second term and simplifying yields:

$$\left[ \frac{\hat{R}^2 - r^2}{2 r \rho} \right] \frac{\partial \bar{P}}{\partial x} \frac{\partial \bar{U}}{\partial r} = \bar{u}v \frac{\partial \bar{U}}{\partial r} - v \left( \frac{\partial \bar{U}}{\partial r} \right)^2$$

Finally, substituting for  $\partial \bar{P} / \partial x$  from equation (25) gives:

$$\left[ 2 \left( \frac{\hat{R}^2 - r^2}{r^D h} \right) (\bar{u}^*{}^2) \right] \frac{\partial \bar{U}}{\partial r} = \bar{u}v \frac{\partial \bar{U}}{\partial r} + v \left( \frac{\partial \bar{U}}{\partial r} \right)^2 \quad \dots \dots (55a)$$

which is analogous to Laufer's mean energy equation for fully developed pipe flow<sup>(39)</sup>.

### 3.5 Turbulent Energy Equation

The derivation of the equation for conservation of turbulent energy begins with the momentum equations for steady flow which are:

$$\frac{\partial U^2}{\partial x} + \frac{\partial UV}{\partial r} + \frac{1}{r} \frac{\partial UW}{\partial \phi} + \frac{UV}{r} + \frac{1}{\rho} \frac{\partial P^*}{\partial x} - \nu \nabla^2 U = 0 \quad \dots \dots \dots (56)$$

$$\frac{\partial UV}{\partial x} + \frac{\partial V^2}{\partial r} + \frac{1}{r} \frac{\partial VW}{\partial \phi} + \frac{V^2 - W^2}{r} + \frac{1}{\rho} \frac{\partial P^*}{\partial r} - \nu \left[ \nabla^2 V - \frac{V}{r^2} - \frac{2}{r^2} \frac{\partial W}{\partial \phi} \right] = 0 \quad (57)$$

$$\frac{\partial UW}{\partial x} + \frac{\partial VW}{\partial r} + \frac{1}{r} \frac{\partial W^2}{\partial \phi} + 2 \frac{VW}{r} + \frac{1}{\rho r} \frac{\partial P^*}{\partial \phi} - \nu \left[ \nabla^2 W + \frac{2}{r^2} \frac{\partial V}{\partial \phi} - \frac{W}{r^2} \right] = 0 \quad (58)$$

These equations are obtained from the Navier-Stokes and continuity equations ( $\rho$  and  $\mu$  constants); for example, equation (56) is obtained by multiplying equation (1) by  $U$  and adding it to the Navier-Stokes equation for the  $x$ -direction. The equations involve the instantaneous velocities and the instantaneous static pressure,  $P^* = \bar{P} + P'$ , and

$$\nabla^2 = \frac{\partial^2}{\partial x^2} + \frac{\partial^2}{\partial r^2} + \frac{1}{r} \frac{\partial}{\partial r} + \frac{1}{r^2} \frac{\partial^2}{\partial \phi^2}.$$

The turbulent energy equation is obtained by multiplying equation (56) by  $U$ , multiplying equation (57) by  $V$ , multiplying equation (58) by  $W$ , adding the three resultant equations together, substituting  $U = \bar{U} + u$ , etc., time-averaging and setting  $\partial(\bar{\quad})/\partial x = 0$  (fully developed flow), and finally subtracting the mean energy equation



(equation (43)). The result, after substantial rearrangement and use of the continuity equation, may be written in the form:

$$X + XI + XII + XIII + \Phi_{td} = 0 \quad \dots \dots \dots (59)$$

where  $\Phi_{td}$  is the turbulent dissipation as given by equation (37).

$$a) \text{ Term } X = \overline{uv} \frac{\partial \bar{U}}{\partial r} + \frac{\overline{uw}}{r} \frac{\partial \bar{U}}{\partial \phi} + (\bar{v}^2 - \bar{w}^2) \frac{\partial \bar{V}}{\partial r} + \bar{vw} \left( \frac{\partial \bar{W}}{\partial r} - \frac{\bar{W}}{r} + \frac{1}{r} \frac{\partial \bar{V}}{\partial \phi} \right) \quad (60)$$

is the rate of production of turbulent energy. It is of course identical to Term IV (equation (47)) but of opposite sign.

$$b) \text{ Term } XI = \frac{1}{r} \frac{\partial}{\partial r} r \bar{V} \bar{q} + \frac{1}{r} \frac{\partial}{\partial \phi} \bar{W} \bar{q} \quad \dots \dots \dots (61)$$

represents convection of the mean turbulent kinetic energy by the secondary velocities.

$$c) \text{ Term } XII = \frac{1}{r} \frac{\partial}{\partial r} r \bar{v} \left( q + \frac{P'}{\rho} \right) + \frac{1}{r} \frac{\partial}{\partial \phi} \bar{w} \left( q + \frac{P'}{\rho} \right) \quad \dots \dots \dots (62)$$

represents convection of turbulent kinetic and pressure energies by the turbulence.

$$d) \text{ Term } XIII = - \frac{\nu}{r} \frac{\partial}{\partial r} \left( r \frac{\partial \bar{q}}{\partial r} \right) - \frac{\nu}{r^2} \frac{\partial^2 \bar{q}}{\partial \phi^2} - 2 \nu \left[ \overline{\left( \frac{\partial u}{\partial x} \right)^2} + \overline{\left( \frac{\partial v}{\partial r} \right)^2} + \right. \\ \left. + \frac{\partial v}{\partial r} \frac{\partial u}{\partial x} + \frac{\partial v}{\partial x} \frac{\partial u}{\partial r} + \frac{1}{r} \frac{\partial u}{\partial \phi} \frac{\partial w}{\partial x} + \frac{1}{r} \frac{\partial v}{\partial \phi} \frac{\partial w}{\partial r} - \frac{\bar{w}}{r} \frac{\partial w}{\partial r} \right] \quad (63)$$

represents energy diffusion by viscous effects.

If Term XIII and  $\Phi_{td}$  are combined, the result is:

$$\begin{aligned} \text{Term XIII} + \Phi_{td} = & -\frac{\nu}{r} \frac{\partial}{\partial r} \left( r \frac{\partial \bar{q}}{\partial r} \right) - \frac{\nu}{r^2} \frac{\partial^2 \bar{q}}{\partial \phi^2} + \frac{\nu}{r^2} (\bar{v}^2 + \bar{w}^2) - \\ & - \frac{2\nu}{r^2} \left[ \bar{w} \frac{\partial \bar{v}}{\partial \phi} - \bar{v} \frac{\partial \bar{w}}{\partial \phi} \right] + \Phi' \quad \dots \dots \dots (64) \end{aligned}$$

$$\begin{aligned} \text{where } \Phi' = & \nu \left[ \overline{\left( \frac{\partial u}{\partial x} \right)^2} + \overline{\left( \frac{\partial u}{\partial r} \right)^2} + \overline{\left( \frac{1}{r} \frac{\partial u}{\partial \phi} \right)^2} + \overline{\left( \frac{\partial v}{\partial x} \right)^2} + \overline{\left( \frac{\partial v}{\partial r} \right)^2} + \right. \\ & \left. + \overline{\left( \frac{1}{r} \frac{\partial v}{\partial \phi} \right)^2} + \overline{\left( \frac{\partial w}{\partial x} \right)^2} + \overline{\left( \frac{\partial w}{\partial r} \right)^2} + \overline{\left( \frac{1}{r} \frac{\partial w}{\partial \phi} \right)^2} \right] \quad \dots \dots \dots (65) \end{aligned}$$

According to equation (59), for any given point in the primary flow cell cross-section, the turbulent energy produced by the interaction between the mean flow and the Reynolds stresses, is either dissipated or transferred; the three transfer mechanisms being convection by the secondary flow, convection by the lateral fluctuating velocities and diffusion by viscous action.

At the two boundaries of the primary flow cell defined by  $\theta = 0$  and  $\Pi/6$ , equation (59) becomes:

$$\begin{aligned} \bar{u} \bar{v} \frac{\partial \bar{u}}{\partial r} + \frac{1}{r} \frac{\partial}{\partial r} \left( r \bar{v} \left( q \pm \frac{P'}{\rho} \right) \right) - \frac{\nu}{r} \frac{\partial}{\partial r} \left( r \frac{\partial \bar{q}}{\partial r} \right) - 2\nu \left[ \overline{\left( \frac{\partial u}{\partial x} \right)^2} + \overline{\left( \frac{\partial v}{\partial r} \right)^2} \frac{\partial \bar{v}}{\partial r} \frac{\partial \bar{u}}{\partial x} + \right. \\ \left. + \frac{\partial \bar{v}}{\partial x} \frac{\partial \bar{u}}{\partial r} + \frac{1}{r} \frac{\partial \bar{u}}{\partial \phi} \frac{\partial \bar{w}}{\partial x} + \frac{1}{r} \frac{\partial \bar{v}}{\partial \phi} \frac{\partial \bar{w}}{\partial r} - \frac{\bar{w}}{r} \frac{\partial \bar{w}}{\partial r} \right] + \Phi_{td} = 0 \quad \dots (66) \end{aligned}$$

Alternatively, by using equation (64), equation (59) becomes;

$$\begin{aligned} \overline{uv} \frac{\partial \bar{U}}{\partial r} + \frac{1}{r} \frac{\partial}{\partial r} r \overline{v \left( q + \frac{P'}{\rho} \right)} - \frac{v}{r} \frac{\partial}{\partial r} \left( r \frac{\partial \bar{q}}{\partial r} \right) - \frac{v}{r} \left[ \frac{4}{r} \overline{w \frac{\partial v}{\partial \phi}} - \frac{(\bar{v}^2 + \bar{w}^2)}{r} \right] + \\ + \Phi' = 0 \quad \dots \dots \dots (67) \end{aligned}$$

which is the same as Laufer's turbulent energy equation for fully developed pipe flow<sup>(39)</sup>.

### 3.6 Mean Total Energy Equation

The equation for conservation of both the mean energy and turbulent energy is obtained by combining equations (43) and (59).

The resultant total energy equation is:

$$\begin{aligned} \frac{\bar{U}}{\rho} \frac{\partial \bar{P}}{\partial x} + \frac{1}{r} \frac{\partial}{\partial r} r \bar{V} \left( \bar{Q}' + \frac{\bar{P}}{\rho} \right) + \frac{1}{r} \frac{\partial}{\partial \phi} \bar{W} \left( \bar{Q}' + \frac{\bar{P}}{\rho} \right) + \frac{1}{r} \frac{\partial}{\partial r} r \left[ \overline{v q'} + \overline{v \left( q + \frac{P'}{\rho} \right)} \right] + \\ + \frac{1}{r} \frac{\partial}{\partial \phi} \left[ \overline{w q'} + \overline{w \left( q + \frac{P'}{\rho} \right)} \right] - \frac{v}{r} \frac{\partial}{\partial r} \left( r \frac{\partial \bar{Q}'}{\partial r} \right) - \frac{v}{r^2} \frac{\partial^2 \bar{Q}'}{\partial \phi^2} + \\ + 2 v \left( \frac{\bar{V}}{r} \frac{\partial \bar{V}}{\partial r} + \frac{\bar{W}}{r} \frac{\partial \bar{W}}{\partial r} \right) - 2 v \left( \frac{1}{r} \frac{\partial \bar{V}}{\partial \phi} \frac{\partial \bar{W}}{\partial r} - \frac{1}{r} \frac{\partial \bar{W}}{\partial \phi} \frac{\partial \bar{V}}{\partial r} \right) - \\ - 2 v \left[ \left( \frac{\partial u}{\partial x} \right)^2 + \left( \frac{\partial v}{\partial r} \right)^2 + \frac{\partial v}{\partial r} \frac{\partial u}{\partial x} + \frac{\partial v}{\partial x} \frac{\partial u}{\partial r} + \frac{1}{r} \frac{\partial u}{\partial \phi} \frac{\partial w}{\partial x} + \right. \\ \left. + \frac{1}{r} \frac{\partial v}{\partial \phi} \frac{\partial w}{\partial r} - \frac{w}{r} \frac{\partial w}{\partial r} \right] + \Phi_{dd} + \Phi_{td} = 0 \quad \dots \dots \dots (68) \end{aligned}$$

The meanings of the various terms are as described earlier. The production term no longer appears in the equation. The energy input due to the axial pressure drop is simply transferred (by three mechanisms) from where it originates to locations within the primary flow cell where it is converted into internal energy by viscous dissipation.

#### 4.0 EXPERIMENTAL FACILITY AND EQUIPMENT

The experimental program entailed design and construction of a wind tunnel, test-sections and probe traversing mechanisms, and development (including hardware construction) of a three-wire probe system for turbulence measurements. The experimental facility and the equipment used in the research are described in this section.

##### 4.1 Wind Tunnel

A plan view of the wind tunnel is shown in Figure 6. Each component is described briefly in Appendix A. The wind tunnel was designed in accordance with modern practice as a general purpose low-speed facility. Construction was carried out under contract by a Winnipeg firm. The wind tunnel is located in the Turbulence Laboratory of the Department of Mechanical Engineering, University of Manitoba.

The wind tunnel was calibrated for mass flow rate using the contraction cone (pressure drop) as the primary element and an Airflow Developments Ltd. 0 - 0.5 inch water gauge manometer as the secondary element. Calibration was accomplished by running the tunnel in the open circuit mode and using portions of the Department of Mechanical Engineering Air Flow Measurement (Experiment No. 302) apparatus--

pitot-static tube traverse, circular pipe, ten-point log-linear rule. The calibration is shown in Figure 7. It was used mainly to determine approximate operating points (fan and damper settings) for the various tests at the desired Reynolds numbers. Actual bulk velocities for the primary flow cell were obtained by numerical integration of the mean velocity field as determined by pitot tube traverse. The only other instrumentation on the wind tunnel was a thermometer located downstream of the test-section to monitor tunnel air temperature.

#### 4.2 Test-Sections

Three test-sections were constructed using 5.08 cm outside diameter tubes with spacings giving P/D ratios of 1.50, 1.35 and 1.20 (designated Test-Section IA, IB and IC respectively). A cross-section of Test-Section IA is shown in Figure 3. The outer ring of twelve partial rods were wood, fabricated integral with the hexagonal plywood casing. The inner seven rods were removable aluminum alloy tubes, and each tube was used in the same position for each test-section. Access for installing probes in the traversing mechanisms was via a long hinged section of the casing. The long edges of this access panel were hidden behind two rods as indicated in Figure 3. The short edges were located far upstream and downstream of the measuring station so that any flow disturbances would not affect the measurements. The panel

was securely sealed externally with masking tape during all measurements. Further details on the test-sections are provided in Appendix A.

#### 4.3 Traversing Mechanisms

Three tubes (as indicated in Figure 3) were fitted with traversing mechanisms. Arrangements for positioning a probe (hot-wire, pitot tube or static pressure) at any location within (and slightly beyond) a primary flow cell were made through a combination of tube (hence probe) rotation and the traversing mechanism which moved the sensor in a direction normal to the tube wall. The basic design requirements for the traversing mechanism were:

- a) 19mm of probe travel with 20:1 magnification of probe position;
- b) Containment within the tube so as not to disturb the flow, i.e. mechanism, control rod and probe leads/tubing confined to the interior of the instrumented tubes; and
- c) Reasonable provision for probe replacement,

After considerable design effort, a relatively simple mechanism was eventually devised and constructed as shown in Figure 8.

To place a probe into service, the probe was first mounted on the traversing mechanism and adjusted for height and parallelism with

respect to the top surface. The assembly was then inserted and fastened to the tube, and the slider was engaged in mesh. The probe/holder was held firmly by the coil spring against the slider, thus providing a fixed relationship between changes in the longitudinal position of the slider/push rod and changes in the lateral position of the probe. By scaling the push rod, due to the 20:1 magnification, the relative accuracy of probe position was within about  $\pm 0.02\text{mm}$ . The absolute position of the probe was established insitu by direct measurement (over distances of the order of 1 cm) of the distance between the tube surface and the center of the sensor using a caliper/ruler. The absolute accuracy of probe position was within about  $\pm 0.15\text{ mm}$ .

Regarding central tube rotation, gauging at various axial positions indicated that bowing/eccentricity were negligible over the 30 degrees of rotation required to traverse the primary flow cell. The angular position of the probe was determined via a fixed pointer and a 15 cm diameter wheel segment (graduated in  $3^\circ$  increments) concentrically fastened to the central tube. The  $\theta = 0$  position was established by mechanical level.

In performing the actual measurements, the procedure followed was to carefully position the probe at the desired distance from the wall ( $y$ ) and then with fixed  $y$ , rotate the tube in  $3^\circ$  increments.



This scheme provided accurate location of  $y$  (major variable) coupled with random errors in  $\theta$  (minor variable). At the same time, the procedure enhanced isolating small  $\partial(\bar{\phi})/\partial\phi$  gradients in that  $y$  was truly constant.

#### 4.4 Pitot and Static Pressure Probes

These probes were constructed as shown in Figure 9 to fit the traversing mechanisms. The Pitot tube was made from 1.02mm (0.040") O.D. stainless steel tubing. The static pressure probe was constructed from 1.52mm (0.060") O.D. brass tubing and the end of the tubing was capped with a hemispherical plug. The static pressure holes consisted of four equi-spaced, burr-free 0.432mm diameter holes.

Mean axial velocities within the primary flow cell were measured using these probes and a differential pressure manometer. Vacuum grease was used on all connections between the plastic tubing and probes/manometer. The connections at the probes were also leak tested under water. In conducting the measurements, since static pressure variations within the sub-channel were immeasurably small, the Pitot tube was traversed over the grid for the primary flow cell while the static pressure probe remained "parked" approximately in the center of the adjoining flow cell. The static pressure probe was also

used to measure the ambient gauge static pressure at the measuring station.

A total of three manometers were used during the course of the research. One was a R.Fuess (DISA 134b) differential micromanometer having five ranges with minimum/maximum ranges of 0-10mm H<sub>2</sub>O and 0-160mm H<sub>2</sub>O respectively, and an accuracy of  $\pm 0.5\%$  of full scale. The second was a Betz Projection Manometer with a range of 0-400mm H<sub>2</sub>O and an accuracy of  $\pm 0.05\text{mm H}_2\text{O}$ . The third was a Hero micro-manometer with a range of 0-100mm of methanol. Readings were to two decimal places, however accuracy specifications were not available.

#### 4.5 Hot-Wire Equipment

The turbulence measurements were made using linearized constant temperature anemometry. Axial turbulence ( $u'$ ) spectra and micro-scale were obtained using DISA 55F01 or 55F21 single-wire probes<sup>(40)</sup> (1.25mm sensitive wire length; 5 $\mu\text{m}$  wire diameter). The probe support was held by a right-angle mounting tube modified to fit the traversing mechanism. The wire orientation was parallel to the  $\phi$ -direction. The anemometer system was DISA equipment and consisted of a 55D05 anemometer, 55D10 linearizer, 55D31 digital DC voltmeter and a 55D35 RMS voltmeter. Power spectral data were extracted using a Hewlett-Packard Model 3590A

way analyzer with 3594A sweeping local oscillator (constant bandwidth). Micro-scale values were determined using the differentiator incorporated in a DISA 55A06 correlator.

Five of the six Reynolds stress components were measured using the two correlator method<sup>(41)</sup> and special purpose X-probes similar in size and construction to the DISA 55A38 X-array probe<sup>(40)</sup> (1.2mm wire length; 5 $\mu$ m wire diameter). These probes were constructed by DISA to mechanical specifications matching the traversing mechanism. The wire orientations and the voltage-velocity "sign" relationships for the cylindrical coordinate system are illustrated in Figures 10 and 11 for the two types of probe. The two anemometer channels were again DISA equipment and the correlators were both DISA 55A06 units. The matched hot-wire signals were monitored periodically on a Tektronix Type 502 dual-beam oscilloscope.

The Reynolds stresses were originally intended to be measured using a miniature three-wire probe similar to the DISA Triaxial Array Probe<sup>(40)</sup>. A system was developed, however proving was delayed several weeks due to mechanical problems with the probe leads. The performance of the three-wire probe system was eventually found to be fairly satisfactory. But by this time, the above mentioned X-probes had been placed into service, and in view of the established reliability of this

type of probe, X-probe measurements were continued for all tests. A complete account of the three-wire probe system together with operating procedures and the transformation equations, has been reported<sup>(4)</sup> previously. A few results derived from this system are presented in this report.

Local wall shear stress values were measured using a DISA 55A92 subminiature flush-mounting probe<sup>(40)</sup> (0.75mm x 0.15mm nickel film) and a DISA 55A01 anemometer. The probe was mounted flush at the leading edge of the traversing mechanism plug. Insitu calibrations were based on average wall shear stresses obtained from axial pressure drop data. The anemometer output was passed through a DISA 55D25 auxiliary unit where both DC bias and amplification were employed to assist in detecting peripheral variations in the local shear stresses.

The hot-wires were calibrated insitu against the Pitot tube (typically at  $\theta = 30^\circ$  near the sub-channel centerline with the two probes in symmetric positions) prior to each test. For the X-probes, sensitivity match was checked and trimmed if necessary prior to each test, and rechecked at the completion of the test. Since it was not always possible to calibrate at exactly the test temperature, due to the effect of ambient temperature on the calibration<sup>(42)</sup>, the final (shifted) calibration for each test was obtained by "point-matching" the DC voltages to the known mean velocity fields.

## 5.0 EXPERIMENTAL RESULTS AND DISCUSSION

Measurements were made for a total of seventeen test conditions as outlined in Table I. These isothermal tests spanned the three P/D ratios and a Reynolds number range of 12,000 to 84,000. The sub-division of the geometry for each of the three primary flow cells is shown in Figures 12, 13 and 14. Pitot tube and X-probe measurements were made at each node in the cross-section. The experimental data are presented and discussed in this section. This is preceded by experimental evidence of fully-developed flow conditions and an assessment of flow symmetry.

### 5.1 Proof of Developed Flow

For each of the three test-sections, the axial distance from the start of the rod bundle to the measuring station ( $L$ ) was 153.7 cm. Based on equivalent hydraulic diameter ( $D_h$ ), the  $L/D_h$  ratios were 20 for Test-Section IA, 30 for IB and 51 for IC. Based on boundary layer thickness, the  $L/(2 \hat{y}_{\max})$  ratios were 41 for IA, 54 for IB and 78 for IC. The usual criterion for fully developed flow is  $L/D > \sim 40$ . It was therefore necessary to establish whether or not the flows were fully developed for Test-Sections IA and IB. The following experiments were carried out with Test-Section IA to settle this point.

A Pitot tube and static pressure tube were mounted on the end of a 1.90 cm O.D. aluminum alloy tube which was rigged (via a saddle and 'first corner' end support) so as to position the probes on the center-line of the test sub-channel, and allow them to be moved axially over a range encompassing the start of the test-section to a location downstream of the measuring station. The results of these measurements are shown in Figures 15 and 16. The test numbers correspond approximately\* to Table I conditions. The position  $x = 0$  corresponds to the start of the rod bundle. The results indicate the flows became fully developed ( $\partial \bar{U} / \partial x = 0, \partial \bar{P} / \partial x = \text{const.}$ ) by about  $x = 120$  cm.

In addition to the above, the Pitot tube and static pressure tube were removed from the axial traverse rod and replaced by a DISA 55F11 hot-wire probe<sup>(40)</sup>. The procedure was repeated using linearized anemometry to determine relative axial turbulence intensities ( $u' / \bar{U}$ ) along the center-line of the sub-channel. The results shown in Figure 17a are typical of the six runs made. The initial axial turbulence levels were low; typical for a contraction cone exit.

---

\*These tests were conducted early in the program at approximate target Reynolds numbers.

The boundary layers apparently first reached the center of the sub-channel at about  $x = 45$  cm. The turbulence levels then increased uniformly with distance in the mixing region. The boundary layers appeared to become fully developed in the range  $x \approx 120$  to 140 cm.

The front support and spacings for the individual rods (see Appendix A) were provided by 3.2 mm diameter steel rods located along pitch lines. The present test-section had spacer rods only on pitch lines radiating from the central rod; i.e. for the sub-channel under study, two spacer rods at  $\theta = 0^\circ$  and  $60^\circ$ . The original prototype<sup>(2)</sup> of Test-Section IA consisted of plastic tubes and a front support of 3.2 mm rods along every pitch line. The results for this test-section are shown in Figure 17b. As discussed in Reference 2, the initial perturbations were thought due to entrainment effects arising from the wakes from the spacer rods. The absence of this effect in Figure 17a was surprising, however presumably a mixing effect still occurred, but did not extend as far out as the sub-channel centerline. In any case, both configurations produced (seemingly) fully developed flow conditions at about the same  $L/D_h$ .

In view of the above findings, it was concluded that the flows for Test-Section IA (hence also IB) were fully developed at the measuring station. It may also be inferred that since the flows became fully developed by a  $L/D_h$  ratio of about 16, this short starting length may be attributed to some extent to the mixing induced by the

steel support rods at the test-section entrance. It is also noted that other investigators have reported short entrance lengths; for example, Dingee and Chastain (according to Sutherland<sup>(5)</sup>) -  $L/D_h = 12$ , Skinner et al<sup>(8)</sup> -  $L/D_h = 35$ , and Palmer and Swanson -  $L/D_h < 38.4$ .

## 5.2 Flow Symmetry

The rod bundles were assembled with the central rods spaced as evenly as possible. Measurements indicated that gap spacings at the supports for the small test-section were within about  $\pm 4\%$  of the average gap. This situation improved progressively with the two larger test-sections as  $P/D$  increased. Since the geometric array symmetry was least favourable for the small test-section, a series of measurements were conducted to assess the flow symmetry.

Mean axial velocities were measured via Pitot tube at all nodes in the grid (Figure 14) for primary flow cell 1, and at all ostensibly symmetric points in both flow cells 2 and 12 - see Figure 18 for the numbering system used to identify the primary flow cells surrounding the central rod. Based on straight numerical averages of the 66 point velocities in each flow cell, under Test C3 conditions, the average velocity in Cell 2 was found to be 1.45% lower than in Cell 1, and the average velocity in Cell 12 was 2.33% lower than in Cell 1.



Under Test C7 conditions, the results were similar - 1.82% and 3.07% lower for Cells 2 and 12 respectively\*. Assuming positioning errors to be random, these figures may be interpreted as reflecting the geometric asymmetry. The data were analyzed further to detect regional asymmetries through point-by-point comparisons of the velocity fields. In an attempt to decouple random positioning errors from asymmetric effect, the mean velocity at each node was first computed as the arithmetic mean of the three velocities constituting an element in the 66 element set. Next, the deviation of each velocity from its mean was calculated to obtain the 198 deviations. The average of the absolute magnitudes of the deviations was 1.08% under Test C3 conditions and 1.27% under Test C7 conditions. The standard deviations were 1.28% and 1.56% for Test C3 and C7 conditions respectively. The percentage deviations were distributed quite uniformly but with a slight tendency to be largest near the center of the boundary defined by  $r = P/2 \cos \theta$ . Again, this reflected the geometric imperfections.

---

\*Alternatively, comparing Cells 1 and 12 with 2 (the 'median' cell), under Test C3 (C7) conditions, the average velocity in Cell 1 was 1.47% (1.85%) higher than in Cell 2, while Cell 12 was 0.89% (1.27%) lower than Cell 2.

Similar tests were conducted using both u-v and u-w X-probes. The number of data points in each cell was reduced to 17 with measurements taken along radial lines at  $\theta = 30^\circ, 90^\circ, 150^\circ, 210^\circ$  and  $270^\circ$ . The results for  $u'$ ,  $v'$ ,  $w'$  and  $\overline{uv}$  were similar. A typical case was as follows; under Test C3 conditions,  $u'/\bar{u}^*$  for Cell 2 averaged 0.08% higher than for Cell 1, while  $u'/\bar{u}^*$  for Cell 12 averaged 6.10% lower than for Cell 1. For the deviations computed as indicated above for the mean axial velocities, the average of the absolute magnitudes of the 51 deviations was 5.56%. For the same test, the parameter  $w'/\bar{u}^*$  for Cell 2 averaged 0.54% higher than for Cell 1, while Cell 12 averaged 2.09% lower than for Cell 1. The average absolute deviation was 4.07%.

It was concluded at this stage that the flow structure in the primary flow cell under investigation (Cell 1) for Test-Section IC was reasonably symmetric with its immediate neighbours. This included, from a mean axial velocity standpoint, the adjoining flow cell\* sharing

---

\*No turbulence measurements were made in this cell (except across the gap region) due to practical limitations. Portions of this cell could be reached from the central tube, however positioning was complicated and the data required a second-order tensor component transformation. Alternatively, a probe could have been installed in traversing mechanism No. 2 (see Figure 3), but this meant either a second probe (and another two matched anemometer channels) at the same flow conditions, or the same probe at similar but not identical flow conditions.

the common boundary  $r = P/2 \cos \theta$ . Furthermore, the above results, extrapolated to the two larger test-sections, indicated that the general level of achievement with respect to flow symmetry was quite satisfactory. However, in order to explore  $\overline{uw}$  further, the study was expanded to include all primary flow cells surrounding the central tube. Two types of test were conducted. One was to check the turbulence distributions along the six boundaries connecting the sub-channel centerlines. The second test was to position a  $u-w$  X-probe at a fixed distance from the tube surface, and by rotating the central tube, measure  $R_{uw}$  at  $3^\circ$  intervals around the entire perimeter. The value of  $y$  was chosen such that the traverse passed approximately centrally across the primary flow cells.

The results of the first kind for Test-Section IC are shown in Figure 19. The variations for a given  $y/\hat{y}_{\max}$  were especially large in the range 0.6 to 1.0, where there was clear evidence of geometric asymmetry. Since a systematic error in  $\theta$  greater than about  $3^\circ$  was highly improbable, the asymmetry was attributed to a combination of non-equal spacing of rods and triangular skewness induced by the spacing variations. This situation was apparently quite severe with respect to the sub-channel associated with Cells 5 and 6. The sub-channel associated with Cells 1 and 2 showed no skewness, and since it was

representative of  $P/D = 1.20$ , and because it was doubtful that the geometry could be improved significantly, no attempts were made to alter the test-section. But in view of these results, the test was repeated for Test-Section IB ( $P/D = 1.35$ ). The results (Figure 20) were much improved. The scatter for  $u'/\bar{u}^*$  and  $v'/\bar{u}^*$  was about  $\pm 3\%$  while the  $\bar{uv}/(\bar{u}^*)^2$  variations were about  $\pm 0.03$ .

The results of the second kind are shown in Figure 21. The data for Test-Section IB were substantially more uniform than for IC, indicating the improved geometric symmetry. The main observation arising from the data is that  $R_{uw}$  has an antisymmetric character in adjoining cells, i.e. symmetry in pairs. Since

$$\frac{\partial R_{uw}}{\partial \theta} = \frac{1}{u'w'} \frac{\partial \bar{uw}}{\partial \theta} - \frac{\bar{uw}}{u'(w^2)} \frac{\partial w'}{\partial \theta} - \frac{\bar{uw}}{w'(u^2)} \frac{\partial u'}{\partial \theta}, \text{ or}$$

$$\frac{\partial \bar{uw}}{\partial \theta} \approx u' w' \frac{\partial R_{uw}}{\partial \theta} \text{ since } \frac{\partial w'}{\partial \theta} \text{ and } \frac{\partial u'}{\partial \theta} \text{ were small,}$$

it follows that  $\bar{uw}$  has an antisymmetric pattern. As suggested earlier in connection with equation (28), this behaviour is due to the fact that the secondary flow cells are counter-rotating in adjacent primary flow cells.

The above leads to the question as to whether  $\partial \bar{uw}/\partial \theta = 0$

at the radial boundaries of the primary flow cells. Experimentally, both  $\partial u' / \partial \theta$  and  $\partial w' / \partial \theta$  were indicated to be zero at these boundaries (at least for flow Cell 1). Hence for  $\partial u' / \partial \theta = 0 = \partial w' / \partial \theta$ ,  $\frac{\partial \overline{uw}}{\partial \theta} = u' w' \frac{\partial R_{uw}}{\partial \theta}$ , and so both should theoretically be zero at each radial boundary of an idealized geometry. Figure 21 was prepared by simply drawing the lines through the data points taken at  $3^\circ$  intervals. It indicates that the gradients are non-zero at the boundaries. This conclusion is erroneous. Part of the explanation lies with the measuring probe. Since the "X" plane of the u-w X-probe lay in the  $x - \theta$  plane, the probe wires straddled the boundary plane, and consequently there was poor discrimination of  $R_{uw}$  or  $\overline{uw}$  at the boundaries. Bearing this in mind, it is possible that  $\partial \overline{uw} / \partial \theta = 0$  at the boundaries as required by theory, but the constant values of  $\overline{uw}$  over a narrow region in passing through a boundary are difficult to detect if  $\overline{uw}$  varies sharply with  $\theta$  in the same direction on each side of the boundary. By taking measurements nearer to the wall where  $\partial \overline{uw} / \partial \theta$  was shallower, it was possible to demonstrate  $\partial \overline{uw} / \partial \theta = 0$  at the boundaries. This is illustrated in Figure 22 which shows  $R_{uw}$  versus  $\theta$  for primary flow Cell 1 and its boundaries for various fixed distances from the wall.

### 5.3 Friction Factors

Axial pressure gradients ( $\partial \bar{P} / \partial x$ ) at the measuring station were determined from plots of static pressure versus test-section length as illustrated by Figure 23. Static pressures, measured by static pressure probe with respect to ambient atmospheric pressure, were obtained by the axial traverse procedure mentioned in Section 5.1. The 1.90 cm O.D. aluminum alloy tube was replaced by a 1.04 cm O.D. steel tube (containing only static pressure probe tubing) for the traverses for the two smallest test-sections. The static pressure probe was a commercial 1.02mm O.D. probe. It was mounted on the end of the traverse rod such that the static holes were about 20 cm upstream of the end of the rod. Hence any blockage effects were relegated downstream of the measuring position. According to the contraction cone manometer, the presence of the traverse rod did not significantly affect the mass flow rate through the test-section during the course of a traverse. Calculations showed that the equivalent hydraulic diameters of the test-sections were decreased by only 3.40% for Test-Section IA, 1.85% for IB, and 2.17% for IC by the presence of the traverse rod. The static pressure levels at the regular measuring station also agreed well with values for other tests, thereby indicating that the traversing procedure did not significantly

influence the pressure drop.

Average friction velocities for the pressure drop tests were determined from equation (25) based on the experimental axial pressure gradients. The hydraulic diameters for the three test-sections were computed via equation (24) and are listed in Table I. The average friction velocities for the isovel tests are also listed in Table I after corrections by the procedure outlined in Appendix B. The friction factors for the isovel tests were computed using equation (27). The resulting data are shown in Figure 24. The present results are in good agreement (as shown in Figure 24) with the few available results of other investigators in the same P/D and Reynolds number ranges.

Friction factors for all three test-sections were higher than for flow through smooth tubes at the same Reynolds numbers. This is characteristic of rod bundle geometries having  $P/D > \sim 1.1$ <sup>(5) (21)</sup>. For Test-Section IA ( $P/D = 1.50$ ), the experimental friction factors ranged from 23% to 31% (26.8% average) higher than friction factors for smooth pipe flow at the same Reynolds numbers. This is equivalent to friction velocities averaging 12.6% higher than for equivalent pipe flow. For Test-Section IB ( $P/D = 1.35$ ), friction factors ranged from 13% to 18% (14.6% average) higher than friction factors for smooth pipe. (Friction velocities averaged 7.06% higher). For Test-Section

IC ( $P/D = 1.20$ ), friction factors ranged from 11% to 23% (17.4% average) higher than friction factors for smooth pipe. (Friction velocities averaged 8.33% higher). For Test-Section IC, the ratio of rod bundle friction factor to pipe flow friction factor increased with decreasing Reynolds number. There was no similar Reynolds number dependence for the two largest test-sections.

In view of the non-uniform dependence of friction factor on  $P/D$  ratio and Reynolds number, the pressure drop experiments were repeated several months later for both Test-Sections IB and IC. The results were in good agreement with the earlier measurements. It was subsequently found that the dependence could be described quantitatively by the following correlation equation. It was postulated that  $f = C Re^{-n}$ , the same form as in pipe flow, but that both  $C$  and  $n$  were functions of  $P/D$  ratio. The least-squares-fit equation was:

$$f = C Re^{-n}; 10^4 < Re < 10^5, 1.2 \leq P/D \leq 1.5 \quad \dots \dots \dots (69)$$

$$\text{where } C = \frac{0.287}{\left[ \frac{D_h}{D} - 0.30 \right]^{1/2}} = \frac{0.287}{\left[ \frac{2\sqrt{3}}{\pi} \left( \frac{P}{D} \right)^2 - 1.30 \right]^{1/2}}$$

$$\text{and } n = 0.368 \left( \frac{P}{D} \right)^{-1.358}.$$



The friction factor lines predicted by this equation for the three P/D ratios are shown in Figure 24. The standard deviation of the seventeen data points from equation (69) based on equal Reynolds numbers, amounted to 1.83% of the average friction factor or 0.933% of the average friction velocity.

#### 5.4 Local Wall Shear Stress Distributions

Variations in the local wall shear stresses about the tube perimeter for Test-Section IC ( $P/D = 1.20$ ) were determined via anemometry using a flush-mounted hot film probe. The long side of the rectangular film was aligned in the x-direction so as to maximize angular discrimination. The results are shown in Figure 25, where  $\bar{\tau}_w$  is the average wall shear stress for primary flow cell 1, i.e. over  $\theta = 0^\circ$  to  $300^\circ$ . The procedure followed is outlined in Appendix C.

The results are compared with the findings of other investigators in Figure 26. Curve C which shows the trend found by Subbotin et al<sup>(37)</sup> is approximate as it was taken from a small-scale, rather poor, reproduction of the published data which consisted of a multitude of data points. Both the data of Subbotin et al<sup>(37)</sup> (similar conditions to the present results) and Hall and Syenningsson<sup>(38)</sup> ( $P/D = 1.217$ , relatively high Reynold number) show peaks at  $\theta \approx 20^\circ$  compared to

$\theta \approx 24^\circ$  for the present results. This is likely due to an asymmetry effect in the present test-section\*. Otherwise, the agreement, especially between curves A and B, is good,

Some important observations can be made on the basis of the similar distributions in Figure 26. Local wall shear stresses do not increase monotonically from  $\theta = 0^\circ$  to  $\theta = 30^\circ$  as is predicted by computational schemes using universal velocity distributions and ignoring secondary flows. For example, Bender and Switick<sup>(19)</sup>, for  $P/D = 1.20$ , predict  $T_w/\bar{T}_w$  to vary from about 0.88 at  $\theta = 0^\circ$ , to 1.00 at  $\theta = 15^\circ$ , to about 1.12 at  $\theta = 30^\circ$ , i.e. variations of about  $\pm 12\%$  compared to about  $\pm 3\frac{1}{2}\%$  in practise. Hence it may be inferred that secondary flows are operational and act to homogenize local wall shear stresses. Furthermore, since secondary flows act such that an inflow towards the wall tends to increase  $T_w$  (compared to non-secondary flow predictions), whereas an outflow tends to decrease  $T_w$ , one may also infer a counterclockwise circulation in primary flow Cell 1.

---

\*The distributions for the six pairs of primary flow cells surrounding the central tube showed substantial variations. In fact, wall shear stress levels were about 3% above average over the upper portion of the central tube (Cells 1-6 inclusive), and below average over the lower portion.

Local wall shear stress variations for Test-Section IB ( $P/D = 1.35$ ) are shown in Figure 27 as determined via Preston tube (the 1.02mm O.D. Pitot tube described in Section 4.4) using the appropriate relation of Patel<sup>(43)</sup>. The variations fall in the range of  $\pm 2\%$  with the peak this time occurring at  $\theta \approx 180^\circ$ . Measurements at the lower Reynolds numbers were not practical due to the low pressure differentials. Measurements via anemometry for this test-section were also made but the results were not reproducible because of the small variations in  $T_w$ .

Measurements of local wall shear stress were not attempted for Test-Section IA ( $P/D = 1.50$ ), however it is safe to assume, through extrapolation of the above results, that local wall shear stresses must be practically uniform, with variations in  $T_w/\bar{T}_w$  probably no greater than about  $\pm 1\%$ .

As mentioned above, measurements by hot film probe of the local wall shear stresses in Test-Section IB, indicated that the variations about the central tube were very small. Reliable distributions could not be obtained due to lack of sensitivity. However, during the course of this work, it was observed that the RMS values of the fluctuating local wall shear stress showed a consistent increase of about 3% for each of the twelve primary flow cells when

moving from the position facing the gap ( $\theta = 0^\circ$ ) to the position facing the sub-channel centerline ( $\theta = 30^\circ$ ). As a result of this, a preliminary investigation was carried out to assess the use of a wall shear stress probe as an experimental tool for probing the viscous sublayer structure.

The results of this limited study are shown in Figures 28, 29 and 30 which include data taken for fully developed air flow through a 10 cm I.D. pipe. The hot film was operated with a constant over-heat ratio of about 0.53, and the long side of the film was aligned in the main flow direction for all measurements. For both pipe flow and rod bundle flow, the RMS value of the fluctuating wall shear stress (or friction velocity) increased with Reynolds number. For pipe flow, the friction velocity "intensities" were nearly constant at about 6%, hence since  $\bar{u}^* \propto \sqrt{f U_b^2}$  and  $f \propto Re^{-0.20}$ , for a given system,  $(u^*)' \propto \bar{u}^* \propto Re^{0.90}$  which was approximately the case (Figure 28). If the probe were responding only to conditions right at the surface, the instantaneous wall shear stress would be:

$$\tau_w = \mu \left. \frac{dU}{dy} \right|_w \quad \text{and since} \quad \bar{\tau}_w = \mu \frac{d\bar{U}}{dy},$$

the RMS fluctuating wall shear stress would be;

$$T'_w = \mu \left. \frac{du}{dy} \right|_{rms} \quad \text{or} \quad \frac{T'_w}{T_w} = \frac{d(u'/\bar{u}^*)}{dy^+} \approx 0.27$$

according to experimental measurements<sup>(44)</sup>. Since intensities of only about half this value were realized ( $(u^*)'/\bar{u}^* \approx 0.06$ ;  $T'/\bar{T} \approx 0.12$ ), the probe was apparently responding to events in a region above it. Certainly from a heat transfer viewpoint, the probe signal should reflect variations in the thermal boundary layer which occupied the hydrodynamic sub-layer, and the response is probably of a 'space-average' nature. It is now well known that turbulent shear stresses exist in the viscous sub-layer<sup>(45)-(50)</sup>, hence, for pipe flow, the response is an integration of a fluid shear stress distribution having an instantaneous form:

$$T = -\rho u v + \mu \frac{du}{dy}, \text{ whence}$$

$$(T')^2 = \overline{(\rho \hat{u}\hat{v})^2} - 2\rho\mu \overline{(\hat{u}\hat{v} \frac{du}{dy})} + \mu^2 \overline{\left(\frac{du}{dy}\right)^2},$$

$$\text{where } \hat{u}\hat{v} = uv - \bar{u}\bar{v}.$$

The term  $(du/dy)$  is inherently associated with  $u$  fluctuations, but  $(\hat{u}\hat{v})$  depends on both  $u$  and  $v$  fluctuations. The signs associated with

$(du/dy)$  and  $(\hat{u}\hat{v})$ , and hence the correlation  $(\hat{u}\hat{v} du/dy)$ , depend on the event i.e. sweep, ejection, outward interaction or wallward interaction<sup>(51)</sup>. Undoubtedly, the fact that  $T'/\bar{T} < 0.27$  is due either to the term involving  $(\hat{u}\hat{v} du/dy)$  or to the smoothing effect associated with space averaging. It is noted that the normalized spectrum of wall shear stress for pipe flow (Figure 29) bears a fair similarity to Lyatkher's prediction<sup>(44)</sup>. This, to some extent, supports the above conjectures concerning the probe response.

For rod bundle flow,  $(u^*)'$  was found to be approximately proportional to Reynolds number, and  $(u^*)'/\bar{u}^*$  increased with Reynolds number (Figure 28). These differences from pipe flow suggest the possibility of a secondary flow influence on the probe. According to Figure 30, the spectra differ significantly in the low wavenumber range of about 1 to 10  $\text{cm}^{-1}$ . The preponderance of low frequency fluctuations may be associated with sublayer waves initiated by the secondary flow.

The above described work was not pursued further due to lack of time. However, the technique appears worthy of further study and development. The initial work might include, for example, changing the orientation of the film (hence reducing "residence time" effects) and lowering the probe over-heat ratio so as to reduce the depth of

active layer. Concerning the latter, Eckelmann<sup>(42)</sup> has recently achieved a value of  $T'_w/\bar{T}_w$  of 0.24 for an oil channel using an over-heat ratio of 0.02.

### 5.5. Mean Axial Velocity Distributions

Mean axial velocity distributions within the primary flow cells under investigation are shown in Figures 31 to 33 inclusive in the form of isovel plots (lines of constant velocity) for the seventeen test conditions. The velocity head readings were converted to velocities via a computer program using air densities corresponding to the actual tunnel air temperature and absolute pressure, and corrected for humidity effects. The cell average velocities ( $U_b$ ), listed in the Figures and used to normalize the distributions, were obtained by numerical integration of the experimental data. The isovel plots were prepared manually by interpolation.

In evaluating  $U_b$ , the region  $0 \leq y \leq 1.27\text{mm}$  was handled by assuming that universal velocity distributions applied for the sublayer and buffer layer. The velocity measurements next to the tube wall, after correcting for displacement error ( $y = 0.635\text{mm}$  shifted to  $0.813\text{mm}$ ) in accordance with the recommendations of Ower and Pankhurst<sup>(53)</sup>, matched the assumed velocity profiles for this region. Displacement

errors on the Pitot tube due to velocity gradient were negligible in the remainder of the flow field. Axial velocities were measured to an accuracy estimated to be typically within about 2%, with a range of less than 1% to about 5% for the lowest Reynolds number tests. Positional accuracy has been discussed in Section 4.3. No corrections were made for turbulence effects on the readings from the Pitot and static pressure tubes since correction procedures have still to be properly established. According to consensus opinion<sup>(53)-(56)</sup>, the results (presented uncorrected) may be about 1% too high because of turbulence effects.

The isovel plots for each P/D ratio are similar which indicates that  $U_b$ , as a scaling factor, is successful in removing Reynolds number effect except near the sub-channel centerline. The experimental values of  $\bar{U}/U_b$  at the sub-channel centerline were approximately constant at about 1.175 for P/D = 1.50, but varied from about 1.16 to 1.20 with decreasing Reynolds number for P/D = 1.35 and 1.20. Actually all seventeen isovel plots are fairly similar in over-all distribution considering the P/D range and the fact that Reynolds number was varied by a factor of over 7. The use of  $U_b$  as a scaling factor for P/D as well, is especially effective in the region  $y < \hat{y}_{min}$ . The ratio  $\bar{U}/U_b$  consistently achieved values of about 1.07 at the gap center.



This is not unexpected as the isovels in the near-wall region are basically circular arcs concentric with the tube. For the region  $y > \hat{y}_{\min}$ , the inclination of the isovel lines show a distinct  $P/D$  dependence as the distributions go through a transition to where the isovels tend to become concentric with the sub-channel centerline.

The present results for  $P/D = 1.20$  are in good agreement with the experimental results of Subbotin et al<sup>(37)</sup> ( $P/D = 1.20$ ,  $Re = 44,700$ ) and, allowing for a decreasing  $\bar{U}/U_b$  with increasing Reynolds number, with the results of Kjellstrom and Stenback<sup>(21)</sup> ( $P/D = 1.217$ ,  $Re = 149,000$ ). An extrapolation in  $P/D$  of the present results would also appear to agree well with the experimental results of Eifler and Nijssing<sup>(36)</sup> ( $P/D = 1.15$ ,  $Re = 28,000$ ).

The present results have also been compared (within the limits possible) to the several prediction methods available in the literature. Similarities were generally poor with the closest predictions due to Buleev<sup>(15)</sup> ( $P/D = 1.20$ ,  $Re = 24,000$ ), followed by Bender and Switick<sup>(19)</sup> ( $P/D = 1.2$  and  $1.3$ ,  $Re = 50,000$ ). Both predictions are substantially in error in the gap region which is not surprising since although the methods employ different models and varying degrees of empiricism, only the method of Gosman et al<sup>(22)</sup> (which has still to be applied successfully) clearly recognizes

secondary flow.

As may be seen from the isovel plots, the local mean axial velocity for each test is a complex function of position ( $r$ ,  $\phi$  or  $y$ ,  $\theta$ ) where the  $\theta$  dependence is relatively weak compared to  $y$  for the region  $y < \hat{y}_{\min}$ , but comparable\* to the  $y$  dependence for the region  $y > \hat{y}_{\min}$ . The variations in  $\bar{U}$  in the peripheral and radial directions are discussed in the following paragraphs.

Figure 34 shows the distributions of  $\bar{U}$  in the peripheral direction for several fixed radii for each test-section at the same Reynolds number (Test condition 5,  $Re = 36,000$ ). The results shown for each P/D ratio are typical of the P/D ratio for all Reynolds numbers. For  $P/D = 1.50$  and  $1.35$ , the maximum velocity for a given  $y$  generally occurs at  $\theta = 300^\circ$ . For  $P/D = 1.20$ , the velocities for small  $y$  exhibit maxima at about  $\theta = 120^\circ$ . This behaviour continues for  $y = 0.813\text{mm}$  (not shown in Figure 34) where  $y^+ \approx 56$ . One would therefore expect a closer correlation than is evident with the local wall shear stress distribution (Figure 25). This 'Bulging' phenomenon also appears in the data of Kjellstrom and Stenback<sup>(21)</sup>. A possible explanation in terms of secondary flow is suggested in Section 5.9.

---

\* On an 'over-the-range' basis, i.e.,  $0 \leq \theta \leq \pi/6$  and  $0 \leq y \leq \hat{y}$ .

The variations of  $\bar{U}$  in the radial direction were tested for a logarithmic distribution. The results are summarized in Table II. All data points were included in the analyses, and the average friction velocities were determined via equations (27) and (69).

For the form:

$$u^+ = A \ln y^+ + B,$$

typical "universal" coefficients<sup>(56)</sup> for turbulent pipe flow and turbulent boundary layers are  $A = 2.50$  and  $B = 5.5$  (Nikuradse) and  $A = 2.44$  and  $B = 4.9$  (Clauser). For the present rod bundle flows, the average values for  $A$ ,  $B$  and the standard deviation\* for all tests for each test-section were as follows:

<u>P/D</u>	<u>A</u>	<u>B</u>	<u><math>\sigma(\%)</math></u>
1.50	1.96	6.85	1.63
1.35	2.50	4.81	1.55
1.20	2.16	6.38	1.10

The coefficients for  $P/D = 1.35$  were closest to the conventional coefficients, whereas its  $\bar{u}^*$  values were also nearest to fully developed pipe flow values. The average standard deviation was lowest for

---

\*See Table II for definition of standard deviation ( $\sigma$ ).

$P/D = 1.20$ . Since actual velocities generally exceed log plot velocities for  $y^+ > \sim 500$ , this is probably due to its narrow  $y^+$  range compared to the others (see Table II). The apparent Reynolds number effect for  $P/D = 1.50$  (Table II and Figure 35) is also considered due to this reason.

Some of the dimensionless velocities for Test A1 (second highest standard deviation) are plotted against  $y^+$  in Figure 36 together with LSF lines to illustrate the calibre of fit. The data for  $\theta$  values around  $15^\circ$  lie best on the LSF line for all data points. The data for  $\theta = 0^\circ$  fall considerably below this line, but it is noted that using  $u^* = 0.98 \bar{u}^*$ , for example, for these data points would remove about half the separation between lines A-A and B-B. It appears, in general, that using local friction velocities would decrease the standard deviation but the LSF line would not change significantly.

The ratio of boundary layer thickness to rod diameter for the rod bundle geometries were in the range  $0.10 < (\hat{y}/D) < 0.37$ . In order to allow for any effect of transverse curvature, the form:

$$u^+ = A' \ln \left[ y^+ (1 + y/D) \right] + B'$$

was examined, and the results are included in Table II. This approach has been discussed by Willmarth and Yang<sup>(57)</sup>. The average values for

A', B' and the standard deviation for all tests for each test-section were as follows;

<u>P/D</u>	<u>A'</u>	<u>B'</u>	<u>σ(%)</u>
1.50	1.81	7.43	1.42
1.35	2.33	5.42	1.55
1.20	2.05	6.80	1.05

The only significant improvement is a modest decrease in the standard deviation for P/D = 1.50 for which transverse curvature effects are largest.

The distributions of the mean axial velocity in the radial direction in a velocity defect form:

$$\frac{\bar{u}_y - \bar{u}}{\bar{u}^*} = -A'' \ln \left( \frac{y}{\hat{y}} \right) + B''$$

are shown in Figure 37 for the three P/D ratios at a common Reynolds number. For pipe flow, the coefficients A'' and B'' are 2.44 and 0.8 respectively<sup>(56)</sup>. The chain lines shown for reference in Figure 37 correspond to B'' = 0 and A'' = A for the particular test as listed in Table II, and it is noted that the line for P/D = 1.50 is a poor representation of the data. The solid lines shown in Figure 37 correspond to B'' = 0 and A'' = 2.208 where A'' is the average value

for A for all seventeen tests (Table II), and, coincidentally, also very near the average value for Tests A5, B5 and C5. This line ( $A'' = 2.208$ ) offers a fair representation of the data for all three P/D ratios. It therefore appears that a velocity defect representation tends to reduce the P/D dependence. Unfortunately it does not appear that the data scatter would be improved significantly by using the local values for the friction velocity.

It is simply noted, in summary at this point, that the modified forms of the "law of the wall" and the "outer law" are apparently due to the nature of the present helical flows. Similar situations exist for rectangular ducts<sup>(58)</sup> <sup>(59)</sup> and eccentric annular ducts<sup>(60)</sup> which also involve secondary flows. The non-uniform variation with P/D of the coefficients in the wall law relationship and their relation to the conventional values, is linked directly to  $\bar{u}^*/u_p^*$ , the ratio of the rod bundle friction velocity to the friction velocity for fully developed pipe flow at the same Reynolds number.

## 5.6 Normal Stresses and Turbulent Kinetic Energy

The results of the turbulence measurements are presented and discussed in this and succeeding sections. The following notes apply

to these results.

- a) In view of the large volume of experimental data and the Reynolds number similarity for the results for each test-section, the results presented here are for only two tests for each P/D ratio. These tests are A2 and A5, B3 and B6, and C4 and C6 which were the second highest and second lowest Reynolds numbers for each P/D ratio. The experimental data for the remaining tests have been documented\* in Reference 3. Unless otherwise stated, the results for these tests were similar to those presented here.
- b) The data presented here for  $u'$ ,  $v'$ ,  $R_{uv}$  and  $\overline{uv}$  were obtained via the u-v X-probe (Figure 10), whereas the data for  $w'$ ,  $R_{uw}$  and  $\overline{uw}$  were obtained via the u-w X-probe (Figure 11). The typical agreement between the  $(u'/\bar{u}^*)$  values measured by single-wire probe and the two types of X-probe is illustrated in Figure 38. Also demonstrated is the fact that  $v' \approx w'$  at the sub-channel centerline--cross-refer to equation (12) and the ensuing comment.

---

\*Corrections for "yaw", as applicable, were not made at this stage.

- c) The experimental values obtained via X-probe for the quantities  $v'$ ,  $w'$ ,  $\overline{uv}$  and  $\overline{uw}$  were multiplied by the factor 1.1117 as a correction for "yaw" (tangential cooling with inclined hot-wire). This correction factor for DISA probes is in accordance with the recommendation of Lawn<sup>(61)</sup> whose correction factors are identical to the latest<sup>(62)</sup> analyses of Champagne and Sleicher<sup>(63)</sup>. (The correlation coefficients and  $u'$  required no correction).
- d) Regarding signs for the shear stresses, since  $\overline{uv}$  was physically negative, its "experimental" sign was positive for the reason indicated in Figure 10. It is presented here as positive as a matter of convenience. Conversely, since  $\overline{uw}$  was found (experimentally) to be mainly negative, it was physically mainly positive (see Figure 11). It also is presented with its "experimental" sign, i.e. mainly negative. The correct signs for  $\overline{uv}$  and  $\overline{uw}$  were of course used for all numerical calculations associated with the momentum and energy equations.
- e) Concerning the accuracy of the turbulence measurements, a recent study by Thornton-Trump<sup>(64)</sup>, who estimated X-probe anemometry (without linearizers) errors using the technique of Kline and McClintock<sup>(65)</sup>, showed that maximum errors (20:1 odds) were about  $\pm 13\%$  for  $u'$ ,  $v'$  and  $w'$ , and about  $\pm 21\%$  for  $\overline{uv}$ ; however trend



errors were only about  $\pm 3\%$  for these parameters. The resulting conclusion (which probably represents the opinion of most hot-wire experimenters) was that whereas hot-wire anemometry may not give accurate absolute results, trends are usually reasonably accurate. In reality, it is the trend accuracy which really matters. For some situations, levels may even be "pinned" by some theoretical consideration. In numerical evaluations of the governing fluid-mechanical equations, it is the gradients (obtained from the trends) which are of main importance. For these reasons, a realistic estimate of trend accuracy is both necessary and sufficient. The problem of forming a detailed estimate of the absolute accuracy for a given hot-wire anemometry system is extremely difficult, if not impossible, if all known factors are attempted to be taken into account. For X-probe linearized anemometry, there are potential errors in the signals leaving the linearizers due to incorrect wire angle (manufacture, stretching, etc.), misalignment of the probe to the flow, unmatched frequency response, etc. Calibration (against a Pitot tube of accuracy within say  $\pm 2\%$ ) and matching of channel sensitivities using a DVM with an accuracy of 0.1% of full scale, generally leave residual systematic errors. The effects of small mis-alignment of the

probe and mis-matching of sensitivities have been assessed by Lawn<sup>(61)</sup> and are usually not too serious. Operational errors due to drift induced by temperature changes or wire contamination, may follow. The final readings at the correlator(s) are influenced by instrument errors; e.g. meter accuracy of  $\pm 2\%$  at full scale, ratiometer accuracy to  $\pm 0.03$ . Then of course, fairing a line through a given set of data tends to remove random errors but does not affect systematic errors. Having thus indicated the complexity of the situation, the only practical recourse for establishing trend accuracy is to examine actual repeatability. The trend accuracies determined this way for the present results are considered to be within  $\pm 3\%$  for  $u'$ ,  $v'$  and  $w'$ , within  $\pm 5\%$  for  $\overline{uv}$ , and within about  $\pm 10\%$  for  $\overline{uw}$ .

The experimental results related to the normal stresses are presented first. The radial distributions of the turbulence intensities are shown in Figures 39 ( $u'$ ), 40 ( $v'$ ) and 41 ( $w'$ ). The abscissa of each graph is the radial distance from the wall ( $y$ ) normalized by the radial distance (for the particular  $\theta$ ) to the line of symmetry ( $\hat{y}$ ).

The ordinates\* are the root-mean-square values of each fluctuating velocity normalized by the average friction velocity ( $\bar{u}^*$ ). The average friction velocity for each test was determined by the procedure indicated in Appendix B. Lines showing the distributions of the turbulence intensities for fully developed pipe flow as determined by Laufer<sup>(39)</sup>, are included in the Figures for reference purposes.

The present data are similar in distribution to pipe flow but the data generally lie below the pipe flow lines. For  $P/D = 1.50$ , the offsets between the pipe flow lines and the mean data lines, increased progressively with decreasing Reynolds number. For  $P/D = 1.35$ , the offsets did not vary with Reynolds number and amounted to only about 5 to 10% of the pipe flow values. For  $P/D = 1.20$ , the offsets again did not vary with Reynolds number but amounted to 10% or more.

The present results are in general agreement with the data of Kjellstrom and Stenback<sup>(21)</sup> ( $P/D = 1.217$ ,  $Re = 149,000 - 355,000$ ). Their axial turbulence results practically coincided with Laufer's distribution, but their radial and peripheral turbulence intensities were about 20% below the pipe flow lines. The Reynolds number dependence for the present results

---

\*The ordinates are also the square root values of each normal stress normalized (and made dimensionless) by the average shear stress, i.e. for example  $\left( \rho(u')^2 / \rho (\bar{u}^*)^2 \right)^{1/2} = u' / \bar{u}^*$

for  $P/D = 1.50$ , could not be explained. The offsets ranged from about 15% for Test A1 to about 50% or more for Test A6. A systematic error in the hot-wire measurements was considered unlikely in view of the fact that the data from both X-probes behaved in the same way. The possibilities of either a systematic error in the pressure drop tests (i.e. high  $\bar{u}^*$  values) or incomplete flow development were also considered improbable, but perhaps should not be ruled out completely. In any event, if the low Reynolds number tests for  $P/D = 1.50$  are excluded, the generalization (for all other data) can be made that the offsets are roughly equal to the fraction  $(\bar{u}^* - u_p^*)/u_p^*$  of the rod bundle values, where the fraction represents the amount by which rod bundle friction velocity exceeds the friction velocity for fully developed pipe flow at the same Reynolds number. However whereas  $u' \approx u_p'$  and (more approximately)  $v' \approx v_p'$ , even this broad generalization breaks down in that definitely  $w' < w_p'$  for  $P/D = 1.50$  and 1.20. Another peculiarity in the data are the high  $v'/\bar{u}^*$  values for  $y/\hat{y} < 0.2$  (Figure 40, especially 40d). These occurred at  $y^+$  values in the range  $\sim 30$  to 80 and more, i.e. within the conventional "constant shear" layer.

It is also apparent in Figures 39, 40 and 41 that the turbulence intensities, scaled on average friction velocity, show azimuthal dependence in that the  $15^\circ$  data consistently lie above the  $0^\circ$  and  $30^\circ$  data. For the

"near-wall" region ( $y/\hat{y} < 0.4$ ), it appears that the data could be represented by a single line if the local (rather than average) friction velocities were used. But in the "core" region ( $y/\hat{y} > 0.4$ ), the spreads are excessive and the data differ by up to about 20%. Since the data of Kjellstrom and Stenback<sup>(21)</sup> exhibit a similar characteristic, the possibility of a systematic error can be discounted. The behaviour is therefore likely associated with secondary flow.

The radial distributions of the mean turbulent kinetic energy ( $\bar{q}$ ) defined by equation (39) are shown in Figure 42. The data points shown are the values computed directly from the normalized normal stresses, i.e.

$$\frac{\bar{q}}{(\bar{u}^*)^2} = \frac{1}{2} \left[ \left( \frac{u'}{\bar{u}^*} \right)^2 + \left( \frac{v'}{\bar{u}^*} \right)^2 + \left( \frac{w'}{\bar{u}^*} \right)^2 \right] .$$

In addition to the pipe flow line<sup>(39)</sup>, the average line from the data of Kjellstrom and Stenback<sup>(21)</sup> is also shown for comparison. The angular dependence in the "core" region, mentioned above, now shows up quite prominently.

The peripheral distributions of the turbulence intensities nearest to the wall were such that the values increased gradually with  $\theta$  consistent with the decreasing  $y/\hat{y}$ . Farther out in the flow, the

same pattern held but with increasing  $y$ , there was a tendency for  $v'$  and  $w'$  to peak slightly in the region  $18^\circ < \theta < 21^\circ$ . The distributions along the primary flow cell boundary defined by  $y = \hat{y}$  (no longer peripheral) were rather interesting. Each turbulence intensity increased gradually leaving the gap to achieve a maximum in the region  $\theta \approx 18^\circ$ , and then decreased more rapidly towards the sub-channel centerline. The behaviour is illustrated in Figure 43 which shows the distributions of the mean turbulent kinetic energies on the  $y = \hat{y}$  boundary for each P/D ratio at a common Reynolds number of 36,000. A counter-clockwise circulation of secondary flow can be inferred from these distributions. Turbulent kinetic energy is brought in to the peak region by secondary flow coming from regions relatively nearer to the wall where turbulent energy levels are higher. The decrease in turbulent kinetic energy from the peak region towards the gap would correspond to the inward turning of the secondary currents towards the wall.

As indicated by the Figures and preceding discussion, the normal stresses and mean turbulent kinetic energy scale only approximately on the average friction velocity, and are thus not completely independent of Reynolds number and P/D ratio. The average friction velocity is a function of both Re and P/D (equations 69 and 27), so

it is of interest to examine in more detail the actual rms values of the fluctuating velocities as functions of  $Re$  and  $P/D$ . The  $u'$  values at the center of the half gap (i.e.  $\theta = 0^\circ$ ,  $y/\hat{y} = 0.5$ ) have been plotted in Figure 44 as a function of  $P/D$  for various Reynolds numbers. The linearity over the  $P/D$  range is illustrated by this Figure. For a given  $P/D$ ,  $u'$  almost doubles for a doubling in  $Re$ . This is consistent with the fact that  $\bar{u}^* = U_b \sqrt{f/8}$  where  $f = C Re^{-n}$  and  $n \approx 0.25^*$ , hence for a fixed point in the flow field,  $u' \propto \bar{u}^* \propto U_b^{7/8}$ . For a given Reynolds number,  $u'$  decreases as  $P/D$  increases over the range  $1.2 \leq P/D \leq 1.5$ . The  $u'$  values increase more or less linearly by a factor of about 2.5 in going from  $P/D = 1.5$  to  $P/D = 1.2$ . For a given  $Re$ ,  $f \approx \text{constant}$  (Figure 24) so that  $u' \propto \bar{u}^* \propto U_b$ . The hydraulic diameter ( $D_h$ ) of the primary flow cell is a function of  $P/D$  (equation 24); and for the present experiments ( $D = \text{constant}$ , variable tube spacing),  $D_h$  decreases almost linearly by the factor 2.52 in going from  $P/D = 1.5$  to  $P/D = 1.2$ . Hence for a given  $Re$ ,  $U_b$  increases almost linearly by the same factor. Since it is logical to expect  $P/D$  ratio effects to be accentuated in the gap region, it follows that the effect of tube spacing on the turbulence parameters is of a well-behaved linear

---

\*Actual values from equation (69) are  $n = 0.212, 0.245$  and  $0.287$  for  $P/D = 1.50, 1.35$  and  $1.20$  respectively.

nature in the range  $1.2 \leq P/D \leq 1.5$ . For  $P/D > 1.5$ , the curves presumably flatten out with  $u' \propto (P/D)^{-2}$  and the stacking continues with decreasing separations as the levels fall. For  $P/D < 1.2$ , the anticipated behaviour, as illustrated in Figure 44, is probably very non-linear as secondary flows become increasingly restricted by the narrowing gap, and undoubtedly the effect would be dependent on Reynolds number.

### 5.7 Shear Stresses and Correlation Coefficients

The radial distributions of the correlation coefficients  $R_{uv} \equiv \overline{uv}/u'v'$  are shown in Figure 45. The distributions due to Laufer<sup>(39)</sup> and Guitton<sup>(66)</sup> for fully developed pipe flow are included for comparison purposes. The distributions are similar to pipe flow especially in the region  $y/\hat{y} < 0.4$ . But at the lowest Reynolds numbers (A6, B7 (and even B6 - Figure 45d) and C7), the  $R_{uv}$  values nearest to the wall dropped to as low as 0.25 for Test B7. For  $P/D = 1.35$  and 1.20, this seemed to be associated with high  $v'$  values (see Figure 40d). For  $y/\hat{y} > 0.4$ , the angular dependence appeared to vary with  $P/D$  ratio, but since systematic positioning errors were possible, the trends are not reliable. In fact, the negative  $R_{uv}$  values near  $y = \hat{y}$  for  $P/D = 1.20$  are considered due to a combination of systematic positioning error



and asymmetry. The u-w X-probe results (Figure 41e & f for  $w'$ ) were apparently not influenced, but  $u'$  (Figure 39e & f),  $v'$  (Figure 40e & f) and  $\overline{uv}$  (Figure 46e & f, presented later), all u-v X-probe data, were all affected. But at the same time, the effect increased with decreasing Reynolds number, and since the estimated\* positioning error was abnormally high, asymmetry was also probably involved.

The radial distributions of the normalized shear stresses  $\rho \overline{uv} / \rho (\overline{u^*})^2$  are shown in Figure 46. The data corresponding to  $\theta = 0^\circ$  and  $30^\circ$  for  $P/D = 1.35$  agree quite well with the theoretical distributions (Figure 5) for the radial boundaries. The curvature is also discernible for  $P/D = 1.50$  at the higher Reynolds number. Otherwise the data characteristics are compatible with the preceding observations. The present data are in general agreement with the results of Kjellstrom and Stenback<sup>(21)</sup>. Their data for  $\theta = 30^\circ$  are shown in Figure 46e. Their test-section ( $P/D = 1.217$ ) consisted of 15.65 cm O.D. tubes, but transverse curvature effects were similar geometrically to test-section IC ( $P/D = 1.20$ ).

---

\*A difficult task since the probe orientation beyond  $y = \hat{y}$  is no longer radial.

Concerning the boundary  $y = \hat{y}$ , both theoretically and practically,  $\overline{uv} = 0$  at  $\theta = 0^\circ$  and  $30^\circ$ , i.e. at each end of the boundary. But it is not clear, because of discontinuities involved with the present coordinate system, as to whether or not  $\overline{uv} = 0$  elsewhere. Mean axial velocity gradients exist along the boundary between its terminal points, so it might be guessed (from a mixing length viewpoint) that  $\overline{uv}$  is non-zero, or more generally that shear stresses are finite. Experimentally,  $\rho\overline{uv}$ ,  $\rho\overline{uw}$  and also  $\rho\overline{vw}$  were indicated to be non-zero at this boundary. But since the principal axes of the Reynolds stress tensor rotate on passing across the boundary, in view of probe size and coordinate system complications, experimental results at the boundary cannot be taken at face value. The question therefore remains open.

The relationship between the mean turbulent kinetic energy (essentially the trace of the Reynolds stress tensor and hence an invariant) and  $\overline{uv}$  (generally the primary shear stress) is of considerable practical interest particularly for computation purposes. Harsha and Lee<sup>(67)</sup> have shown that the linear relation  $|\overline{uv}| = 0.3 \bar{q}$  (evaluated at the same spatial position) holds fairly well for wakes, jets and boundary layer flows. This equation also provides a good representation of the data for straight conical diffuser flows<sup>(68)</sup>. The relationship was

tested using the present turbulence data; the results shown in Figure 47 are typical. It is concluded for rod bundle flows that  $|\overline{uv}| = 0.3 \bar{q}$  provides a fair correlation of the data for the region  $y/\hat{y} < \sim 0.9$ . The limit is necessary for bounded flows since near the center of the flow,  $\bar{q}$  remains finite while  $\overline{uv}$  tends to zero.

The radial distributions of the correlation coefficients  $R_{uw} \equiv \overline{uw}/u'w'$  are shown in Figure 48. The results for all tests were similar in most respects. For  $\theta = 15^\circ$ , the experimental (sign) values decreased with increasing  $y/\hat{y}$ . For  $\theta = 30^\circ$ , the experimental values increased with increasing  $y/\hat{y}$  and passed through zero in the vicinity of  $y/\hat{y} \approx 0.7$ . For  $\theta = 0^\circ$ , the variations were dependent on P/D ratio. Concerning magnitudes, the  $R_{uw}$  values ranged from about +0.20 (near the center of the sub-channel) to about -0.28 (typically at  $\theta \approx 15^\circ$  and  $y/\hat{y} \approx 0.9$ ).

The peripheral distributions of the normalized shear stresses  $\rho \overline{uw}/\rho(\bar{u}^*)^2$  are shown in Figure 49. The distributions vary with distance from the wall. All distribution sets had certain features in common. Values were small and positive near the center of the sub-channel. Also for  $y/\hat{y}_{\max} \approx 0.5$ ,  $\partial(\overline{uw}/(\bar{u}^*)^2)/\partial\theta$  changed sign as  $\theta$  went from  $0^\circ$  to  $30^\circ$ , and equalled zero at about  $\theta = 12^\circ$ . This behaviour is considered to be associated with the secondary flow.

For the near-wall region where  $\overline{uv}$  was large,  $\overline{uw}$  reached values of up to about one-third of  $\overline{uv}$ , being especially large for  $P/D = 1.35$ . For the region  $0.8 < y/\hat{y} < 1.0$ ,  $\overline{uw}$  was comparable in magnitude to  $\overline{uv}$ , and exceeded  $\overline{uv}$  as  $y$  approached  $\hat{y}$ .

Kjellstrom and Stenback<sup>(21)</sup> have reported a few preliminary results for  $\overline{uw}/(u^*)^2$ , namely the mean values of three experiments ( $Re = 149,000, 271,000$  and  $355,000$ ;  $P/D = 1.217$ ) for  $\theta = 0^\circ$  and  $30^\circ$  as functions of  $y/\hat{y}$ . Their data bands are shown in Figure 49e for the two angles. Their data contained considerable scatter, but the general trend was for the largest negative values to occur nearest to the wall with the values tending towards zero with increasing  $y/\hat{y}$ . These characteristics are similar to the present data, however the data of Kjellstrom and Stenback<sup>(21)</sup> are too limited to permit a definitive comparison.

Some experimental data on the shear stress  $\rho\overline{vw}$  were obtained via three-wire probe for test-section IA ( $P/D = 1.50$ ). Some sample results are given in Table III. Unfortunately, as noted in an earlier report<sup>(4)</sup>, whereas the three-wire probe data for the normal stresses and  $\overline{uv}$  were in fair agreement with X-probe data, this was not the case for  $\overline{uw}$  and presumably also  $\overline{vw}$ . Certainly zero values for  $\overline{vw}$  were not obtained at the radial boundaries as required by theory.

Nonetheless it appeared that  $\overline{vw}$  was comparable in magnitude to  $\overline{uw}$ . Its physical sign was the same as  $\overline{uw}$ , but nearest to the wall its experimental sign switched to negative, but this may have been due to a wall effect on the probe.

Values were computed for the eddy diffusivity in the radial direction,  $\epsilon_r$ , as defined by equation (8). Some typical data are shown in Figure 50 which includes for reference the distribution for fully developed pipe flow as given by Hinze<sup>(56)</sup>. The  $\epsilon_r$  values are substantially larger than for pipe flow for the region  $y/\hat{y} > 0.3$ . Rapier and Redman<sup>(16)</sup>, in predicting mean axial velocity distributions for triangular array rod bundles, have assumed a diffusivity profile as follows:

$$\frac{\epsilon_r}{\bar{u} \cdot \hat{y}} = 0.4 \frac{y}{\hat{y}} \left[ 1 - \frac{y}{\hat{y}} \right], \quad 0 < \frac{y}{\hat{y}} < 0.5; \text{ and}$$

$$\frac{\epsilon_r}{\bar{u} \cdot \hat{y}} = 0.10, \quad 0.5 \leq \frac{y}{\hat{y}} < 1.0$$

This profile is a good practical representation of the present experimental data.

The concept of an eddy diffusivity in the peripheral direction,  $\epsilon_\phi$ , as defined by equation (9) was difficult to apply since in many

regions of the flow field (e.g. near the wall),  $\partial \bar{U} / \partial \phi$  tended to zero while  $\bar{u}v$  remained finite. For the far-wall region where  $\partial \bar{U} / \partial \phi$  was sizeable (see Figure 34), the dimensionless parameter  $\epsilon_{\phi} / \bar{u}^* \hat{y}$  assumed typical values of about 0.30. Hence in general  $\epsilon_{\phi}$  exceeds  $\epsilon_r$  by a factor of at least two or three.

### 5.8 Axial Turbulence Power Spectra and Microscale

Power spectral data were obtained only for the axial fluctuating velocity. One-dimensional spectra were taken at three locations in the flow fields. These locations were designated A (near-wall), B (gap center) and C (sub-channel center)--see Figures 12, 13 and 14 for actual locations. The results\* are presented in Figure 51 in absolute analog form such that the area under each curve equals the square of the total RMS voltage generated by the single-wire probe, i.e. represents  $(u')^2$ . The curves are typical of the turbulence phenomenon, and cover a wide wavenumber range. The largest contribution of energy to the total  $u'$  value is provided by velocity fluctuations

---

\*The upper frequency limit for the measuring system was  $5 \times 10^4$  Hz set by the anemometer. No corrections were made for finite wire length effects(69)(70).

less than about 500 Hz (the largest eddies). The main effect of decreasing tube spacing was to flatten the spectra at the low frequencies. Consequently for  $P/D = 1.20$ , velocity fluctuations having frequencies up to about 200 Hz contributed most powerfully and more or less equally to the total  $u'$  value. For  $P/D = 1.50$ , the comparable figure was about 80 Hz. Accepting the notion that the largest eddies are limited by the physical size of the flow channel, an obvious conjecture is that eddy splitting may occur as  $P/D$  decreases thereby increasing the "aspect ratio" of wetted perimeter to gap width.

Values for the Taylor microscale,  $\lambda \equiv \bar{U} u' / \left[ \overline{(du/dt)^2} \right]^{1/2}$ , were determined for four test conditions; Test-Sections IB and IC, each at two Reynolds numbers. The results are shown in Figures 52 ( $P/D = 1.35$ ) and 53 ( $P/D = 1.20$ ). The trends within each Figure are considered fairly reliable, but the absolute accuracy is doubtful. Preliminary measurements for the four test conditions yielded microscale values in the range 0.1 to 0.8 mm, but the trends with respect to spatial distribution and Reynolds number effect were the same as the present results. In view of the small magnitudes, the tests were repeated later for Test-Section IC, and these results (higher  $\lambda$  values) are shown in Figure 53. Diagnostic checks showed that pre-amplification was required to make the results independent of further amplification or choice of differentiator

time constant ( $10^{-4}$  sec, was used). Still later, it was found in conjunction with other microscale measurements in the Turbulence Laboratory, that microscale values were dependent on high frequency cut-off. Since Test-Section IB had been reinstalled at this stage, microscale tests were rerun for  $P/D = 1.35$ . The linearized signal was passed through a 55D25 Auxiliary Unit with the low-pass filter set at 10 KHz (based on "noise" break in the power spectra) before entering the 55A06 differentiator circuit. The resulting data are shown in Figure 52. Since these data differ from those in Figure 53 by the filtering procedure, the apparent effect of  $P/D$  ratio (for the same Reynolds number) is not reliable. In addition, the absolute accuracy is questionable since some of the microscale values are smaller than the 1.25 mm sensitive length of the DISA 55F01 probe which was used, and no corrections<sup>(69)</sup> have been made.

Regarding the microscale trends considered valid, for most\* tests, the  $\lambda$  values decreased uniformly with increasing  $y/\hat{y}$ . This behaviour is opposite to that found by Lawn<sup>(71)</sup> for fully developed pipe flow. For a given  $P/D$  ratio, the average microscale values increased

---

\*For Test B3, for  $y/\hat{y} < 0.5$ ,  $\lambda$  decreased towards the wall as in pipe flow.



with Reynolds number. This trend is also opposite to that for pipe flow<sup>(71)</sup>. If the turbulent dissipation is approximated by the isotropic relation  $\Phi_{td} = 15 \nu \overline{u^2}/\lambda^2$ , this implies that dissipation rates immediately adjacent to the wall, increase with Reynolds number differently than pipe flow, which is possible if energy is brought in by the secondary velocities which scale on friction velocity. In general, the spatial distribution of microscale and the Reynolds number effect are different than for pipe flow, and this must be attributed to secondary flow.

Concerning the turbulent energy equation, i.e.

$$X + XI + XII + XIII + \Phi_{td} = 0 \quad \dots \dots \dots (59)$$

it is noted that Term XI, convection of the mean turbulent energy by the secondary flow (a second-order effect according to Gessner<sup>(32)</sup>), could by closure be estimated roughly using the present experimental data by:

- a) approximating Term X (turbulence production) by equation (47a),
- b) assuming Term XII (convection by turbulence) to be the same as for fully developed pipe flow (perhaps a poor assumption in view of the second term in equation (62)), and
- c) combining Term XIII (viscous diffusion) and  $\Phi_{td}$  as in equation (64) where the fourth term is neglected while  $\Phi'$  is estimated by the Bradshaw method<sup>(72)</sup> which was recently tested successfully by Lawn<sup>(71)</sup> for fully developed pipe flow.

However, in view of the assumptions involved and the limited  $\overline{u^2}$  power spectral data, this approach was not pursued in depth. Rather the emphasis was placed on the momentum and mean energy equations. As suggested indirectly by Gessner<sup>(32)</sup> and by Hoagland<sup>(28)</sup>, information on the secondary flows is most profitably extracted at the momentum equation and mean energy equation levels.

### 5.9 Secondary Flows

The basic secondary flow pattern for primary flow cell 1 is thought to be a single cell of counter-clockwise circulation for all three P/D ratios as indicated in Figures 54 to 56 inclusive (upstream views). This picture is based on the following considerations.

- a) The pattern is consistent with Prandtl's original postulate<sup>(27)</sup> which predicts, in particular, a downflow adjacent to the  $y = \hat{y}$  boundary where isovel curvatures are high. For  $P/D = 1.20$ , the "bulging" of the isovels towards the  $\theta = 0$  boundary is quite pronounced.
- b) The counter-clockwise circulation is predictable for the limiting case of  $P/D = 1.00$  from square duct results. The radial boundary (only one at  $\theta = \pi/6$ ;  $\overline{w} = 0$ ) corresponds to the symmetry line joining the duct center to the mid-wall, whereas the  $y = \hat{y}$  boundary

( $v' \approx w'$ ) corresponds to the corner bisector. From this vantage point, the main role of the secondary flow would seem to be to transport momentum/energy into the gap region. Its ability to accomplish this task would surely depend on the gap size.

- c) As observed earlier, this pattern may be inferred from the local wall shear stress distributions (Section 5.4) and from the mean turbulent kinetic energy distributions at the  $y = \hat{y}$  boundary (Section 5.6).
- d) The proposed circulation is supported by the results of calculations employing equation (28) (momentum) and equation (49) (mean energy). These are discussed below.

The calculations involving equation (28) were concentrated at  $\theta = 3^\circ$  and  $27^\circ$  and  $y/\hat{y} \approx 0.5$  ( $\partial \bar{U}/\phi \approx 0^*$ ). The results for the various tests quite consistently indicated  $\bar{V}$  to be negative at  $\theta = 3^\circ$  and positive at  $\theta = 27^\circ$  for all three  $P/D$  ratios. The magnitudes of

---

\*If the calculations are made at the radial boundaries,  $\partial \bar{U}/\partial \phi = 0$  and the equation is completely valid in this respect. But  $\partial \bar{UW}/\partial \phi$  is also zero, so its effect is excluded. Then the dilemma between theory and practical measurement arises as to the existence of  $\bar{V}$  in the first place.

$\bar{V}$  were indicated to be about 4% of  $\bar{u}^*$  which corresponds to about  $\frac{1}{4}\%$  of  $U_b$ . This also makes  $\bar{V}$  only about 5% of  $v'$ , its companion rms velocity. The key factor in the calculations involving equation (28) was the term  $\partial(\bar{uv}/(\bar{u}^*)^2)/\partial y$  in relation to  $4/D_h$  (constant for each P/D ratio). As can be seen from Figure 46, the distributions of  $\bar{uv}/(\bar{u}^*)^2$  with respect to  $y/\hat{y}$  were roughly the same for  $\theta = 0^\circ$  and  $30^\circ$ , hence the actual dimensional gradients were much steeper at  $\theta = 3^\circ$  than at  $\theta = 27^\circ$ . To emphasize this point; if the distributions were identical and linear, the ratio of the gradient at  $0^\circ$  to the gradient at  $30^\circ$  would be 1.46, 1.60 and 1.93 for  $P/D = 1.50, 1.35$  and  $1.20$  respectively. The gradients  $\partial(\bar{uw}/(\bar{u}^*)^2)/r \partial \phi$  were significant but, compared to  $\partial(\bar{uv}/(\bar{u}^*)^2)/\partial y$ , provided only what might be described as a modifying influence on  $v^+$ .

The results of the calculations involving equation (49) are described in Appendix D where the energy balance is discussed. The dimensionless convection of mean energy by the secondary flow (called Term B in Appendix D) was indicated to be roughly about the same magnitude as convection by the turbulence, which in turn suggested that the secondary velocities were probably less than  $\frac{1}{2}\%$  of the bulk average axial velocity. The distributions of the values for Term B for Tests A3, B3 and C3 ( $Re \approx 60,000$ ) are shown in Figures 54,

55 and 56 respectively. The proposed secondary flow pattern is consistent in most regions with the signs of the Term B values. The centers of the secondary flow cells were indicated to occur at  $\theta \approx 15^\circ$  as shown in the Figures. However, it is noted that some caution must be exercised in interpreting the zero values. Physically, zero values should occur at the center of the secondary flow cell. But zero values also occur when the net transport equals zero at a point, i.e. energy convected in by the secondary flow is offset by energy convected out by the secondary flow. For example, in the gap region the Term B values consistently go from negative to positive when proceeding in the wall direction, and so of course equal zero at some point. A zero contour also exists near and parallel to the wall.

The proposed secondary flow pattern provides a possible explanation as to why the  $15^\circ$  data for the normal stresses lie consistently above the  $0^\circ$  and  $30^\circ$  data for the outer flow region. The explanation involves the same reasoning used in Section 5.6. The counter-clockwise circulation is such that the fluid entering the outer region at  $\theta = 15^\circ$  comes from regions relatively closer to the wall where the turbulent energy levels are higher. This fluid "mixes" and moves downward and wallward. The same explanation may to some extent account for the parallel situation with  $\bar{u}\bar{v}$  although probably  $\bar{u}\bar{w}$  has a

modifying influence here. It is also noted that the "bulging" phenomena noted in Section 5.5 in connection with the peripheral distributions of  $\bar{U}$  near the wall for  $P/D = 1.20$ , may be due to an outflow of secondary flow as indicated in Figure 56,

The vorticity technique outlined in Section 3.2 was applied to the present data but the results were either inconclusive or contradictory. One pattern which emerged for  $P/D = 1.20$ , indicated two counter-rotating cells separated by  $\theta \approx 18^\circ$ . The technique is considered unreliable because of the distinct possibility that the two terms in equation (32) involving  $\sqrt{w}$  are important and perhaps even dominant. In fact, for the present coordinate system, the measurements are more or less normal to the  $y = \hat{y}$  boundary (the analog of the corner bisector in square ducts), hence the realization obtained of the Reynolds stress tensor components are comparable to Gessner's latest work<sup>(32)</sup> in which the shear stresses dominate.

Attempts at measuring the secondary velocities via X-probe (Figures 10 and 11) and three-wire probe<sup>(4)</sup> were unsuccessful. The measuring systems lacked the required sensitivity to properly extract the very small secondary velocities. This was compounded by errors incurred by imperfect matching of anemometer channels, relative drift and signal processing. In addition, axial velocity gradient effects

and wall effects on the probes were significant. The u-w X-probe, in particular, was useless near the wall because of high errors due to axial velocity gradients. Nonetheless, the X-probes were useful to some extent when used judiciously in a qualitative manner. After matching the channels at the sub-channel centerline, by quickly\* moving the probe to a strategic position, the sign (direction) of the particular secondary velocity could be observed from the ensuing unbalance between the DC voltages of the two anemometer channels. The indications were admittedly often barely perceptible, but the information, in general, supported the proposed secondary flow pattern.

Token support was also provided by the three-wire probe system. The three-wire probe was used in both Test-Section IA (A1 and A2) and Test-Section IB (B3). A concerted effort was made for Test B3. The three channels were matched at the sub-channel centerline, and only the DC readings were taken at each point in order to keep the test time as short as possible to minimize any relative drift. The match were checked periodically and trimmed if necessary. The measurements were repeated twice; each of the three trials produced the same pattern. For the outer flow region,

---

\*To obviate any relative drift.

there was a general downflow with distinct wallward turning in the gap region. But for  $y < \sim 5 \text{ mm}$ , the results indicated a relatively large outflow from the wall which progressively deflected downward with increasing  $y$ . This pattern is obviously impossible, however if the data for the region adjacent to the wall are dismissed on the grounds of either or both axial velocity gradient effect or/and wall effect, the remaining pattern is consistent with the proposed model. For the outer region, the magnitudes of  $\bar{V}$  were indicated to be as high as 1% of  $U_b$  near the gap to about 0.1% of  $U_b$  (typical) near the  $\theta = 30^\circ$  boundary. Values for  $\bar{W}$  near the  $y = \hat{y}$  boundary were of the order of  $1/3\%$  of  $U_b$ . These values, unfortunately, may not be very reliable as the probe may have been influenced also by axial velocity gradients in the peripheral direction.

The only other measurements known of secondary velocities in triangular array rod bundles are those due to Hall and Svenningsson<sup>(38)</sup> who worked with the test rig of Kjellstrom and Stenback<sup>(21)</sup> (see Figure 2,  $P/D = 1.217$ ) and used hot-wire anemometry\*. They measured the radial

---

\*The technique is not clear--apparently a rotatable single inclined wire; six measurements per point with different angles between the hot-wire and the axial velocity direction.



distributions of the peripheral secondary velocity,  $\bar{W}$ , in two primary flow cells at  $\theta = 0^\circ, 15^\circ, 30^\circ, 45^\circ$  and  $60^\circ$ . Their results ( $Re = 270,000$ ) indicated  $\bar{W}$  to be about 1% of the bulk average axial velocity. For one primary flow cell, the velocity distribution at  $\theta = 15^\circ$  was consistent with the present proposed model of secondary flow. But all other cross-sections showed a flow in the same direction, i.e. secondary flows crossed the primary flow cell boundaries. The authors, in effect, acknowledged the possibility of a systematic error, and recommended further investigation using a more advanced measurement technique. Another possibility which can be suggested is that there may have been a finite array effect in which secondary flows actually existed between the central sub-channel and the three symmetric neighbouring sub-channels (Figure 2). The present test-sections are superior to those used by other investigators in this respect.

## 6.0 CONCLUDING REMARKS

Mean velocity and turbulence measurements were made over a Reynolds number range of 12,000 to 84,000, in the central sub-channels of three test-sections (simulating infinite equilateral triangular arrays) for which the tube spacings ( $D = \text{const.}$ ) were varied to provide P/D ratios of 1.20, 1.35 and 1.50. Based on the equivalent hydraulic diameter concept, friction factors were found to be functions of both P/D ratio and Reynolds number (Equation (69)). Spatial distributions of the mean axial velocities scaled on  $U_b$  (isovel plots), were substantially independent of Reynolds number and P/D ratio, but the radial distributions were modified forms of the universal logarithmic laws. Attempts at direct measurements of the secondary velocities were unsuccessful, however, based on the available evidence (Section 5.9), it is concluded that the secondary flow for each P/D ratio, was very probably a single cell of counter-clockwise circulation for primary flow cell 1. The magnitudes of the secondary velocities were very small--probably less than  $\frac{1}{2}\%$  of the bulk average axial velocities.

The turbulence data were found to scale only fairly well on the average friction velocity. The effect of P/D ratio could not be removed completely because  $\bar{u}^*$  was a weak function of P/D ratio. The

function, equation (69), is such that  $P/D = 1.35$  is closest and most parallel to pipe flow (Figure 24), and so the results for this  $P/D$  ratio bear the closest resemblance to fully developed pipe flow.

Three, possibly inter-related, anomalies of the present data are discussed below.

- a) The calculations on the approximate mean energy balance (Appendix D) indicated that secondary flows are smaller/less effective (or perhaps, more to the point, less required) for  $P/D = 1.35$  than for both the larger and smaller  $P/D$  ratios. The reason for this is puzzling--it would seem that it must somehow be related to the shape of the cross-sectional area of the primary flow cell, but if so, the geometric factor is well camouflaged\*.
- b) The radial distributions of  $\overline{uv}/(\overline{u}^*)^2$  for  $P/D = 1.20$  and  $1.50$ , failed to meet the theoretical distributions (equation (19)) at the radial boundaries (Figure 5 neglecting viscous shear stresses). This is thought to be mainly\*\* because of mean flow shear stresses and the practical problems of boundary

---

\*There is no reason to fault the  $D_h$  concept--it may not be exact, but it is sufficiently approximate.

\*\*The point becomes stretched for  $P/D = 1.50$  at the lower Reynolds number.

measurements as already discussed in Section 3.1 in the development of equation (21). These two  $P/D$  ratios were indicated to have higher secondary flows than  $P/D = 1.35$ .

- c) The possibility exists that the "effectiveness" of secondary flow increases with decreasing Reynolds number. The turbulence results for  $P/D = 1.50$  suggest that secondary flows become increasingly more effective in transporting energy to the wall as the Reynolds number decreases. However it is odd that the effect applies noticeably only to  $P/D = 1.50$ . The apparent effect may of course be false. As noted in Section 5.6, the flow may not have been completely developed (perhaps the secondary flow was still in its asymptotic stage), but the only evidence (Section 5.1) is contrary to this.

One single possibility which tends to polarize the above anomalies is a systematic error in  $\bar{u}^*$ . The effect of the axial traverse rod on the axial pressure drop may have been more significant than was realized. Assuming the effects to have been proportional to the decreases in the equivalent hydraulic diameters (noted in Section 5.3), the systematic error would be greatest for  $P/D = 1.50$  and least for  $P/D = 1.35$ . But whereas this explanation "fits" qualitatively, the required systematic errors are too large (certainly for  $P/D = 1.50$ )

to be plausible. Furthermore, it must be remembered that the present results are supported by the results of Kjellstrom and Stenback<sup>(21)</sup> (notably Figure 46e). Hopefully, experimental information on secondary flows will provide some elucidation on the above noted discrepancies.

Recommendations for future work in the present research area, are noted below in order to priority.

- a) Further attempts at anemometry measurements of secondary velocities possibly using a very sensitive rotatable single wire. Restricting the technique to a single channel has many practical advantages in regard to drift, read-out, etc. The size of the wire should also be small compared to the flow field to minimize velocity gradient errors. A practical geometry for the first measurements might be a single large sub-channel of  $P/D = 1.00$  with special attention paid to geometric accuracy. Access for the measurements would be from the open downstream end of the test-section. This would establish the basic secondary flow pattern and its true magnitudes.
- b) Predictions of the mean axial velocity fields using the method of Gosman et al<sup>(22)</sup> and the present turbulence data for the source terms. If the problem can be solved, the stream functions will yield the secondary velocities. Extrapolations in  $P/D$  ratio may

be possible by this method,

- c) Turbulence measurements of the same type made here for P/D ratios in the range  $1.20 < P/D \leq 1.00$  under fully developed flow conditions. A wider Reynolds number range than currently covered is desirable, with the tests more widely spaced in Reynolds number\*, however circumstances may dictate otherwise for the low P/D ratios. Measurements of  $\overline{w}$  would be useful. This non-linear P/D range should prove very interesting.
- d) The work might be further extended to simulated infinite square arrays before proceeding to secondary flow measurements between heterogeneous sub-channels such as square-triangular, or three rods in an equilateral array in a circular tube (a natural extension to Kacker's work<sup>(25)</sup>), etc. Certainly much more work remains to be done before tackling complicated flows such as developing flow, wire wrap effects, etc.

In addition to contributing to the field of turbulence, the present research is considered to provide a significant contribution to the technology of heat exchanger design and nuclear fuel channel

---

\*The present spacing was influenced by the first turbulence results which were obtained for  $P/D = 1.50$  and showed Reynolds number effect.

design. As far as is known, except for the work of Kjellstrom and Stenback<sup>(21)</sup> at one P/D ratio, the present results are the only published data on turbulence structure in rod bundles. The similarity of the turbulence characteristics to fully developed pipe flow comes as no surprise, since this was to some extent expected by many on the basis of similarity to pipe flow in regard to friction factors and convective heat transfer coefficients. Fundamentally, of course, rod bundle flows are quite different than pipe flow (axisymmetric, no secondary flow), but practically, because of the low levels of secondary flow, a fair similarity to pipe flow remains.

The present work is also (hopefully) of value by its emphasis on the important role played by secondary flow. For homogeneous sub-channels, the high mixing rates are undoubtedly due in large part to secondary flows. Enthalpy transfer between sub-channels should readily occur due to transfer of thermal energy by the secondary flow cells at the gaps as they flow parallel to each other in thermal communication and are mixed by turbulent diffusion. It is also apparent that different "mixing" correlations should be employed for homogeneous sub-channels (secondary flows confined) and heterogeneous sub-channels (secondary flow between sub-channels). Furthermore,

although any actual design will have finite array effects, it is obviously preferable in the interests of temperature uniformity that adjacent sub-channels in a design be heterogeneous (as in Figure 1) rather than homogeneous. The preceding observations stem simply from the secondary flow viewpoint.



## 7.0 ACKNOWLEDGEMENTS

The research for this thesis project was sponsored through a research contract by Atomic Energy of Canada Limited. The author is grateful for this financial support, and wishes to thank Dr. S. Banerjee of the Whiteshell Nuclear Research Establishment for his continuous cooperation and for his guidance in the initial planning of the experiments.

The author also acknowledges contributions by the following persons of the Mechanical Engineering Department: Dr. R.S. Azad (thesis supervisor) for many hours of helpful discussions, A. Kovalcik (turbulence laboratory technician) for assisting with the experimental measurements and the drawings, and R.H. Hummel (Ph.D. student) for his invaluable assistance with the electronics associated with the three-wire probe system.

Special thanks are also due to my wife, Yvonne, for her interest and encouragements.

## 8.0 REFERENCES

1. A.C. Trupp, N.W. Wilson and R.S. Azad: "Turbulent Structure of Axial Fluid Flow in Triangular Array Rod Bundles--First Annual Progress Report (1 July 1969 - 30 June 1970)", The University of Manitoba, Department of Mechanical Engineering Publication ER 25.11, July 1970.
2. A.C. Trupp and R.S. Azad: "Turbulent Structure of Axial Fluid Flow in Triangular Array Rod Bundles--Second Annual Progress Report (1 July 1970 - 30 June 1971)", The University of Manitoba, Department of Mechanical Engineering Publication ER 25.13, July 1971.
3. A.C. Trupp and R.S. Azad: "Turbulent Structure of Axial Fluid Flow in Triangular Array Rod Bundles--Third Annual Progress Report (1 July 1971 - 30 June 1972)", The University of Manitoba, Department of Mechanical Engineering Publication ER 25.19, July 1972.
4. A.C. Trupp and R.S. Azad: "A Three-Wire Probe System for Turbulence Measurements", The University of Manitoba, Department of Mechanical Engineering Publication ER 25.18, July 1972.
5. Symposium on "Heat Transfer in Rod Bundles", ASME Winter Annual Meeting, New York, 1968.
  - a) J.T. Rogers and N.E. Todreas: "Coolant Interchannel Mixing in Reactor Fuel Rod Bundles--Single-Phase Coolants".
  - b) L.S. Tong: "Pressure Drop Performance of a Rod Bundle".
  - c) R.A. Axford: "Summary of Theoretical Aspects of Heat Transfer Performance in Clustered Rod Geometries".
  - d) W.A. Sutherland: "Experimental Heat Transfer in Rod Bundles".
  - e) O.E. Dwyer: "Heat Transfer to Liquid Metals Flowing In-line Through Unbaffled Rod Bundles: A Review".
6. R.G. Rosehart and J.T. Rogers: "Turbulent Interchange Mixing Between Sub-channels in Close-packed Nuclear Reactor Fuel Bundles; Part 1--Single Phase Coolant Generalized Correlation", Atomic Energy of Canada Ltd, Power Projects Rep. R69PP1, February, 1969.

7. K. Singh and C.C. St. Pierre: "Single Phase Turbulent Mixing in Simulated Rod Bundle Geometries", Paper presented at the Fourth Western Canadian Heat Transfer Conference, Winnipeg, Manitoba, May 29-31, 1972.
8. V.R. Skinner, A.R. Freeman and H.G. Lyall: "Gas Mixing in Rod Clusters", Int. J. Heat Mass Transfer, Vol. 12, pp. 265-278, 1969.
9. D.S. Rowe: "A Mechanism for Turbulent Mixing Between Rod Bundle Subchannels", Am. Nuc. Soc. Trans., Vol 12, No. 2, p. 805, November, 1969.
10. D.S. Rowe: "A Thermal-Hydraulic Subchannel Analysis for Rod Bundle Nuclear Fuel Elements", Paper presented at the Fourth International Heat Transfer Conference, Paris-Versailles, 1970, 'Heat Transfer, 1970', Vol. III, Paper FC 7.13, Elsevier Publ. Co., Amsterdam.
11. E.M. Sparrow and A.L. Loeffler: "Longitudinal Laminar Flow Between Cylinders Arranged in Regular Array", AIChE J. Vol. 5, p. 325, 1959.
12. G.I. Hadaller and S. Banerjee: "A Variational Technique Applied to Laminar Flow in Triangular Rod Arrays", Proceedings Third Canadian Congress of Applied Mechanics, Calgary, Alberta, May, 1971 (Also Atomic Energy of Canada Ltd. Rep. AECL-3916).
13. E.M. Sparrow, A. L. Loeffler and H.A. Hubbard: "Heat Transfer to Longitudinal Laminar Flow Between Cylinders", ASME Trans. J. Heat Transfer, Vol. 83, Series C, p. 415, 1961.
14. R.G. Deissler and M.F. Taylor: "Analysis of Axial Turbulent Flow and Heat Transfer Through Banks of Rods or Tubes", Reactor Heat Transfer Conference 1956, collected papers and reports: TID-7529, Part 1, Book 2, p. 416, 1957.
15. N.I. Buleev: "Theoretical Model for Turbulent Transfer in Three-Dimensional Fluid Flow", Paper presented at the Third United Nations Conference on the Peaceful Uses of Atomic Energy, Paper A/CONF. 28/P/329, May, 1964.

16. A.C. Rapier and J.D. Redman: "The Calculation of Velocity Distributions in Rod Clusters", TRG Rep. 838(W), 1964 .
17. R. Nijssing, I. Gargantini and W. Eifler: "Analysis of Fluid Flow and Heat Transfer in a Triangular Array of Parallel Heat Generating Rods", Nuc. Eng. and Design, Vol. 4, pp. 375-398, 1966.
18. O.E. Dwyer: "Analytical Study of Heat Transfer to Liquid Metals Flowing In-line Through Closely Packed Rod Bundles", Nuc. Sci. and Eng., Vol. 25, pp. 343-358, 1966.
19. D.J. Bender and D.M. Switick: "Turbulent Velocity Distributions in a Rod Bundle", ASME 68-WA/HT-36, 1968.
20. K.W. Cook: "Velocity Distributions in Sodium-Cooled Fast Reactor Fuel Channels", ASME 69-WA/NE-9, 1969.
21. B. Kjellstrom and A. Stenback: "Pressure Drop, Velocity Distributions and Turbulence Distributions for Flow in Rod Bundles", AB Atomenergi, Sweden, Rep. AE-RV-145, (RL-1236), 1970.
22. A.D. Gosman, W.M. Pun, A.K. Runchal, D.B. Spalding and M. Wolfshtein: "Heat and Mass Transfer in Recirculating Flows", Academic Press, 1969.
23. N.W. Wilson, R.S. Azad and A.C. Trupp: "An Analysis of the Effect of Secondary Flows on the Longitudinal Velocity Distribution in Square Ducts", Paper No. 11, Symposium on Internal Flows, University of Salford, April 20-22, 1971.
24. B. Kjellstrom: "Transport Processes in Turbulent Channel Flow--STU Project 70-409/U340 (Final Report)", AB Atomenergi, Sweden, Rep. AE-RL-1344, 1972,
25. S.C. Kacker: "Some Aspects of Fully Developed Turbulent Flow in Non-Circular Ducts", J. Fluid Mech., Vol. 57, Pt. 3, pp. 583-602, 1973.
26. J. Nikuradse: "Untersuchungen uber die Geschwindigkeitsverteilung in Turbulenten Stromungen", Ph.D. Thesis Gottingen, 1926, Also VDI-Forschungsheft 281, Berlin, 1926.

27. L. Prandtl: Proc. Second Int. Congr. of Applied Mech., 1926, p. 71 et seq Zurich, 1927 (Also translated as NACA TM-435).
28. L.C. Hoagland: "Fully Developed Turbulent Flow in Straight Rectangular Ducts - Secondary Flow, Its Cause and Effect on the Primary Flow", Ph.D. Thesis, Massachusetts Institute of Technology, 1960.
29. E. Brundrett and W.D. Baines: "The Production and Diffusion of Vorticity in Duct Flow", J. Fluid Mech., Vol. 19, pp. 375-394, 1964.
30. F.B. Gessner and J.B. Jones: "On Some Aspects of Fully-Developed Turbulent Flow in Rectangular Channels", J. Fluid Mech., Vol. 23, Pt. 4, pp. 689-713, 1965.
31. B.E. Launder and W.M. Ying: "Secondary Flows in Ducts of Square Cross-Section", J. Fluid Mech., Vol. 54, Pt. 2, pp. 289-295, 1972.
32. F.B. Gessner: "The Origin of Secondary Flow in Turbulent Flow Along a Corner", J. Fluid Mech., Vol. 58, Pt. 1, pp. 1-25, 1973.
33. J.O. Hinze: "Secondary Currents in Wall Turbulence", Phys. Fluids Suppl., Vol. 10, pp. S122-125, 1967.
34. H.G. Lyall: "Measurement of Flow Distribution and Secondary Flow in Ducts Composed of Two Square Interconnected Sub-Channels", Paper No. 33, Symposium on Internal Flows, University of Salford, April 20-22, 1971.
35. L.D. Palmer and L.L. Swanson: "Measurements of Heat Transfer Coefficients, Friction Factors and Velocity Profiles for Air Flowing Parallel to Closely Spaced Rods", Paper presented at the 1961 International Heat Transfer Conference August 28-September 1, 1961, University of Colorado, ASME International Developments in Heat Transfer, Part III, pp. 535-542, 1961-62.
36. W. Eifler and R. Nijssing: "Experimental Investigation of Velocity Distribution and Flow Resistance in a Triangular Array of Parallel Rods", Nuc. Eng. and Design, Vol. 5, pp. 22-42, 1967

37. V.I. Subbotin, P.A. Ushakov, Y.D. Leychenko and A.M. Alexandrov: "Velocity Field of Turbulent Fluid Flow in a Longitudinal Streamline of Clusters of Rods", USAEC translation Rep. AEC-tr-7189, issued Feb., 1971.
38. C. Hall and P.J. Syvenningsson: "Secondary Flow Velocities in a Rod Bundle of Triangular Array", AB Atomenergi, Sweden, Rep. AE-RL-1326, 1971.
39. J. Laufer: "The Structure of Turbulence in Fully Developed Pipe Flow", NACA Rep. 1174, 1954.
40. DISA Probe Manual, DISA Elektronik A/S, Herlev, Denmark.
41. Manual-DISA Random Signal Indicator and Correlator Type 55A06-- Description and Operating Instructions, DISA Elektronik A/S, Herlev, Denmark.
42. P.W. Bearman: "Corrections for the Effect of Ambient Temperature Drift on Hot-Wire Measurements in Incompressible Flow", DISA Information No. 11, May, 1971.
43. V.C. Patel: "Calibration of the Preston Tube and Limitations on its Use in Pressure Gradients", J. Fluid Mech., Vol. 23, Pt. 1, pp. 185-208, 1965.
44. V.M. Lyatkher: "Turbulent Fluctuations in the Viscous Sublayer", Soviet Physics--Doklady, Vol. 13, No. 5, pp. 389-391, 1968.
45. E.R. Corino and R.S. Brodkey: "A Visual Investigation of the Wall Region in Turbulent Flow", J. Fluid Mech., Vol. 37, Pt. 1, pp. 1-30, 1969.
46. A.K. Gupta: "An Experimental Investigation of the Viscous Sublayer Region in a Turbulent Boundary Layer", Ph.D. Dissertation, University of Southern California, January, 1970.
47. H.T. Kim, S.J. Kline and W.C. Reynolds: "The Production of Turbulence Near a Smooth Wall in a Turbulent Boundary Layer", J. Fluid Mech., Vol. 50, Pt. 1, pp. 133-160, 1971.
48. K. Narahari Rao, R. Narasimha and M.A. Badri Narayanan: "The Bursting Phenomenon in a Turbulent Boundary Layer", J. Fluid Mech., Vol. 48, Pt. 2, pp. 339-352, 1971.

49. W.R.B. Morrison, K.J. Bullock and R.E. Kronauer: "Evidence of Waves in the Sublayer", J. Fluid Mech., Vol. 47, Pt. 4, pp. 639-656, 1971.
50. W.W. Willmarth and S.S. Lu: "Structure of the Reynolds Stress Near The Wall", J. Fluid Mech., Vol. 55, Pt. 1, pp. 65-92, 1972,
51. J.M. Wallace, H. Eckelmann and R.S. Brodkey: "The Wall Region in Turbulent Shear Flow", J. Fluid Mech., Vol. 54, Pt. 1, pp. 39-48, 1972.
52. H. Eckelmann: "An Experimental Investigation of a Turbulent Channel Flow with a Thick Viscous Sublayer", Max-Planck-Institut Fur Stromungsforschung Rep. No. 101/1973, January 1973.
53. E. Ower and R.C. Pankhurst: "The Measurement of Air Flow", Pergamon Press, 1966.
54. E. Ower: "The Measurement of Air Flow", Chapman and Hall Ltd., 1949.
55. H. Fiedler: "Sources of Errors and Corrections in Measurements with Pitot Tubes", Hermann Fottinger Institut Fur Stromungstechnik, Technische Universitat Berlin, Nov., 1964.
56. J.O. Hinze: "Turbulence--An Introduction to its Mechanism and Theory", McGraw-Hill, 1959,
57. W.W. Willmarth and C.S. Yang: "Wall-Pressure Fluctuations Beneath Turbulent Boundary Layers on a Flat Plate and a Cylinder", J. Fluid Mech., Vol. 41, Pt. 1, pp. 47-80, 1970.
58. H.J. Leutheusser: "Turbulent Flow in Rectangular Ducts", Amer. Soc. of Civil Engrs., J. of the Hydraulics Division, Vol. 89, No. HY3, pp. 1-19, May, 1963
59. H.J. Tracy: "Turbulent Flow in a Three-Dimensional Channel", Amer. Soc. of Civil Engrs., J. of the Hydraulics Division, Vol. 91, No. HY6, pp. 9-35, Nov., 1965.
60. V.K. Jonsson and E.M. Sparrow: "Experiments on Turbulent Flow Phenomena in Eccentric Annular Ducts", J. Fluid Mech, Vol. 25, Pt. 1, pp. 65-86, 1966,

61. C.J. Lawn: "Turbulence Measurements With Hot Wires at B.N.L.", Central Elec. Gen. Board, Berkeley Nuclear Labs. Rep. RD/B/M 1277, April, 1969.
62. J.C. Hill and C.A. Sleicher: "Equations for Errors in Turbulence Measurements with Inclined Hot Wires", Physics of Fluids, Vol. 12, No. 5, pp. 1126-1127, May, 1969.
63. F.H. Champagne and C.A. Sleicher: "Turbulence Measurements With Inclined Hot-Wires, Part 2: Hot-Wire Response Equations", J. Fluid Mech., Vol. 28, Pt. 1, pp. 177-182, 1967.
64. A.B. Thornton-Trump: "Error Analysis of a Hot-Wire Anemometer and Processing Circuit", University of Manitoba, Department of Mechanical Engineering Publication ER 25.14, July, 1971.
65. S.J. Kline and F.A. McClintock: "Describing Uncertainties in Single-Sample Experiments", Mech. Eng., Vol. 75, Jan, 1953.
66. D.E. Guitton: "Correction of Hot Wire Data for High Intensity Turbulence, Longitudinal Cooling and Probe Interference", McGill University, Mechanical Engineering Research Laboratories Rep. No. 68-6, August, 1968.
67. P.T. Harsha and S.C. Lee: "Correlation Between Turbulent Shear Stress and Turbulent Kinetic Energy", AIAA Journal, Vol. 8, No. 8, August, 1970.
68. A.C. Trupp, R.S. Azad, N.W. Wilson and P.A.C. Okwuobi: "Turbulence Characteristics in a Straight Conical Diffuser", Paper No. 9, Symposium on Internal Flows, University of Salford, April 20-22, 1971.
69. F.N. Frenkiel: "Effects of Wire Length in Turbulence Investigations with a Hot-Wire Anemometer", Roy. Aero. Soc, Quart. Vol. 5, pp. 1-24, May, 1954.
70. J.C. Wyngaard: "Measurement of Small-Scale Turbulence Structure with Hot Wires", J.Sci. Instr. (J. of Physics E), Series 2, Vol. 1, pp. 1105-1108, 1968.



71. C.J. Lawn; "The Determination of the Rate of Dissipation in Turbulent Pipe Flow", J. Fluid Mech. Vol. 48, Pt. 3, pp. 477-505, 1971.
72. P. Bradshaw; "Conditions for the Existence of An Inertial Sub-range in Turbulent Flow", Nat. Phys. Lab. Aero. Rep. No. 1220, January 1967 (Also N.P.L. Reports and Memoranda No. 3603, January, 1967).

## APPENDIX A

### Description of Wind Tunnel Design and Construction

A plan view of the closed-circuit wind tunnel is shown in Figure 6. Almost all components were fabricated from 3/4 inch thick 7-ply mahogany plywood. Each component is described in the following paragraphs--the numbering system corresponds to that used in Figure 6.

#### 1. Test-Section:

A cross-sectional view is shown in Figure 3. The measuring station was located approximately 1.5 m downstream from the start of the rod bundle. The individual rods were fitted with bullet-shaped end caps at the flow entrance. The rods were supported and spaced by pins through these end caps and by a ring cage about 30 cm downstream from the measuring station. In order to promote flow symmetry, all seven inner tubes extended through Items 2 to 4 inclusive, and protruded through the first corner wall where they were again supported. Probe leads, contained in the three instrumented tubes, exited at this location. The traversing mechanism was also operated from the first corner exit.

#### 2. Transition Piece:

The constant-area ( $603.87 \text{ cm}^2$ ) cross-section was changed from hexagonal to square.

3. Diffuser:

This diffuser was kept short to limit the total tube length to 3.66 m. It has an  $8^\circ$  total included angle and an area ratio of 2.06:1.

4. First Corner:

The flow was turned  $90^\circ$  through the use of 17 turning vanes made from 16 gauge sheet metal. The vanes were  $90^\circ$  circular arc elements with a chord length of 10.67 cm and a spacing/chord ratio of  $0.257^{(A1)(A5)*}$ . The vanes were slotted as required to pass the inner tubes from the test-section.

5. Diffuser:

$8^\circ$  total included angle; area ratio of 1.94:1.

6. Second Corner:

17 turning vanes, 15.24 cm chord, spacing/chord ratio = 0.250. The extra length on the upstream end was required to keep the tunnel longitudinal center-lines parallel,

7. Duct:

This section adjusted the tunnel length for parallel lateral center-lines.

---

\*See bibliography at the end of this Appendix.

8. Nozzle:

8° total included angle; area ratio = 3.31:1.

9. Canvas Couplings:

These were installed at each end of the fan assembly for vibration isolation. A constant area (729.1 cm<sup>2</sup>) transition piece (preceding the damper) changed the area from square to circular.

10. Damper:

Woods radial vane damper, 30.48 cm dia., 8 vanes, hand operated.

11. Fan Section:

30.48 cm dia. Woods four-stage direct driven type tube axial aerofoil fan (Cat. No. 12K4AF1545) with totally enclosed two-speed (3400/1750 RPM) ball bearing motors. Electrical supply 575V, 3 phase, 60 cycle. Blade angle: 8°/13°/8°/13°. Rated at 500 CFM against a 8 inch water head. Motor H.P.: 1.2 hp/stage. The stages were counter-rotating with each driven by separate identical motors. Being individually driven, the impellers could be idled in various combinations. There were five stage idling combinations at each speed (total of 10) giving approximately 50, 60, 75, 85 and 100% of the peak volume. The pressures developed were up to six times the pressure of a similar single-stage fan.

12. Silencer:

The maximum fan sound pressure level was approximately 90 dB. A Woods Type C silencer provided attenuations of sound level of about 17 dB for frequencies of 1000 Hz.

13. Diffuser:

This long diffuser had an  $8^\circ$  total included angle and an area ratio of 9.47:1. Boundary layer separation may have occurred to some extent, but caused no problems.

14. Third Corner:

17 turning vanes, 25.1 cm chord, spacing/chord ratio = 0.257.

15. Diffuser:

$8^\circ$  total included angle, area ratio 1.45:1.

16. Fourth Corner:

18 turning vanes, 30.5 cm chord, spacing/chord ratio = 0.234.

17. Duct:

This section of ducting was empty for the rod bundle turbulence study. For future experiments, it could contain a honeycomb or 'egg crate' flow straightener or heating/cooling element.

18. Transition Piece:

The constant-area ( $10034 \text{ cm}^2$ ) cross-section was changed from square to circular.

19. Screen Section:

Damping screens (wire gauzes) upstream of the contraction cone were used to reduce turbulence levels and to promote symmetry in the velocity profile. Design criteria for the screen section are summarized as follows:

- a) Open-area ratio of the screen should be greater than about 0.57 to avoid coalescence of emerging jets and hence flow instability.
- b) Local (wire) Reynolds numbers should be less than about 80 to circumvent turbulent wakes from the wires.
- c) Screens should be separated by about 500 wire diameters to permit turbulence to decay between screens.
- d) A settling chamber of 20 to 40 mesh lengths should be allowed between the final screen and the contraction cone to allow for decay of eddies.

The design meeting these requirements consisted of five screens. The flow first passed through two 8 mesh 22 S.W.G. (0.711 mm dia.) wire screens separated by 30.48 cm, and then three 16 mesh 28 S.W.G. (0.376 mm dia.) wire screens separated by 19.05 cm. A final settling length of 25.4 cm preceded the contraction cone.

The screens were designed to be readily exchanged\*. Schubauer's average turbulence reduction factor<sup>(A4)</sup> was estimated to be about 0.075\*\*. More specifically, experimental data<sup>(A1)</sup> suggested the reduction factors for  $u'$  and  $v'$  to be about 0.008 and 0.055 respectively.

## 20. Contraction Cone:

No completely satisfactory method is available for designing a contraction cone<sup>(A1)</sup>. A recent review by Bosse<sup>(A6)</sup> outlined the various methods for 'theoretical design'. The present contraction cone was designed based on the work of Batchelor and Shaw<sup>(A7)</sup> (6000 streamline). It has a 16.6:1 area ratio and was circular in cross-section. This construction was somewhat novel. Rings cut from plywood sheet to meet the contraction profile, were nailed and glued together. The interior was then tool and hand finished to final dimensions. The theoretical<sup>(A1)</sup> reduction factors for  $u'$  and  $v'$  were 0.095 and 3.5

---

\* For most experiments, it is imperative that the turbulence level of the test-section flow be controllable down to being negligible (e.g. atmospheric turbulence). This was, however, not the case for the rod bundle turbulence study since an equilibrium turbulence field (generated by the rod bundle) was established at the measuring station which was independent (within limits) of the turbulence level of the feed flow.

\*\* This meant, for example, that if the turbulence intensity was 5% entering the screen section, the turbulence level would be reduced to 0.375% entering the contraction cone.

respectively, i.e. contraction, by exerting a selective effect on the components of velocity fluctuations, decreased  $u'$  but increased  $y'$  and  $w'$ .

#### 21. Transition Piece:

The constant-area ( $603.87 \text{ cm}^2$ ) cross-section was changed from circular to hexagonal.

#### Bibliography

- A1) P. Bradshaw and R.C. Pankhurst: "The Design of Low-Speed Wind Tunnels", Progress in Aeronautical Sciences, Volume 5, pp. 1-69, Pergamon Press, 1964, (also published as NPL Aero Rep. 1039).
- A2) R.C. Pankhurst and D. W. Holder: "Wind-Tunnel Technique", Pitman & Sons (London), 1952.
- A3) R.A. Wallis: "Axial Flow Fans", G. Newnes Limited, (London), 1961.
- A4) H.L. Dryden and I.H. Abbott: "The Design of Low-Turbulence Wind Tunnels", NACA Rep. 940, 1948.
- A5) S. Ahmed and E. Brundrett: "Performance of Turning Vanes in a Square Conduit Elbow", ASME 69-FE-32, 1969.
- A6) H.H. Bossel: "Computation of Axisymmetric Contractions", AIAA Journal, Volume 7, No. 10 pp. 2017-2019, October, 1969.
- A7) G.K. Batchelor and F.S. Shaw: "A Consideration of the Design of Wind Tunnel Contractions", Australian Council for Aeronautics Rep. ACA-4, March, 1944.



APPENDIX BFriction Velocity Correction

Tunnel operating conditions for matching tests for a given test-section (e.g. isovel test A1 and pressure drop test A1) were made on the basis of equal pressure drops across the contraction cone of the wind tunnel. This generally amounted to simply selecting 'reference condition' fan and damper settings. Occasionally (due to unusually high or low barometric pressure) it was necessary to shift the damper setting slightly in order to achieve the reference pressure drop across the contraction cone.

The contraction cone had an area ratio of 16.6:1, and the piezometer rings were located at cross-sections of maximum and minimum areas. Consequently, the square of the velocity of the entering air was negligibly small compared to the square of the velocity of the exiting air. As a result, the contraction cone pressure drop,

$$\Delta \bar{P} \propto \rho_c U_c^2$$

Using subscripts 0 and 1 to designate any two 'matched' tests, it follows, for  $\Delta \bar{P} = \text{constant}$ , that;

$$\rho_{c0} U_{c0}^2 = \rho_{c1} U_{c1}^2 \dots \dots \dots (B1)$$

For the average friction velocity ( $\bar{u}^*$ ),

$$(\bar{u}^*)^2 \propto \frac{\bar{T}_w}{\rho} \propto \frac{(d\bar{P}/dx)}{\rho} \propto f U_b^2$$

For turbulent channel flow,  $f = C Re^{-n}$  (equation (69) in the main text) where  $C$  and  $n$  are constants for a given test-section, hence:

$$(\bar{u}^*)^2 \propto \frac{U_b^2}{Re^{1/4}} = \frac{U_b^2}{(\rho U_b D_h / \mu)^{1/4}} \quad \text{or} \quad \bar{u}^* \propto \frac{U_b^{7/8}}{(\rho/\mu)^{1/8}}$$

For the same two 'matched' tests, it follows that:

$$\frac{\bar{u}_0^*}{\bar{u}_1^*} = \left( \frac{U_{bo}}{U_{b1}} \right)^{7/8} \left( \frac{\mu_0}{\mu_1} \right)^{1/8} \left( \frac{\rho_1}{\rho_0} \right)^{1/8} \dots \dots \dots (B2)$$

The factor  $(\mu_0/\mu_1)^{1/8} \approx 1$  since the temperatures for the two 'matched' tests were equal or nearly equal (typical). For steady flow conditions, continuity requires:

$$\frac{\rho_{co} U_{co}}{\rho_{cl} U_{cl}} = \frac{\rho_o U_{bo}}{\rho_1 U_{b1}}$$

which since  $\frac{U_{co}}{U_{cl}} = \left( \frac{\rho_{cl}}{\rho_{co}} \right)^{1/2}$  from (B1), may be rewritten as:

$$\left( \frac{\rho_{co}}{\rho_{cl}} \right)^{1/2} = \left( \frac{\rho_o}{\rho_1} \right) \left( \frac{U_{bo}}{U_{b1}} \right) \dots \dots \dots (B3)$$

For isothermal flow,  $\rho_{co}$  is only slightly greater than  $\rho_o$  due to pressure drop associated with the velocity increase (on entering the test-section) and friction. Similarly,  $\rho_{c1}$  and  $\rho_1$  differ by a similar small percentage.

Consequently,

$$\frac{\rho_{co}}{\rho_{c1}} \approx \frac{\rho_o}{\rho_1}$$

which substituted into (B3) gives:

$$\left(\frac{\rho_1}{\rho_o}\right)^{1/2} = \frac{u_{bo}}{u_{b1}} \dots \dots \dots (B4)$$

Finally, using (B4) in (B2) gives:

$$\frac{\bar{u}_o^*}{\bar{u}_1^*} = \left(\frac{\rho_1}{\rho_o}\right)^{9/16}$$

or,

$$\bar{u}_o^* = \bar{u}_1^* (CF) \dots \dots \dots (B5)$$

where the correction factor,  $CF = \left[\frac{\rho_1}{\rho_o}\right]^{0.5625}$

Correction factors were computed (using  $p$  values for the temperature and corrected for pressure and humidity) to determine friction velocities for the isovel tests from the pressure drop tests. Subsequently,

correction factors were applied to determine friction velocities for the hot-wire tests from the isovel tests rather than the pressure drop tests. The latter procedure was adopted because hot-wire calibrations were based on both insitu pitot tube calibration data and 'point-matching' to velocity field data as determined by the isovel tests.

It is noted that correction factors were generally small, and always in the range 0.98 to 1.02.

APPENDIX CWall Shear Stress Probe

The operating equation for flush-mounted hot-film probes is:

$$T_w^{1/3} = A E^2 + B \quad \dots \dots \dots (C1)$$

where  $E$  = anemometer D.C. voltage

and  $A$  &  $B$  = constants.

Since  $T_w = \rho (u^*)^2 / gc$ , this equation may be rewritten as:

$$E^2 = C (u^*)^{2/3} + D \quad \dots \dots \dots (C2)$$

The calibration was accomplished by operating the wind tunnel at test conditions where  $\bar{u}^*$  was known from the pressure drop data. The constants  $C$  and  $D$  were subsequently determined by plotting  $E^2$  versus  $(u^*)^{2/3}$  which gave a linear relationship.

Wall shear stress variations about the tube perimeter were obtained as follows for a given test. The anemometer DC voltage was biased to leave approximately half a volt which was measured on the 1 volt range of a DISA digital voltmeter (accuracy of 0.1% of full scale). Readings were taken at 30 increments of tube rotation. Immediately following each reading, the position was returned to  $\theta = 0^\circ$  and the voltage was recorded. This procedure enabled a data set of voltages with respect to the voltage at  $\theta = 0^\circ$ , i.e. relative level. This procedure was

necessary since probe drift was significant compared to the relative voltages. Let  $E_0$  = D.C. voltage from calibration curve corresponding to the particular test, and

$$E = E_0 + e$$

where  $e$  = relative voltage  $\equiv E(\theta) - E(\theta = 0^\circ)$

$$\text{i.e. } E(\theta = 0^\circ) \equiv E_0.$$

It follows from (C2) that:

$$E^2 - D = C (u^*)^{2/3}, \text{ and}$$

$$E_0^2 - D = C (u^*)^{2/3}, \text{ hence:}$$

$$\left[ \frac{u^*}{u_0^*} \right]^{2/3} = \frac{E^2 - D}{F} \quad \text{where } F = E_0^2 - D = \text{const.}$$

or

$$\frac{T_W}{T_{W0}} = \left[ \frac{E^2 - D}{F} \right]^3 \dots \dots \dots (C3)$$

By defining  $\bar{T}_W$  as  $\bar{T}_W = \frac{1}{N} \sum_{i=1}^N T_i,$

$$\frac{T_W}{\bar{T}_W} = \frac{T_W}{T_{W0}} \frac{T_{W0}}{\bar{T}_W} \dots \dots \dots (C4)$$

The above method is considered to provide good relative accuracy

(trend accuracy) which was of major concern. It is noted that only  $E_0$  and the calibration constant  $D$  entered the computation together with the relative voltage levels.

# APPENDIX D

## Approximate Mean Energy Equation Calculations

The approximate mean energy equation, equation (49) in the main text, may be rewritten as:

$$\begin{aligned}
 & \left\{ -\frac{\bar{U}}{\rho} \frac{\partial \bar{P}}{\partial x} \right\} + \left\{ -\bar{UV} \frac{\partial \bar{U}}{\partial r} - \frac{\bar{UW}}{r} \frac{\partial \bar{U}}{\partial \phi} \right\} + \\
 & \quad \text{Term A} \qquad \qquad \qquad \text{Term B} \\
 & + \left\{ -\frac{\bar{U}}{r} \left( \frac{\partial r \bar{UV}}{\partial r} + \frac{\partial \bar{UW}}{\partial \phi} \right) - \bar{UV} \frac{\partial \bar{U}}{\partial r} - \frac{\bar{UW}}{r} \frac{\partial \bar{U}}{\partial \phi} \right\} + \\
 & \qquad \qquad \qquad \text{Term C} \\
 & + \left\{ \bar{UV} \frac{\partial \bar{U}}{\partial r} + \frac{\bar{UW}}{r} \frac{\partial \bar{U}}{\partial \phi} \right\} + \left\{ \nu \frac{\bar{U}}{r} \left[ \frac{\partial}{\partial r} \left( r \frac{\partial \bar{U}}{\partial r} \right) + \frac{1}{r} \frac{\partial^2 \bar{U}}{\partial \phi^2} \right] + \right. \\
 & \quad \text{Term D} \qquad \qquad \qquad \text{Term E} \\
 & + \left. \nu \left( \frac{\partial \bar{U}}{\partial r} \right)^2 + \nu \left( \frac{1}{r} \frac{\partial \bar{U}}{\partial \phi} \right)^2 \right\} + \\
 & \quad \text{Term E} \\
 & + \left\{ -\nu \left( \frac{\partial \bar{U}}{\partial r} \right)^2 - \nu \left( \frac{1}{r} \frac{\partial \bar{U}}{\partial \phi} \right)^2 \right\} \approx 0 \quad \dots \dots \dots (D1) \\
 & \quad \text{Term F}
 \end{aligned}$$

Each term was made dimensionless by multiplying through by the factor  $(\nu/(\bar{U}^*)^4)$ . Values for each term, except Term B, were computed for the various points in the flow fields using the present experimental data. The value of Term B at each point was determined from the energy balance,



treating equation (D1) as an equality. The magnitudes of the various terms are illustrated by the following samples of the computed data. The sign convention is that an energy gain or energy in is positive whereas an energy loss or energy out is negative.

$\theta$	$A \times 10^3$	$B \times 10^3$	$C \times 10^3$	$D \times 10^3$	$E \times 10^3$	$F \times 10^3$
<u>Test A3, <math>y = 3.18</math> mm</u>						
30	19.14	-4.27	-5.75	-7.57	-1.36	-0.19
24	19.14	-2.77	-6.95	-7.86	-1.36	-0.19
18	19.20	-7.76	-2.05	-7.83	-1.37	-0.19
12	19.26	-1.16	-8.87	-7.67	-1.37	-0.19
6	19.31	-3.57	-6.95	-7.21	-1.38	-0.19
0	19.14	-2.70	-8.03	-6.86	-1.36	-0.19
<u>Test A3, <math>y = 10.80</math> mm</u>						
30	22.53	-9.58	-11.78	-1.02	-0.14	-0.02
24	22.49	-3.60	-17.62	-1.11	-0.14	-0.02
18	22.44	-1.99	-19.17	-1.12	-0.14	-0.02
12	22.34	-2.36	-18.85	-0.97	-0.14	-0.02
6	22.14	-2.84	-18.40	-0.75	-0.14	-0.02
0	22.04	-2.64	-18.80	-0.45	-0.14	-0.02
<u>Test B3, <math>y = 3.18</math> mm</u>						
30	22.44	2.70	-15.65	-8.39	-0.95	-0.15
24	22.28	2.09	-14.73	-8.55	-0.94	-0.15
18	22.28	3.96	-16.82	-8.33	-0.94	-0.15
12	22.28	8.72	-21.31	-8.60	-0.94	-0.15
6	22.16	11.15	-25.13	-7.10	-0.93	-0.15
0	22.05	12.63	-27.10	-6.50	-0.93	-0.15
<u>Test B3, <math>y = 8.26</math> mm</u>						
30	25.88	-10.71	-13.50	-1.49	-0.16	-0.02
24	25.64	-7.09	-16.72	-1.66	-0.16	-0.02
18	25.40	-6.44	-17.24	-1.54	-0.16	-0.02
12	25.10	-6.14	-17.64	-1.15	-0.16	-0.02
6	24.80	-9.39	-14.59	-0.65	-0.15	-0.02
0	24.60	-10.80	-13.42	-0.21	-0.15	-0.02

$\theta$	$A \times 10^3$	$B \times 10^3$	$C \times 10^3$	$D \times 10^3$	$E \times 10^3$	$F \times 10^3$
<u>Test C3, <math>y = 1.91</math> mm</u>						
30	23.96	-14.24	-2.32	-6.30	-0.95	-0.13
24	23.96	-17.55	0.95	-6.28	-0.95	-0.13
18	24.14	-12.26	-4.50	-6.29	-0.95	-0.13
12	24.25	8.62	-26.64	-5.15	-0.95	-0.13
6	24.14	12.47	-30.76	-4.76	-0.95	-0.13
0	23.70	2.91	-20.69	-4.86	-0.93	-0.13
<u>Test C3, <math>y = 4.45</math> mm</u>						
30	26.51	-10.59	-13.78	-1.93	-0.19	-0.02
24	26.47	-4.86	-19.42	-1.98	-0.19	-0.02
18	26.51	-2.39	-22.42	-1.48	-0.19	-0.02
12	26.51	-6.30	-19.32	-0.67	-0.19	-0.02
6	26.14	-13.47	-12.11	-0.34	-0.19	-0.02
0	25.80	-12.34	-13.09	-0.16	-0.19	-0.02

The values for Term A, the dimensionless energy input due to the axial pressure drop (equal to  $4 \nu \bar{U}/D_h (\bar{u}^*)^2$ ), were similar for each P/D ratio. The dimensionless direct dissipations (Term F) were negligibly small in the outer flow fields as was of course expected. Term E, representing viscous diffusion, was also significant only near the wall. Term D, the dimensionless turbulence production, was fairly similar to pipe flow since  $\bar{u}\bar{w} \partial \bar{U}/r \partial \phi$  generally provided a small boost to  $\bar{u}\bar{v} \partial \bar{U}/\partial r$ . Term C (energy convection by the turbulence) was important to the energy balance. Its magnitudes were comparable to Term B for P/D = 1.50 and 1.20, but generally larger than Term B for P/D = 1.35. The distributions of the values for Term C were somewhat erratic for P/D = 1.35 due to the variability and magnitude of the  $\partial \bar{u}\bar{w}/\partial \phi$  gradients,

and this in turn influenced the Term B distributions. In general, since the primary gain (Term A) did not vary much over the region examined, whereas the primary loss (Term D) increased rapidly nearing the wall, the closure term (Term B) was influenced\* most by Term D near the wall and by Term C over the remaining area.

Term B, which was of major interest, represents the dimensionless convection of mean energy by the secondary flows. Further details on the distributions of the values for Term B for Tests A3, B3 and C3 ( $Re \approx 60,000$ ) are given in Figures 54, 55 and 56 respectively. The numbers on these Figures are rounded-off values. However, although the values must be considered of low order accuracy, two main trends are fairly clear. Secondary flows, in effect, transport energy from the outer flow region to the near-wall region where it is consumed by turbulence production and direct dissipation. This implies an upswing in the  $\bar{u}\bar{v}/(\bar{u}^*)^2$  distributions near the wall (for  $P/D = 1.50$  and  $1.20$  at least) and/or sizeable  $\bar{u}\bar{w}$  values in the buffer region combined with finite  $\partial \bar{U}/\partial \phi$  values (quite possible--Figure 34), and also the possibility that direct dissipation is distributed differently than for pipe flow in the layer  $5 < y^+ < \sim 30$ . The same basic role is played

---

\*Computationally not physically.

by Term C. The second trend is a redistribution effect in which energy is brought into the gap region by the secondary flows. The need for this effect increases with decreasing P/D ratio, and is noticeable for both P/D = 1.20 (Figure 56) and P/D = 1.35 (Figure 55).

The computed results concerning the mean energy equation indicated that convection of mean energy by the secondary flows took place at roughly the same rate, on the average, as convection by the turbulence. The following order-of-magnitude calculation is therefore of interest. Suppose  $\overline{UV} \partial \bar{U} / \partial r$  in Term B equaled  $\overline{uv} \partial \bar{U} / \partial r$  in Term C (or Term D). This would be equivalent to  $\overline{UV} = \overline{uv}$  (hence also equal turbulent and mean flow shear stresses). Using equation (27) and  $f \approx 0.025$  (typical):

$$\text{For } \overline{UV} = \overline{uv}, \frac{\bar{V}}{U_b} = \frac{\overline{uv}}{\overline{UU}_b} \approx \frac{\overline{uv}}{U_b^2} \approx \frac{0.5 (\bar{u}^*)^2}{8 (\bar{u}^*)^2 / f} = 1.6 \times 10^{-3}$$

This suggests that the secondary velocities were probably less than 1/2% of the bulk average axial velocity.

TABLE I

SUMMARY OF TEST CONDITIONS  
TRIANGULAR ARRAY ROD BUNDLES - FULLY DEVELOPED FLOW

Test Section	Tube Dia. (cm)	P/D	Hydraulic Dia. (cm)	No. of Pts. in Flow Cell	Test No.	Nominal Reynolds No.	Actual Reynolds No.	Av. Vel. (a) $U_b$ (m/s)	Fric. Vel. (a) $\bar{u}^*$ (m/s)
IA	5.08	1.50	7.5234	137	1	84000	85480	18.60	1.022
					2	72000	73370	15.81	0.863
					3	60000	60330	12.89	0.738
					4	48000	47960	10.16	0.579
					5	36000	36650	7.683	0.457
					6	24000	23860	5.016	0.316
IB	5.08	1.35	5.1287	101	2	72000	72490	23.40	1.222
					3	60000	59880	19.38	1.044
					4	48000	48130	15.44	0.849
					5	36000	35700	11.11	0.630
					6	24000	23510	7.274	0.442
					7	12000	13720	4.217	0.269
IC	5.08	1.20	2.9861	66	3 <sup>(b)</sup>	60000	56020	31.18	1.662
					4	48000	49130	27.06	1.497
					5	36000	35570	19.39	1.116
					6	24000	23760	12.78	0.781
					7	12000	11680	6.247	0.424

NOTES: a) For mean velocity tests - experimental values.

b) Maximum fan capacity - lower Re than A3 and B3.

TABLE II

SUMMARY OF LEAST-SQUARES-FIT RESULTS  
FOR MEAN AXIAL VELOCITY VARIATIONS IN THE RADIAL DIRECTION

FORM:  $u^+ = A \ln y^+ + B$

Test No.	A	B	$y_{\max}^+$	$\sigma(\%)*$
A1	2.1206	5.9274	1151	2.264
2	2.0199	6.5252	1004	1.747
3	1.9892	6.7166	843	1.618
4	1.9974	6.6390	686	1.408
5	1.8289	7.5813	540	1.399
6	1.8011	7.7078	368	1.345
B2	2.4433	5.0370	1052	1.060
3	2.4272	5.1239	890	1.360
4	2.4837	4.7916	734	1.122
5	2.4595	4.9517	565	1.323
6	2.3638	5.4681	392	1.504
7	2.8267	3.4684	244	2.962
C3	2.2231	6.3434	988	0.964
4	2.2208	6.2807	883	1.057
5	2.3270	5.4975	670	0.959
6	2.0538	6.7739	474	1.169
7	1.9527	7.0121	258	1.347

\*Standard deviations are based on the differences between the experimental  $u^+$  values and the  $u^+$  values from the LSF equation for the same  $y^+$ , and are expressed as a percentage of the average  $u^+$  value in the range for each test based on the LSF equation.

Sheet 2 of 2

TABLE II (cont'd)

FORM:  $u^+ = A' \ln \left[ y^+ \left( 1 + \frac{y}{D} \right) \right] + B'$

Test No.	A'	B'	$(y^+(1 + y/D))_{\max}$	$\sigma(\%)^{**}$
A1	1.957	6.618	1572	2.057
2	1.862	7.173	1371	1.545
3	1.835	7.319	1151	1.347
4	1.840	7.231	937	1.216
5	1.686	8.081	737	1.158
6	1.658	8.159	502	1.216
B2	2.282	5.732	1346	1.009
3	2.267	5.785	1138	1.276
4	2.320	5.437	940	1.071
5	2.297	5.548	723	1.256
6	2.204	6.003	501	1.574
7	2.631	4.039	312	3.132
C3	2.111	6.832	1178	0.918
4	2.109	6.756	1053	0.993
5	2.209	5.968	799	0.915
6	1.950	7.150	565	1.097
7	1.854	7.312	308	1.327

\*\*Standard deviations are based on the differences between the experimental  $u^+$  values and the  $u^+$  values from the LSF equation for the same  $y^+ (1 + y/D)$ , and are expressed as a percentage of the average  $u^+$  value in the range for each test based on the LSF equation.

TABLE III

SOME THREE-WIRE PROBE RESULTSTEST A1

$\theta$ (Degrees)	$\frac{u'}{\bar{u}^*}$	$\frac{v'}{\bar{u}^*}$	$\frac{w'}{\bar{u}^*}$	$\frac{\bar{u}v}{(\bar{u}^*)^2}$	$\frac{\bar{u}w}{(\bar{u}^*)^2}$	$\frac{\bar{v}w}{(\bar{u}^*)^2}$
<u><math>y = 3.18 \text{ mm}</math></u>						
30	1.45	1.02	1.28	0.62	-0.26	0.09
24	1.41	0.98	1.22	0.52	-0.14	0.20
18	1.40	0.98	1.22	0.51	-0.20	0.19
12	1.37	0.98	1.20	0.51	-0.19	0.22
6	1.37	0.99	1.20	0.57	-0.29	0.12
0	1.36	0.95	1.18	0.46	-0.18	0.10
<u><math>y = 9.53 \text{ mm}</math></u>						
30	1.03	0.74	0.83	0.37	-0.08	0.05
24	1.04	0.75	0.81	0.39	-0.05	0.07
18	0.98	0.76	0.80	0.38	-0.03	0.09
12	0.90	0.72	0.73	0.30	-0.01	0.09
6	0.81	0.67	0.70	0.22	+0.02	0.09
0	0.74	0.63	0.66	0.17	+0.02	0.08
<u><math>y = 14.61 \text{ mm}</math></u>						
30	0.56	0.53	0.48	0.10	-0.02	0.05
24	0.63	0.56	0.53	0.09	+0.06	0.05
18	0.69	0.60	0.58	0.03	+0.09	0.07



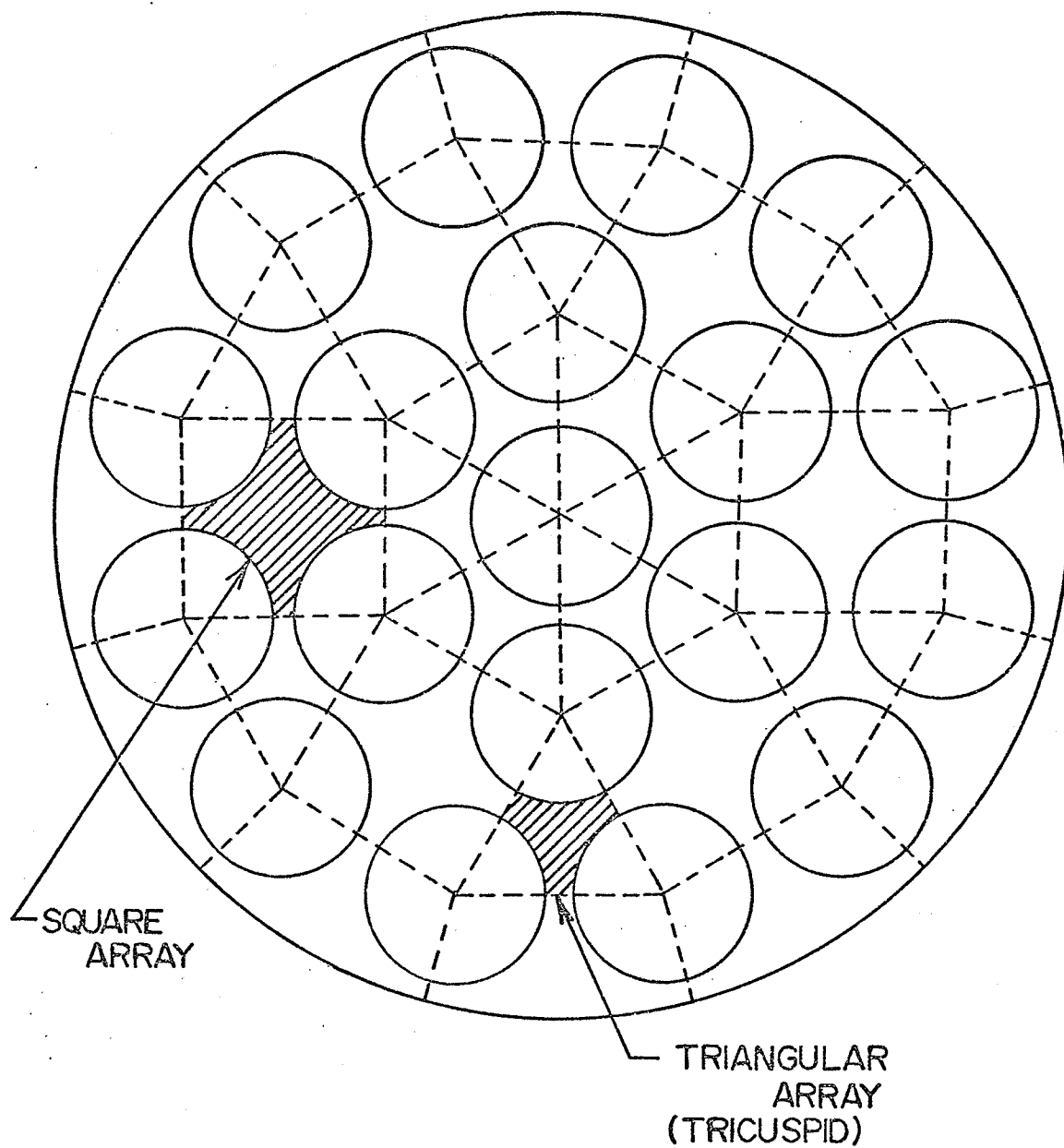
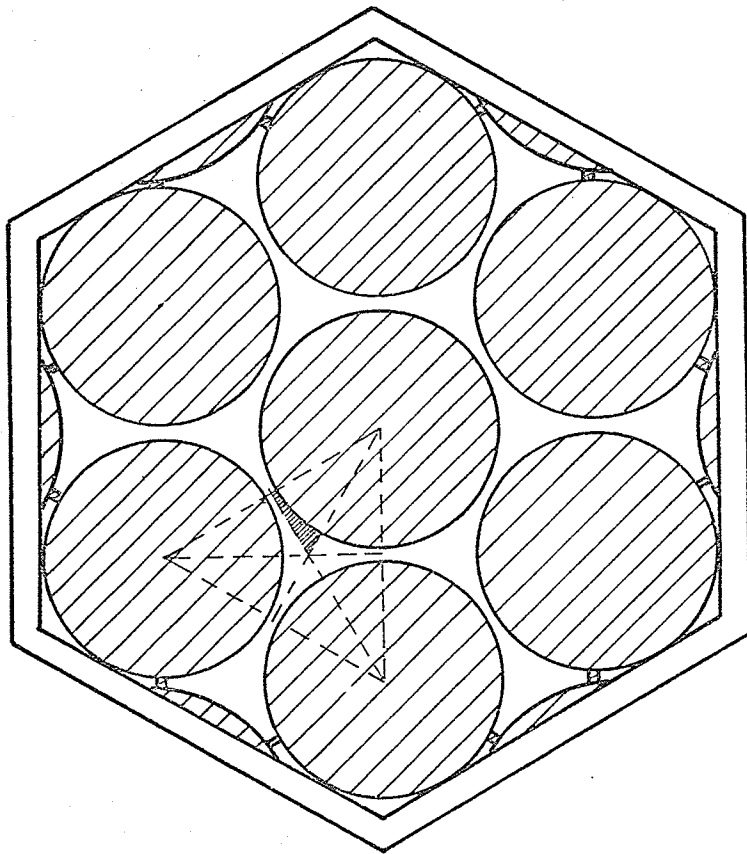
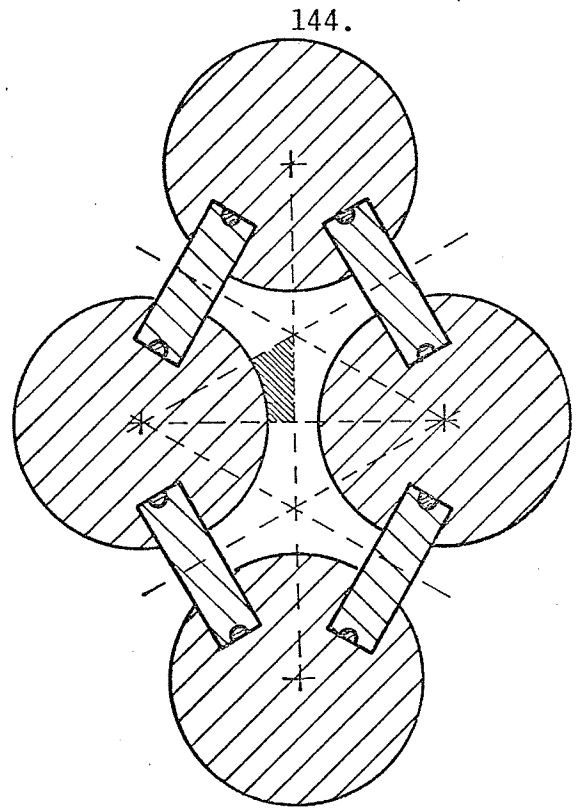


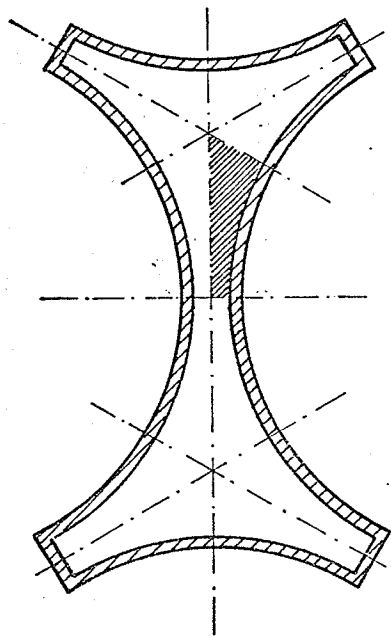
FIG. 1 CROSS-SECTION of TYPICAL NINETEEN ELEMENT FUEL BUNDLE SHOWING the VARIOUS SUB-CHANNELS



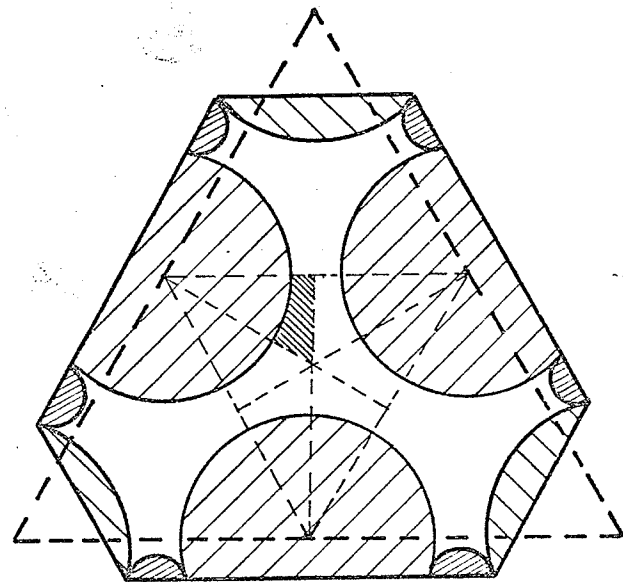
a) Palmer & Swanson



b) Eifler & Nijssing



c) Subbotin et al



d) Kjellstrom & Stenback

FIG. 2 CROSS-SECTIONS of TEST-SECTIONS USED BY PREVIOUS INVESTIGATORS

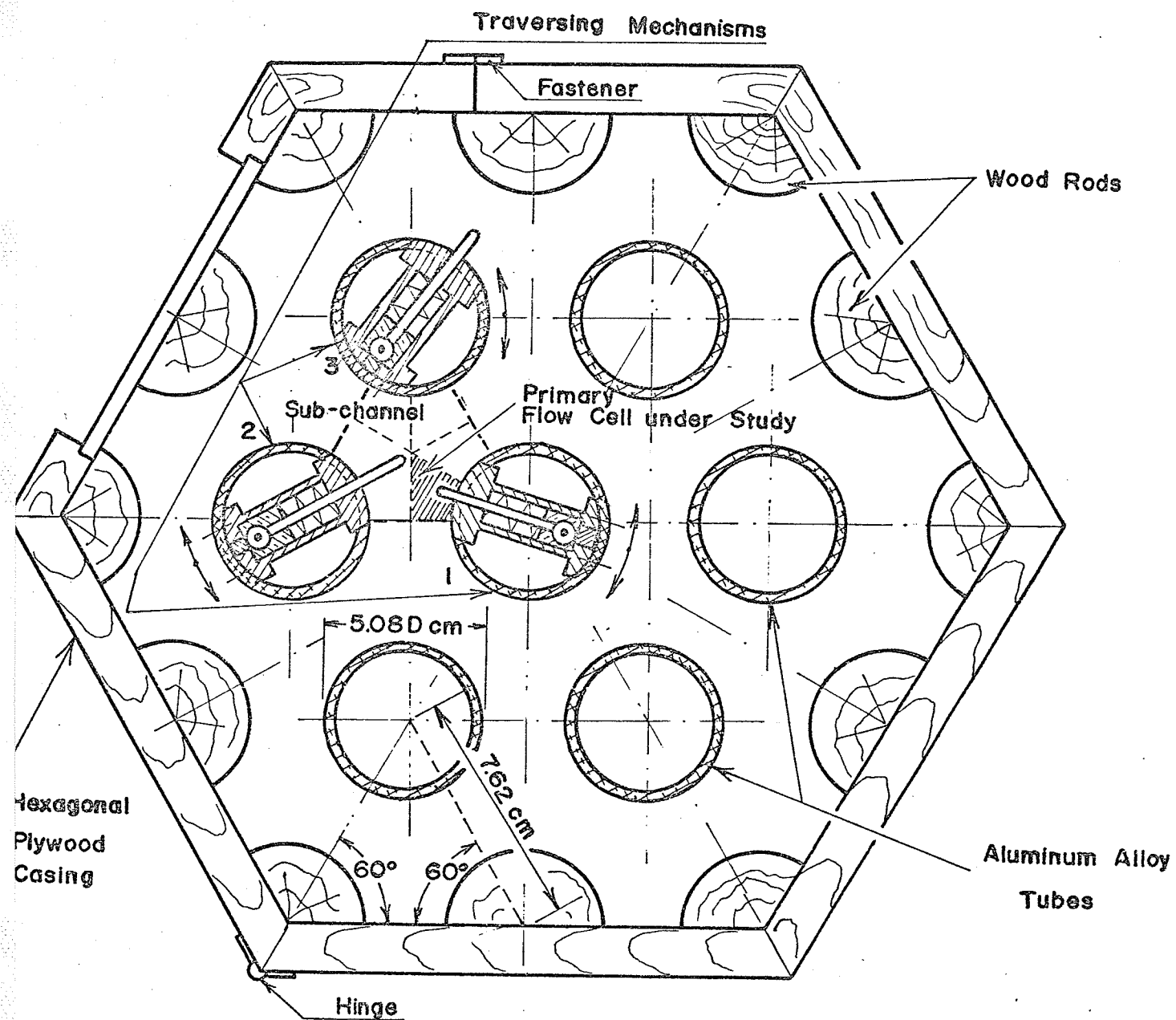


FIG. 3 CROSS-SECTION of TEST-SECTION IA —  $P/D=1.50$   
(Upstream View)

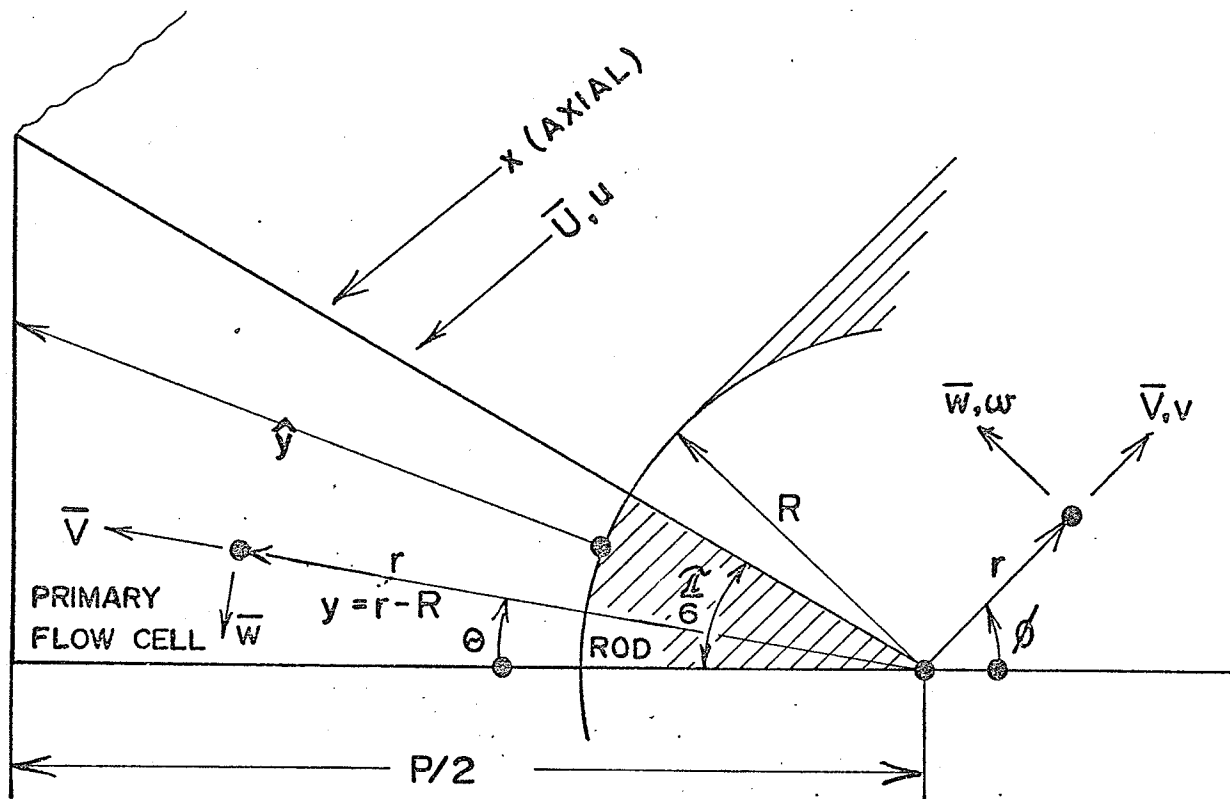


FIG. 4 CYLINDRICAL COORDINATE SYSTEM AND VELOCITY DIRECTIONS

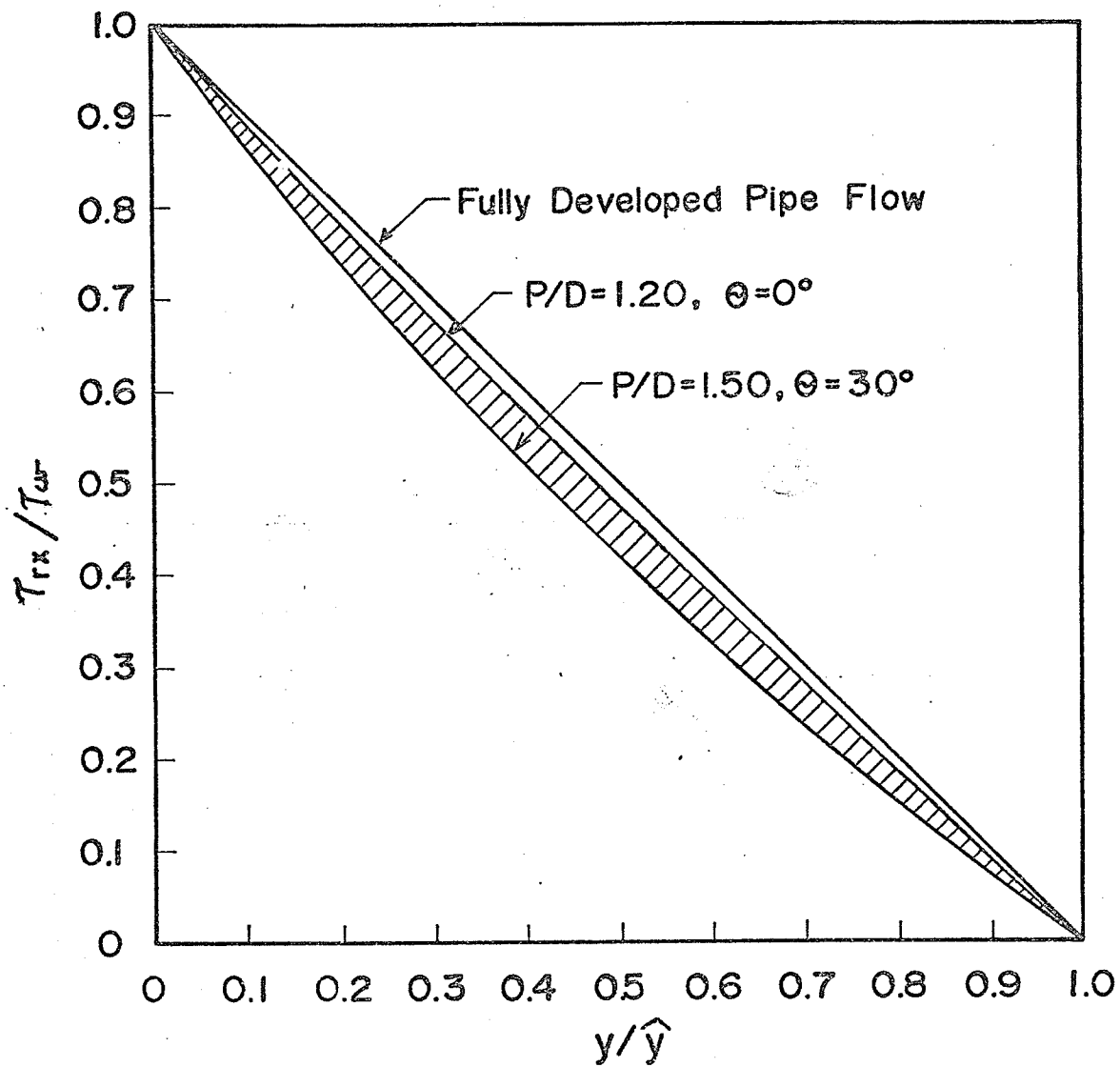


FIG. 5 VARIATION of FLUID SHEAR STRESS AT RADIAL BOUNDARIES of PRIMARY FLOW CELL

## COMPONENTS

① TEST SECTION 1A(P/D=1.50)	O-O	⑪ FANSECTION	O-O
② TRANSITION PIECE	O-O	⑫ SILENCER	O-O
③ DIFFUSER	□-□	⑬ DIFFUSER	□-□
④ FIRST CORNER	□-□	⑭ THIRD CORNER	□-□
⑤ DIFFUSER	□-□	⑮ DIFFUSER	□-□
⑥ SECOND CORNER	□-□	⑯ FOURTH CORNER	□-□
⑦ DUCT	□-□	⑰ DUCT	□-□
⑧ NOZZLE	□-□	⑱ TRANSITION PIECE	□-□
⑨ CANVAS COUPLINGS	□-□	⑲ SCREEN SECTION	O-O
⑩ RADIAL VANE DAMPER	□-□	⑳ CONTRACTION CONE	O-O
		㉑ TRANSITION PIECE	O-O

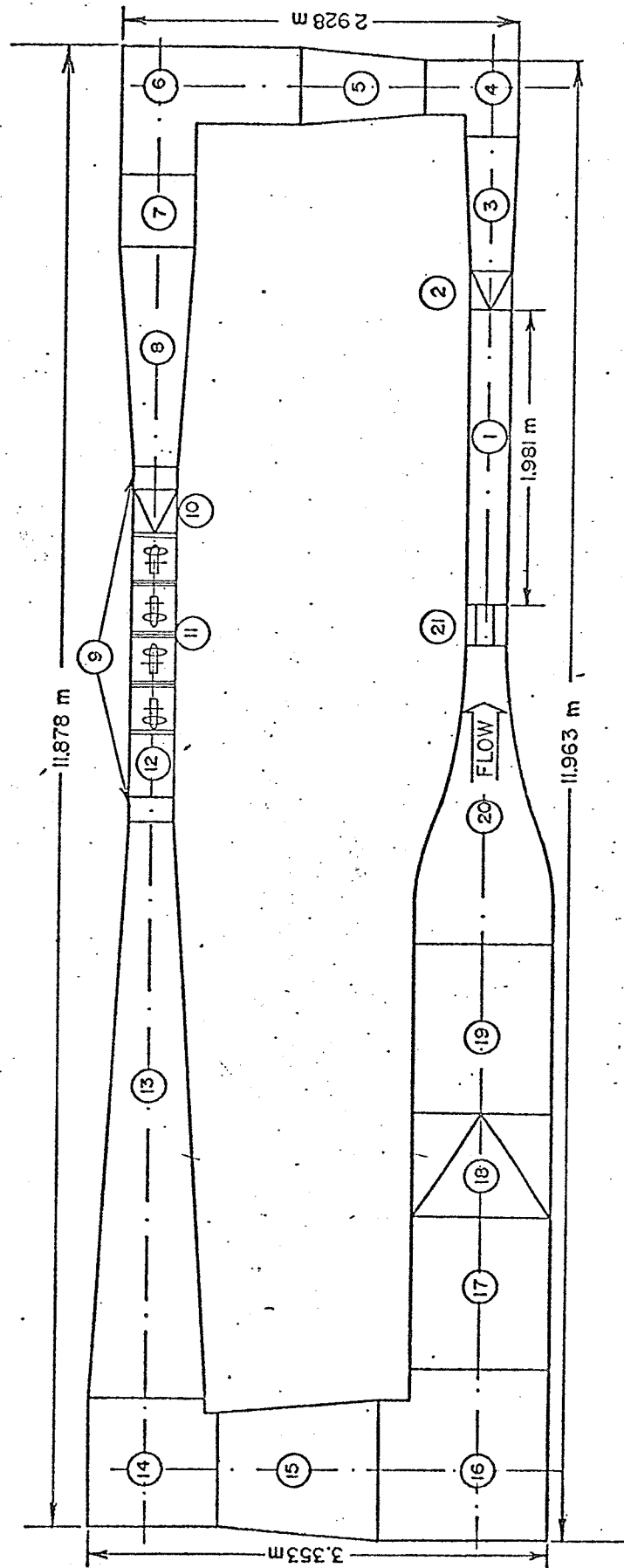


FIG. 6 PLAN VIEW of WIND TUNNEL for ROD BUNDLE TURBULENCE STUDIES

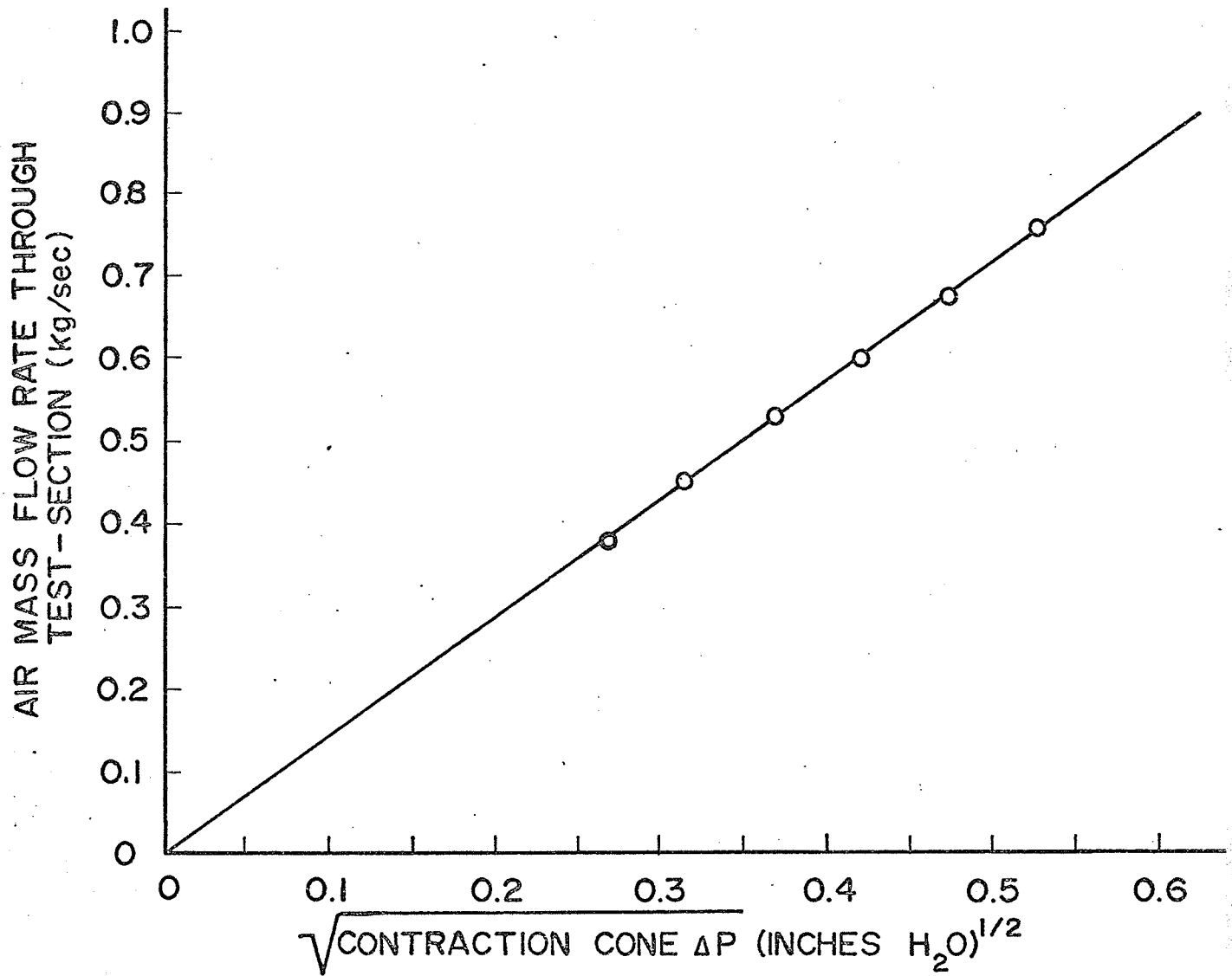


FIG. 7 WIND TUNNEL FLOW CALIBRATION

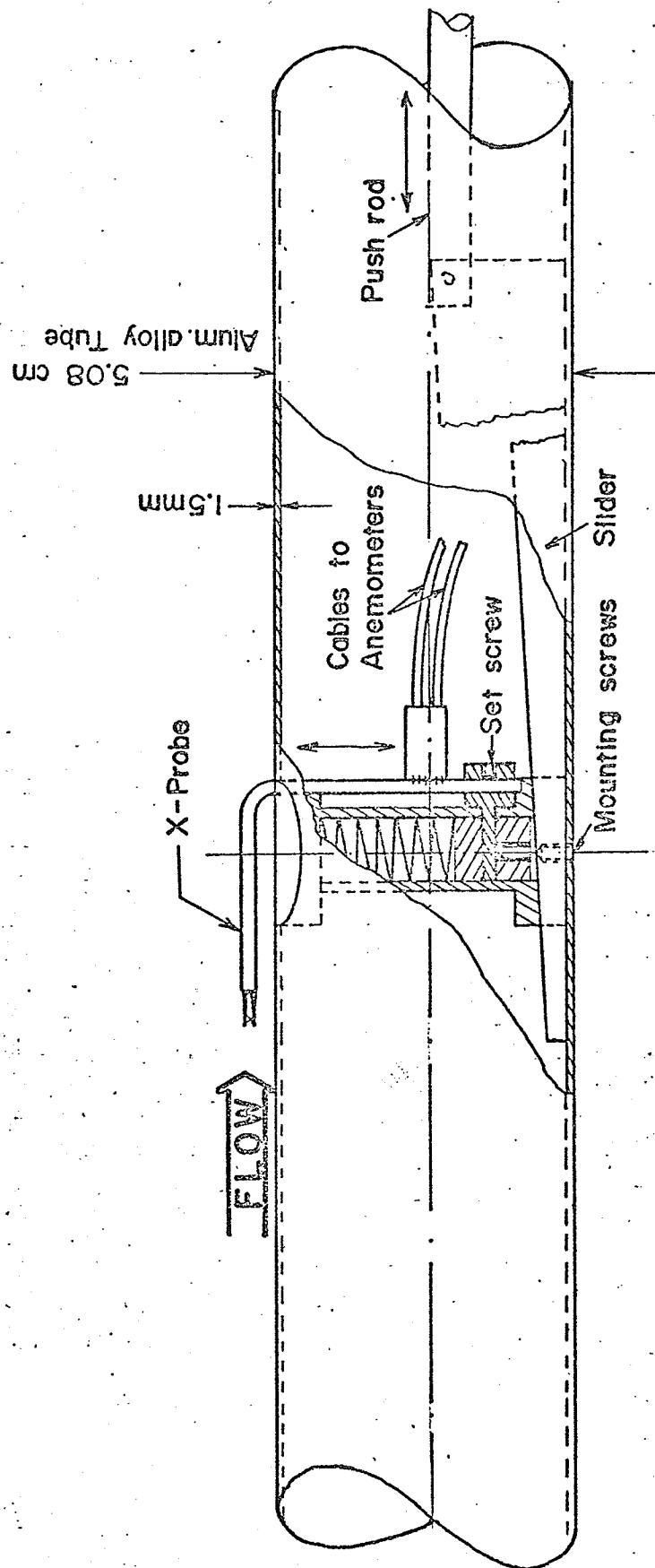
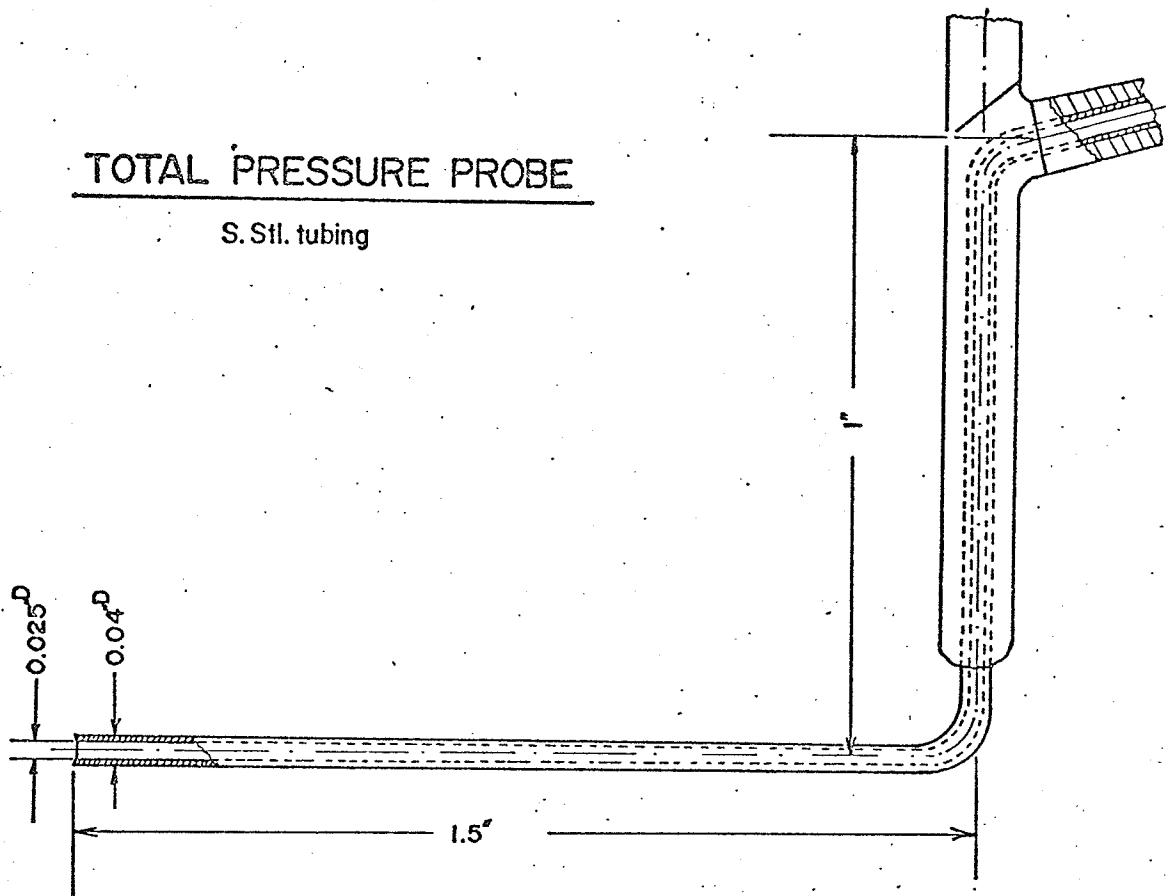


FIG. 8 : PROBE / TRAVERSING MECHANISM-ASSEMBLY



# TOTAL PRESSURE PROBE

S. Stl. tubing



# STATIC PRESSURE PROBE

Brass tubing

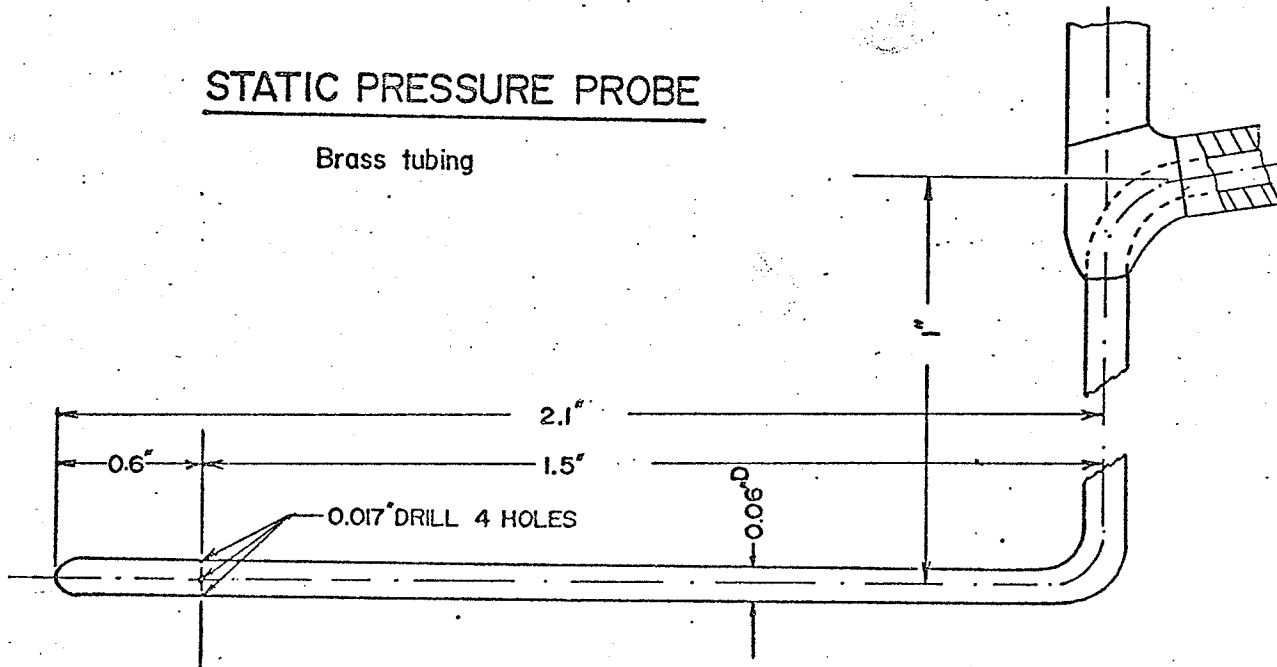
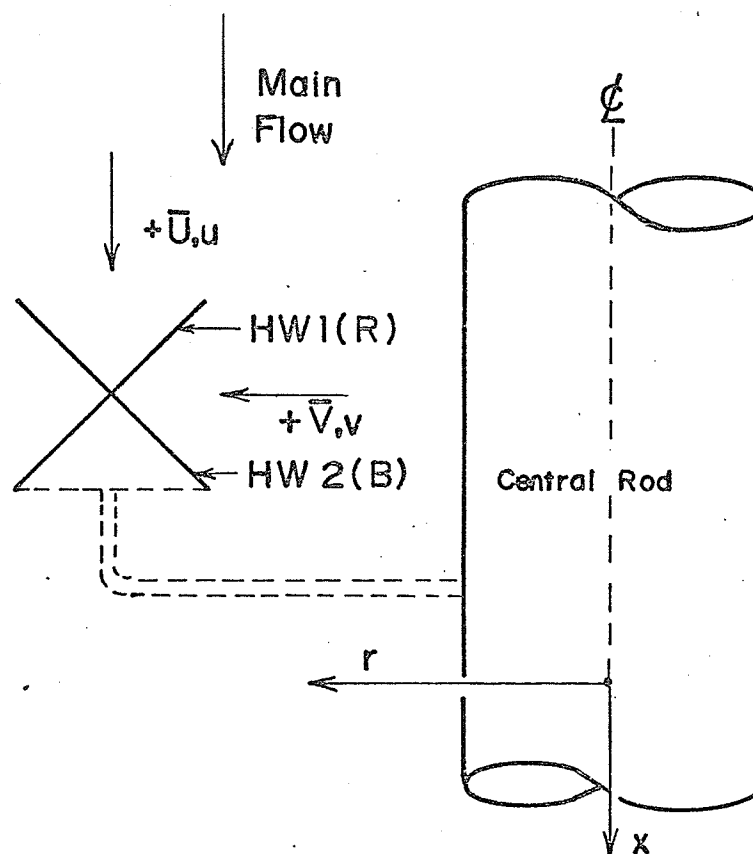


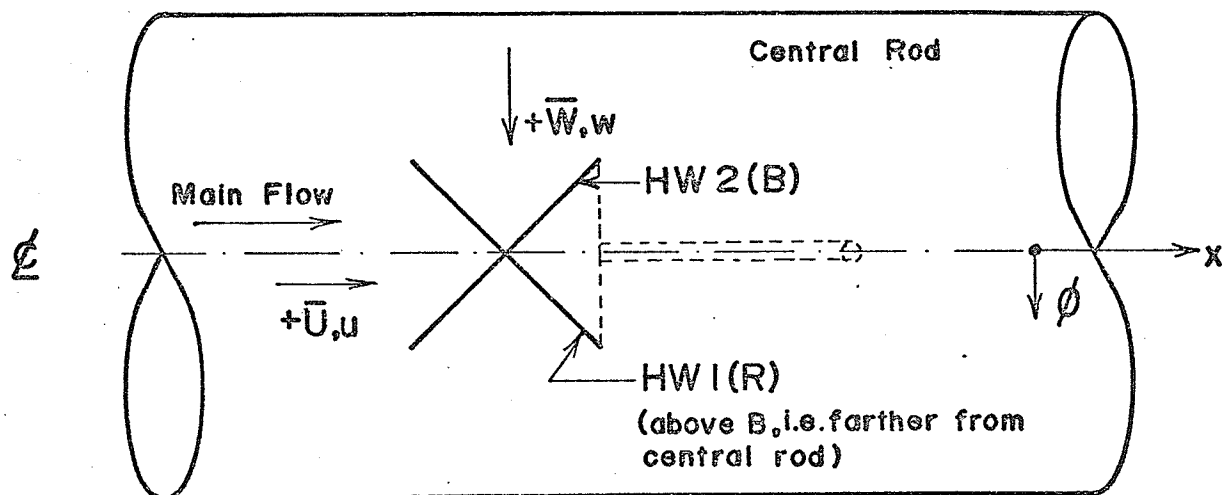
FIG. 9 PITOT AND STATIC PRESSURE PROBES



$$\left. \begin{array}{l} \text{DCR} \propto \bar{U} - \bar{V} \\ \text{DCB} \propto \bar{U} + \bar{V} \end{array} \right\} \begin{array}{l} \bar{U} \propto (\text{DCR} + \text{DCB})/2 \\ \bar{V} \propto (\text{DCB} - \text{DCR})/2 \end{array}$$

$$\left. \begin{array}{l} \text{ACR} \propto u - v \\ \text{ACB} \propto u + v \end{array} \right\} \left. \begin{array}{l} \text{SUM}_{1+2} \propto u \\ \text{DIFF}_{1-2} \propto (-v) \end{array} \right\} S * D \propto (-uv)$$

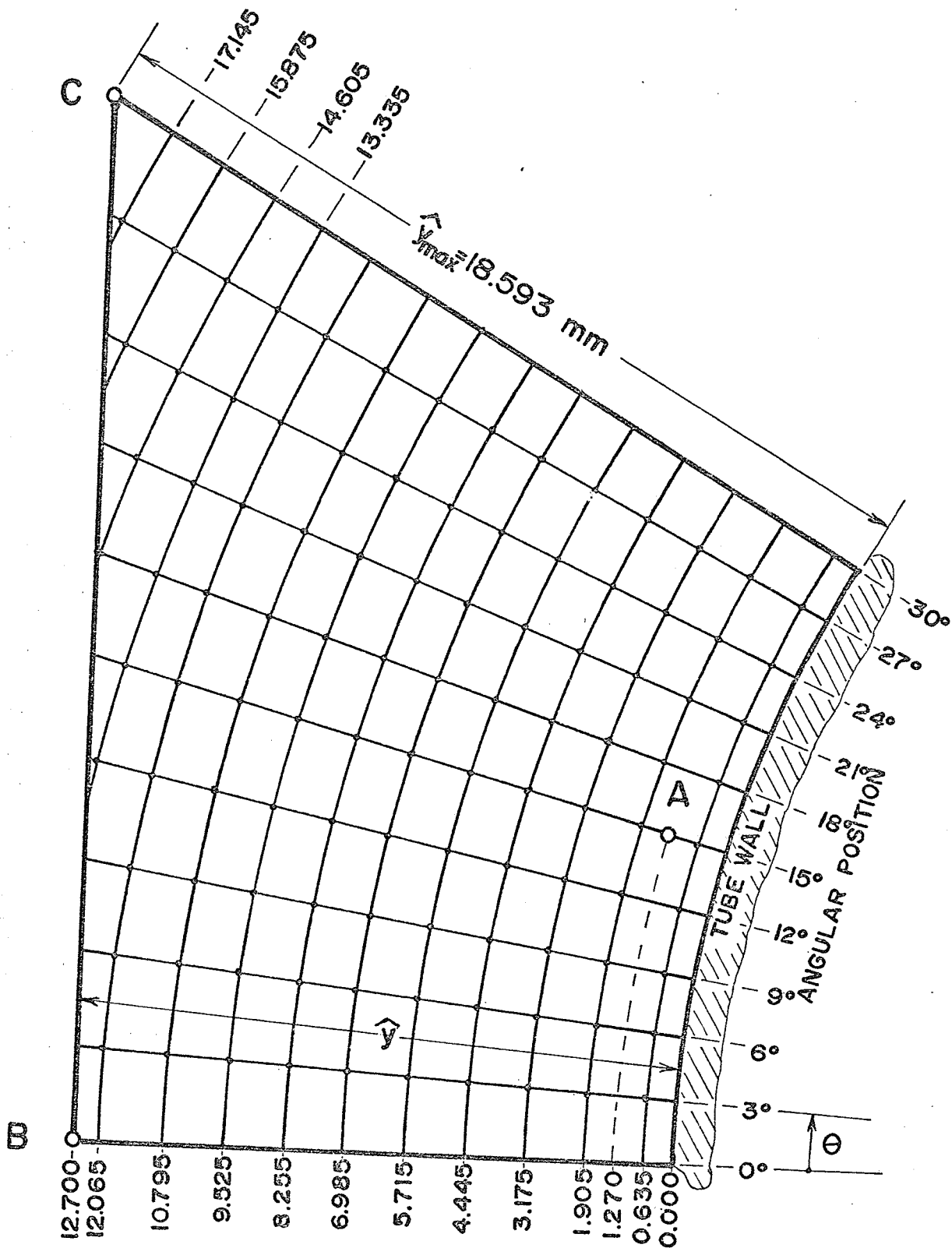
FIG. 10 SCHEMATIC of WIRE ORIENTATION  
FOR  $u-v$  X-PROBE



$$\left. \begin{aligned} \text{DCR} &\propto \bar{U} - \bar{W} \\ \text{DCB} &\propto \bar{U} + \bar{W} \end{aligned} \right\} \begin{aligned} \bar{U} &\propto (\text{DCR} + \text{DCB})/2 \\ \bar{W} &\propto (\text{DCB} - \text{DCR})/2 \end{aligned}$$

$$\left. \begin{aligned} \text{ACR} &\propto u - w \\ \text{ACB} &\propto u + w \end{aligned} \right\} \left. \begin{aligned} \text{SUM}_{1+2} &\propto u \\ \text{DIFF}_{1-2} &\propto (-w) \end{aligned} \right\} S * D \propto (-uw)$$

FIG. II SCHEMATIC of WIRE ORIENTATION  
FOR  $u-w$  X-PROBE



RADIAL DISTANCE from TUBE WALL (y)(mm)

FIG.12 SUB-DIVISION of FLOW CELL GEOMETRY for  
ROD BUNDLE of P/D=1.50

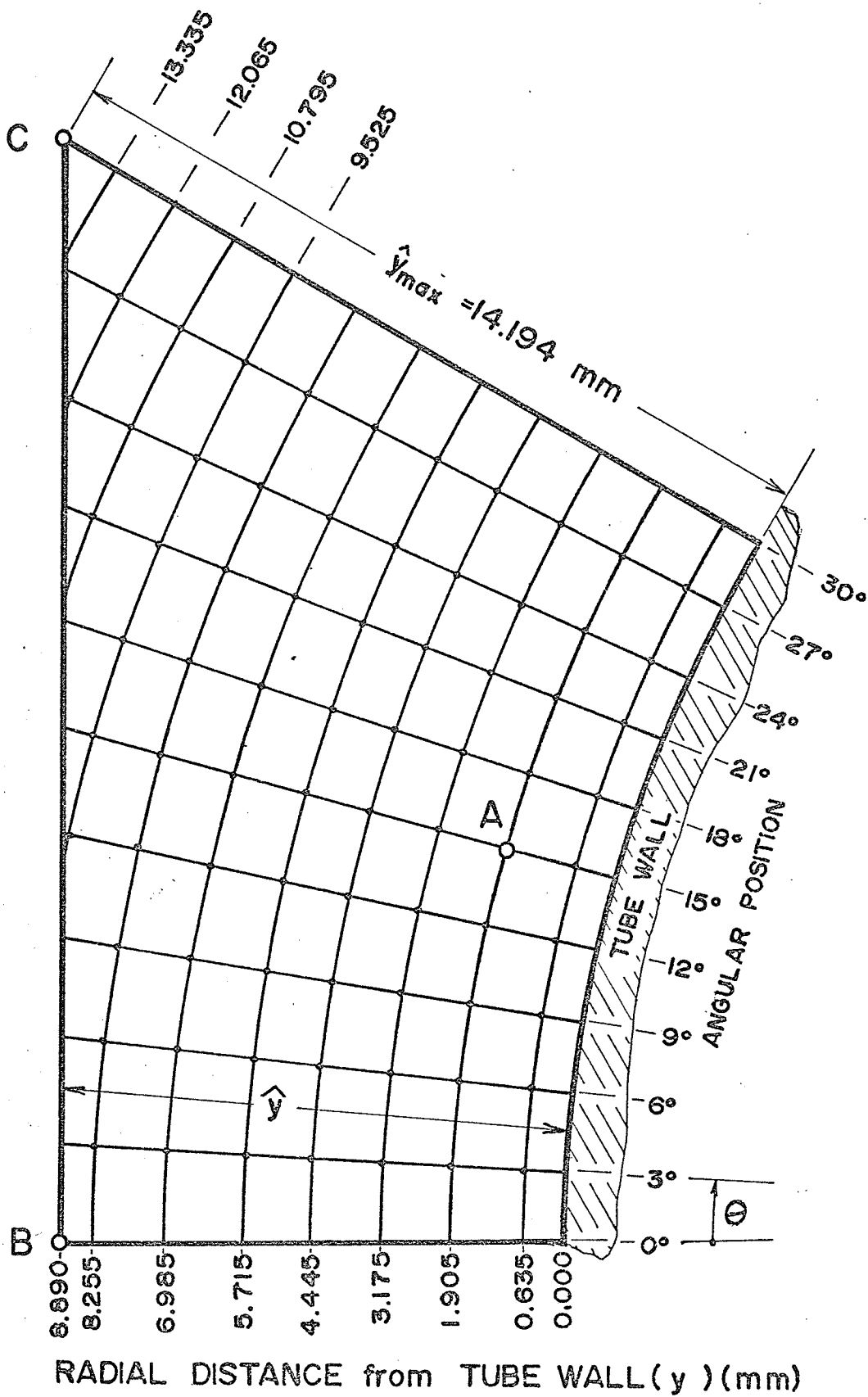
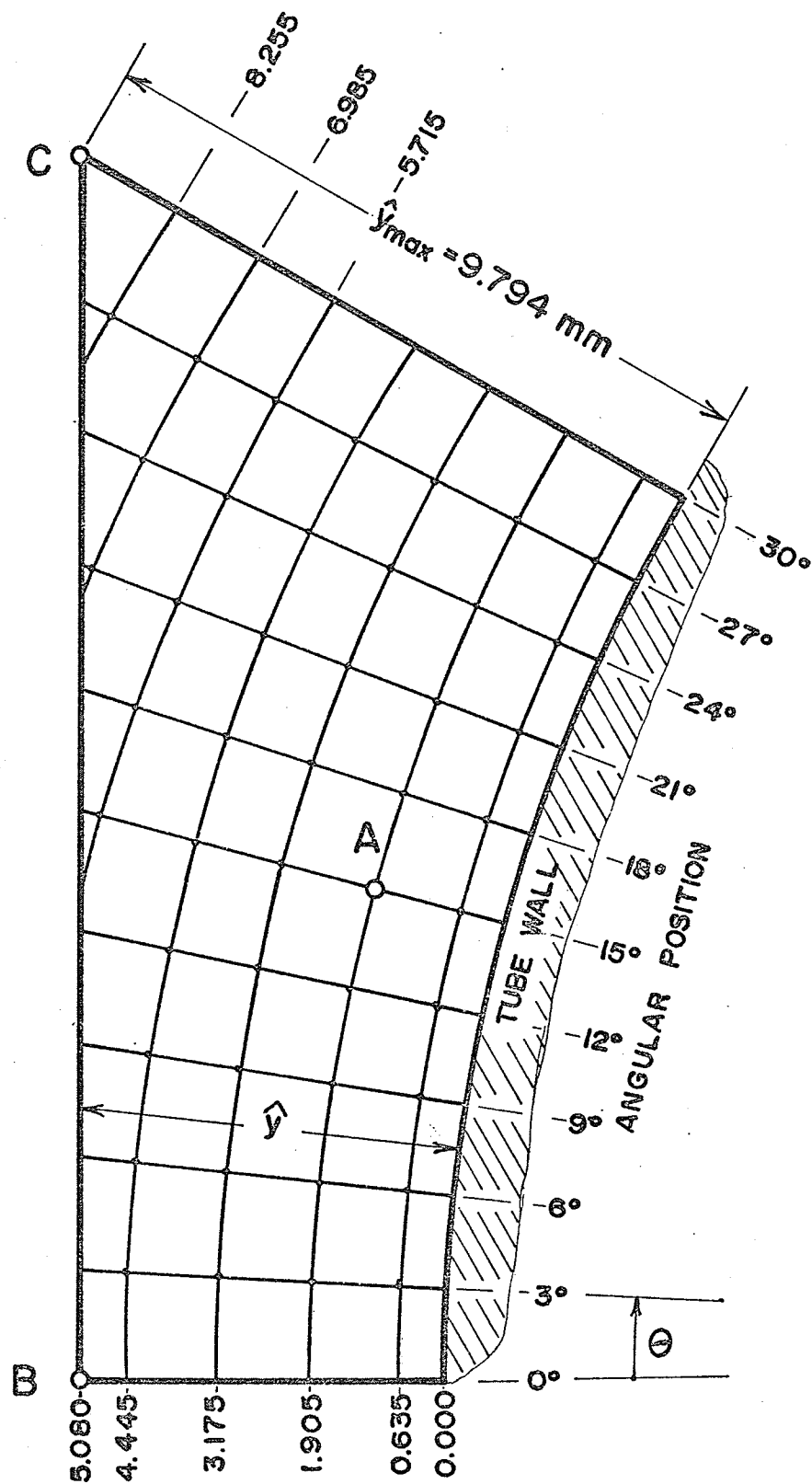


FIG. 13 SUB-DIVISION of FLOW CELL GEOMETRY for  
ROD BUNDLE of  $P/D=1.35$



RADIAL DISTANCE from TUBE WALL( $y$ )(mm)

FIG.14 SUB-DIVISION of FLOW CELL GEOMETRY for  
ROD BUNDLE of  $P/D=1.20$

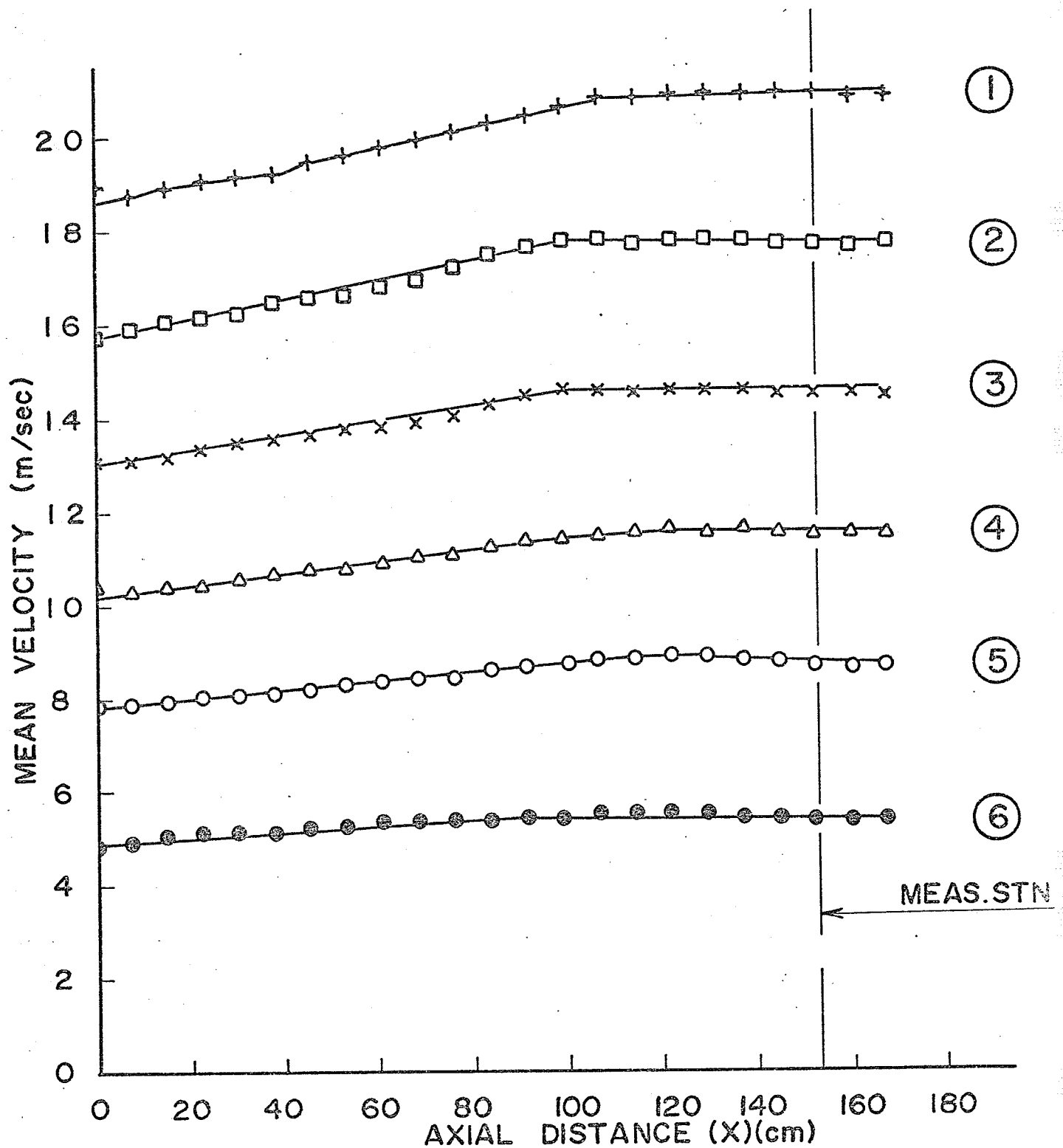


FIG. 15 MEAN VELOCITIES ALONG SUB-CHANNEL CENTER-LINE FOR TEST-SECTION IA (P/D=1.5)

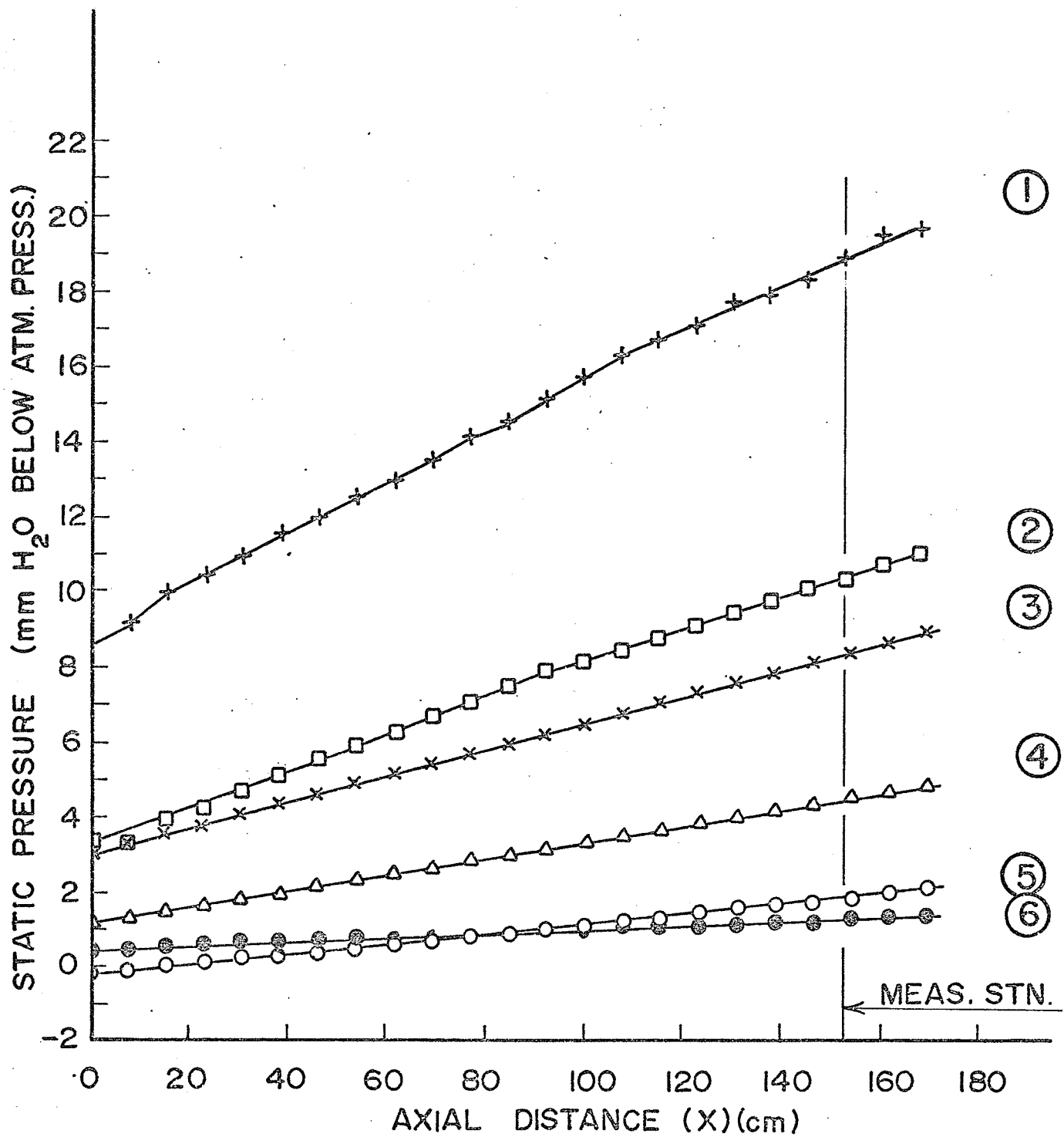


FIG. 16 STATIC PRESSURE ALONG SUB-CHANNEL CENTER-LINE FOR TEST-SECTION IA (P/D=1.50)



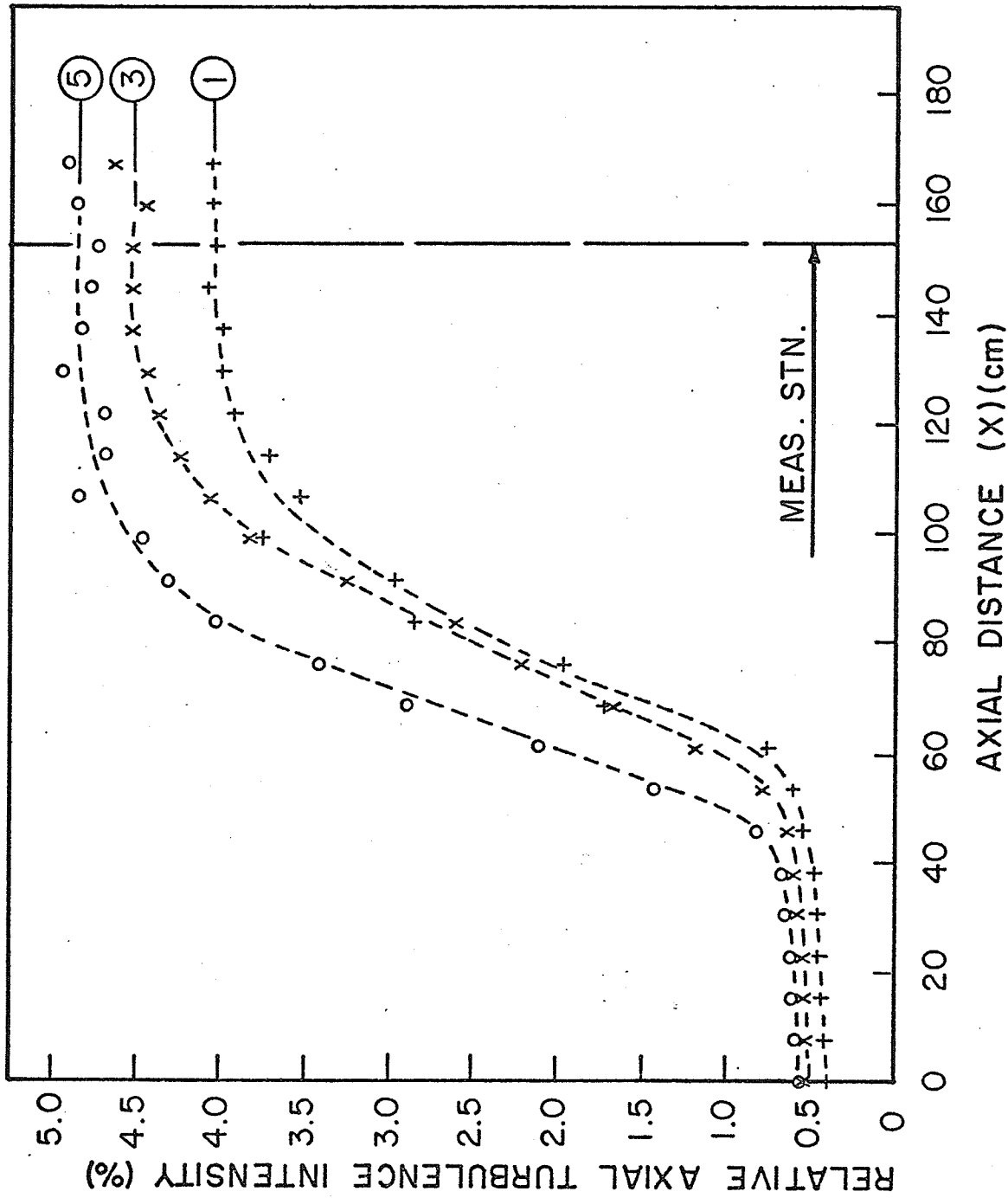


FIG. 17a RELATIVE AXIAL TURBULENCE INTENSITIES ALONG  
SUB-CHANNEL CENTER-LINE FOR TEST-SECTION IA  
(P/D=1.50)

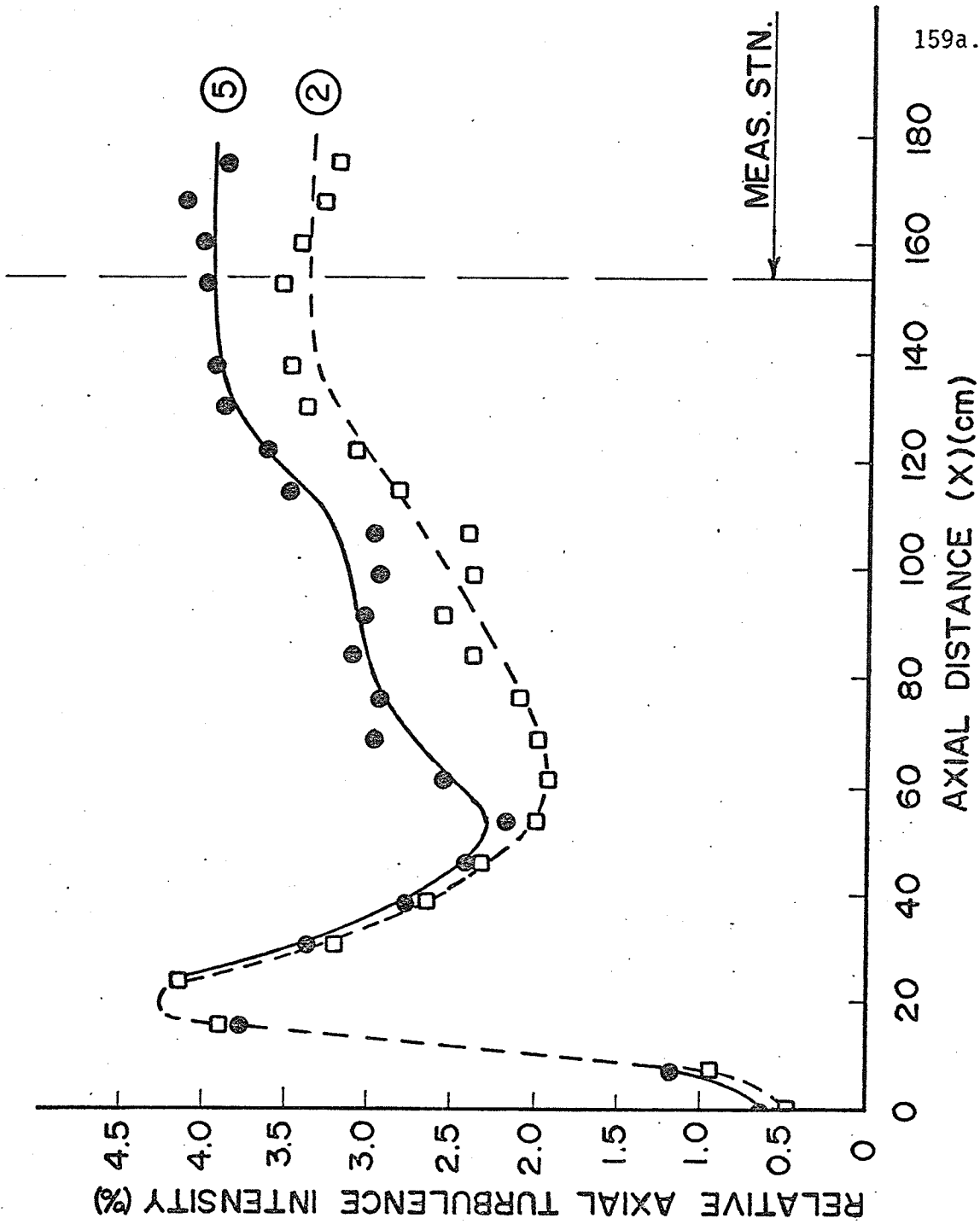


FIG. 17b RELATIVE AXIAL TURBULENCE INTENSITIES ALONG  
SUB-CHANNEL CENTER-LINE FOR TEST-SECTION IA  
(ORIGINAL PROTOTYPE) (P/D=1.50)

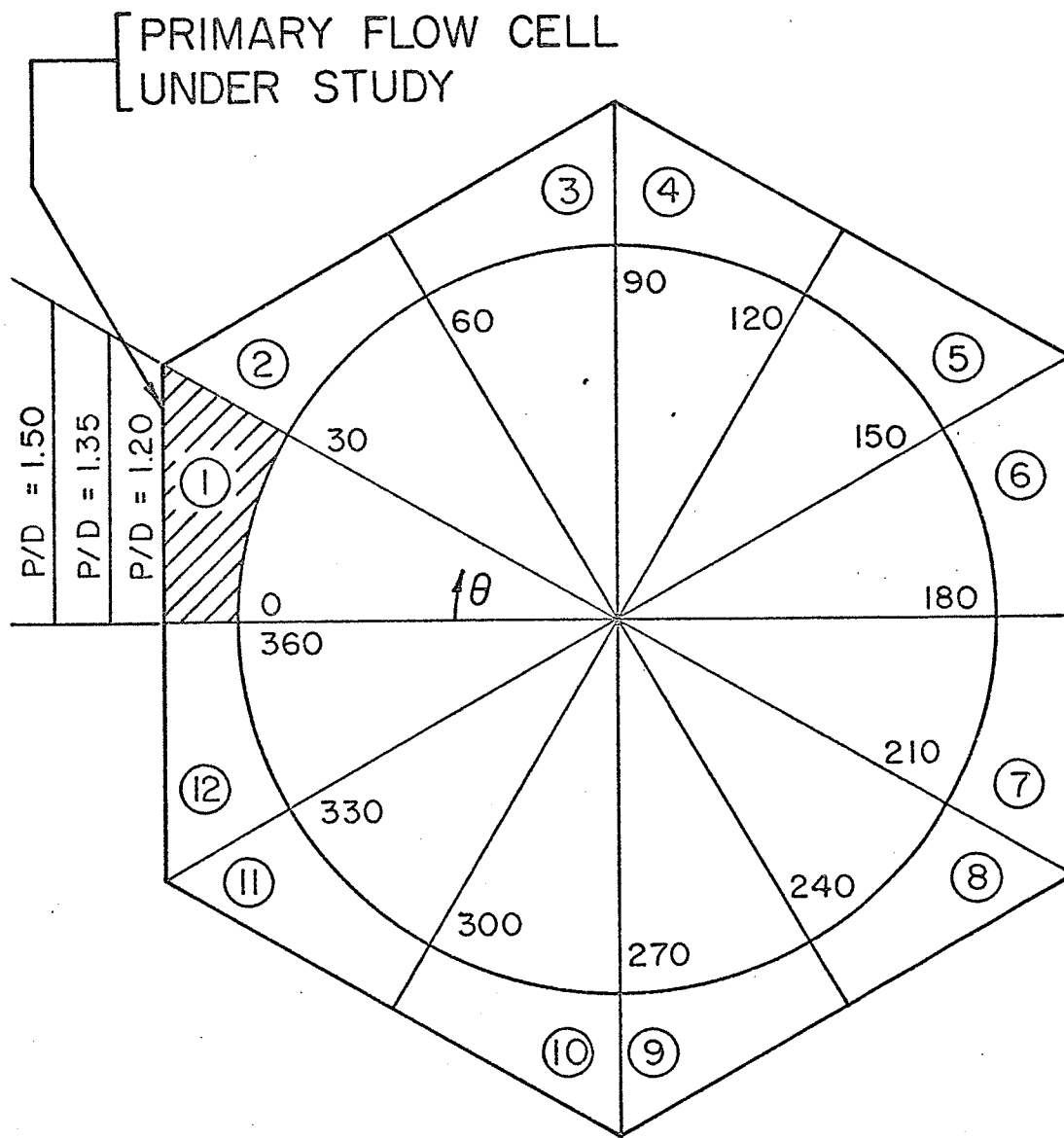


FIG.18 IDENTIFICATION OF PRIMARY FLOW CELLS  
FOR SYMMETRY STUDIES

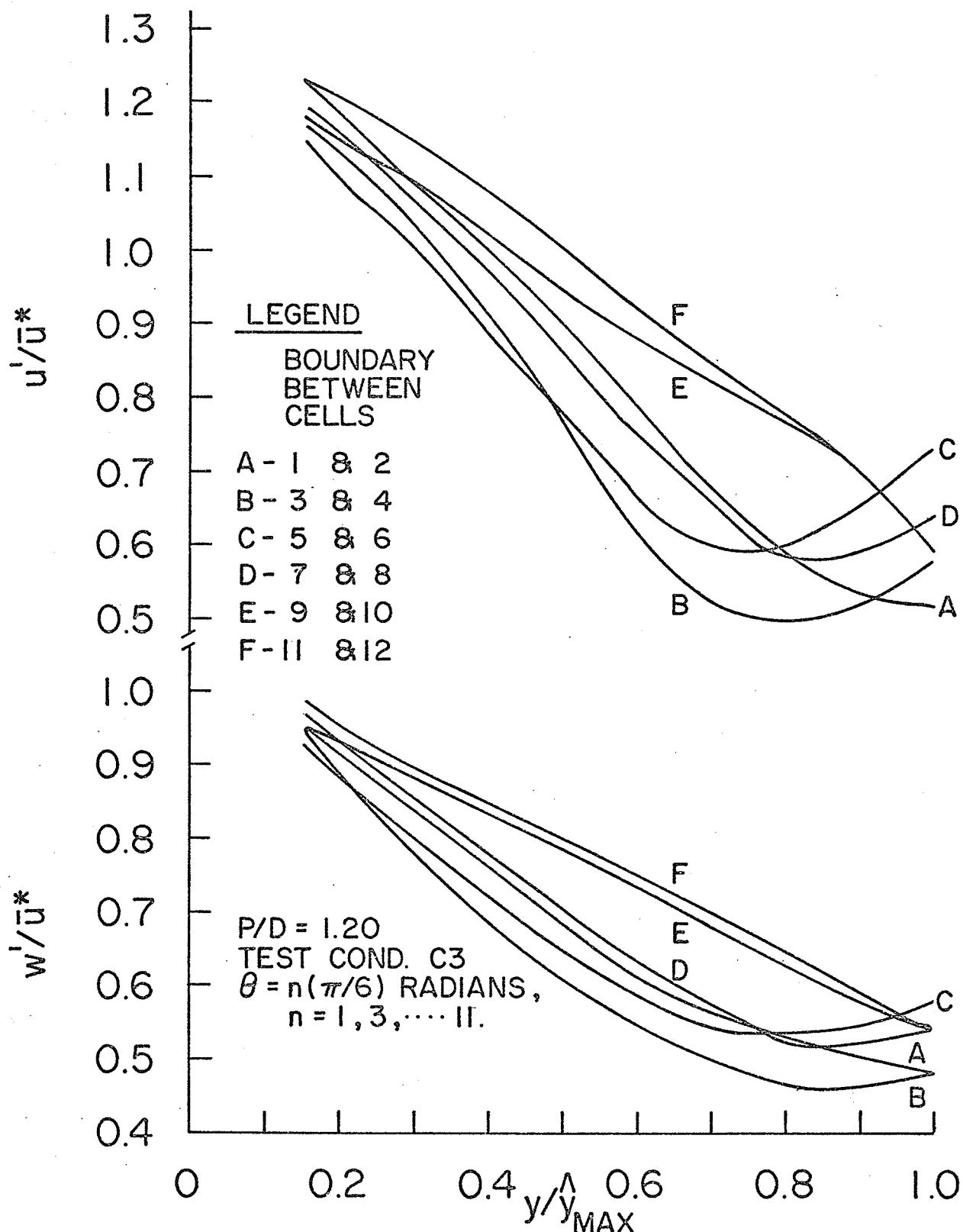


FIG. 19 SOME TURBULENCE DISTRIBUTIONS ALONG  
 $\hat{y}_{MAX}$  BOUNDARIES - TEST - SECTION IC

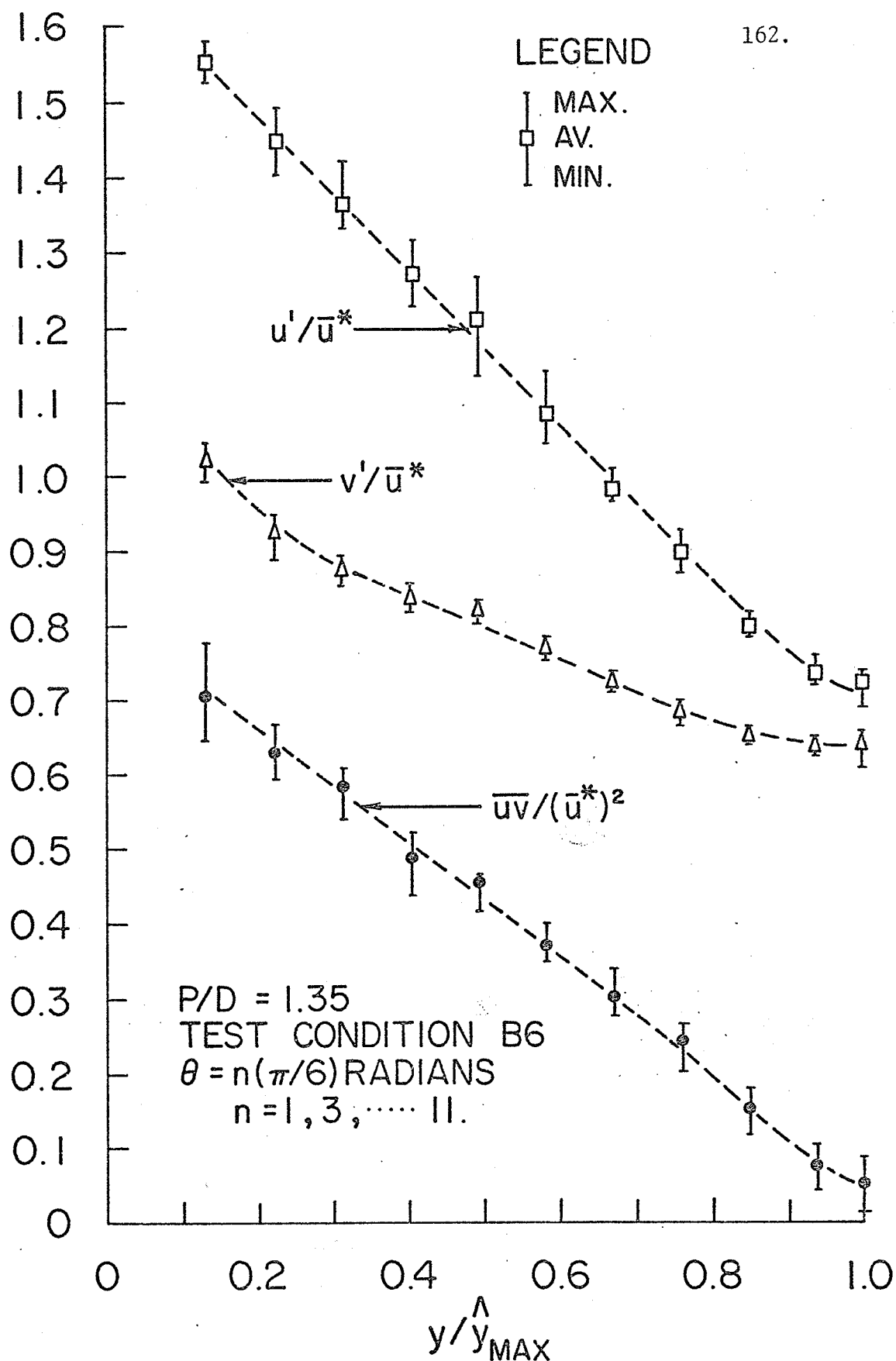


FIG.20 SOME TURBULENCE DISTRIBUTIONS ALONG  
 $y/y_{MAX}^{\Lambda}$  BOUNDARIES-TEST-SECTION IB

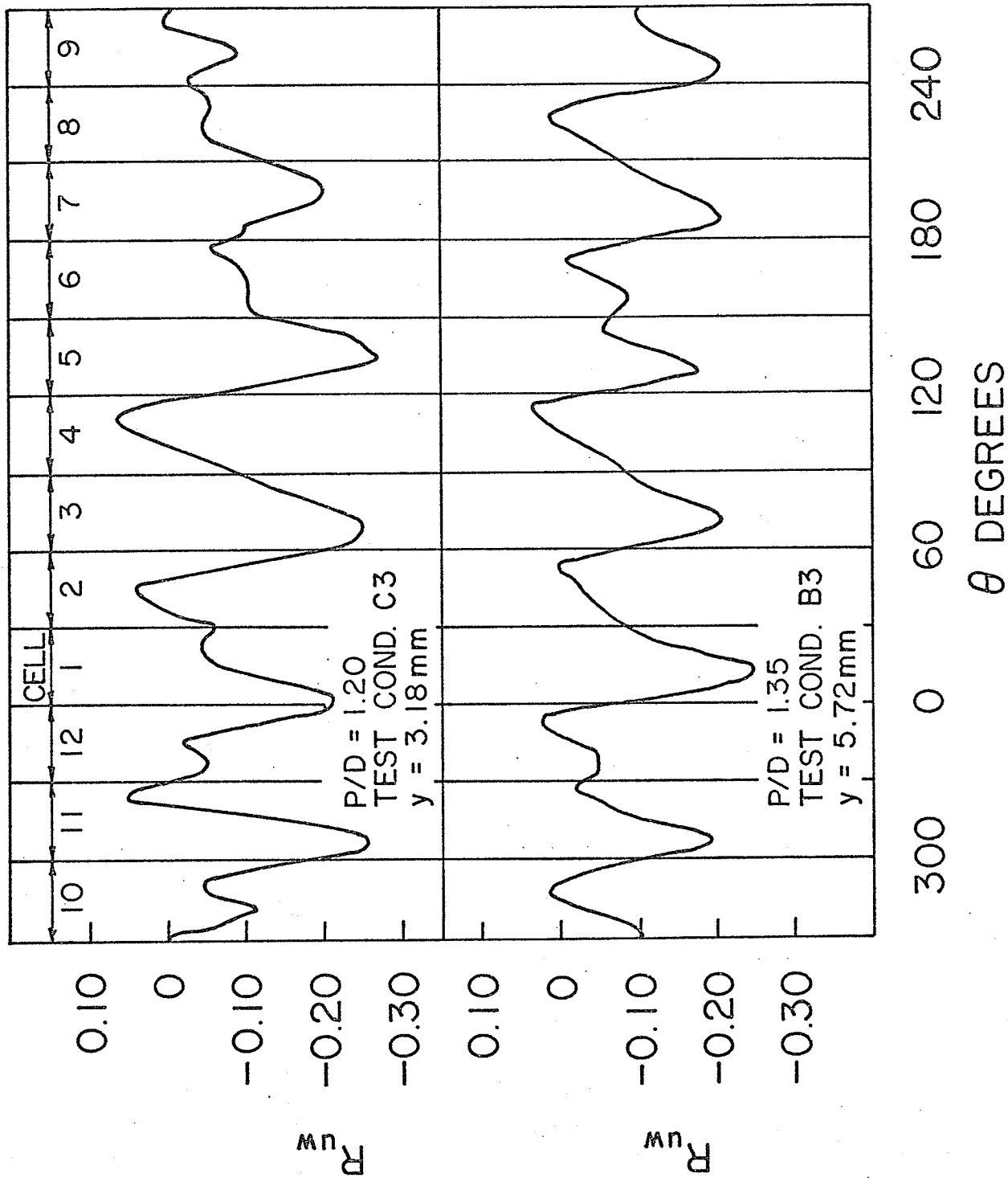


FIG. 21 VARIATIONS OF  $R_{uw}$  AT FIXED DISTANCES FROM CENTRAL ROD SURFACE

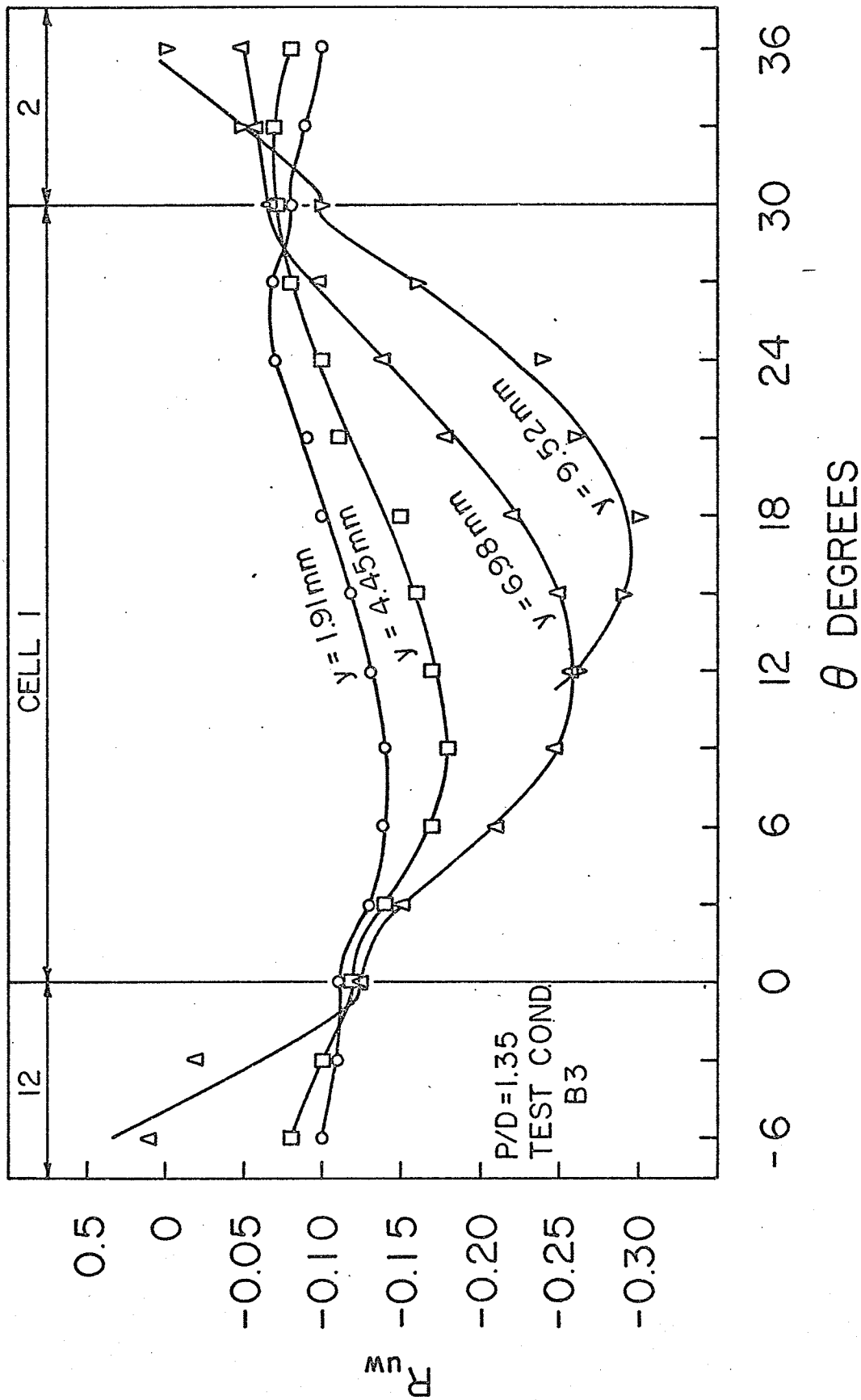


FIG. 22 VARIATIONS OF  $R_{uw}$  ACROSS PRIMARY FLOW CELL I AND ITS RADIAL BOUNDARIES.

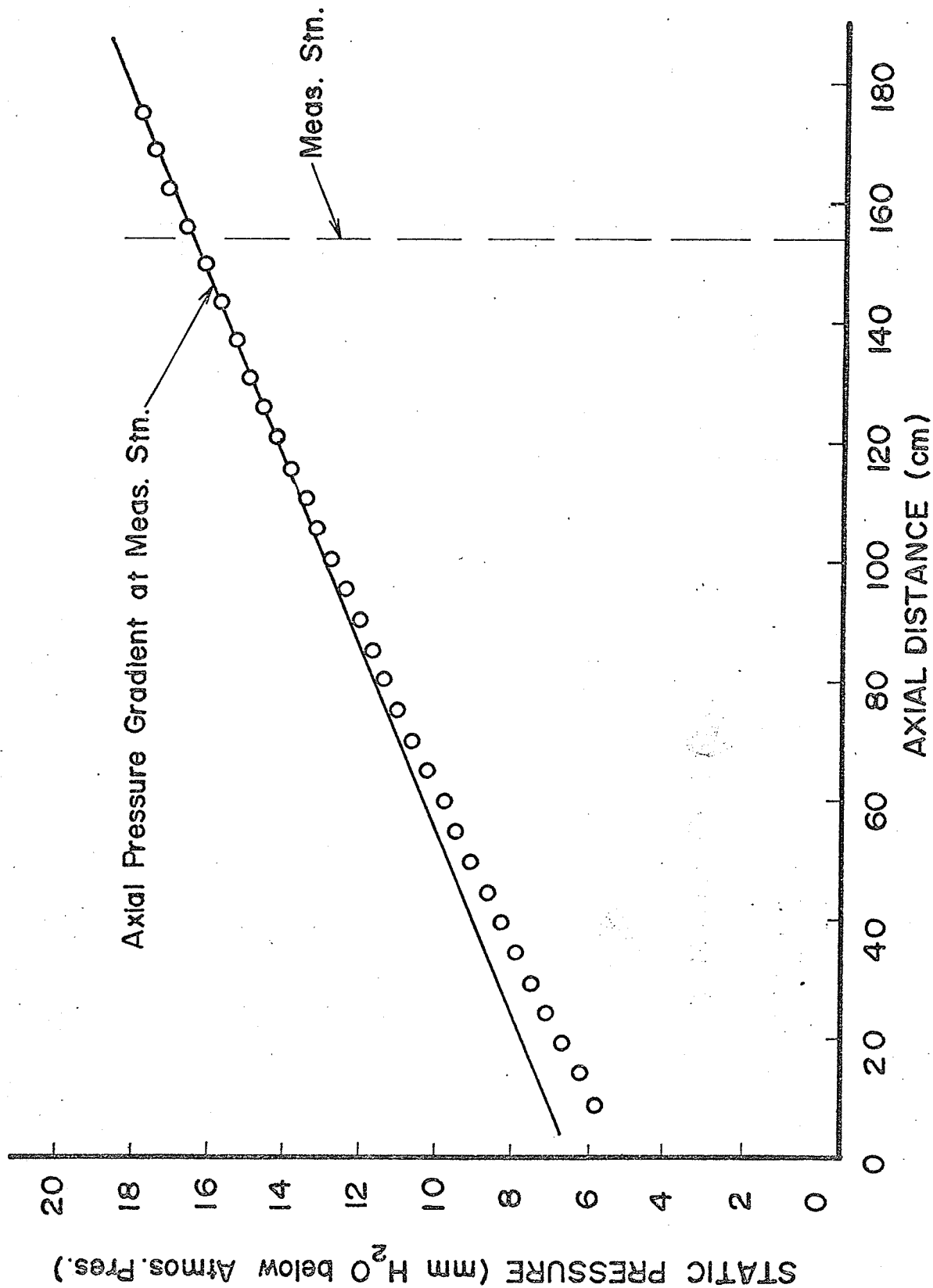


FIG. 23 PLOT of STATIC PRESSURE vs AXIAL DISTANCE along TEST-SECTION  
Test B4



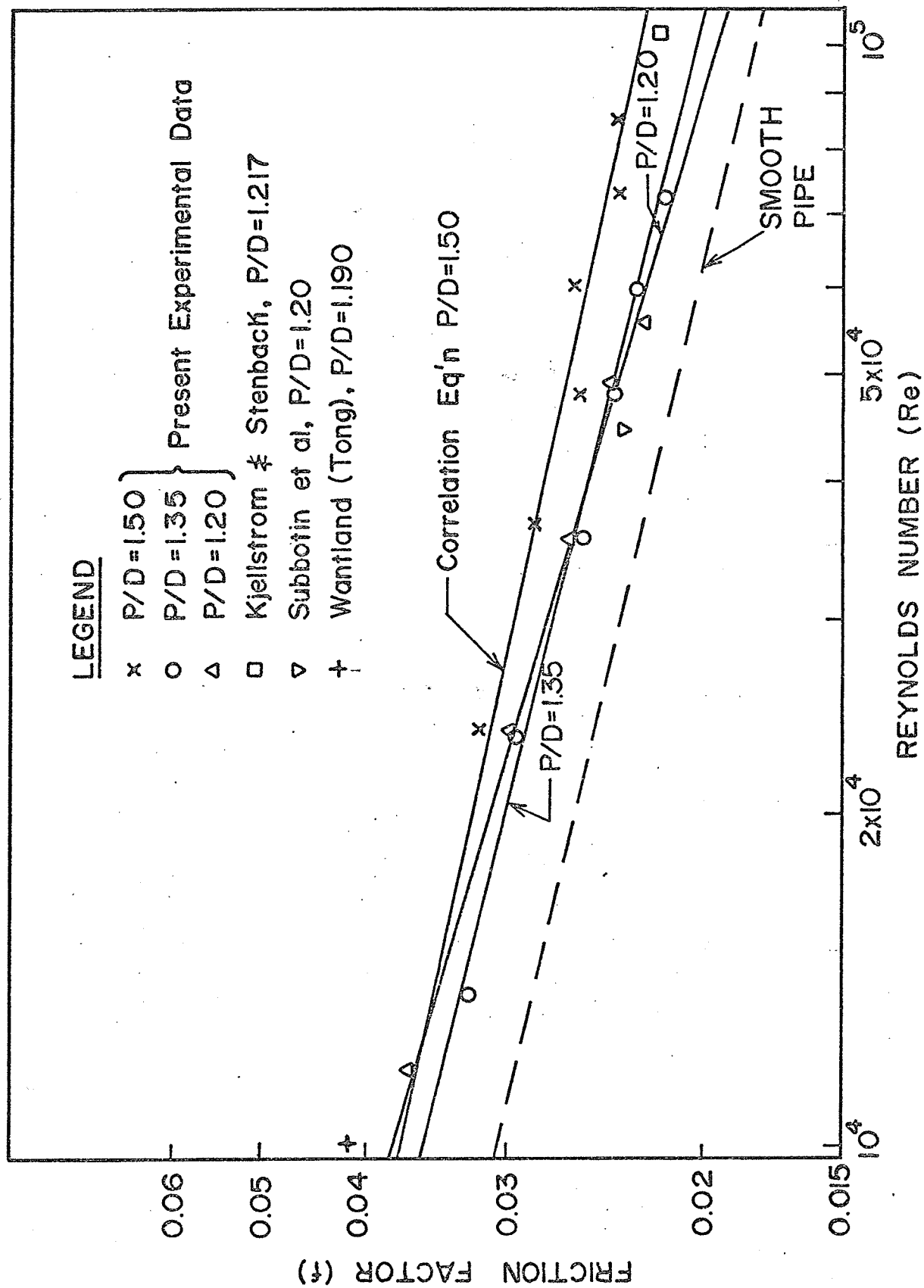


FIG. 24 EXPERIMENTAL FRICTION FACTOR DATA

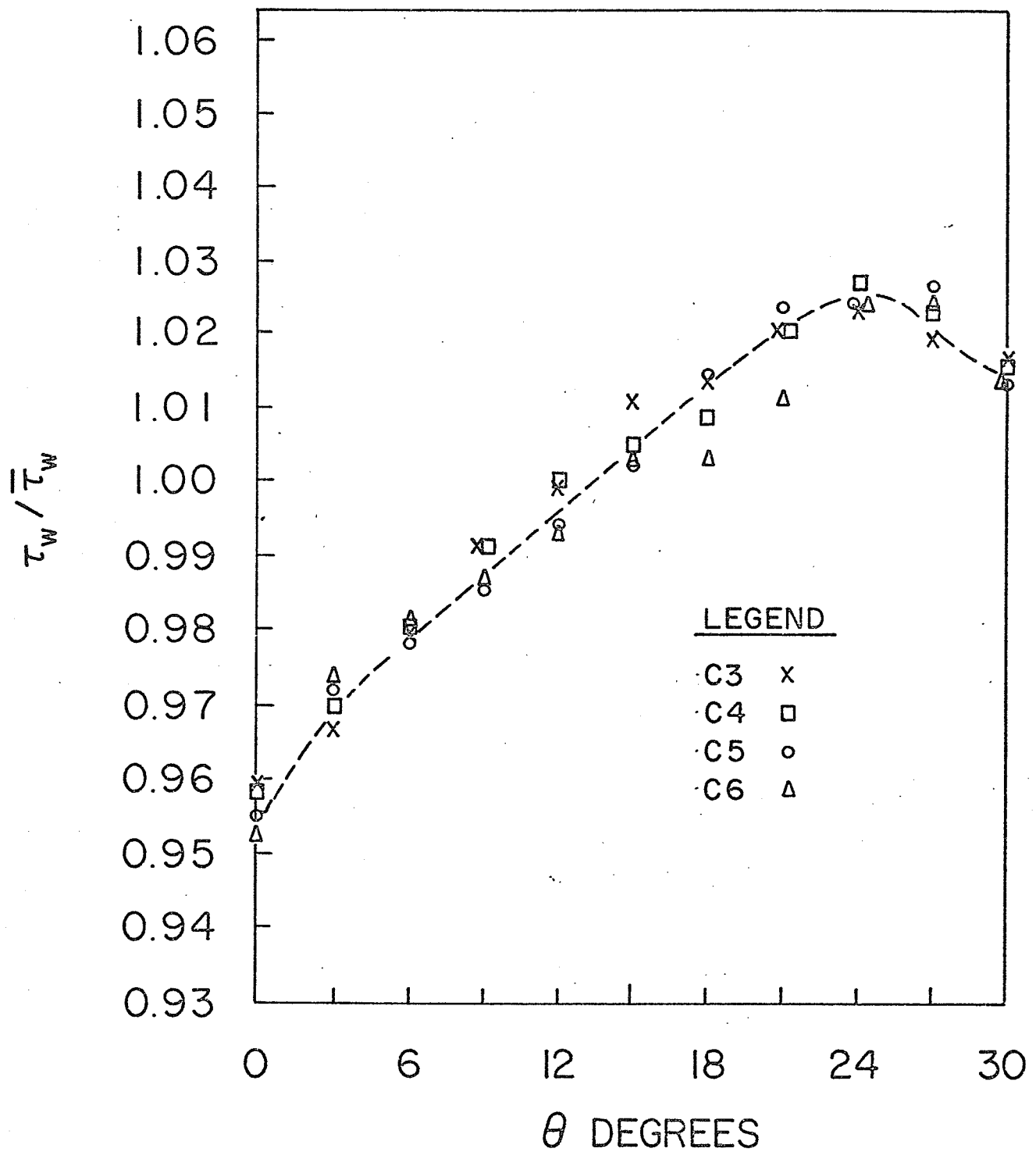


FIG.25 LOCAL WALL SHEAR STRESS VARIATIONS  
P/D = 1.20

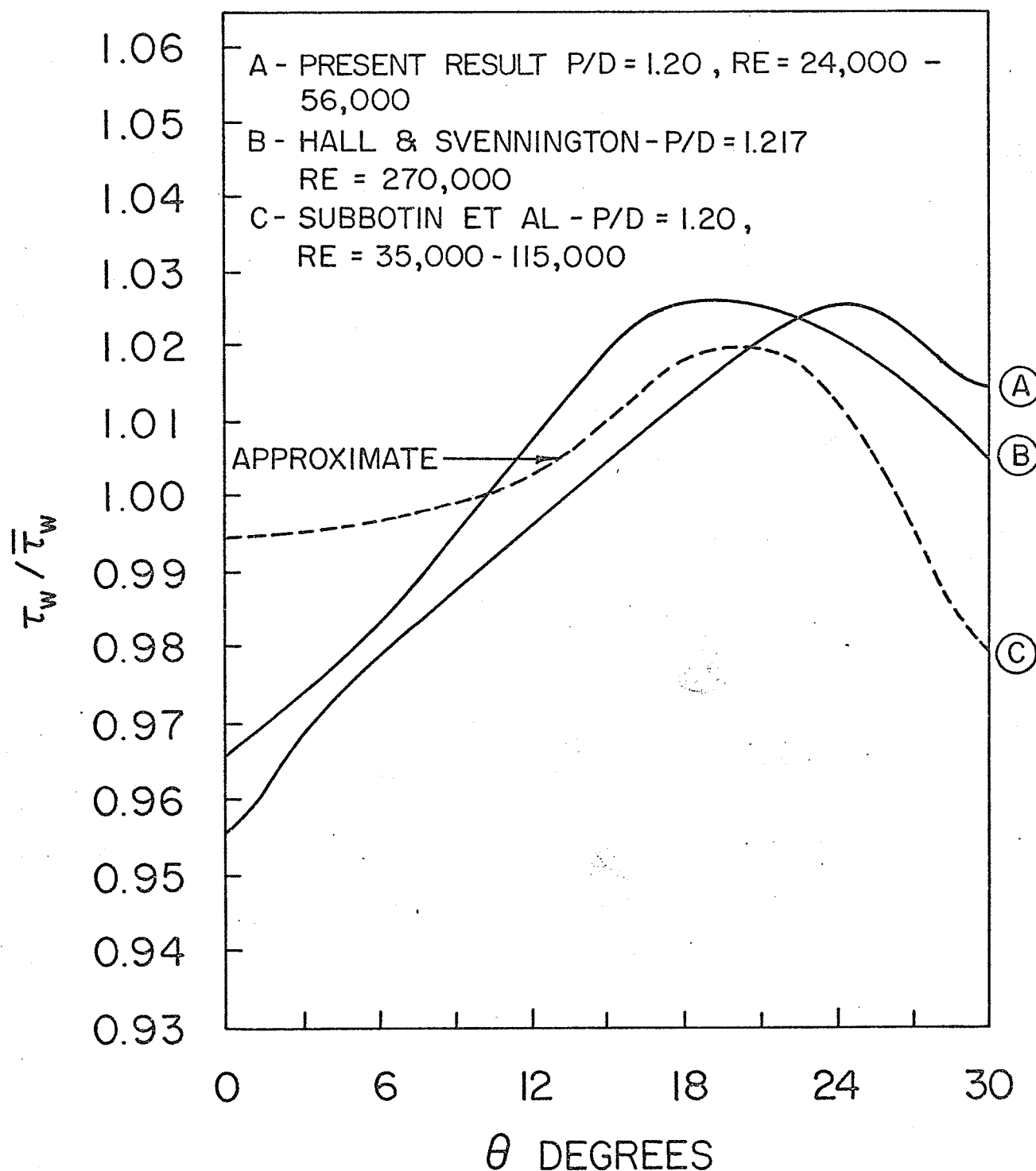


FIG.26 COMPARISON OF WALL SHEAR STRESS DISTRIBUTATION WITH OTHER STUDIES

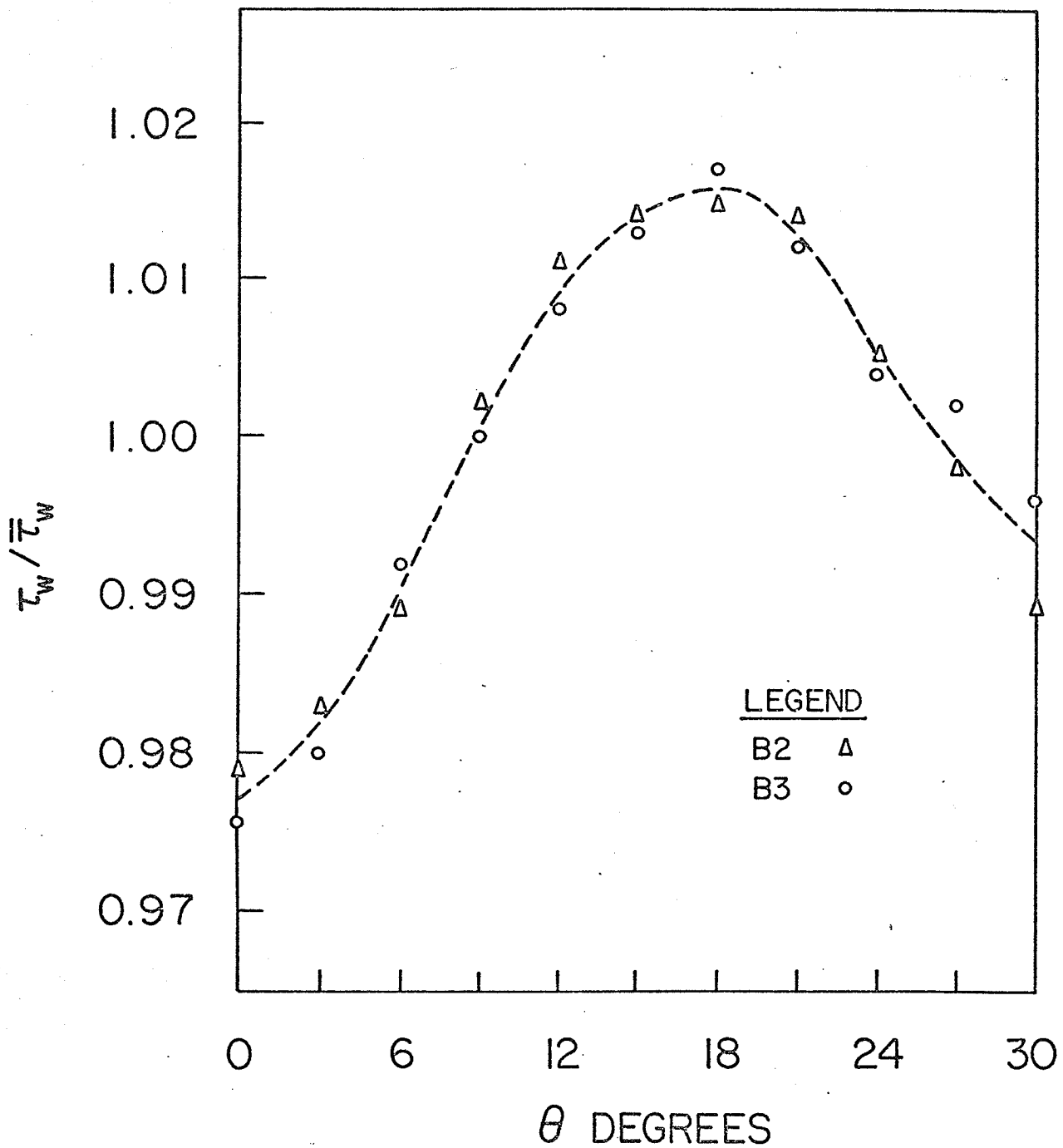


FIG. 27 LOCAL WALL SHEAR STRESS VARIATIONS  
P/D = 1.35

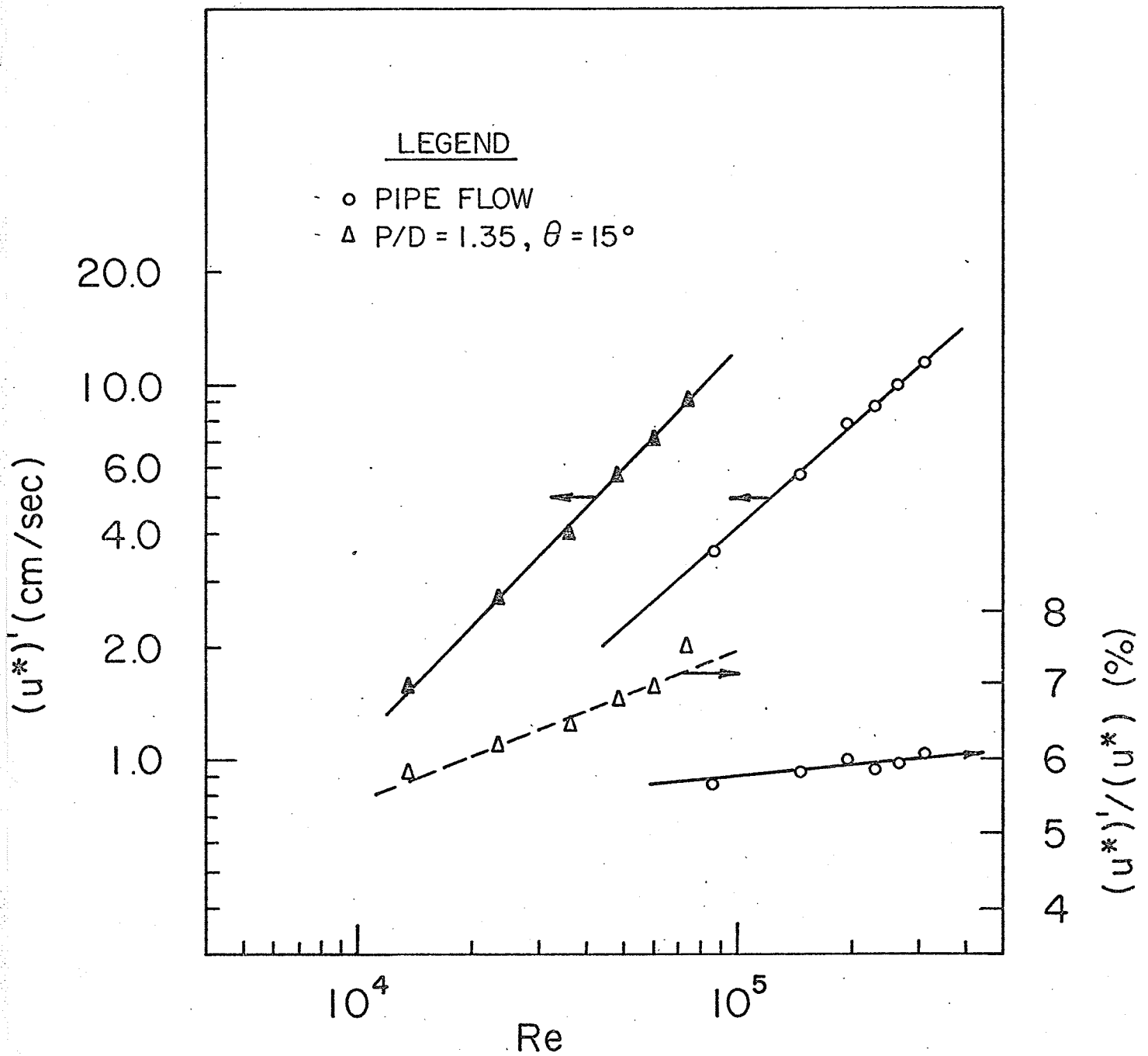


FIG. 28 WALL SHEAR STRESS FLUCTUATIONS

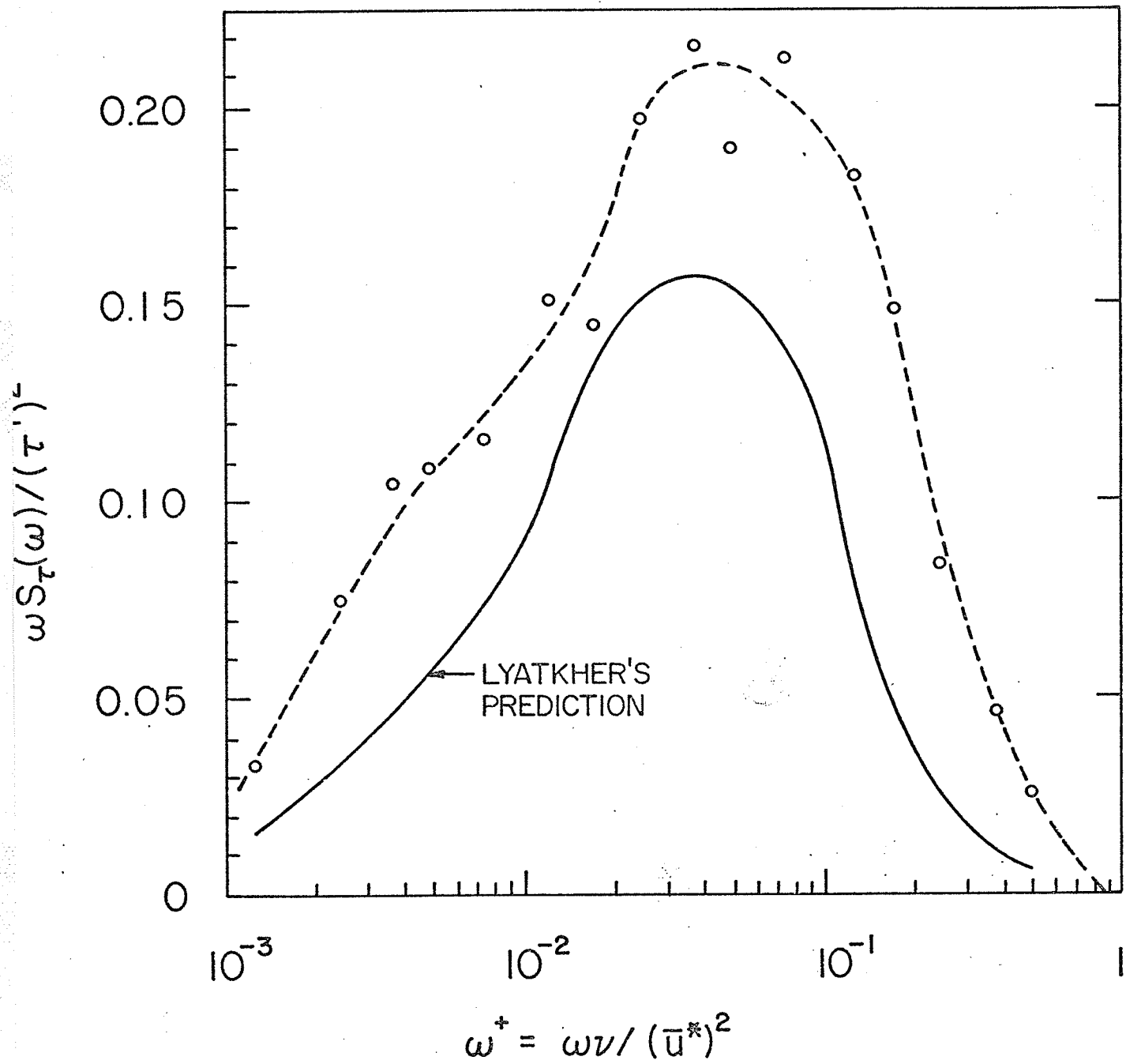


FIG. 29 NORMALIZED SPECTRUM OF WALL SHEAR STRESS FOR PIPE FLOW ( $Re = 86,000$ )

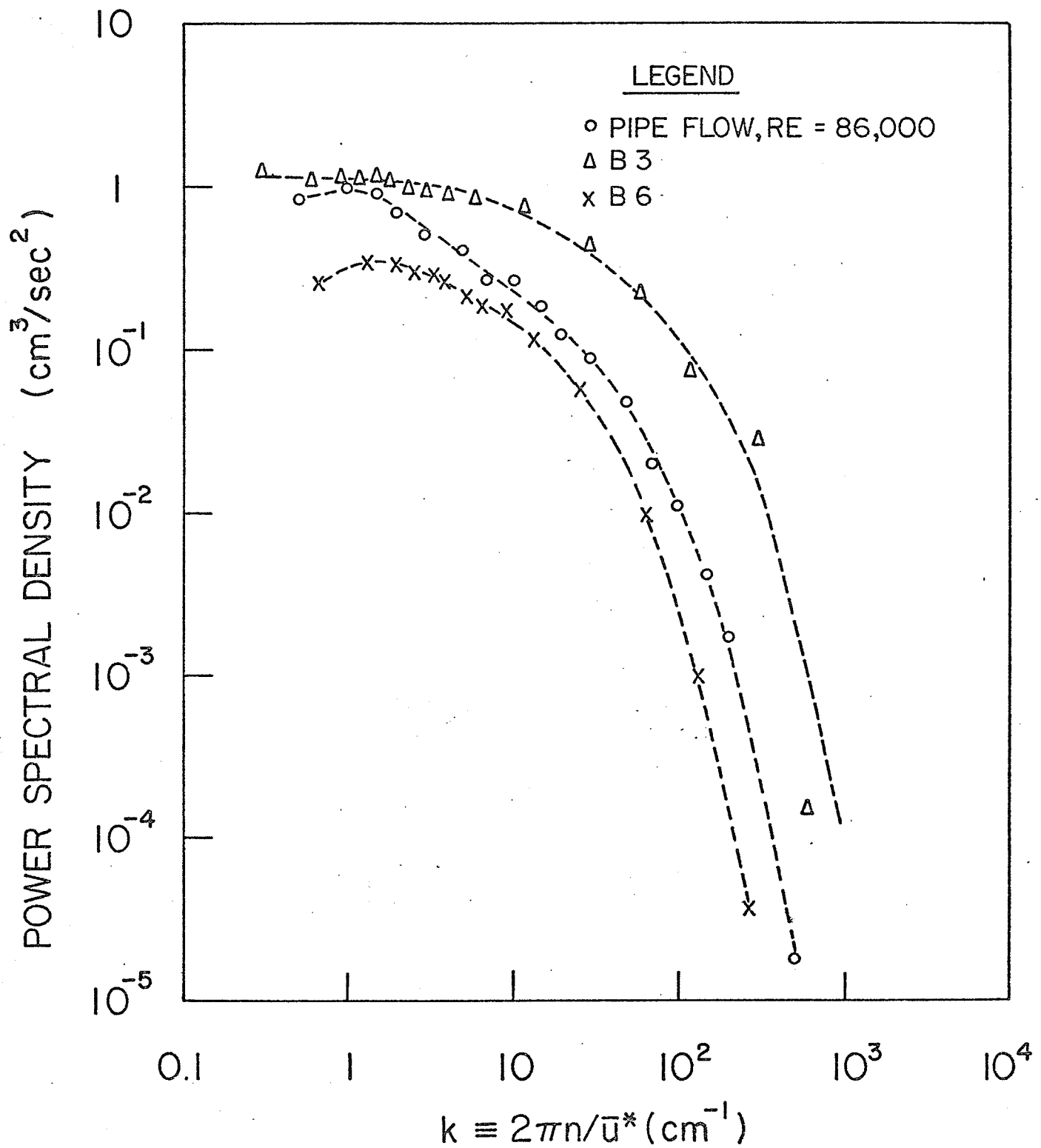
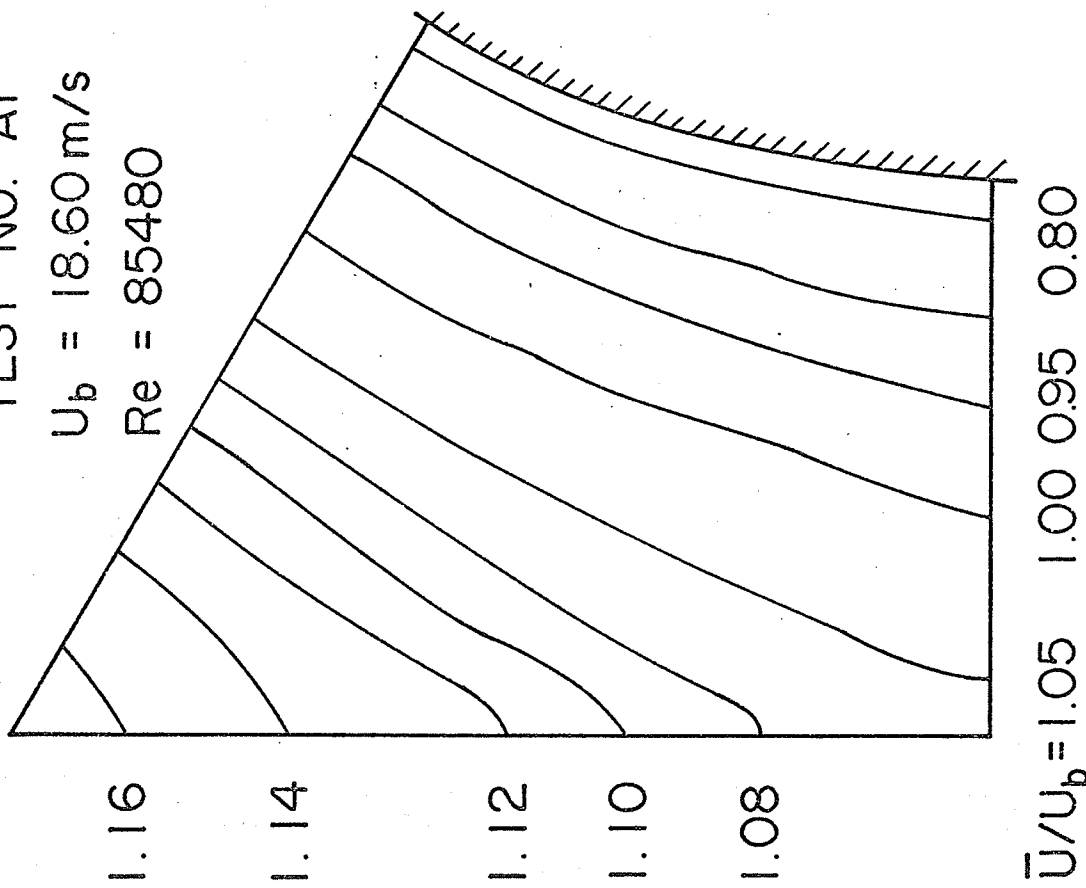
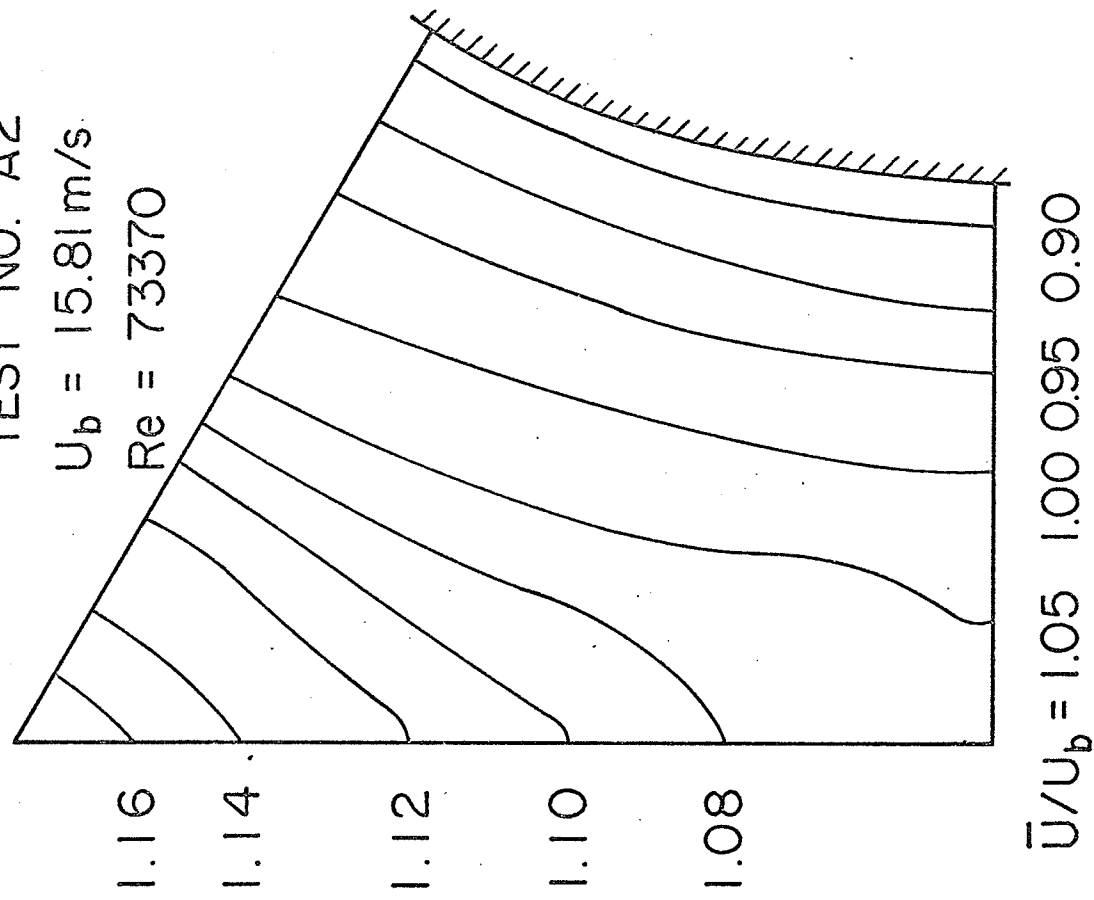


FIG.30 WALL SHEAR STRESS POWER SPECTRA

TEST NO. A1

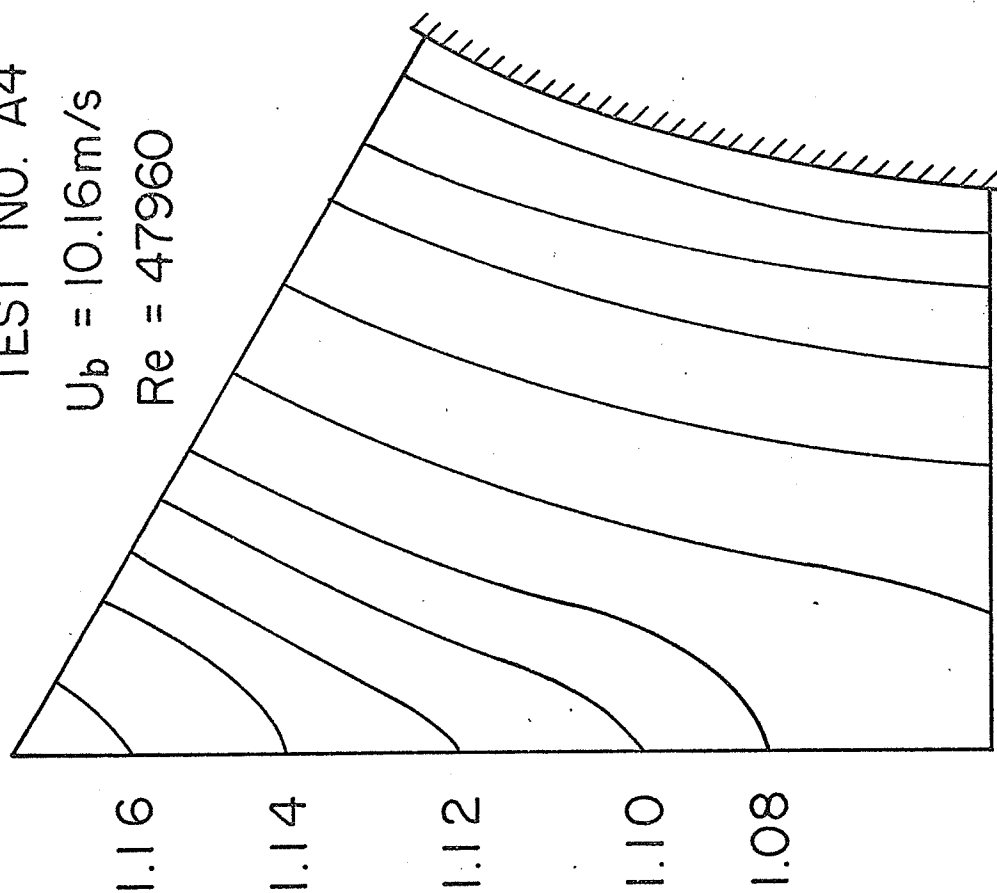
 $U_b = 18.60 \text{ m/s}$  $Re = 85480$ 

TEST NO. A2

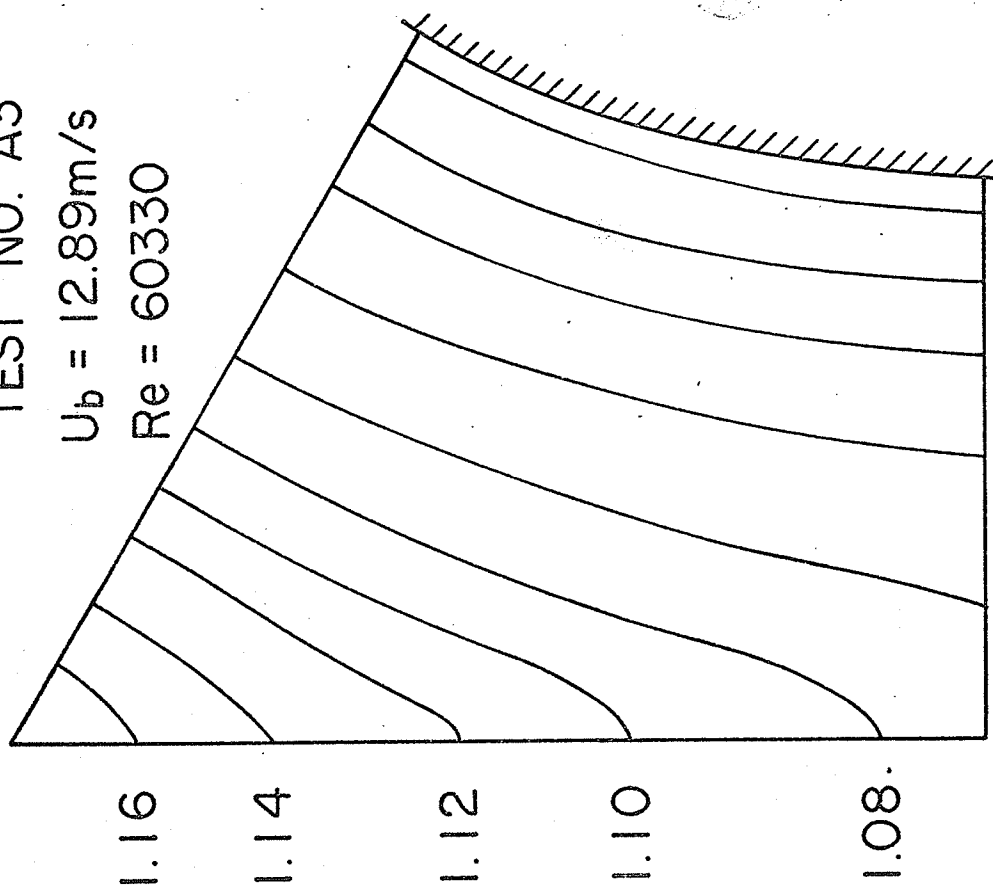
 $U_b = 15.81 \text{ m/s}$  $Re = 73370$ FIG.31a ISOVEL PLOT -  $P/D = 1.50$



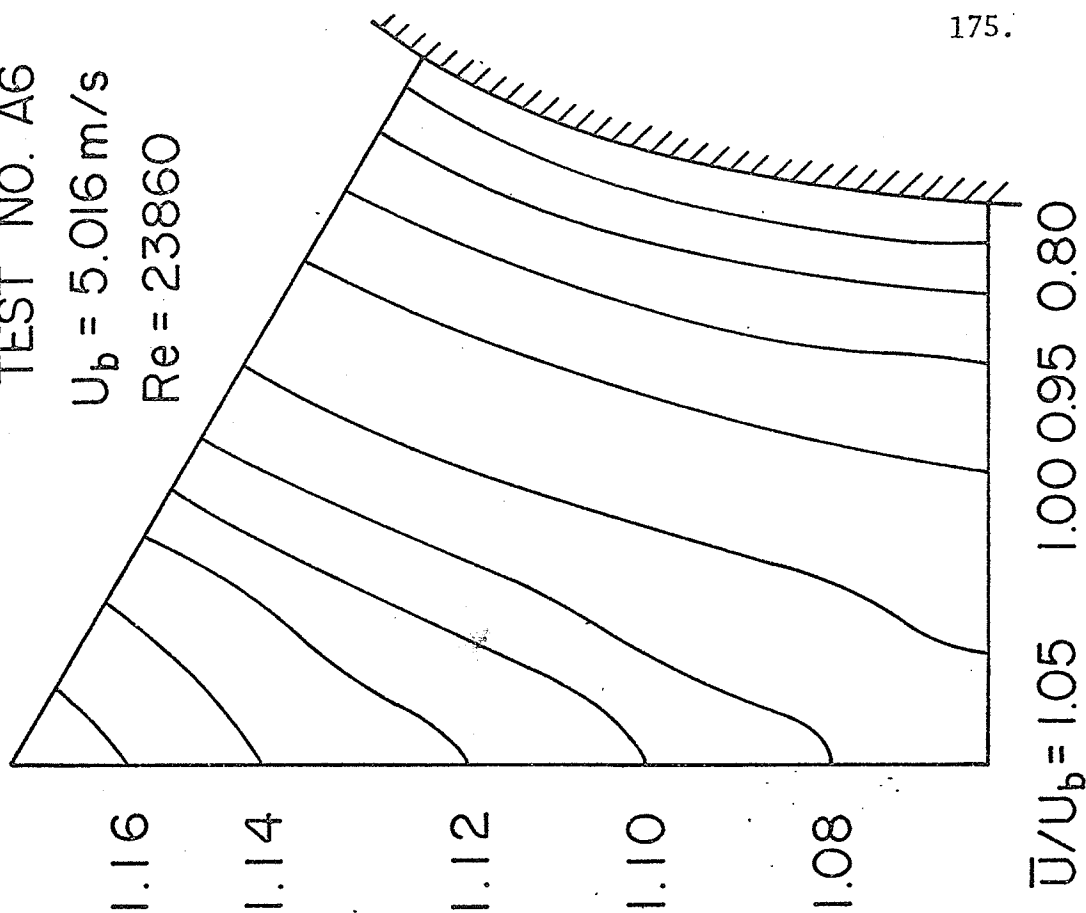
TEST NO. A4

 $U_b = 10.16 \text{ m/s}$  $Re = 47960$  $\bar{U}/U_b = 1.05 \quad 1.00 \quad 0.95 \quad 0.80$ 

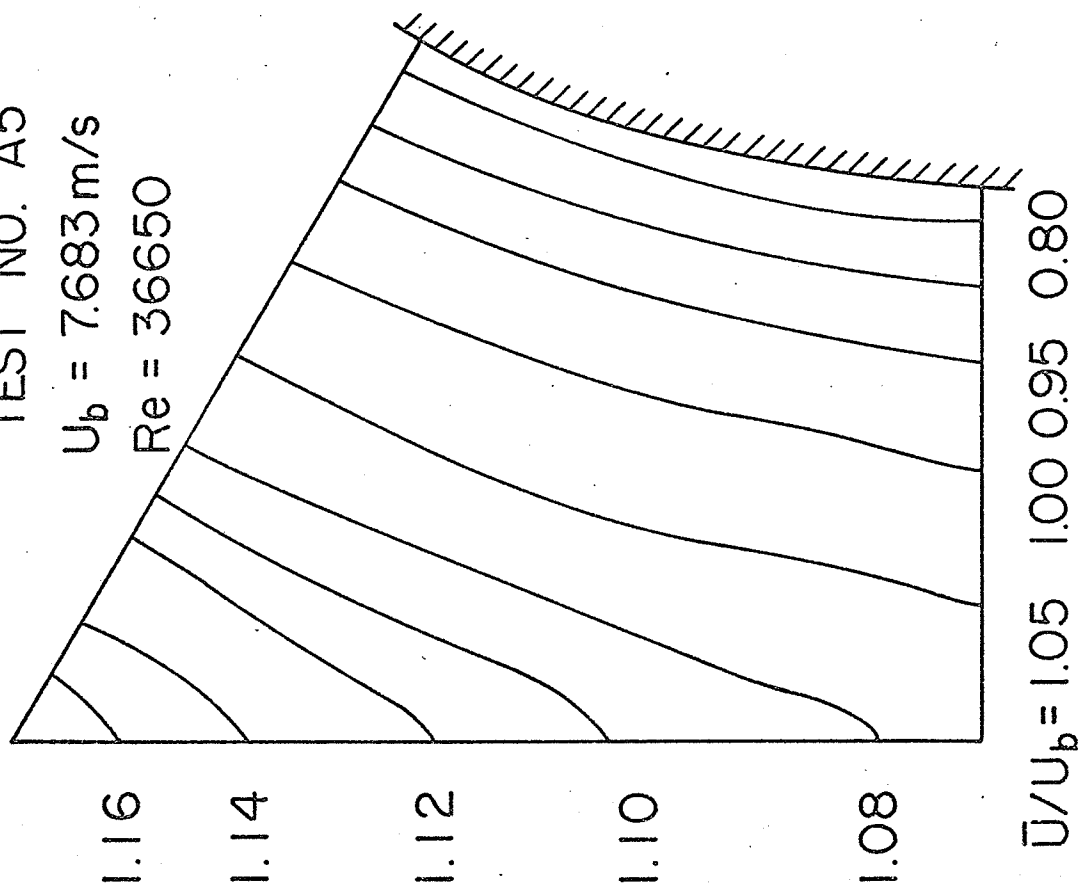
TEST NO. A3

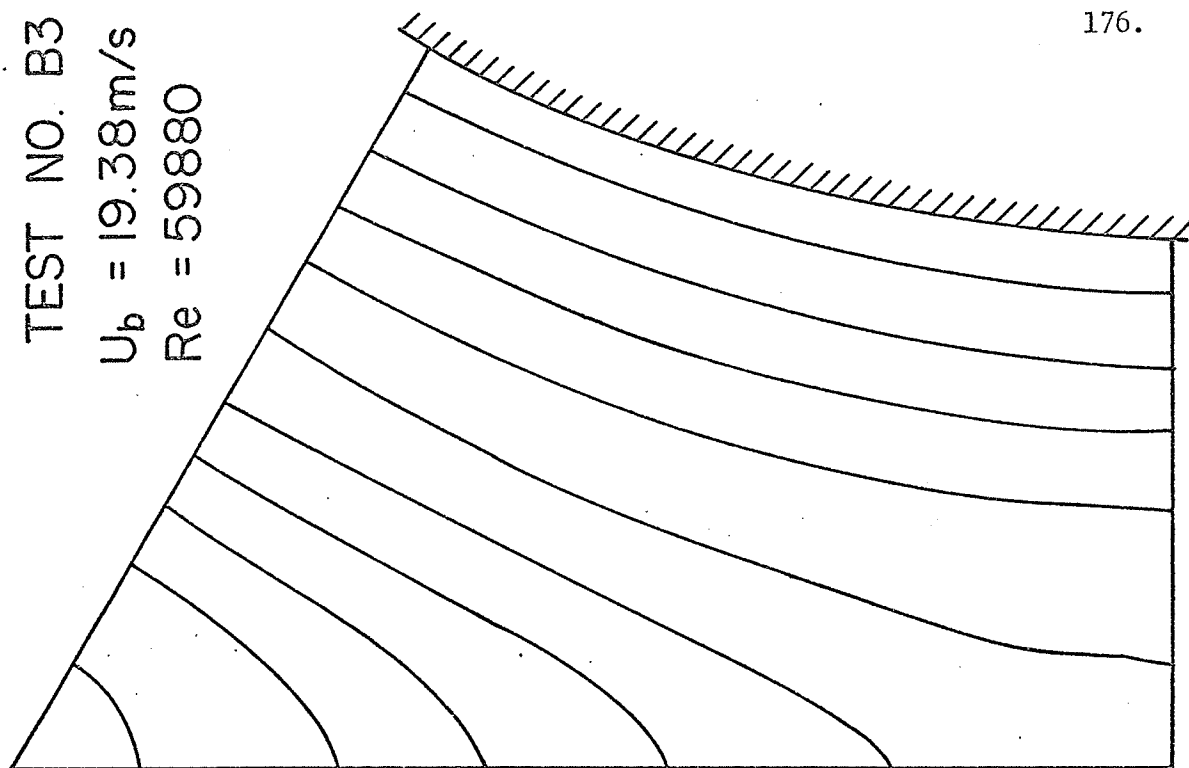
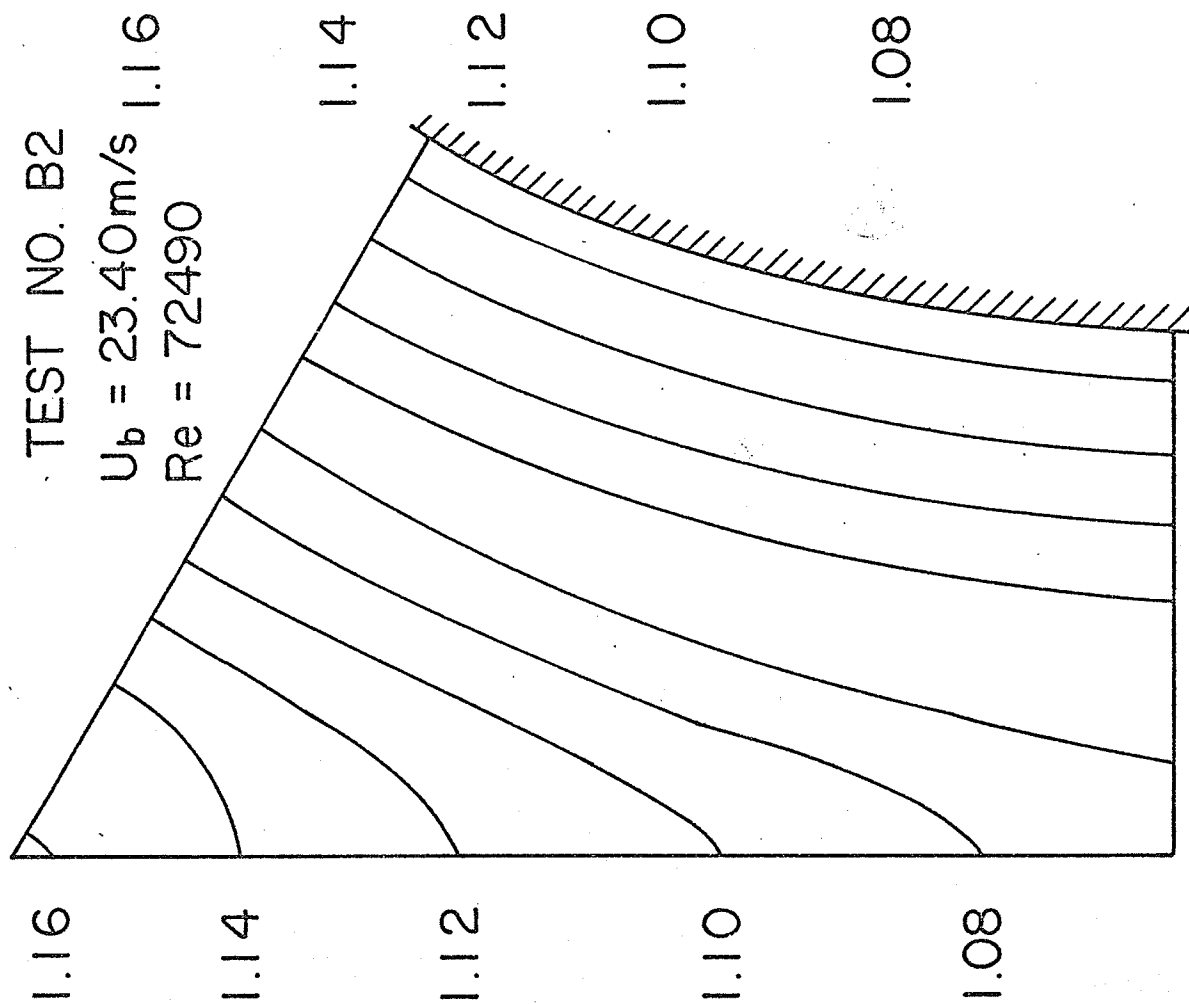
 $U_b = 12.89 \text{ m/s}$  $Re = 60330$  $\bar{U}/U_b = 1.05 \quad 1.00 \quad 0.95 \quad 0.80$ FIG. 3b ISOVEL PLOTS -  $P/D = 1.50$

TEST NO. A6

 $U_b = 5.016 \text{ m/s}$  $Re = 23860$ 

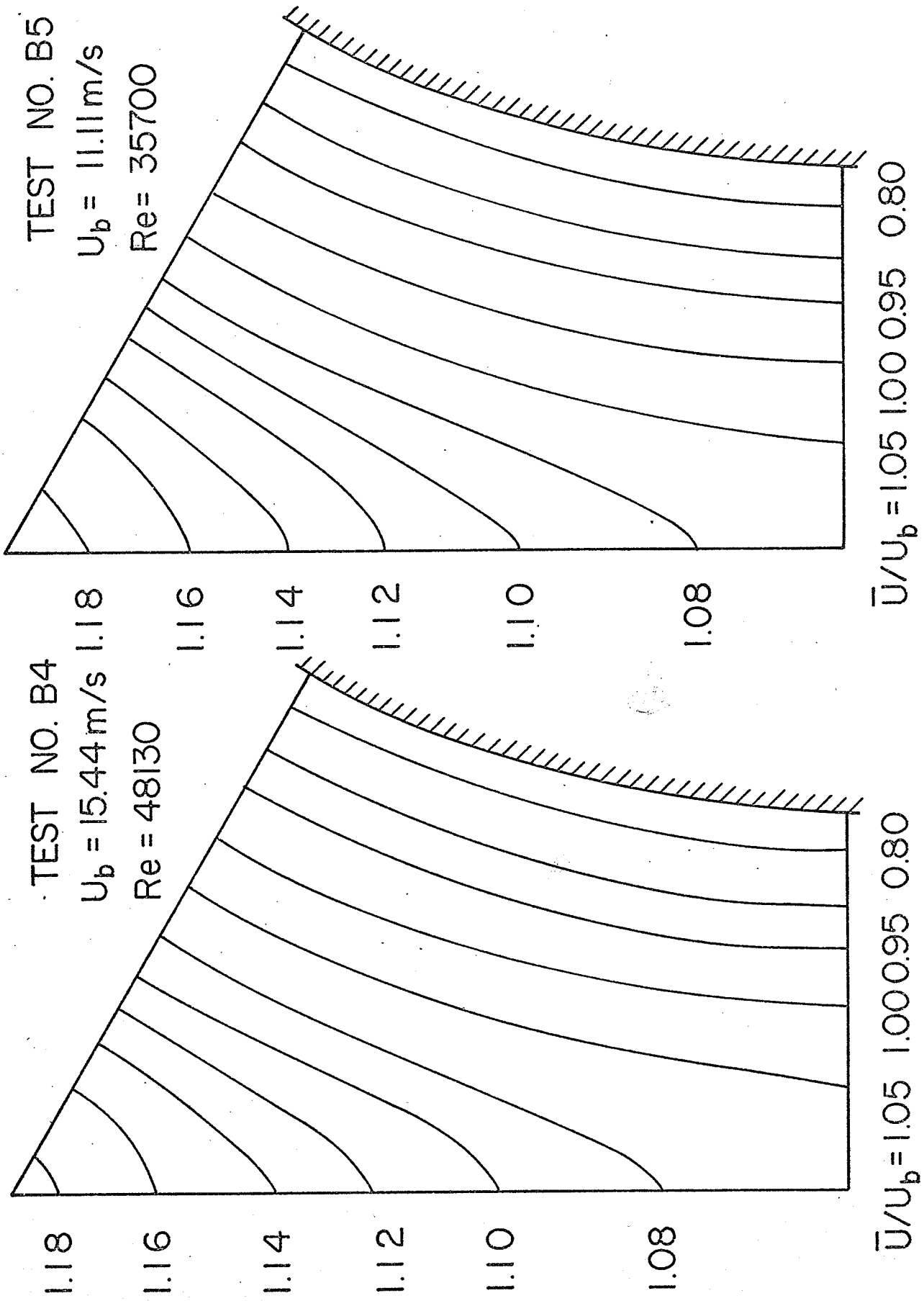
TEST NO. A5

 $U_b = 7.683 \text{ m/s}$  $Re = 36650$ FIG.31c ISOVEL PLOTS -  $P/D = 1.50$



$\bar{U}/U_b = 1.05$  1.00 0.95 0.80  $\bar{U}/U_b = 1.05$  1.00 0.95 0.80

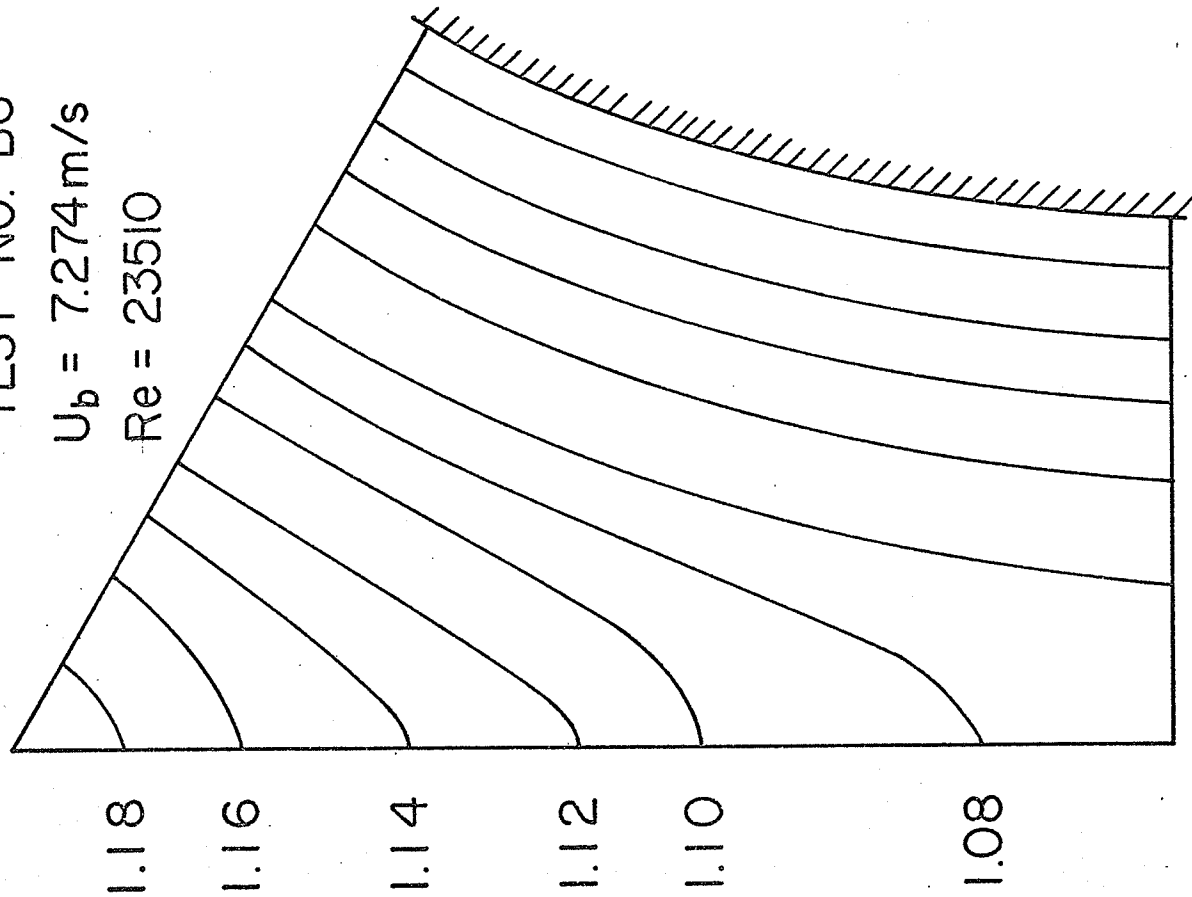
FIG.32aISOVEL PLOTS -  $P/D = 1.35$

FIG. 32b ISOVEL PLOTS -  $P/D = 1.35$

TEST NO. B6

$U_b = 7.274 \text{ m/s}$

$Re = 23510$

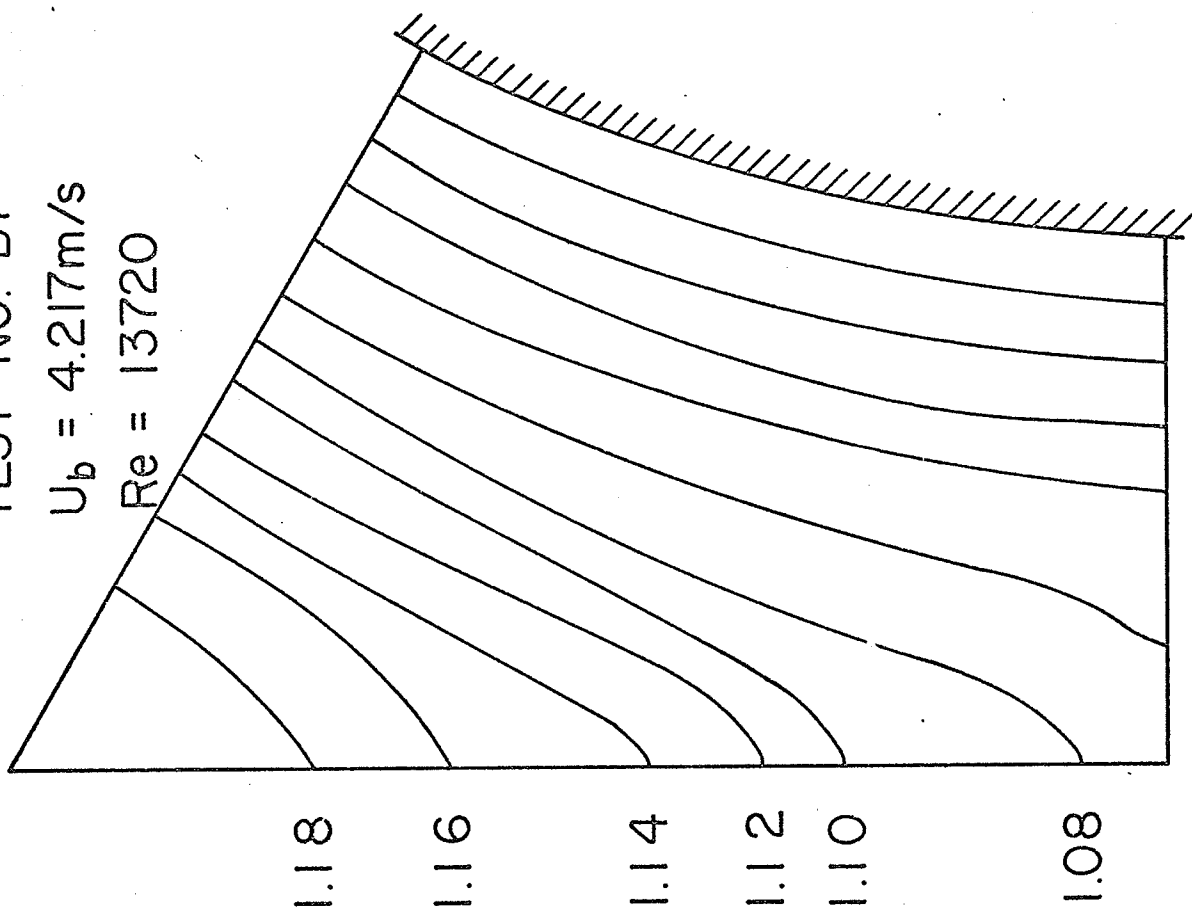


$\bar{U}/U_b = 1.05 \quad 1.00 \quad 0.95 \quad 0.80$

TEST NO. B7

$U_b = 4.217 \text{ m/s}$

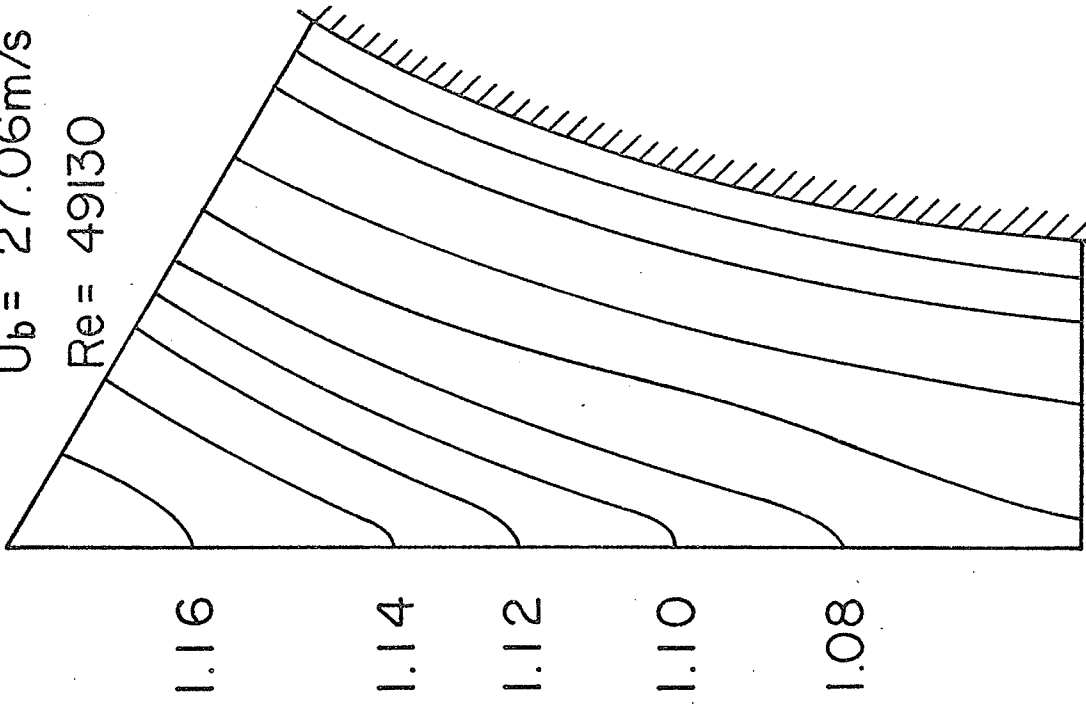
$Re = 13720$



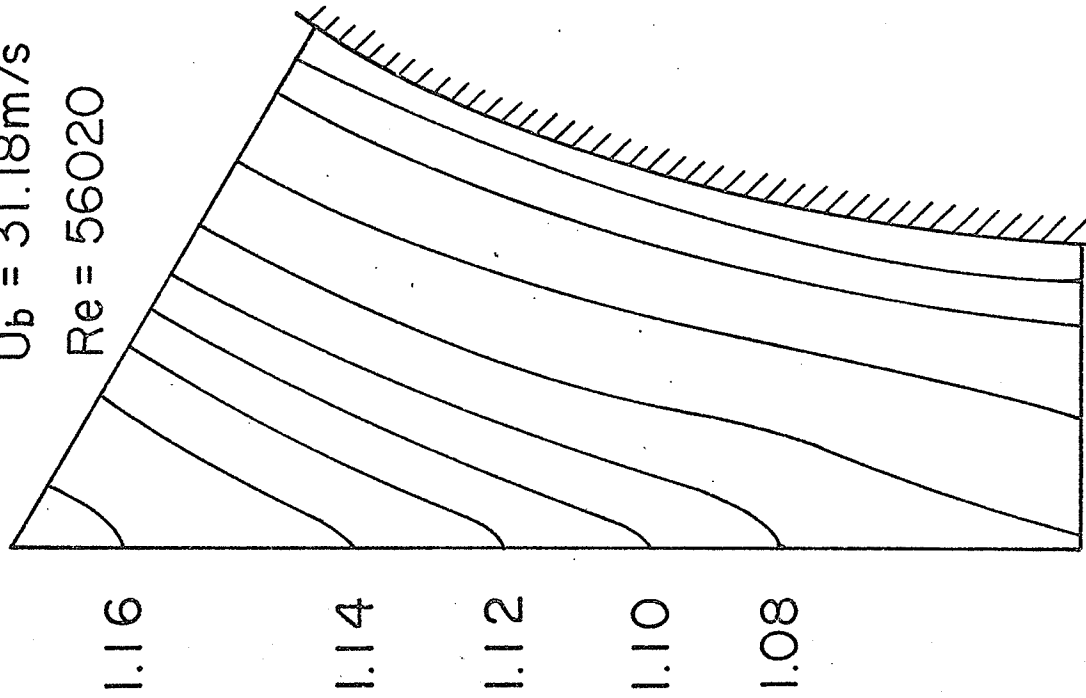
$\bar{U}/U_b = 1.05 \quad 1.00 \quad 0.95 \quad 0.80$

FIG32c ISOVEL PLOTS -  $P/D = 1.35$

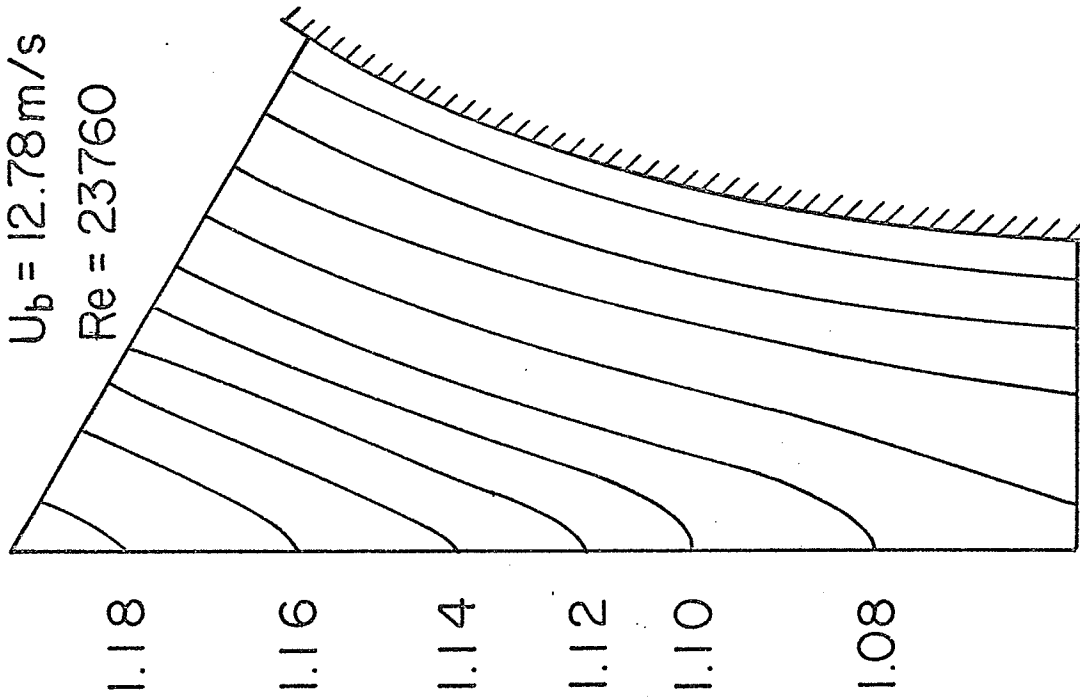
TEST NO. C4

 $U_b = 27.06 \text{ m/s}$   
 $Re = 49130$ 

 $\bar{U}/U_b = 1.05 \ 1.00 \ 0.90 \ 0.80$ 

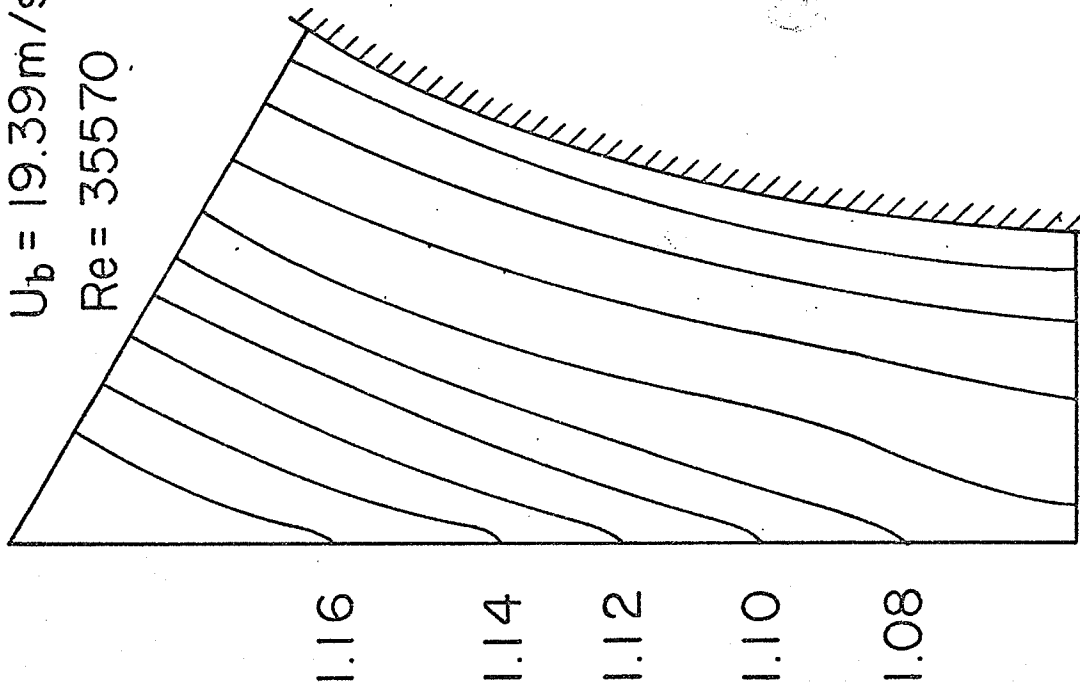
TEST NO. C3

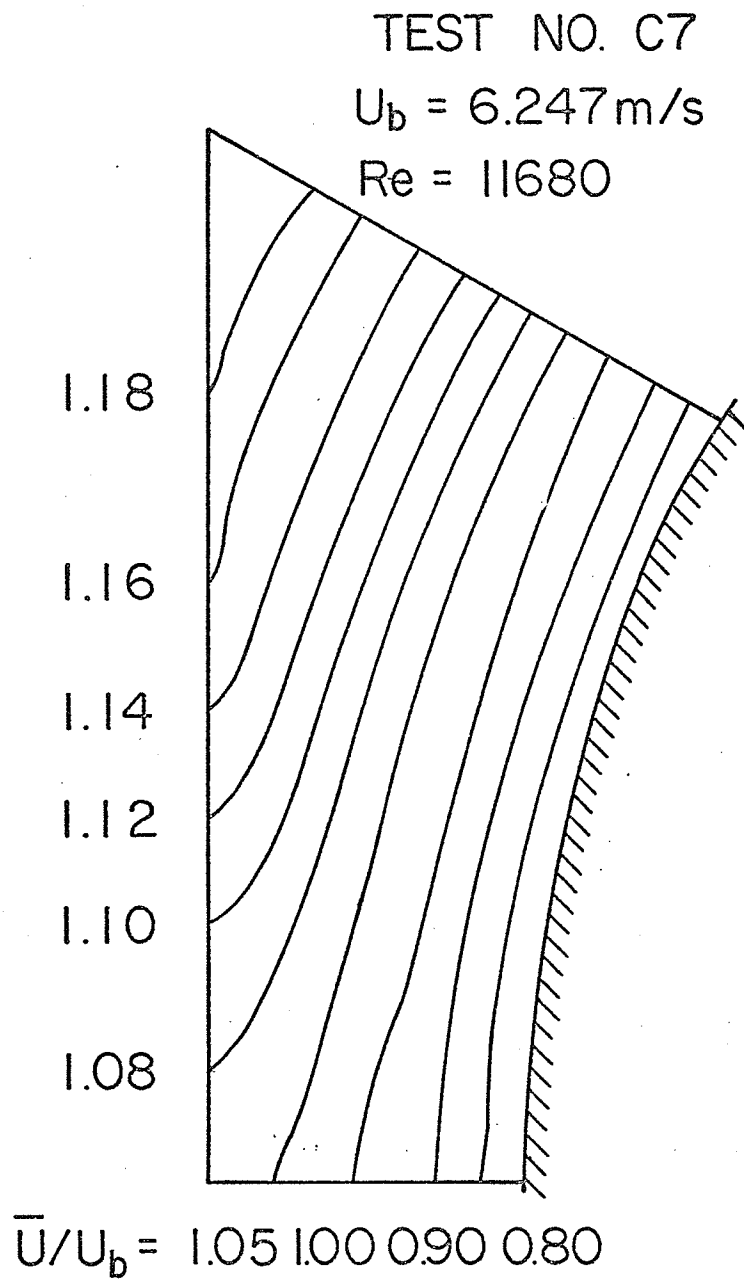
 $U_b = 31.18 \text{ m/s}$   
 $Re = 56020$ 

 $\bar{U}/U_b = 1.05 \ 1.00 \ 0.90 \ 0.80$ 
FIG33a ISOVEL PLOTS -  $P/D = 1.20$

TEST NO. C6

 $U_b = 12.78 \text{ m/s}$  $Re = 23760$  $\bar{U}/U_b = 1.05 \ 1.00 \ 0.90 \ 0.80$ 

TEST NO. C5

 $U_b = 19.39 \text{ m/s}$  $Re = 35570$  $\bar{U}/U_b = 1.05 \ 1.00 \ 0.90 \ 0.80$ FIG33b ISOVEL PLOTS -  $P/D = 1.20$

FIG33cISOVEL PLOT -  $P/D = 1.20$



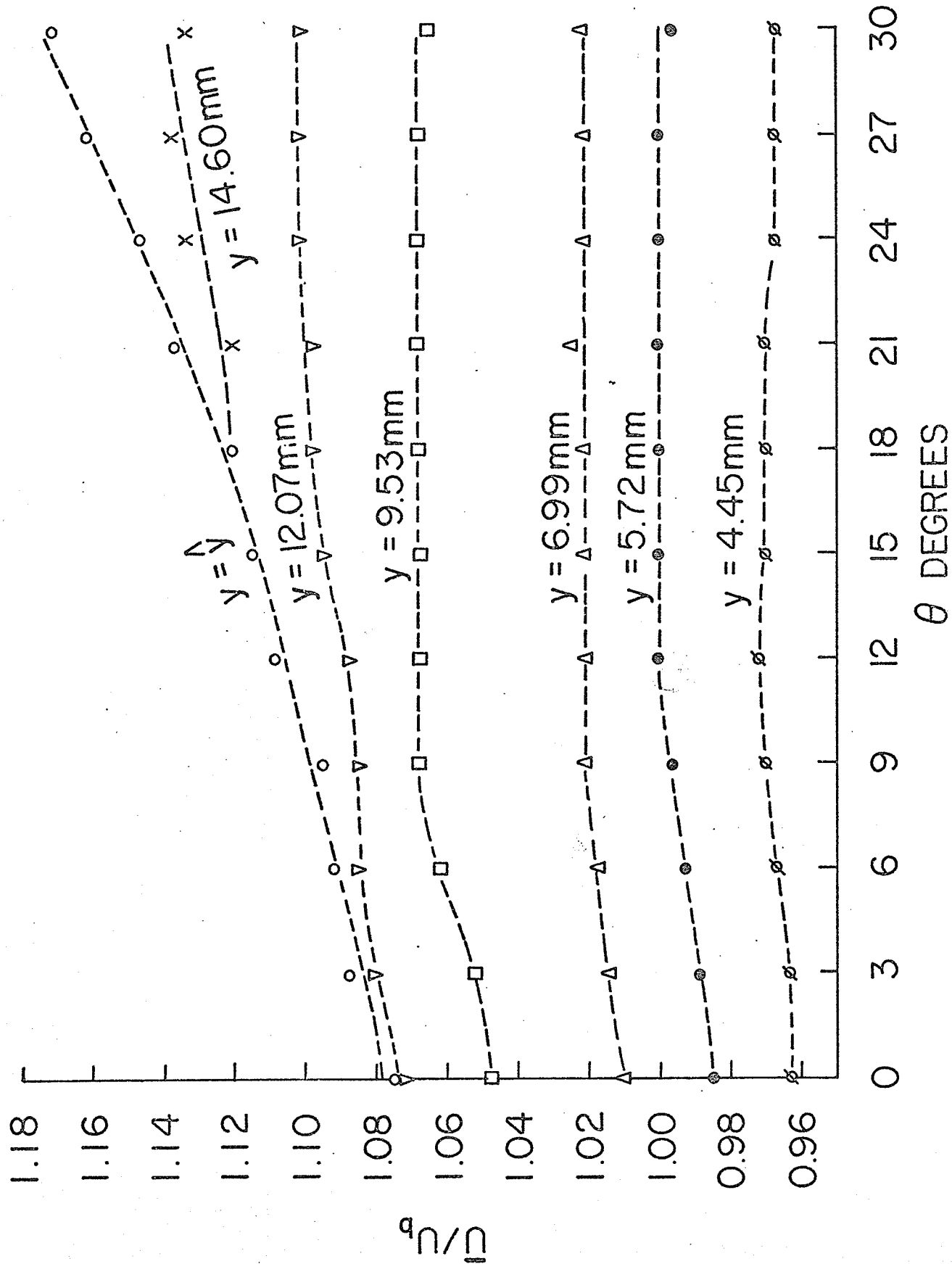


FIG34a DISTRIBUTIONS OF MEAN AXIAL VELOCITY IN THE PERIPHERAL  
DIRECTION  $P/D = 1.50$ , TEST A5

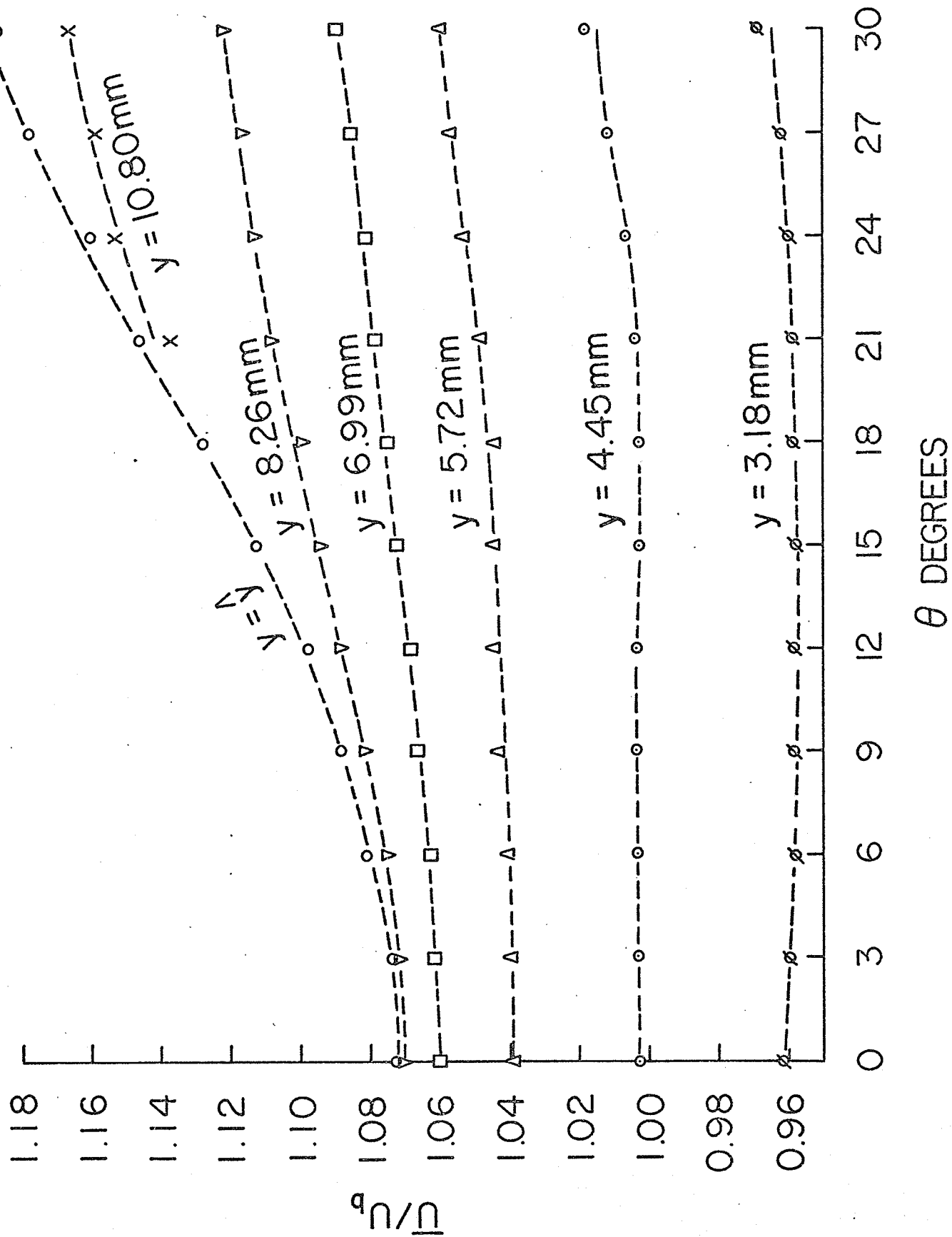


FIG34b DISTRIBUTIONS OF MEAN AXIAL VELOCITY IN THE PERIPHERAL  
DIRECTION  $P/D = 1.35$ , TEST B5

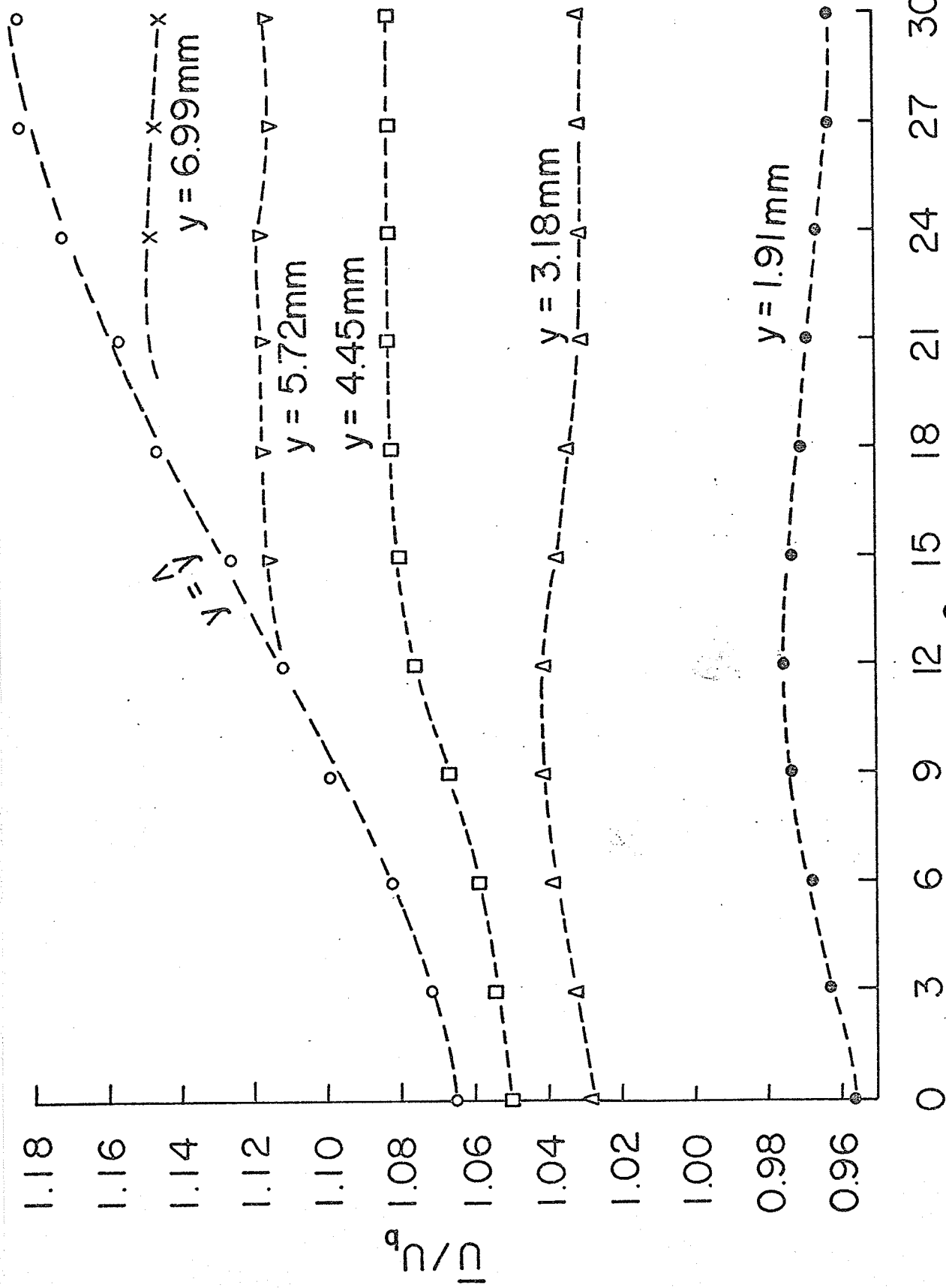


FIG.34c DISTRIBUTIONS OF MEAN AXIAL VELOCITY IN THE PERIPHERAL DIRECTION  $P/D = 1.20$ , TEST C5

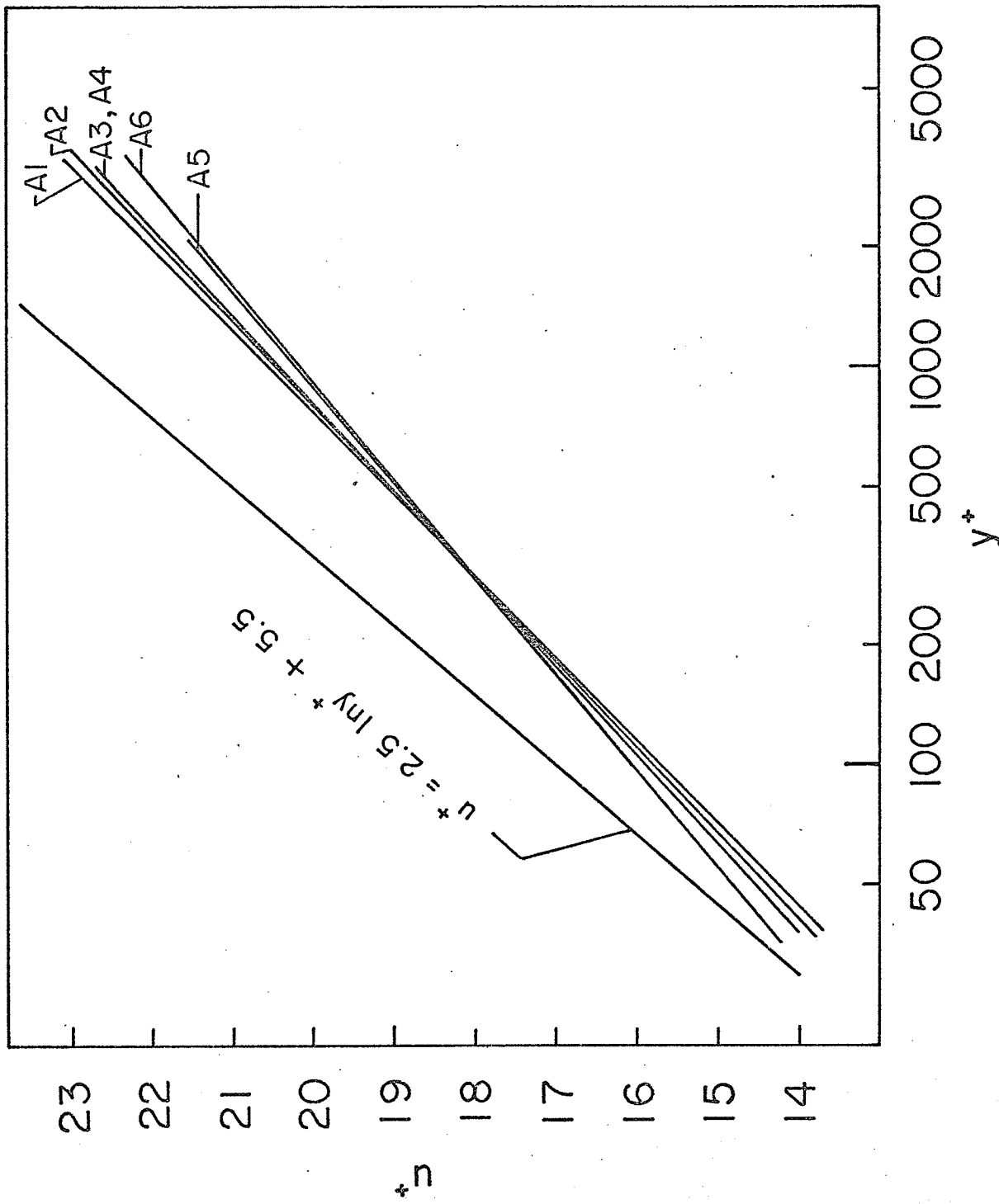


FIG.35 LEAST-SQUARES-FIT LINES -  $P/D = 1.50$  - ALL TESTS  
 $RE = 24,000$  TO  $84,000$

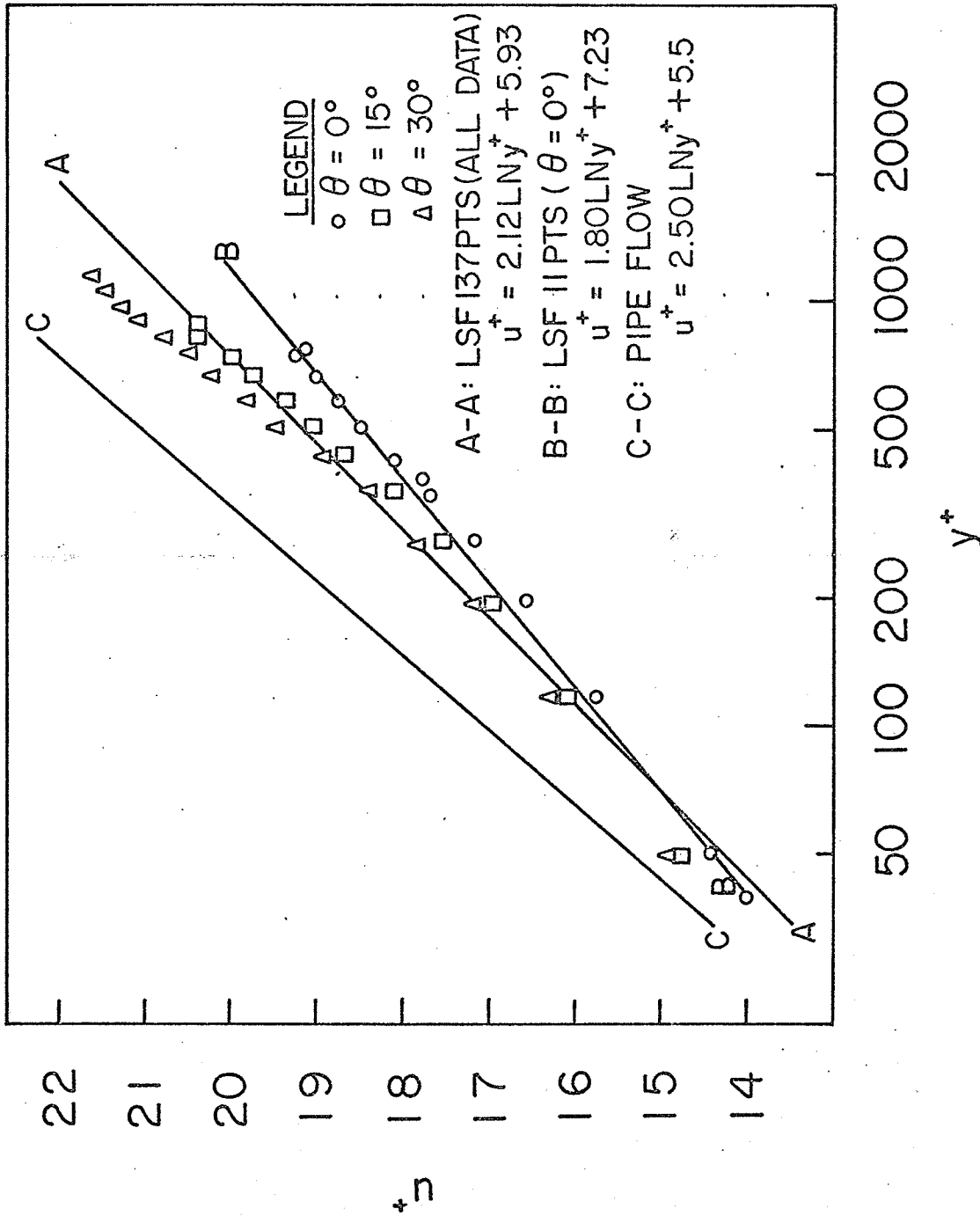


FIG.36 DISTRIBUTION OF MEAN AXIAL VELOCITY IN THE RADIAL DIRECTION -  $P/D \approx 1.50$ , TEST A1

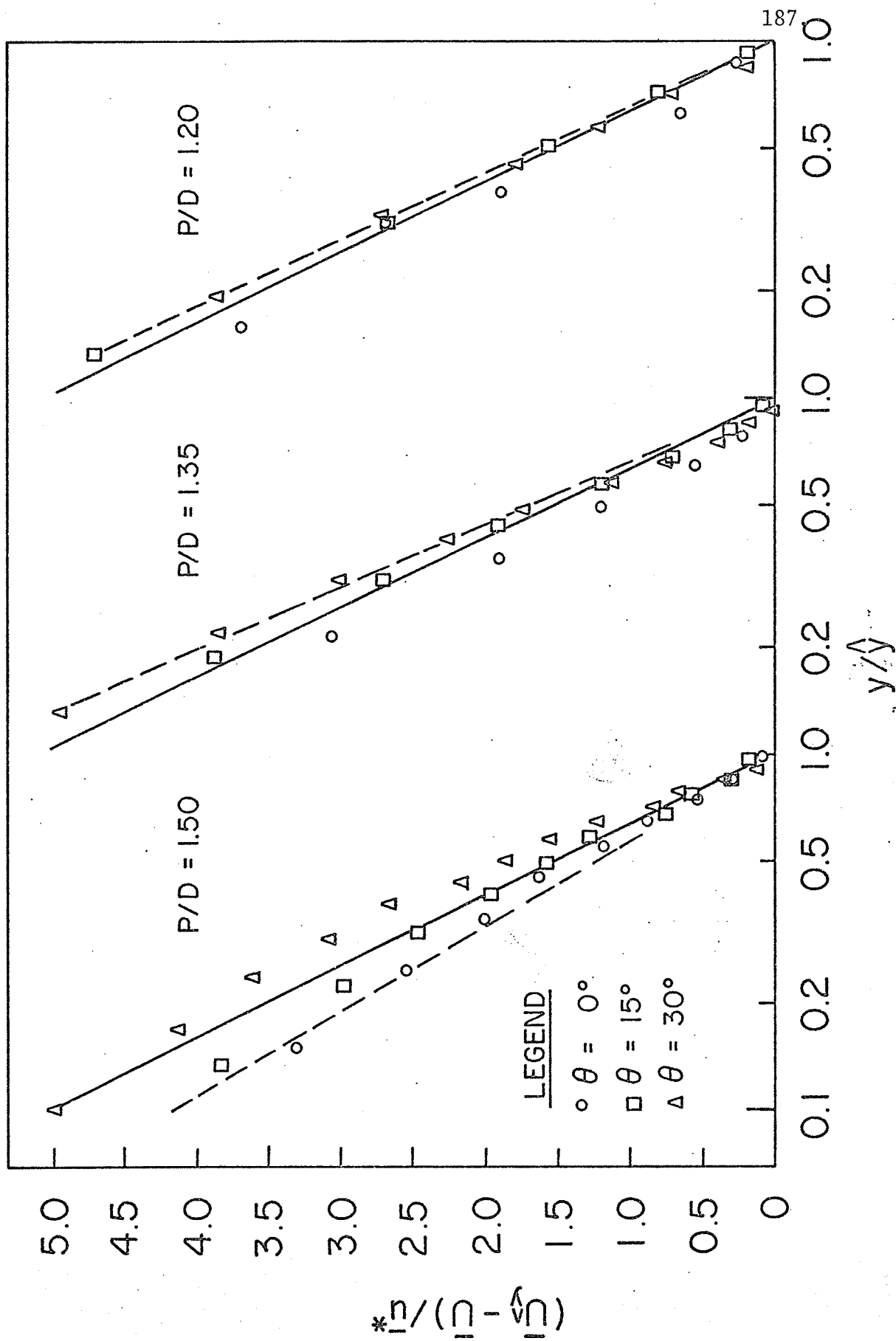


FIG.37 VELOCITY DEFECT PLOTS-TEST COND. 5 -  $Re = 36,000$

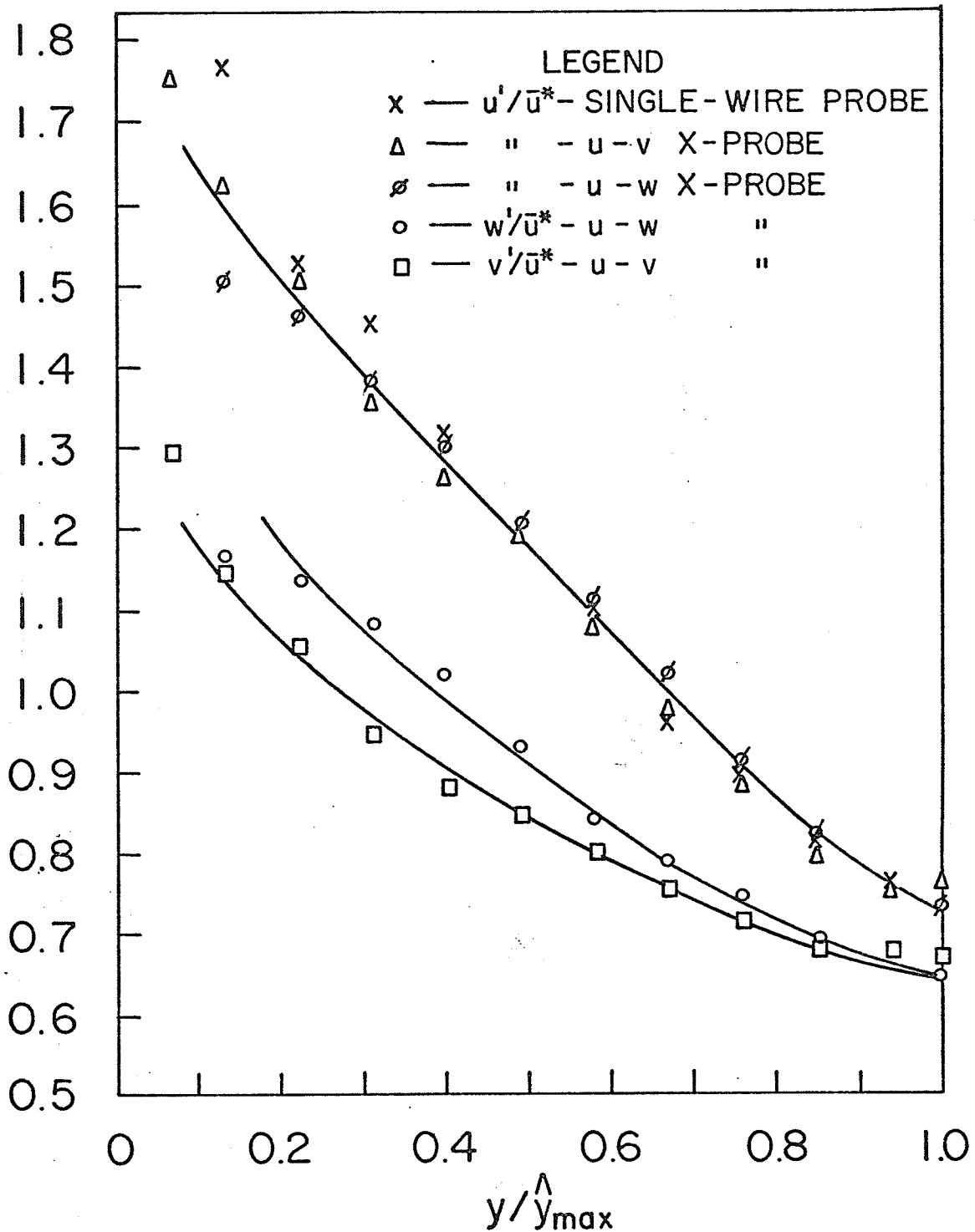


FIG. 38 TURBULENCE INTENSITIES MEASURED BY DIFFERENT PROBES ,  $P/D = 1.35$  , TEST B4  $\theta = 30^\circ$

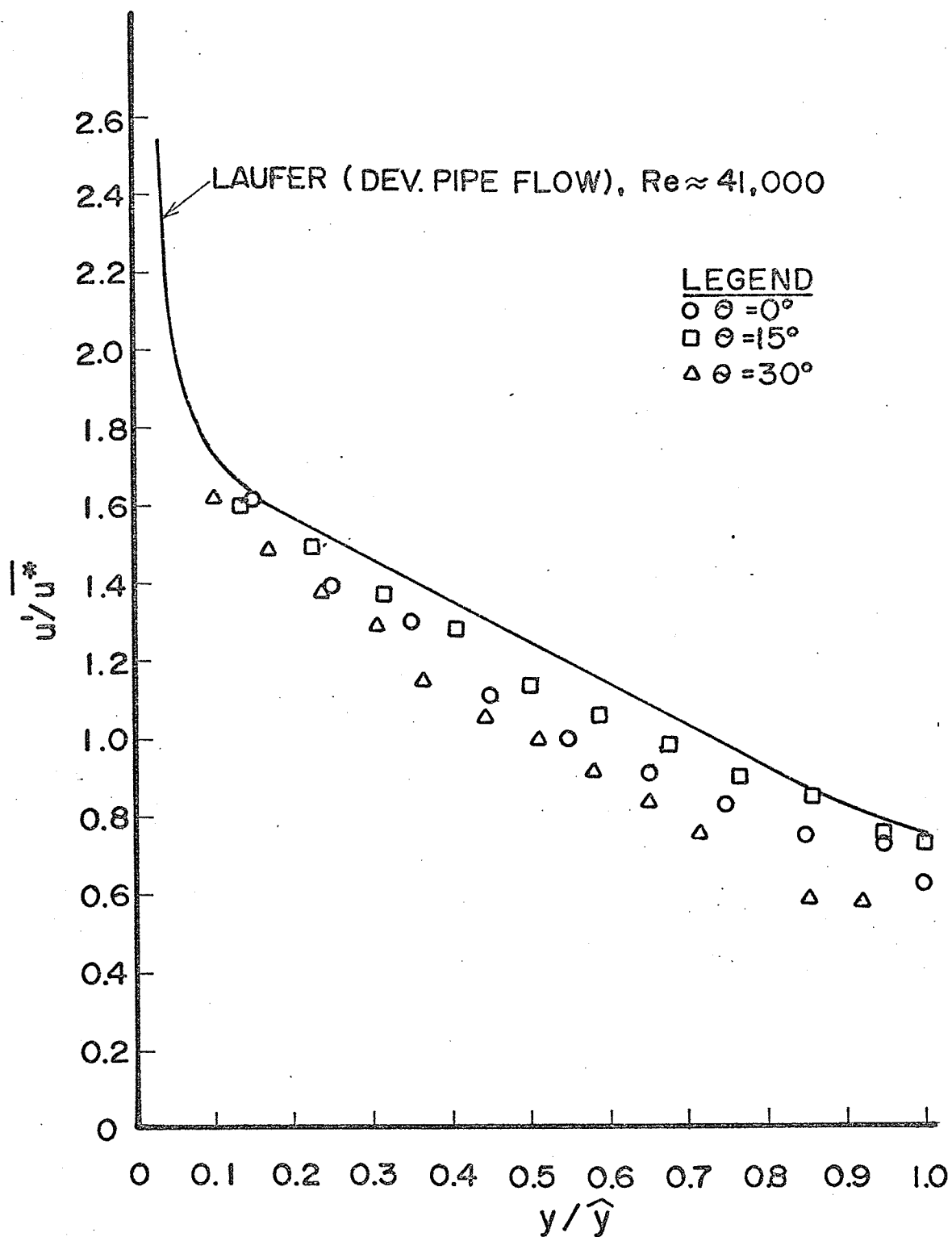


FIG39a AXIAL TURBULENCE DISTRIBUTION  
Test 2,  $P/D = 1.50$



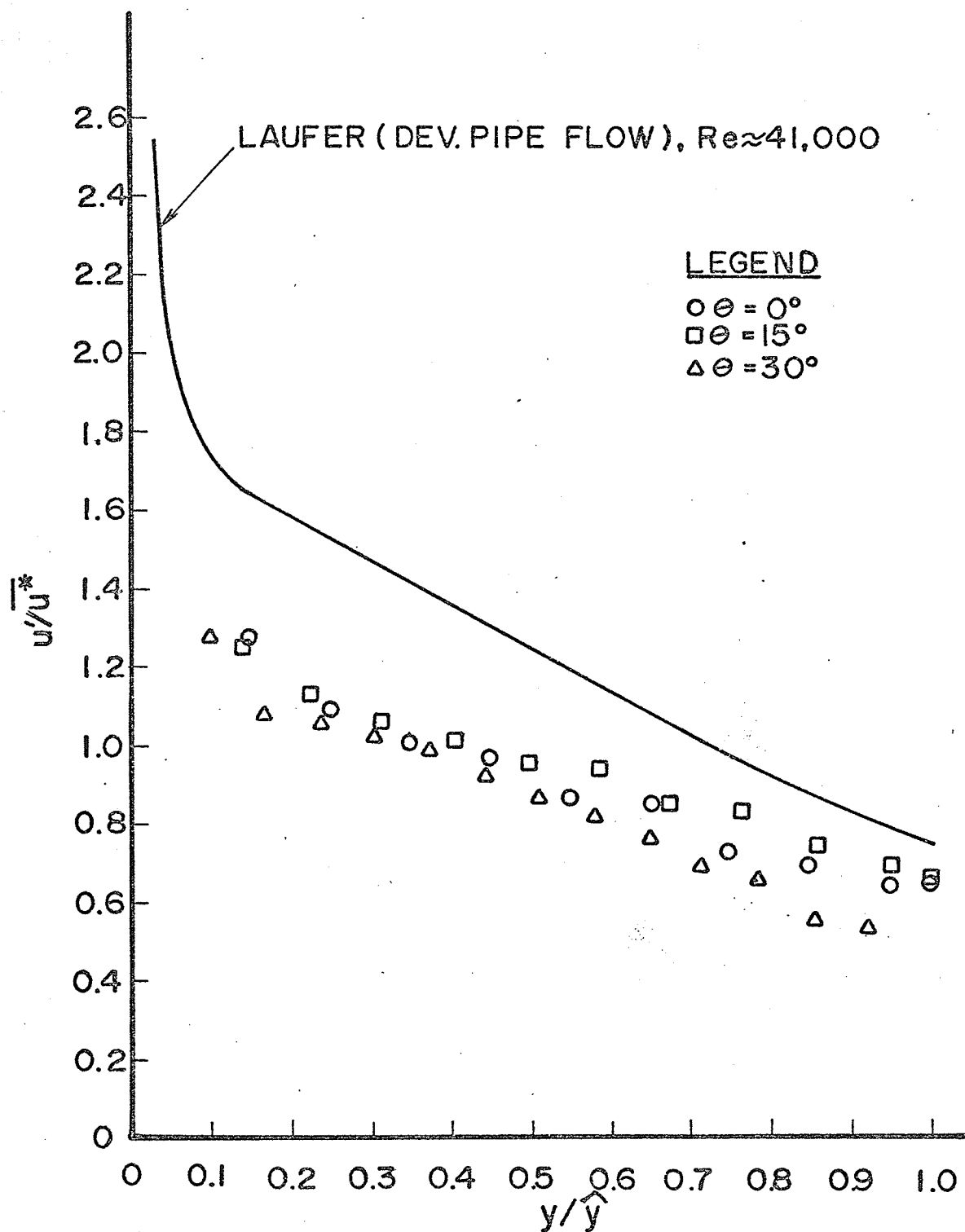


FIG39bAXIAL TURBULENCE DISTRIBUTION

Test 5,  $P/D=1.50$

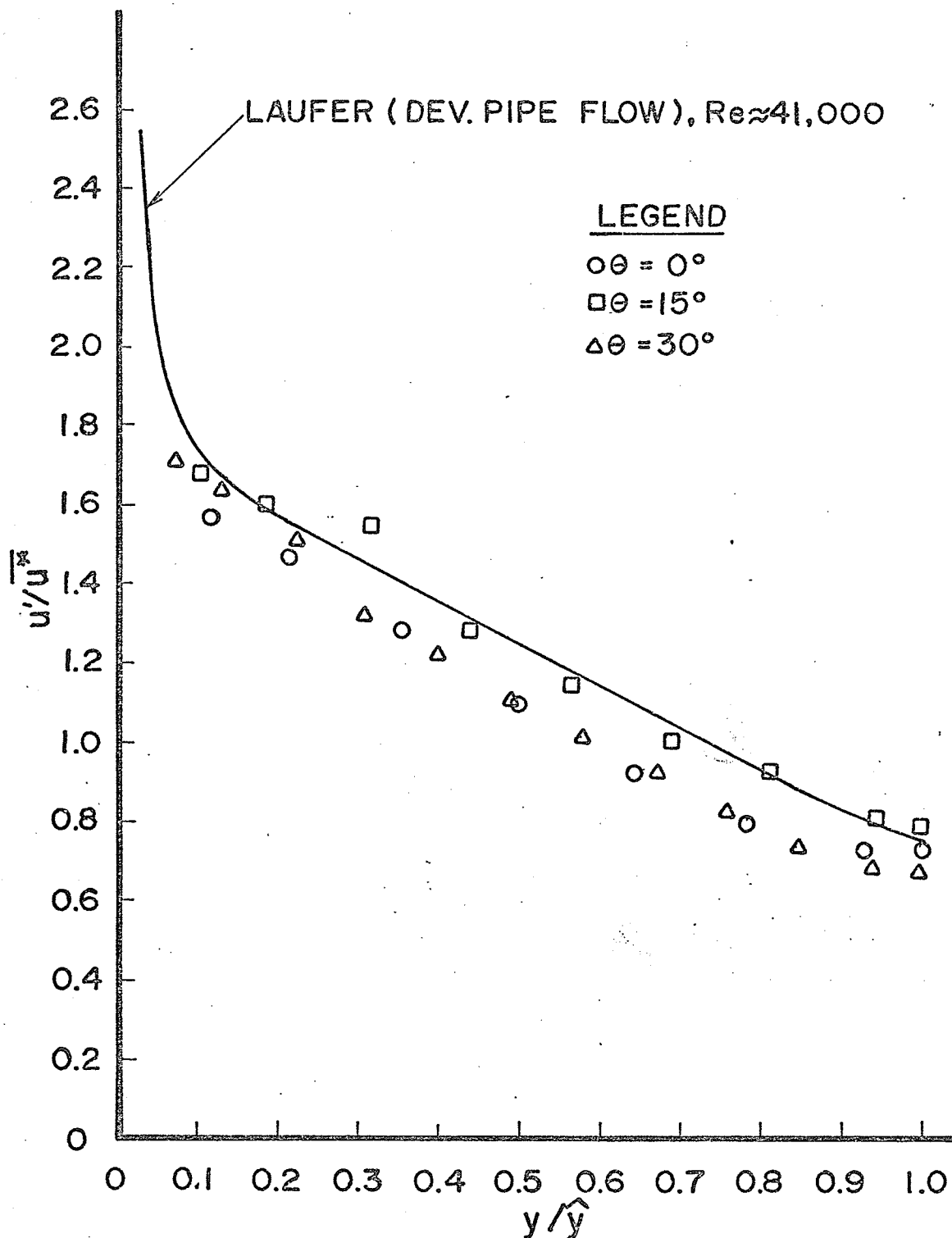


FIG.39c AXIAL TURBULENCE DISTRIBUTION  
Test 3,  $P/D=1.35$

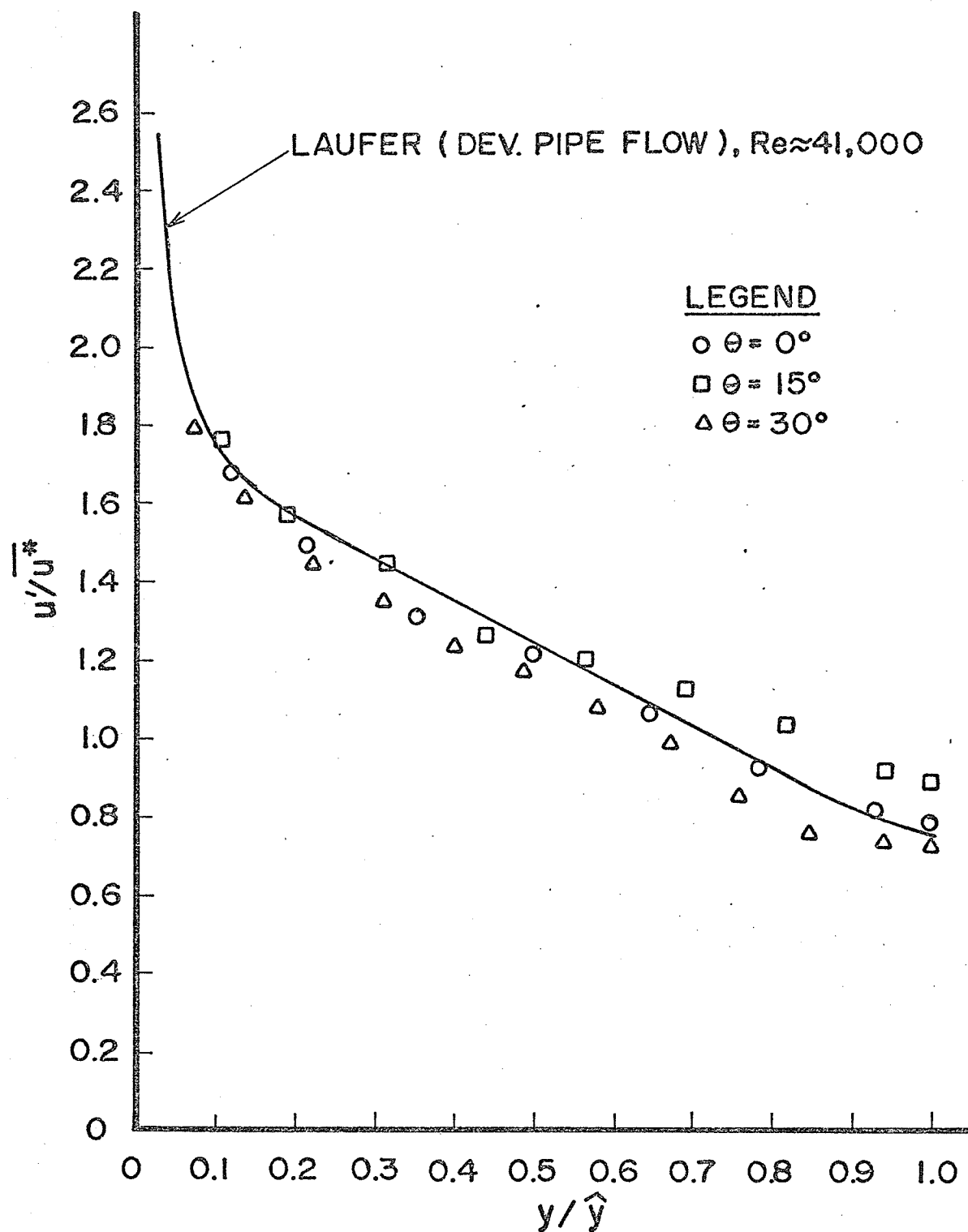


FIG39d AXIAL TURBULENCE DISTRIBUTION  
Test 6,  $P/D=1.35$

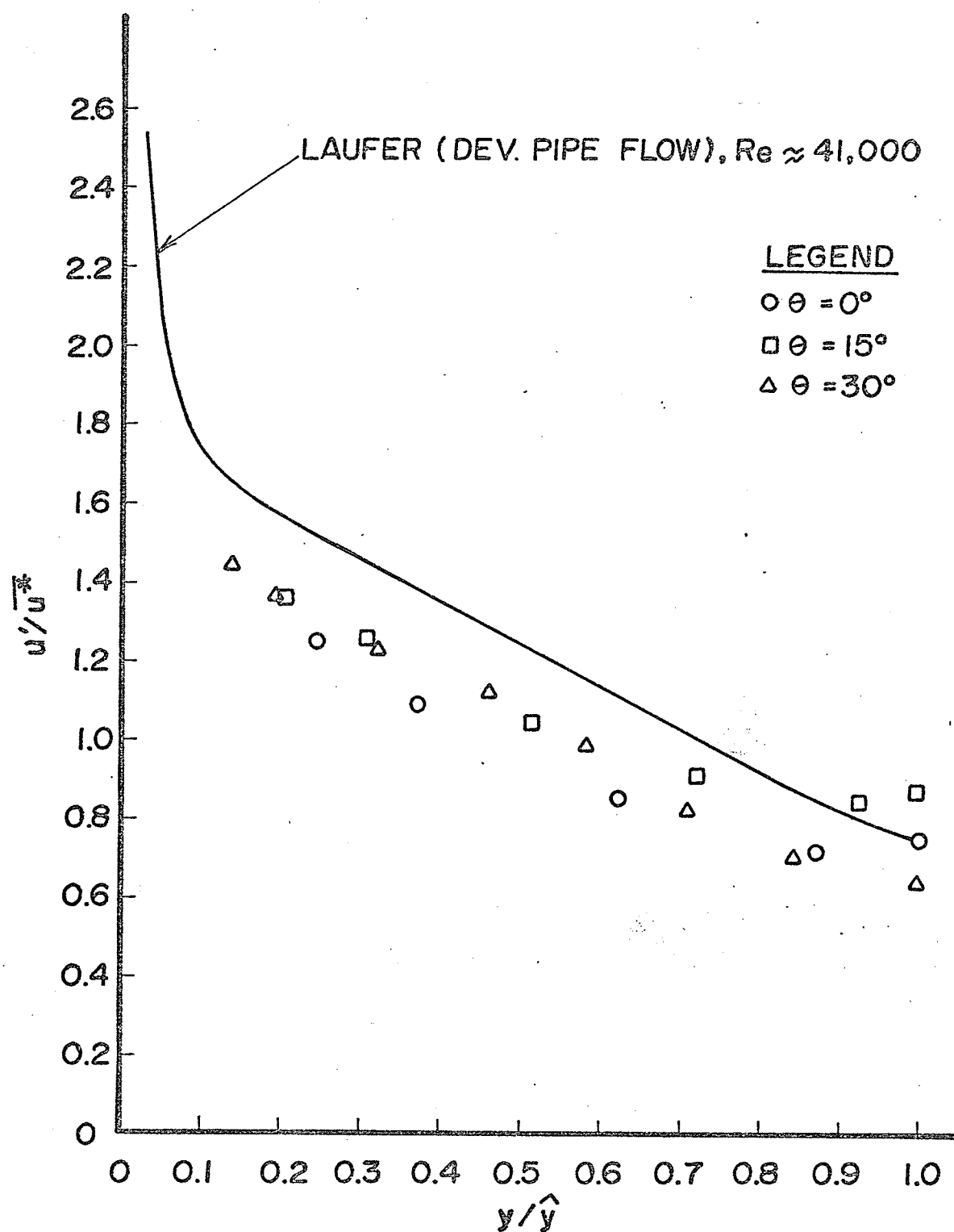


FIG.39e AXIAL TURBULENCE DISTRIBUTION  
Test 4,  $P/D=1.20$

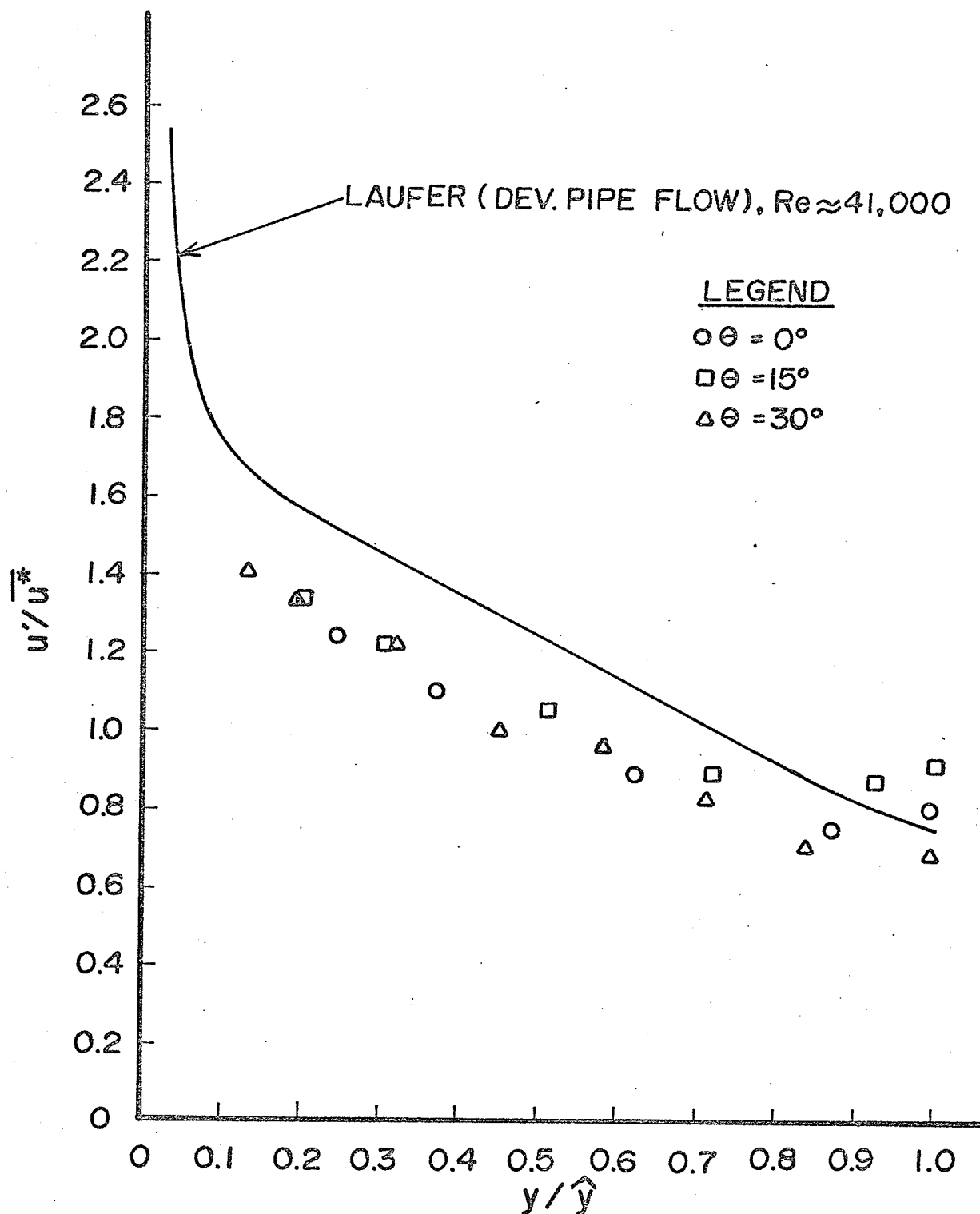


FIG.39f AXIAL TURBULENCE DISTRIBUTION

Test 6,  $P/D = 1.20$

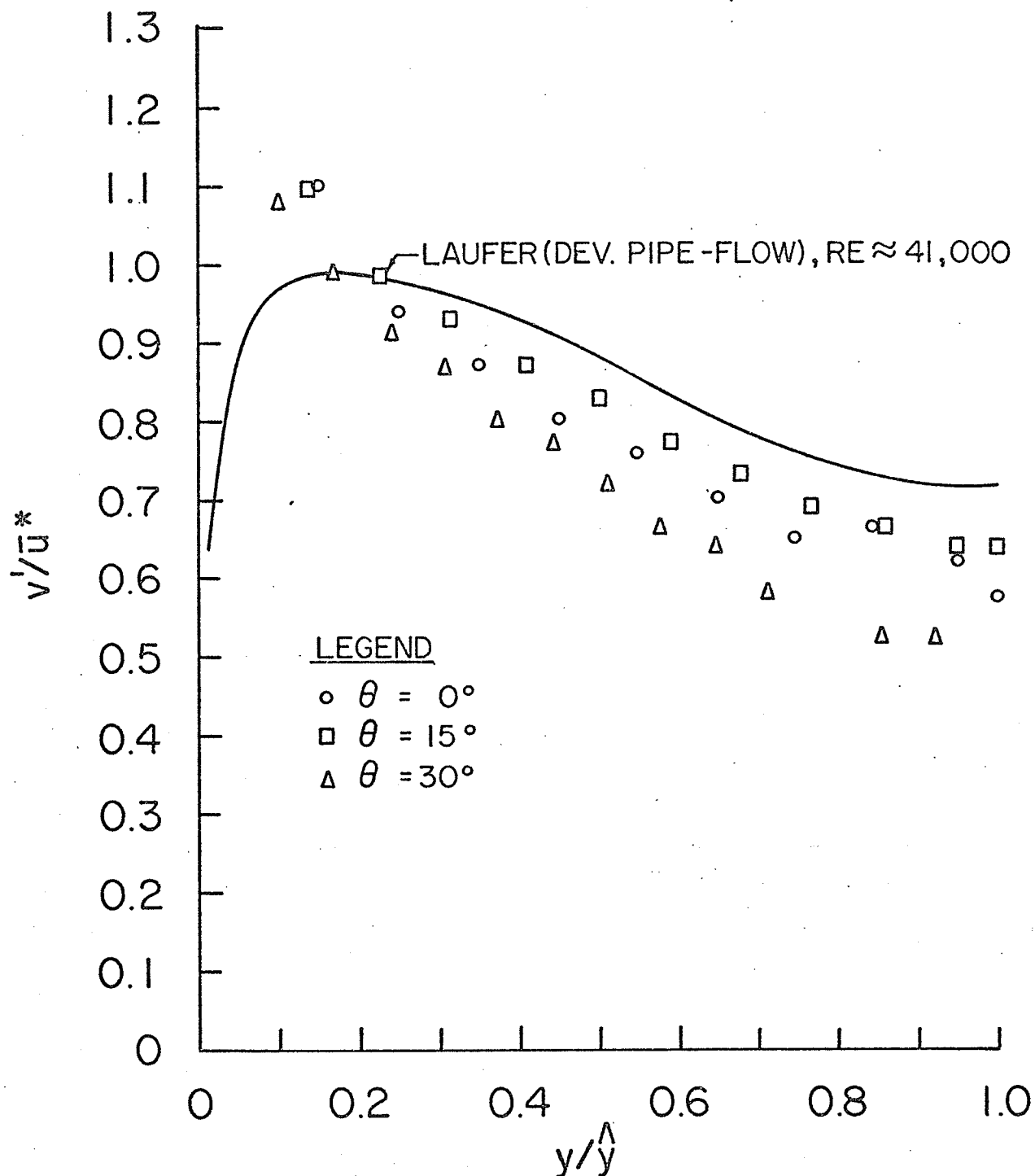


FIG.40a RADIAL TURBULENCE DISTRIBUTION-TEST 2  
P/D = 1.50

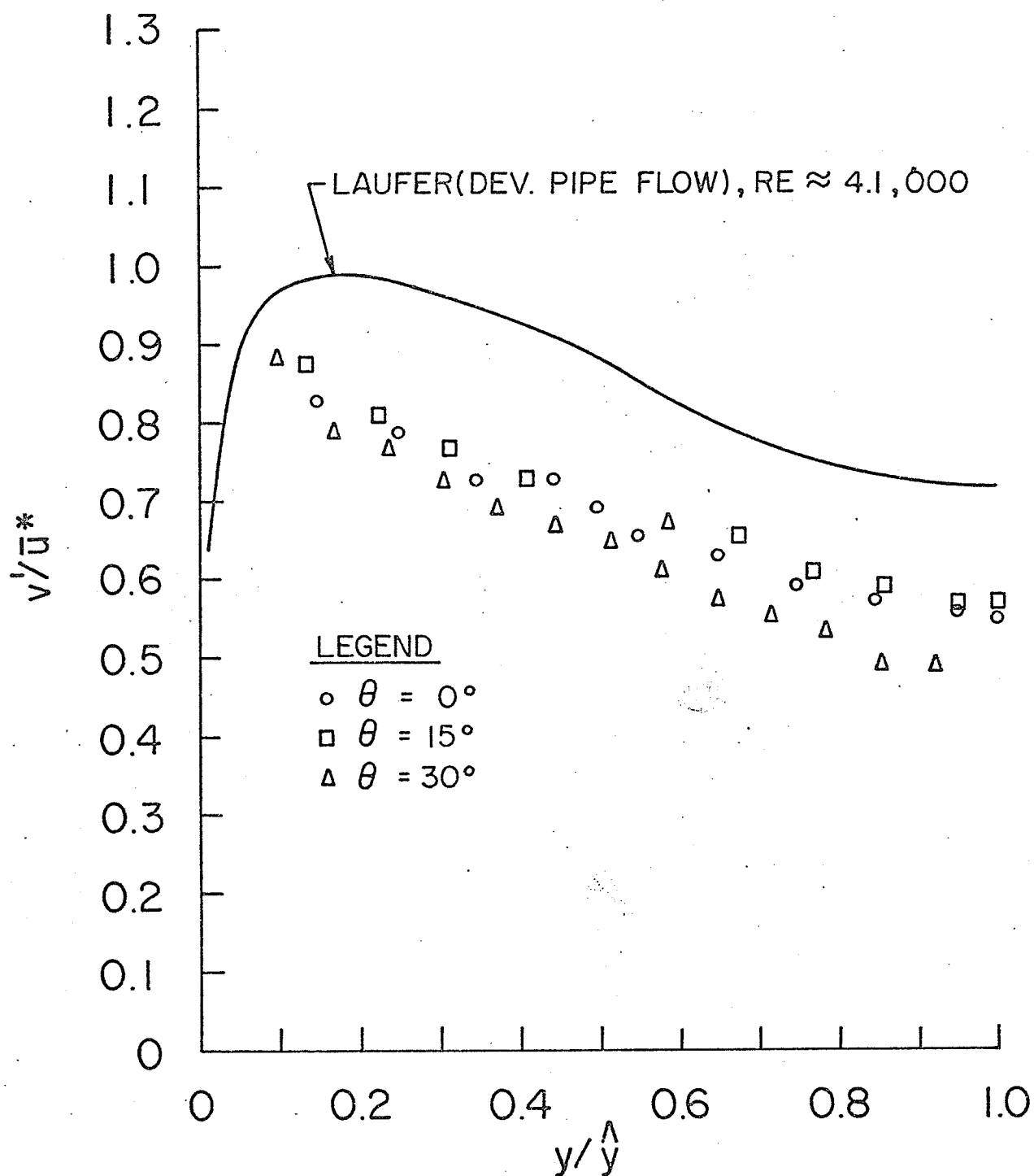


FIG.40b RADIAL TURBULENCE DISTRIBUTION-TEST 5  
 $P/D = 1.50$

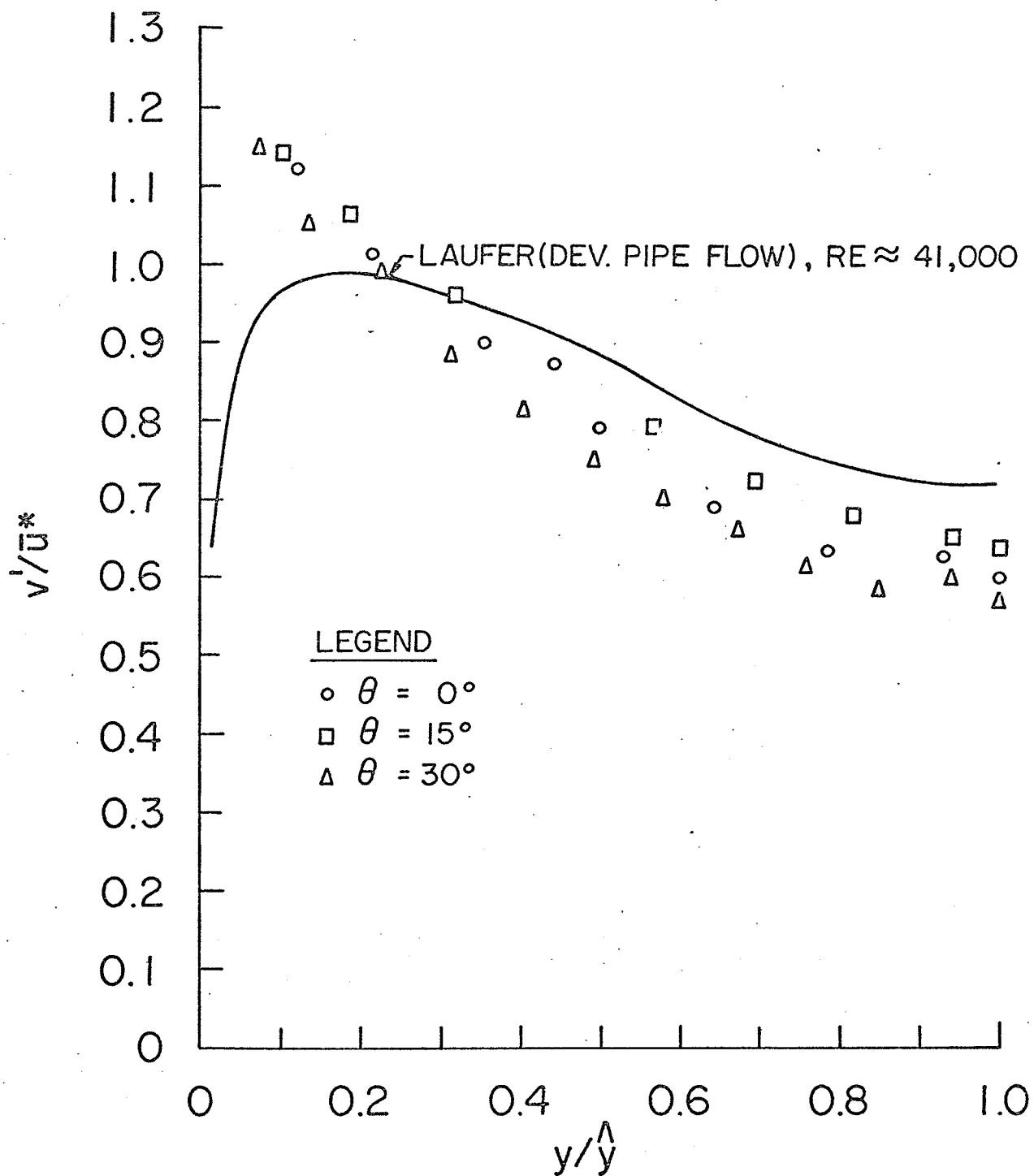


FIG.40c RADIAL TURBULENCE DISTRIBUTION-TEST 3  
 $P/D = 1.35$



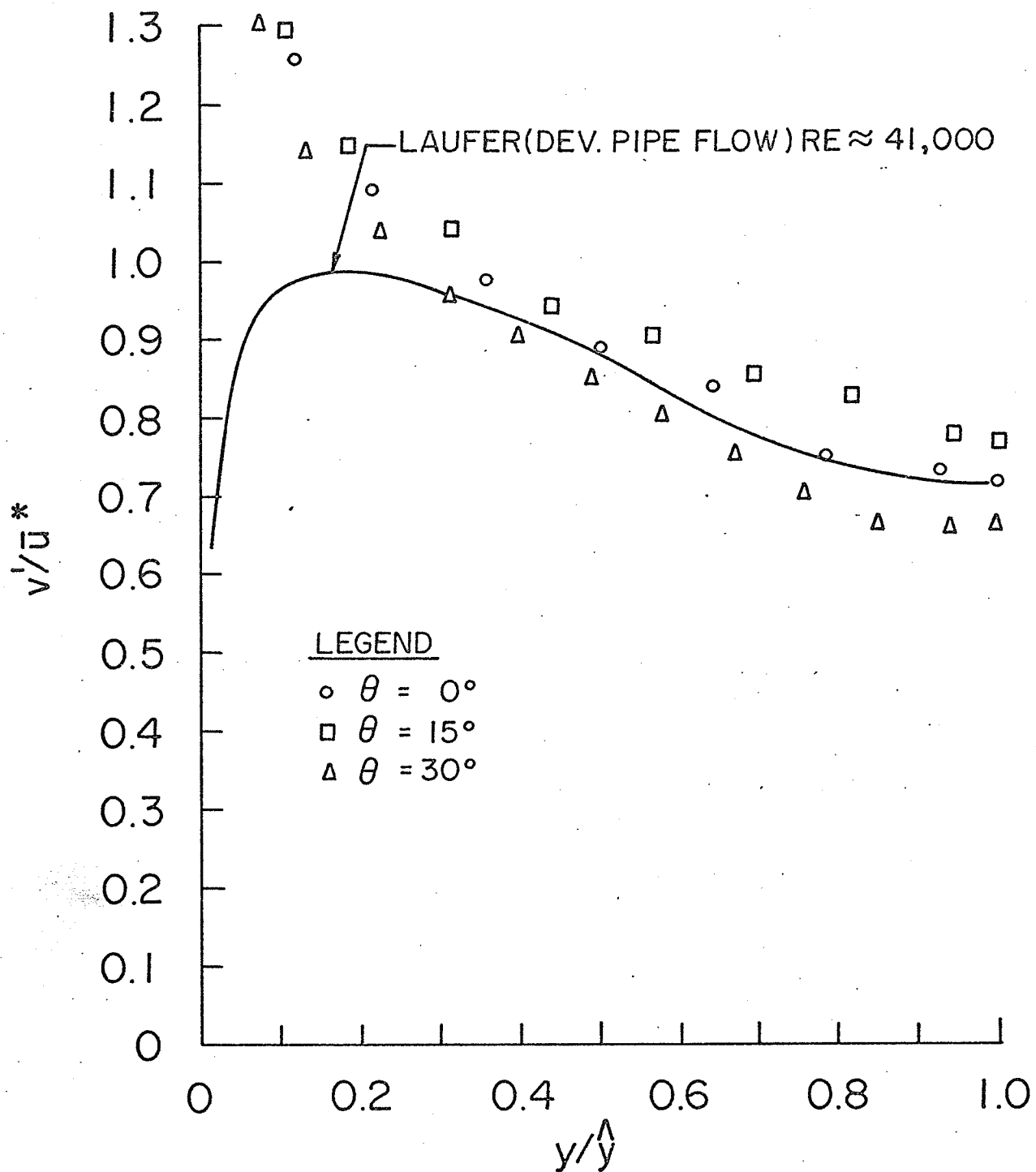


FIG.40d RADIAL TURBULENCE DISTRIBUTION-TEST 6  
P/D = 1.35

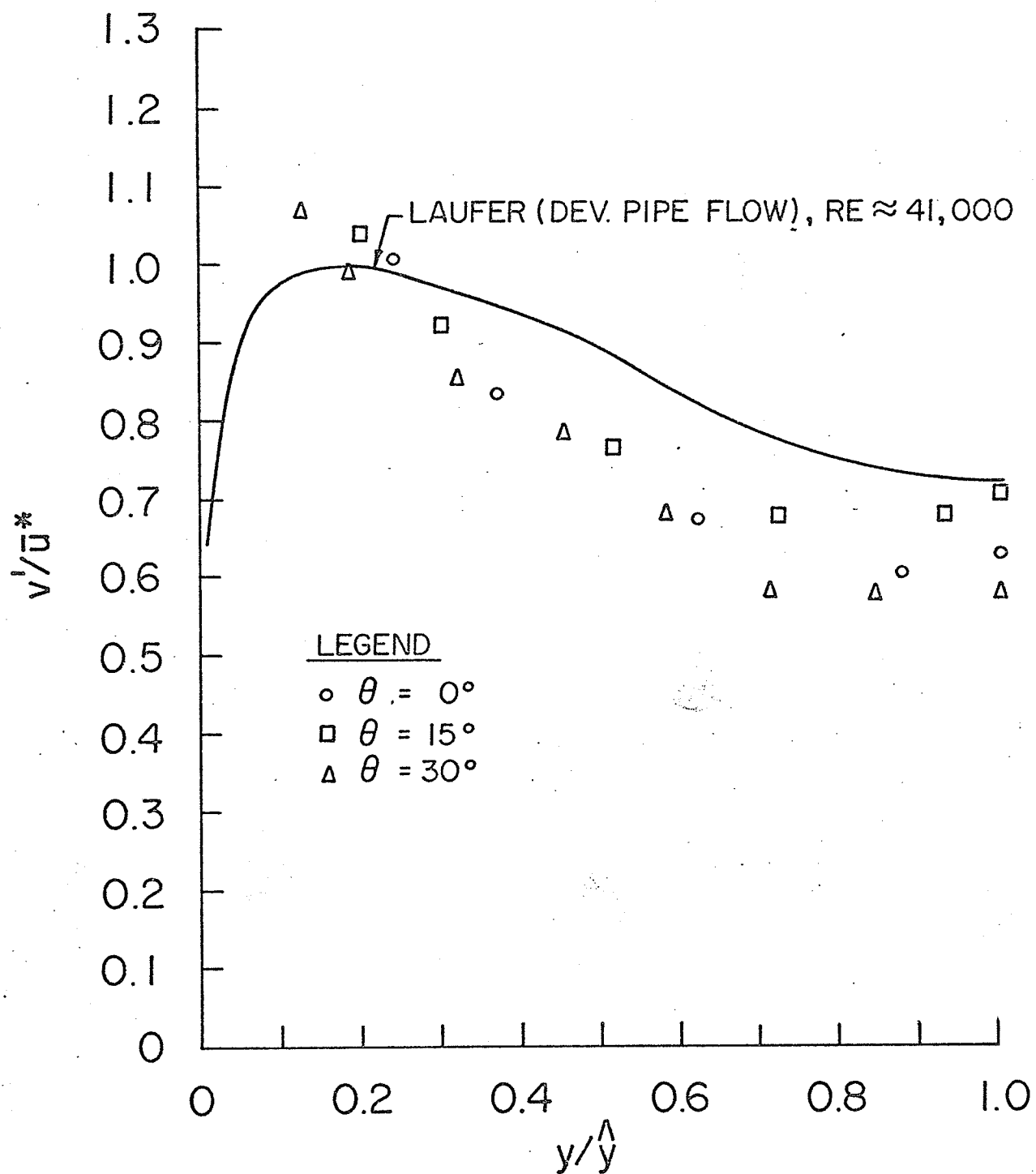


FIG.40e RADIAL TURBULENCE DISTRIBUTION-TEST 4  
 $P/D = 1.20$

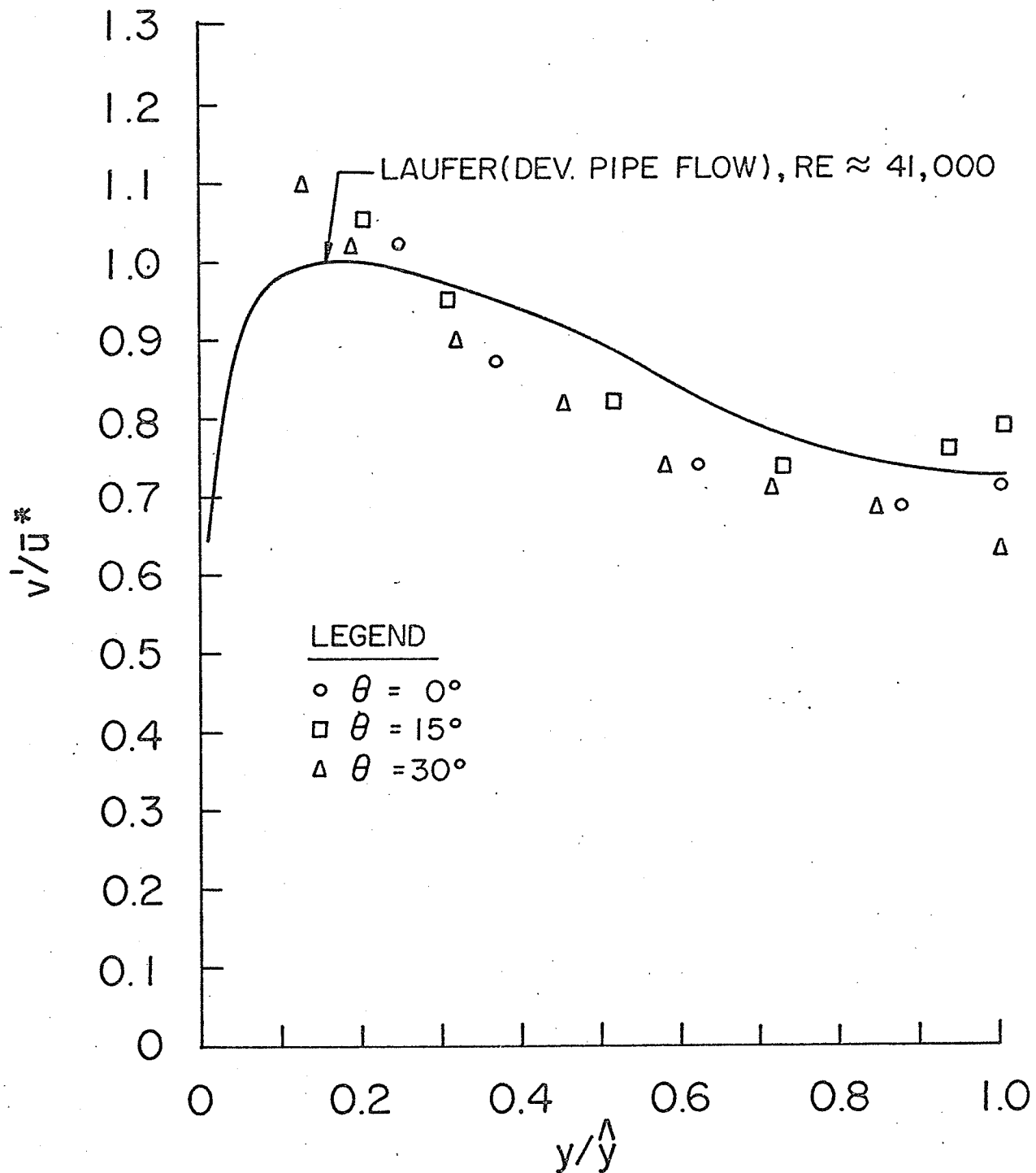


FIG.40f RADIAL TURBULENCE DISTRIBUTION-TEST 6  
P/D = 1.20

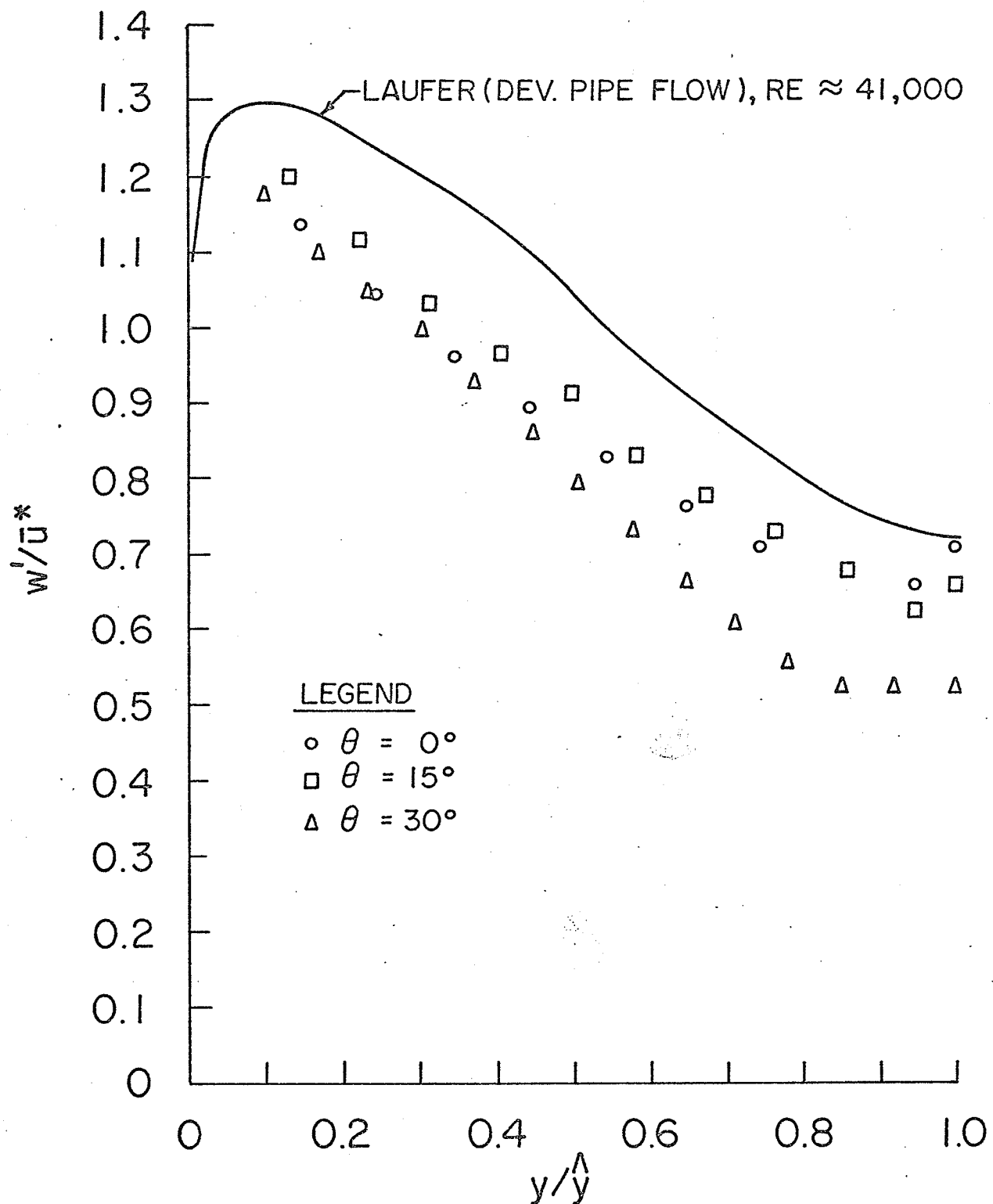


FIG.41a PERIPHERAL TURBULENCE DISTRIBUTION  
TEST 2,  $P/D = 1.50$

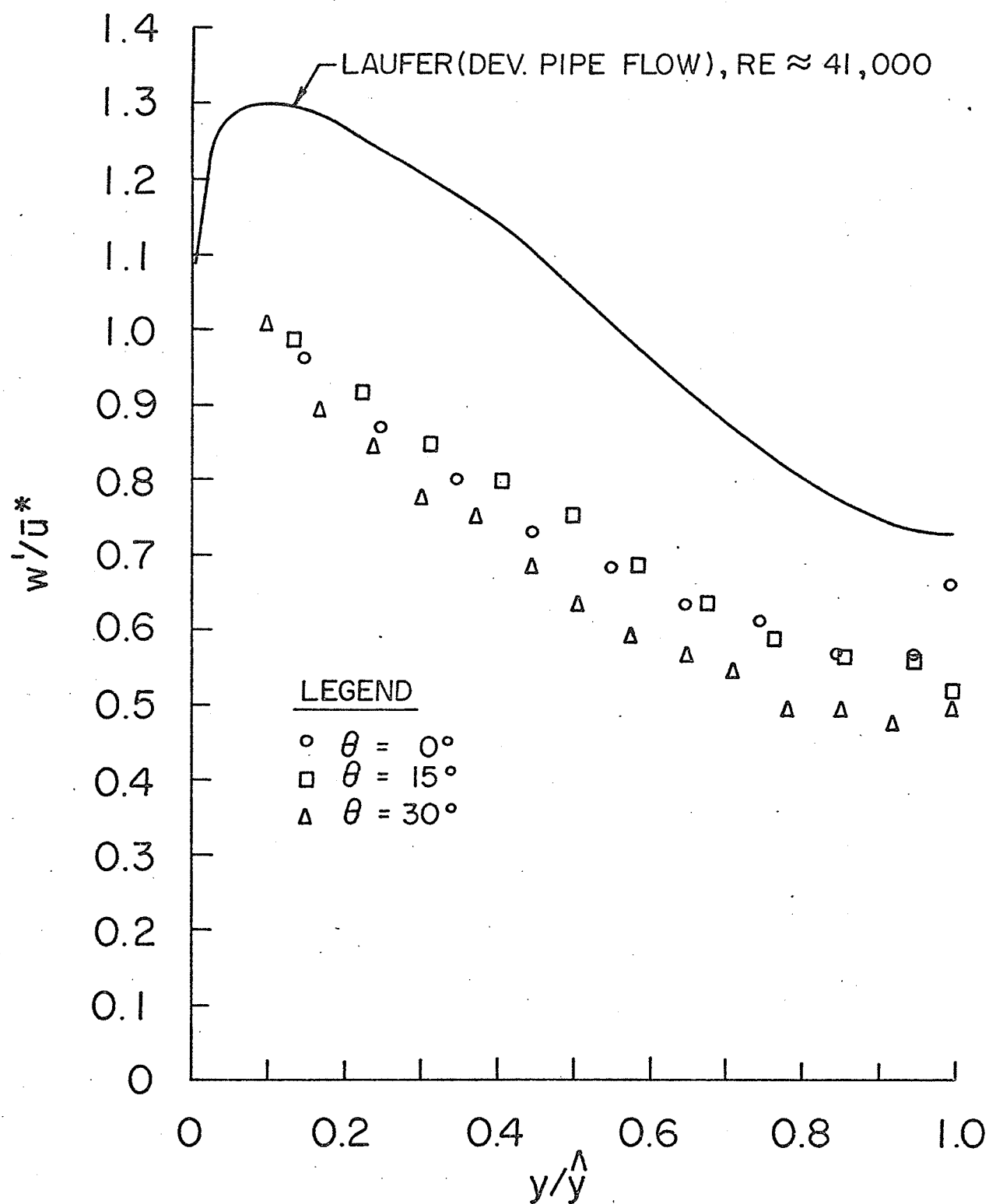


FIG.41b PERIPHERAL TURBULENCE DISTRIBUTION  
TEST 5 ,  $P/D = 1.50$

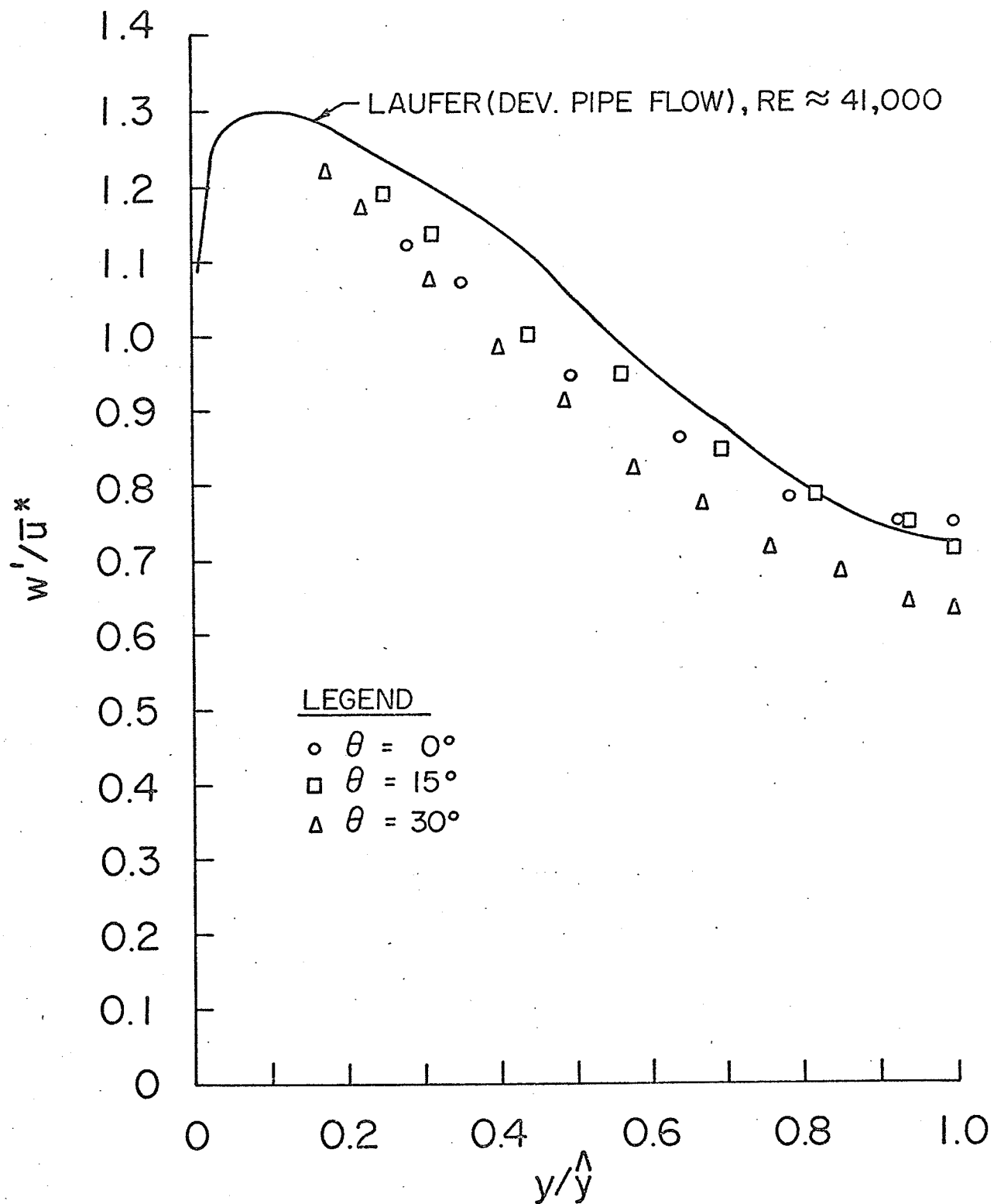


FIG.41c PERIPHERAL TURBULENCE DISTRIBUTION  
TEST 3 ,  $P/D = 1.35$

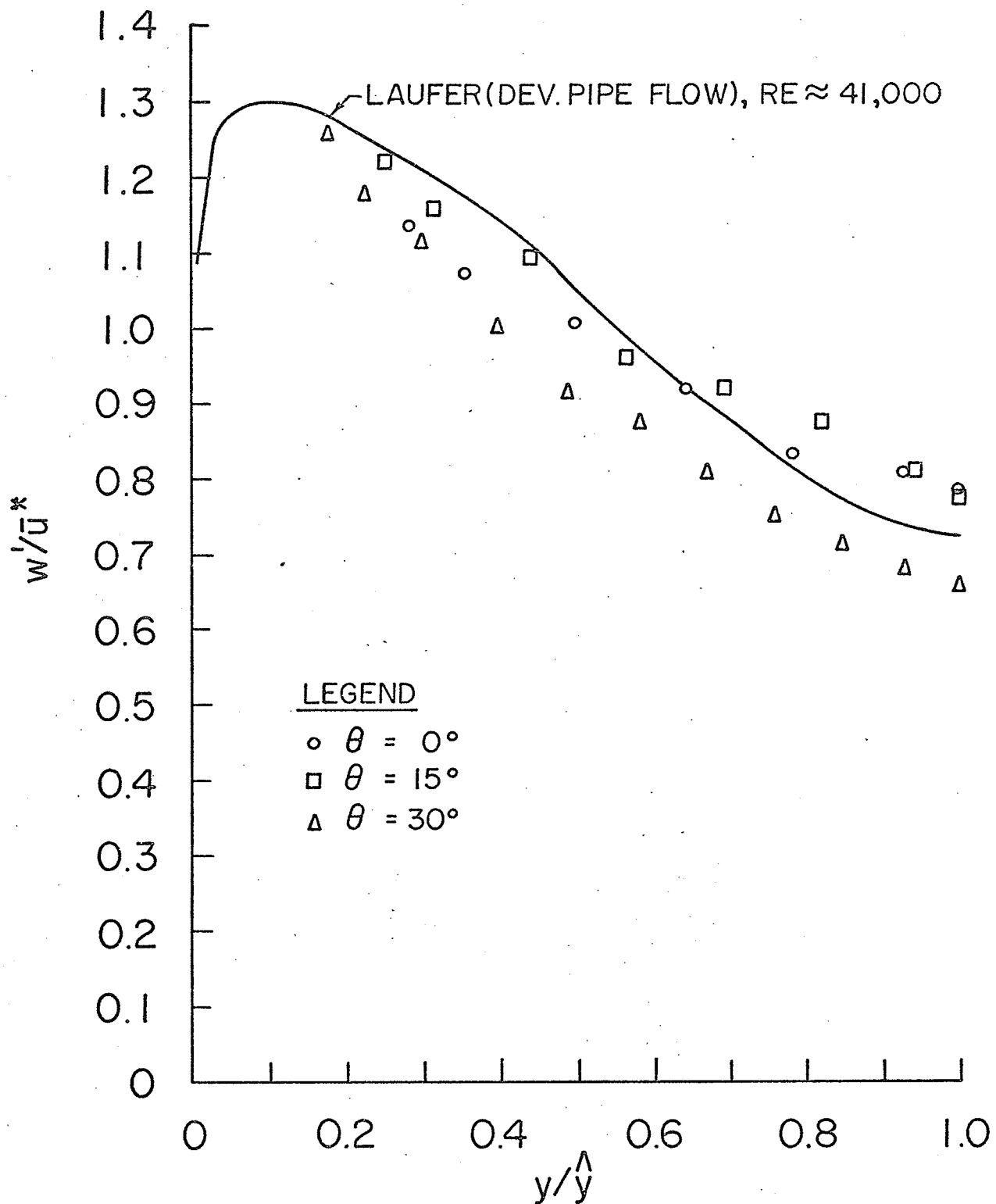


FIG.4Id PERIPHERAL TURBULENCE DISTRIBUTION  
TEST 6 ,  $P/D = 1.35$

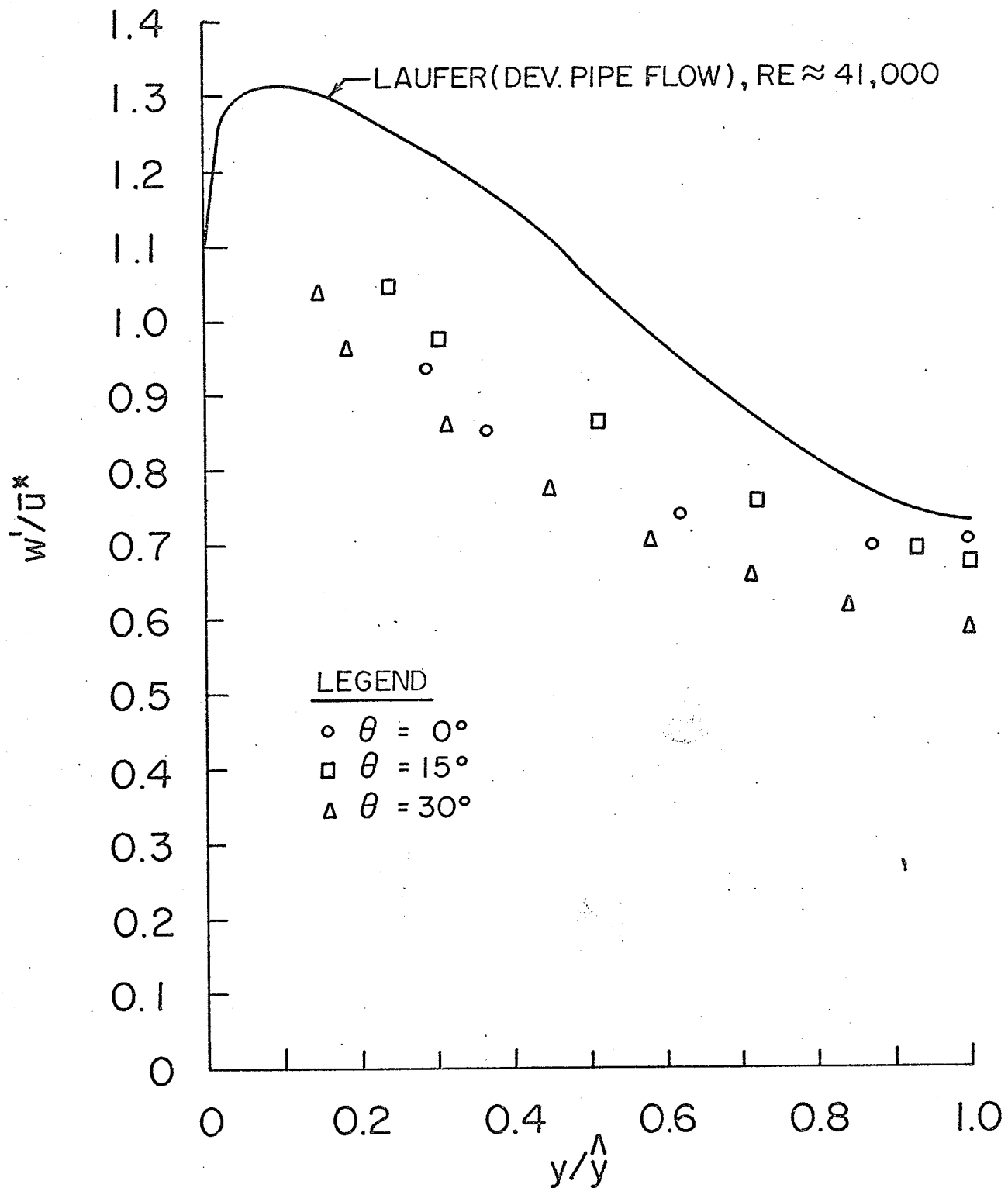


FIG.41e PERIPHERAL TURBULENCE DISTRIBUTION  
TEST 4,  $P/D = 1.20$



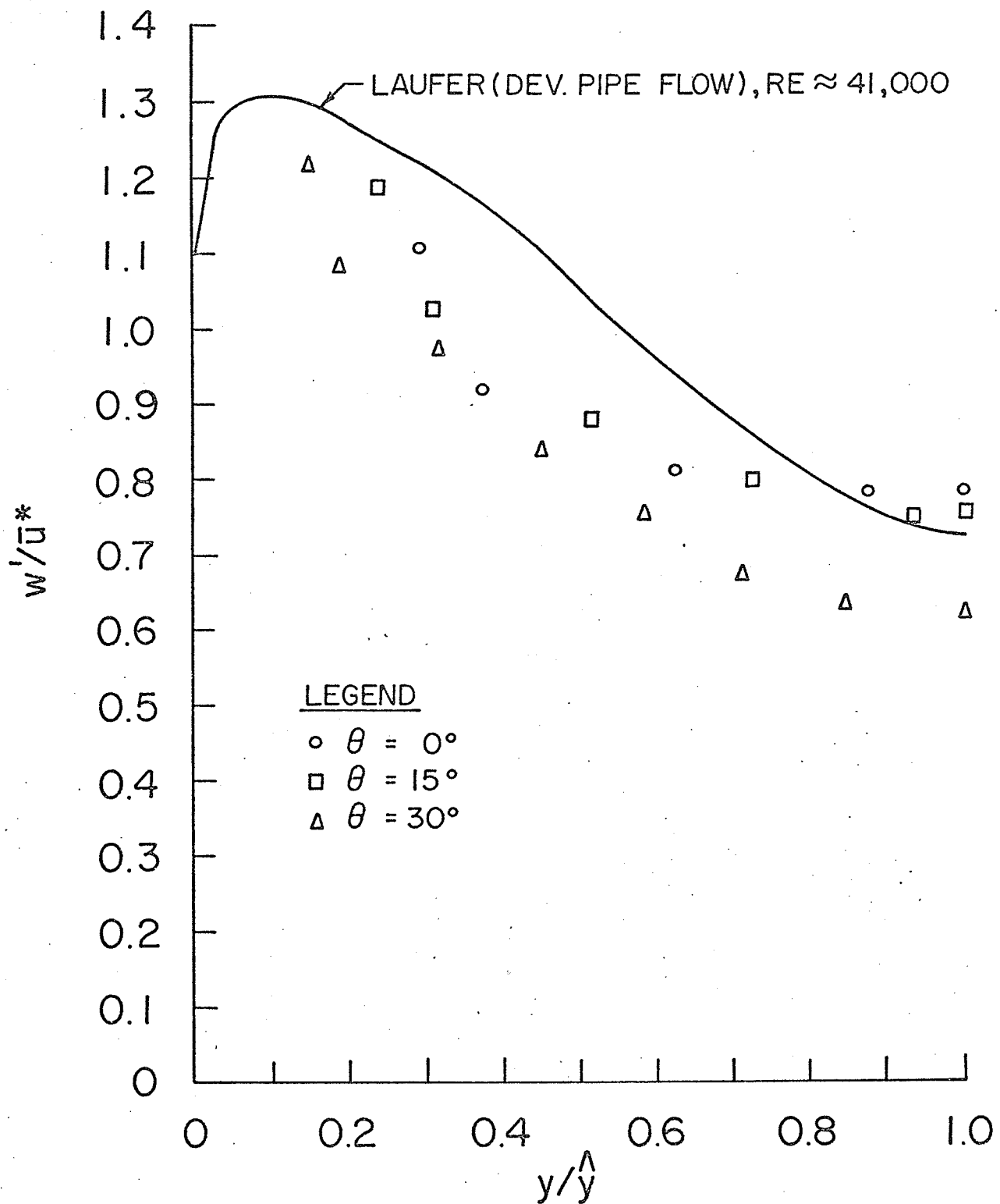


FIG.4If PERIPHERAL TURBULENCE DISTRIBUTION  
TEST 6,  $P/D = 1.20$

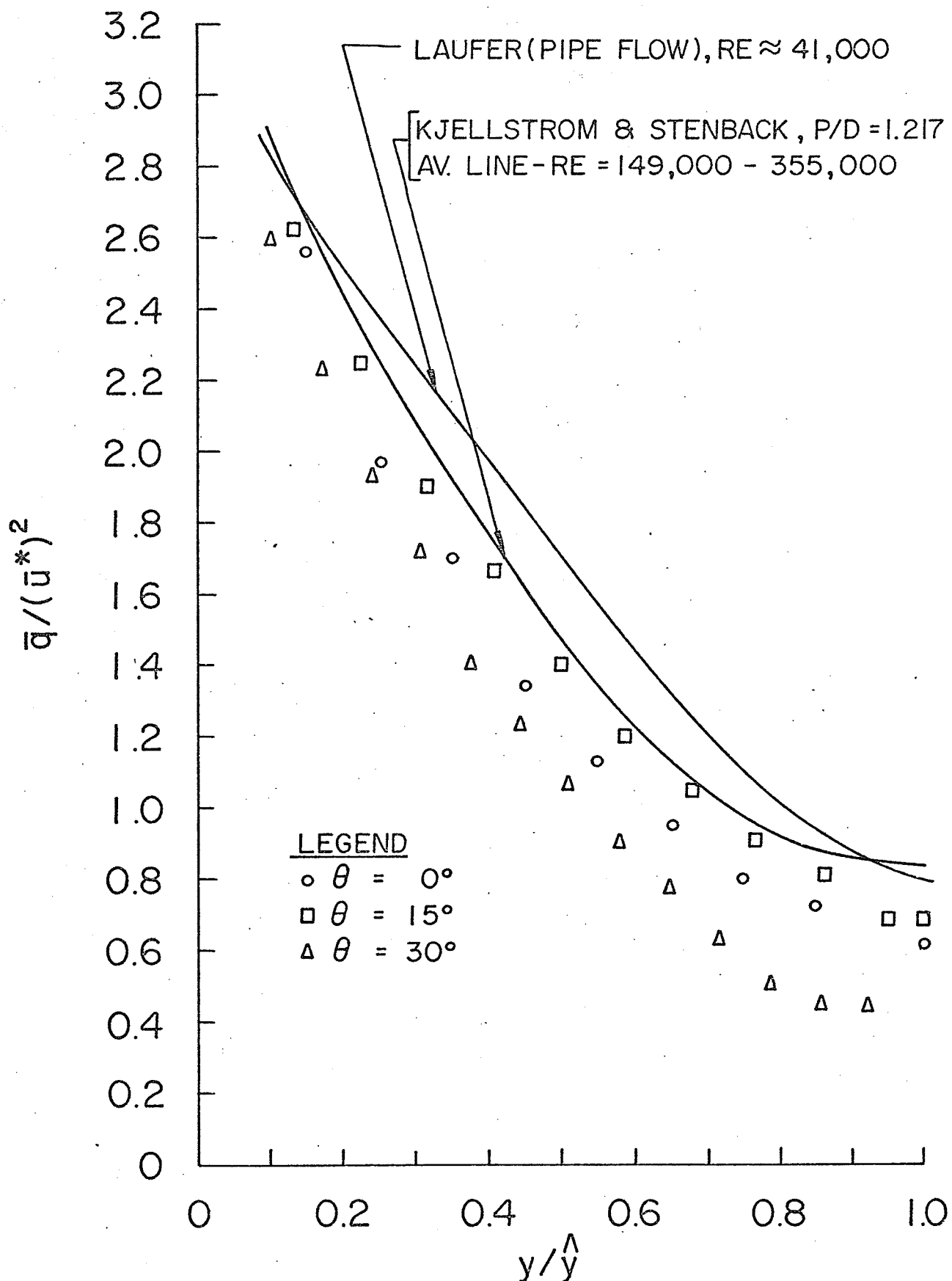


FIG.42a TURBULENT KINETIC ENERGY DISTRIBUTION  
TEST 2,  $P/D = 1.50$

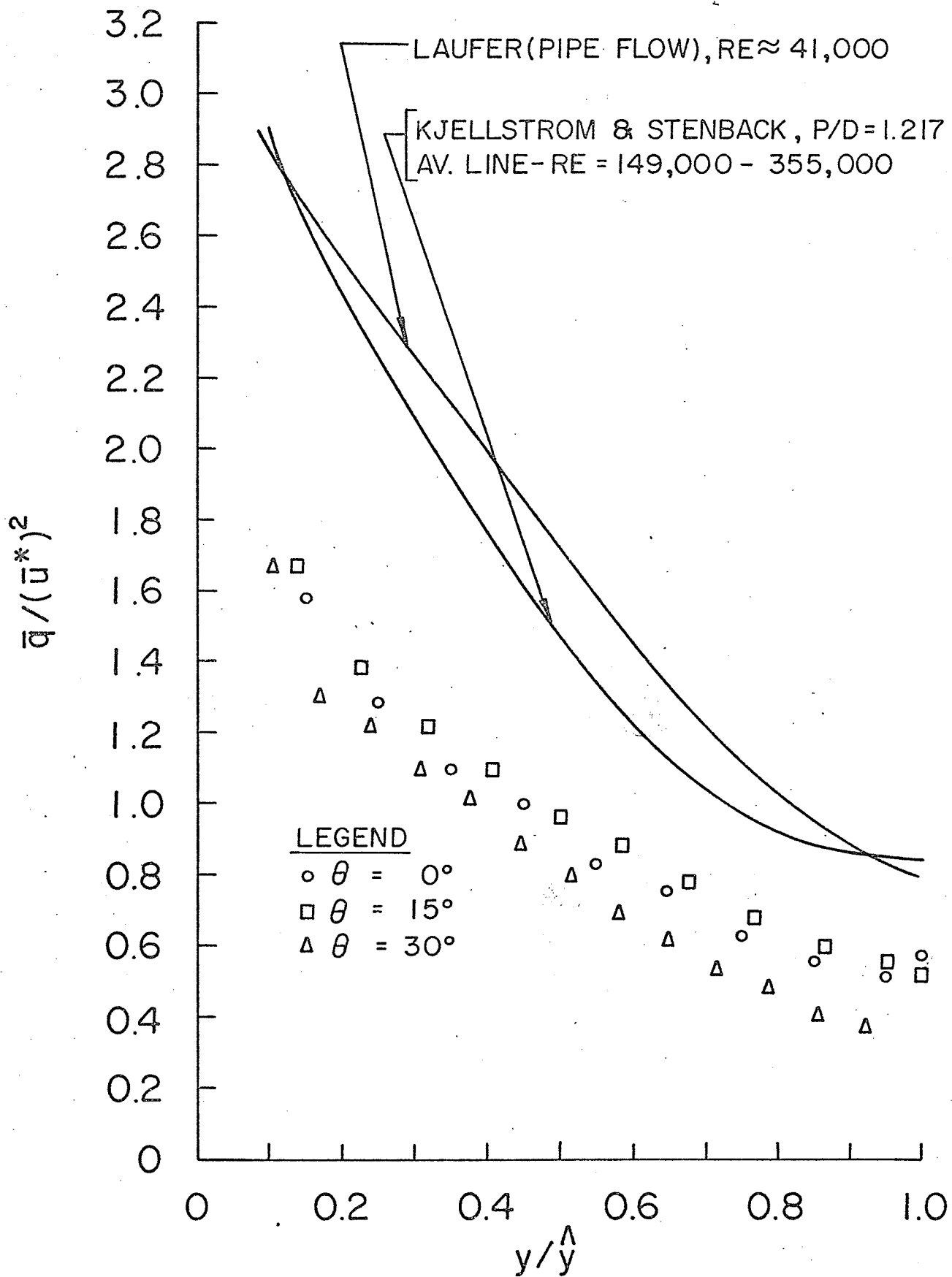


FIG.42b TURBULENT KINETIC ENERGY DISTRIBUTION  
TEST 5,  $P/D = 1.50$

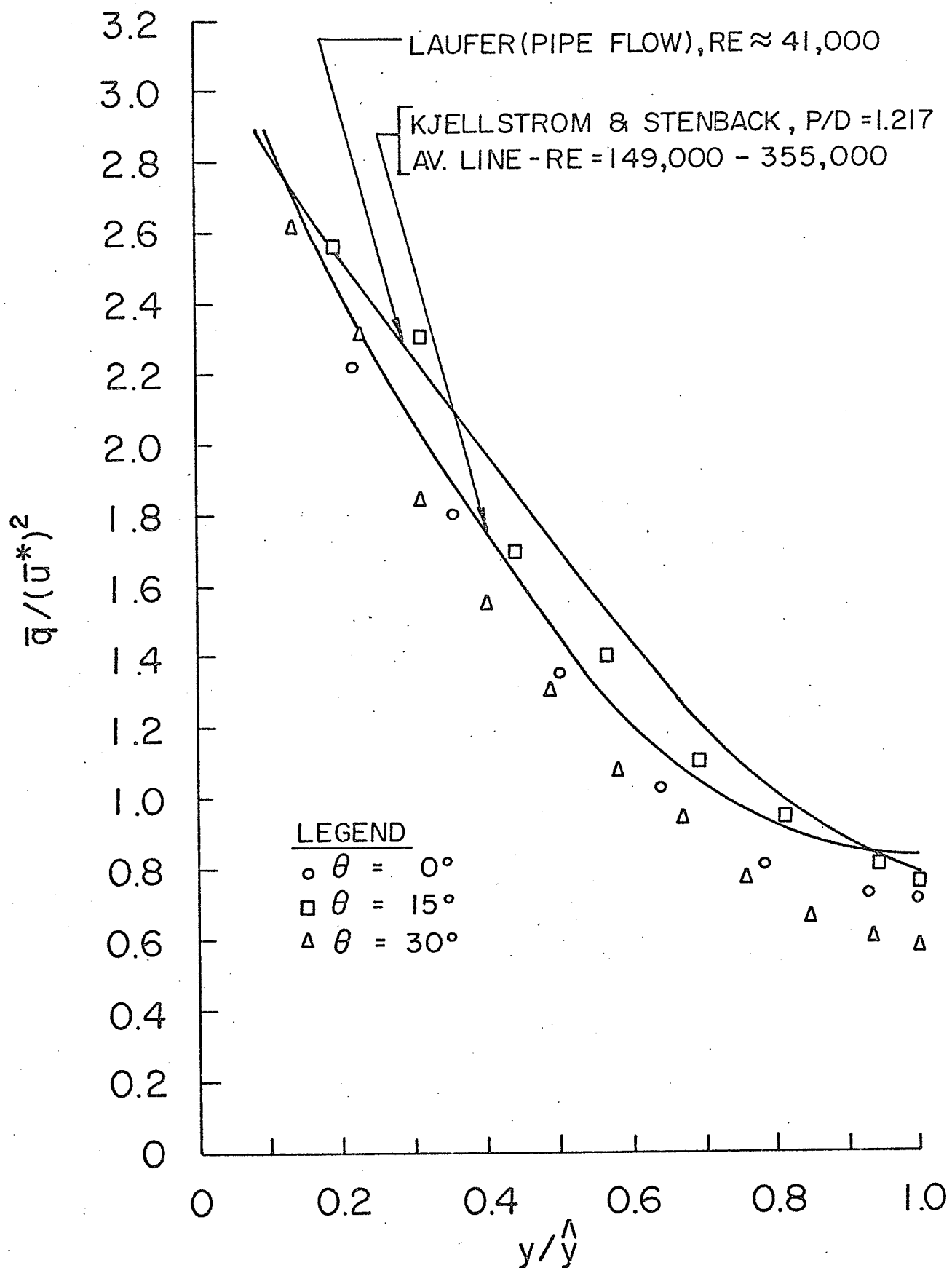


FIG.42c TURBULENT KINETIC ENERGY DISTRIBUTION  
TEST 3,  $P/D = 1.35$

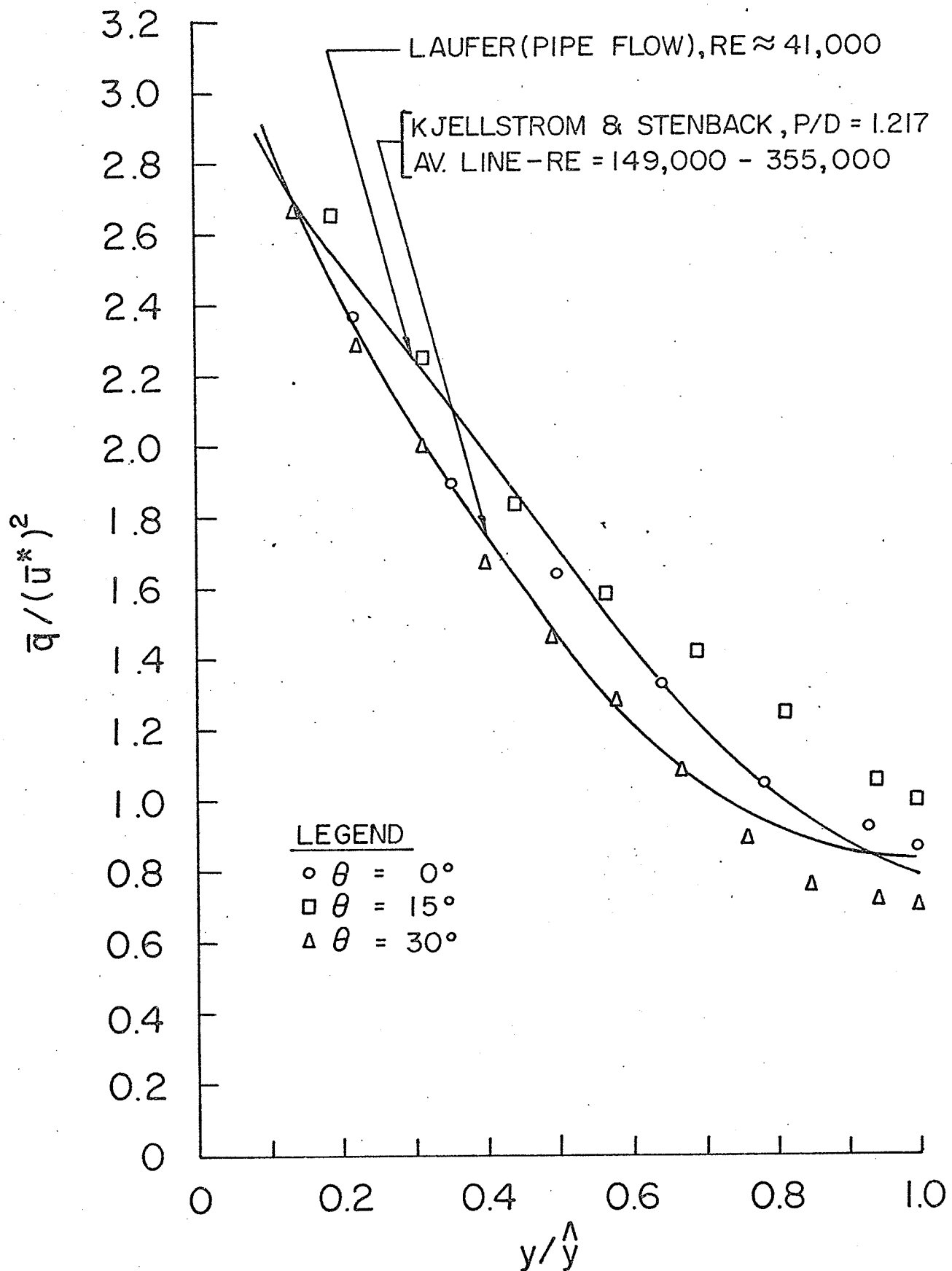


FIG.42d TURBULENT KINETIC ENERGY DISTRIBUTION  
TEST 6,  $P/D = 1.35$

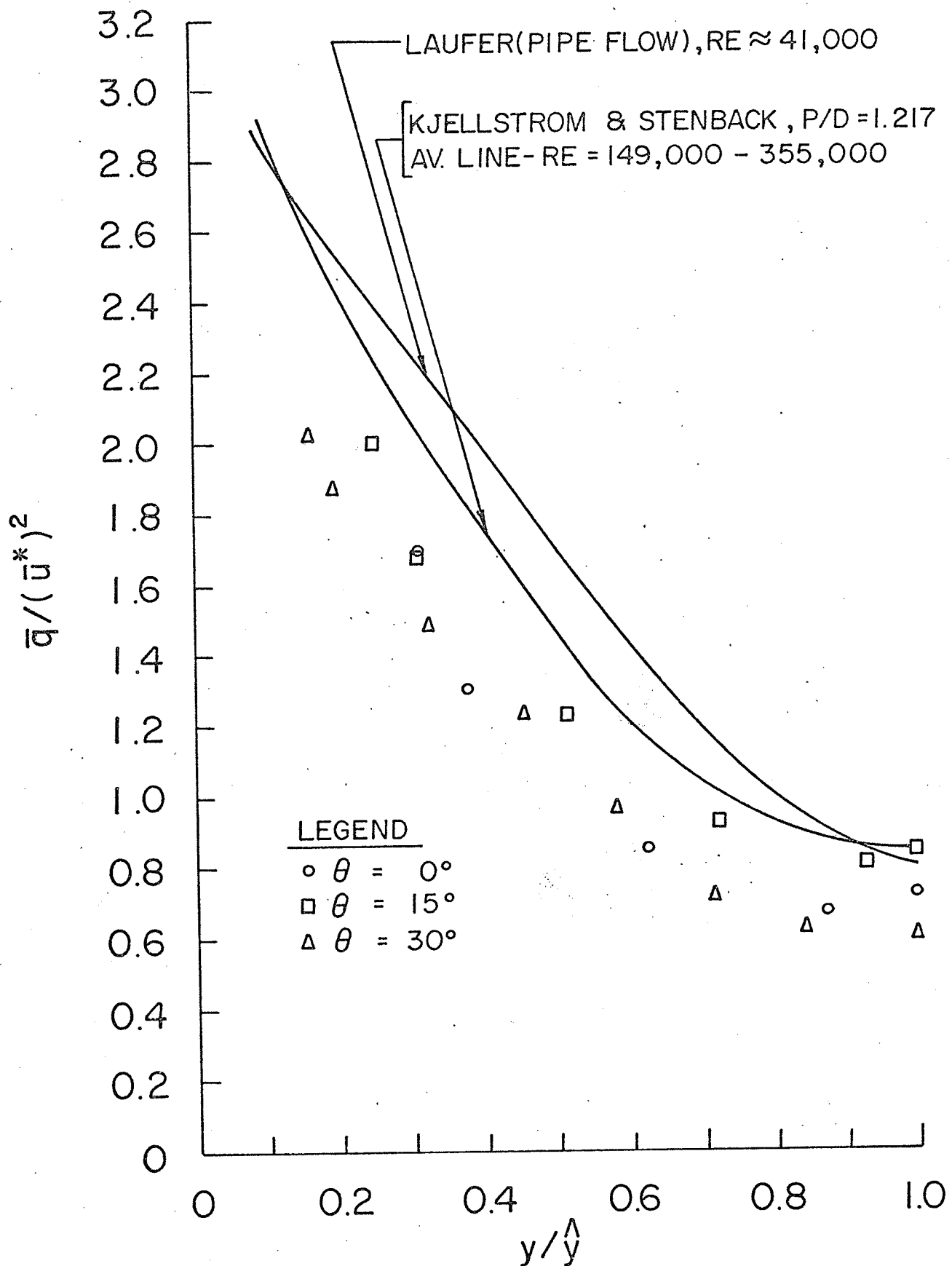


FIG.42e TURBULENT KINETIC ENERGY DISTRIBUTION  
TEST 4,  $P/D = 1.20$

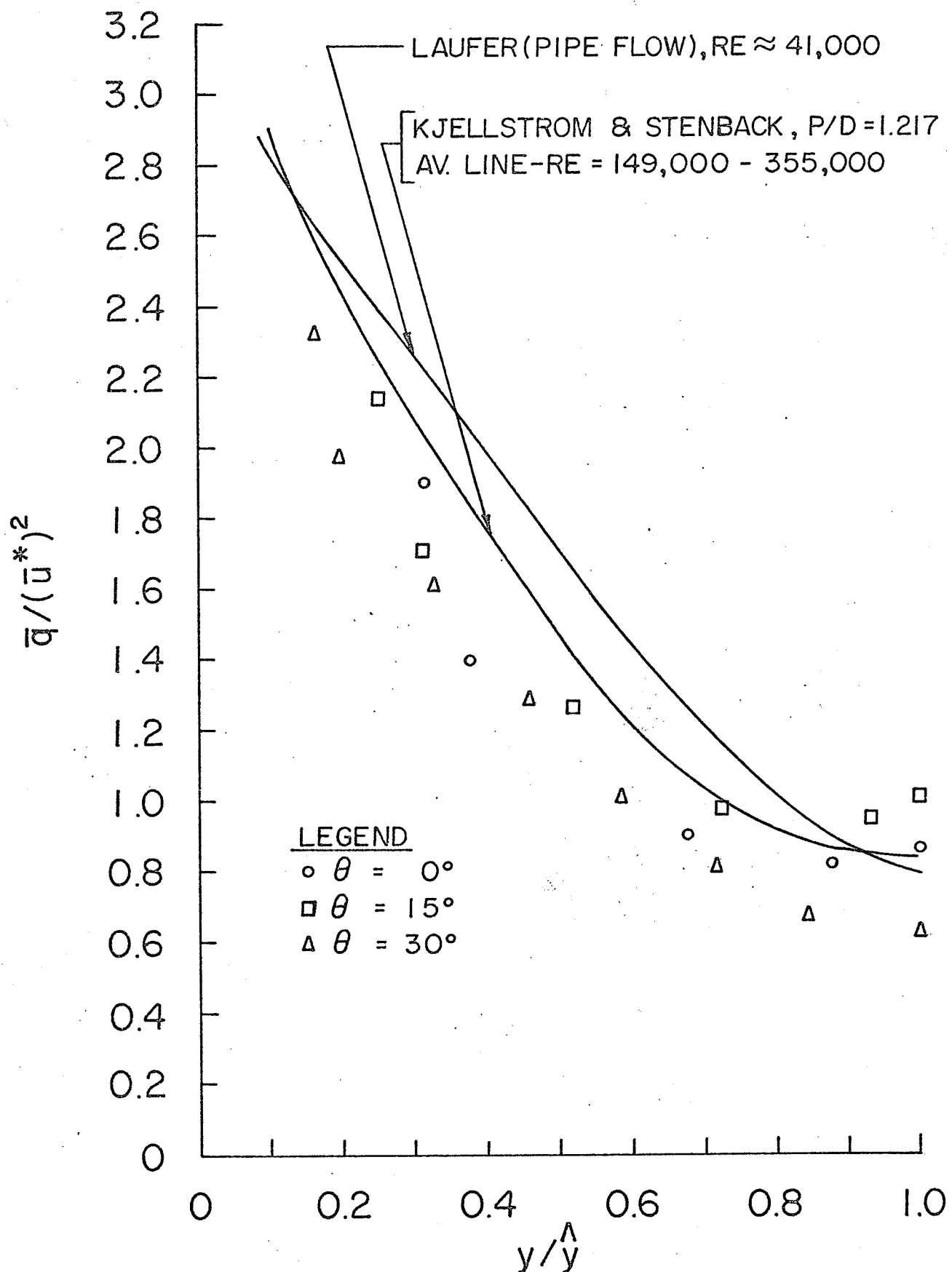


FIG.42f TURBULENT KINETIC ENERGY DISTRIBUTION  
TEST 6,  $P/D = 1.20$

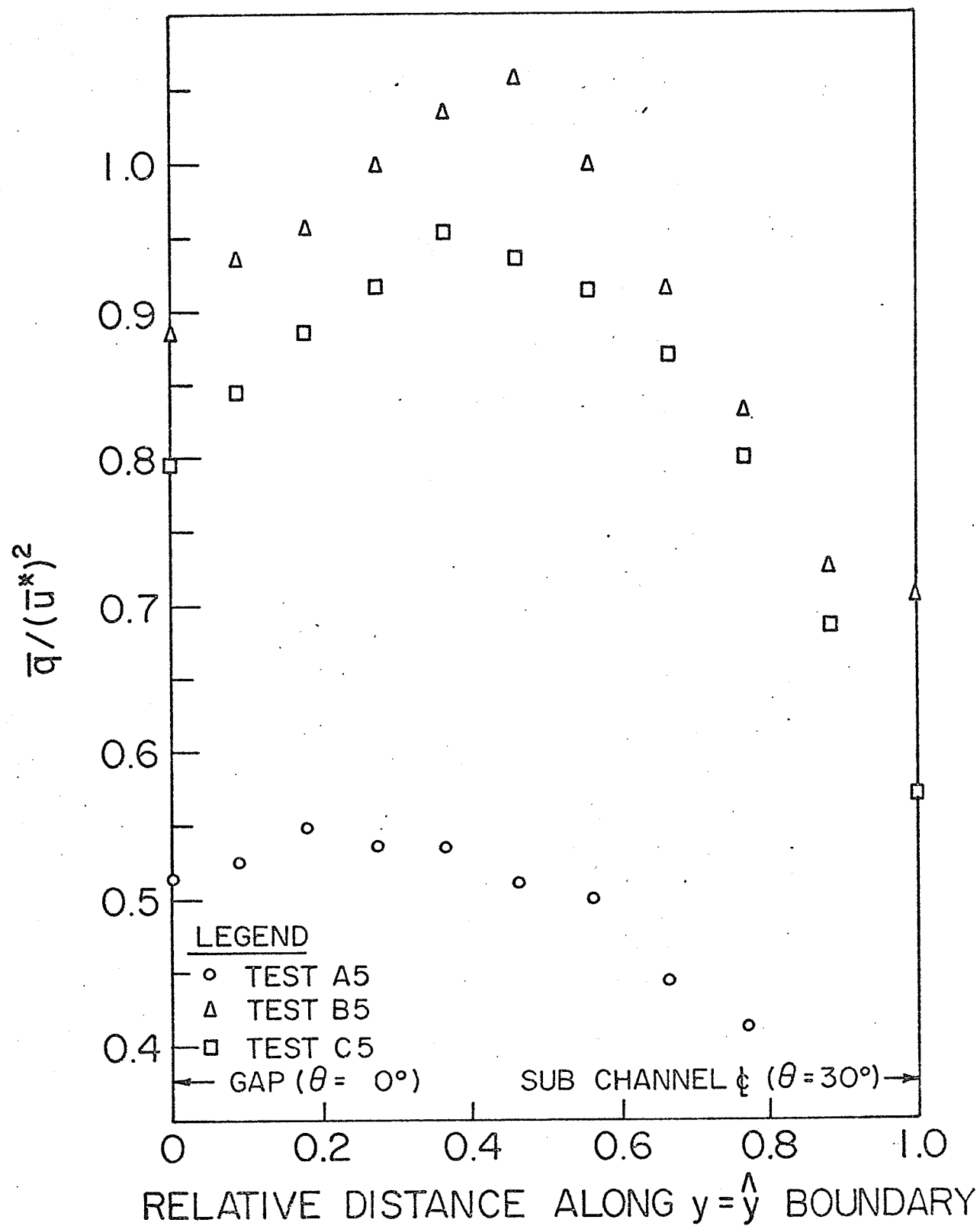


FIG.43 DISTRIBUTIONS OF MEAN TURBULENT KINETIC ENERGY ON  $y = \hat{y}$  BOUNDARY TEST COND. 5  
RE = 36,000



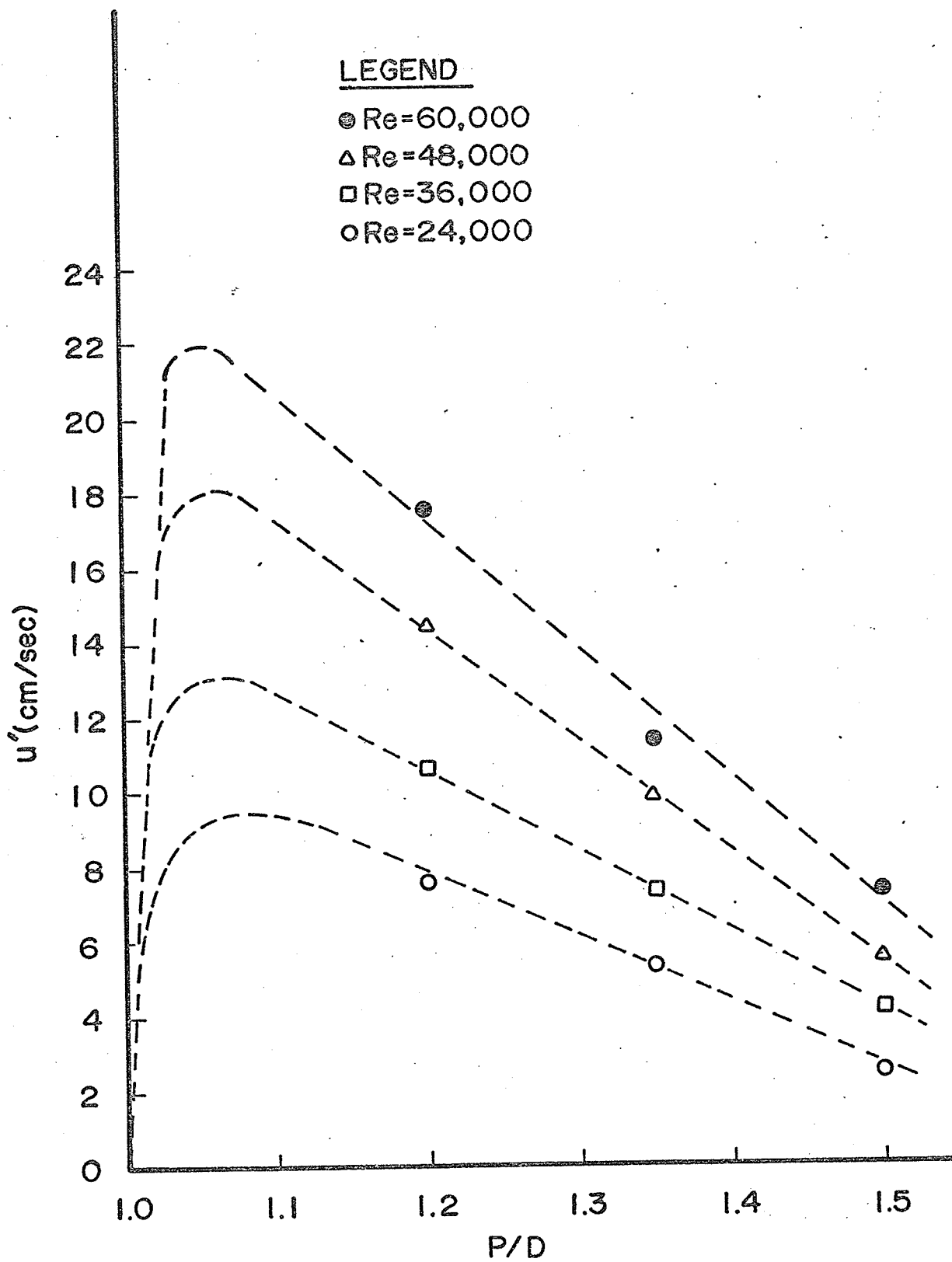


FIG.44 PLOT of  $u'$  at CENTER of HALF GAP as FUNCTION of TUBE SPACING and REYNOLDS NUMBER

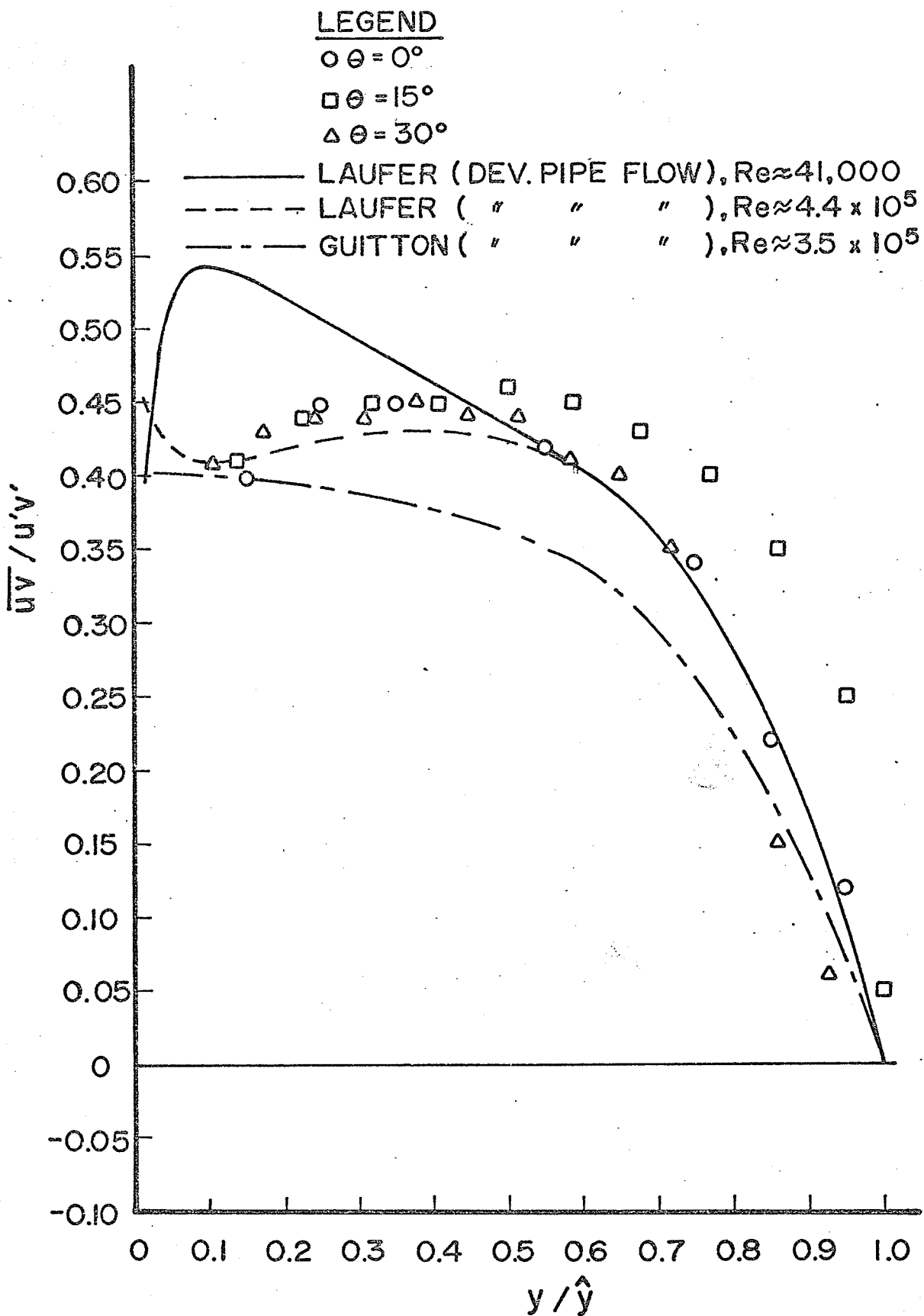


FIG.45a DISTRIBUTION of  $R_{uv}$   
 Test 2,  $P/D = 1.50$

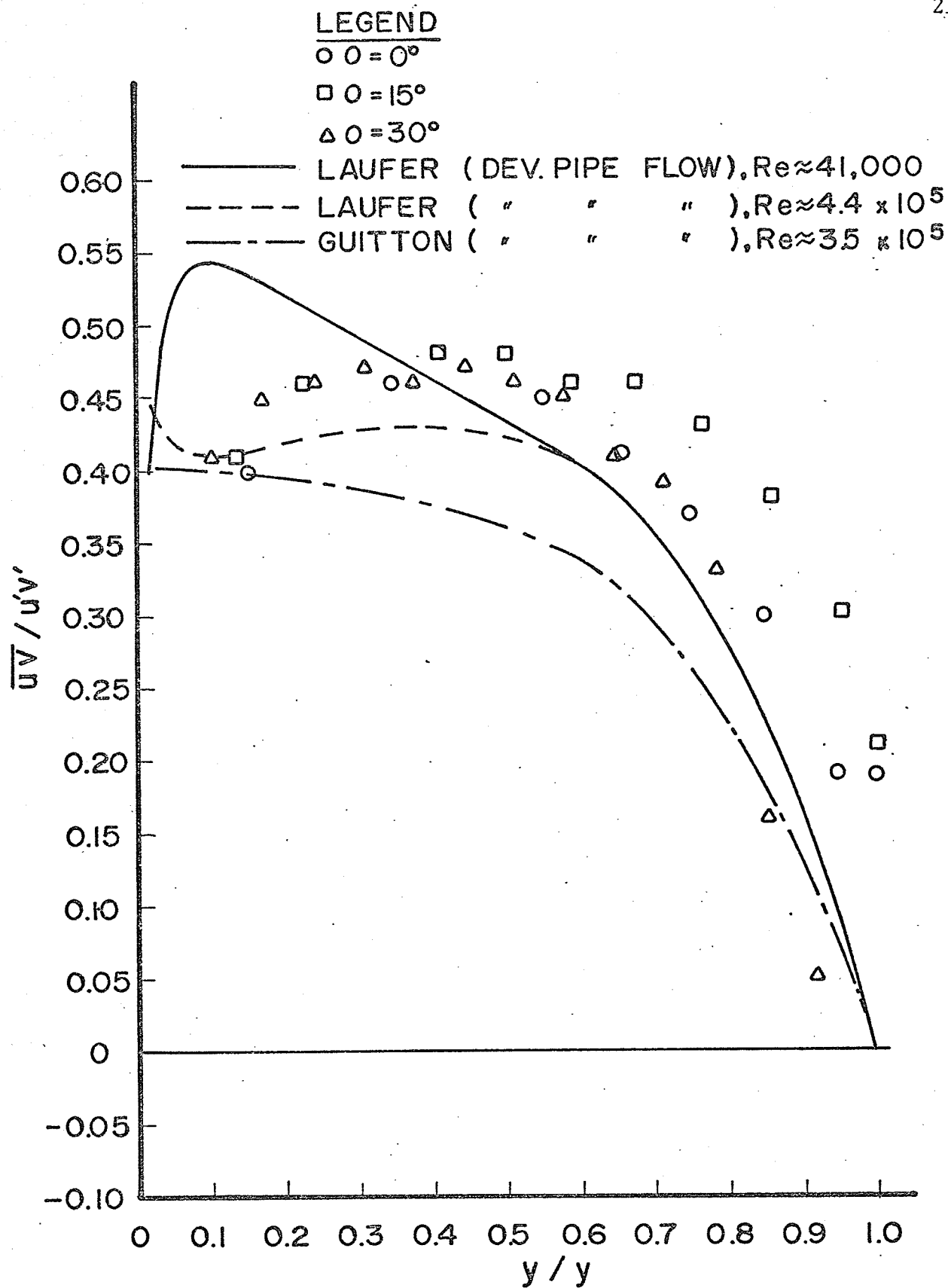


FIG.45b DISTRIBUTION of  $R_{uv}$   
 Test 5,  $P/D=1.50$

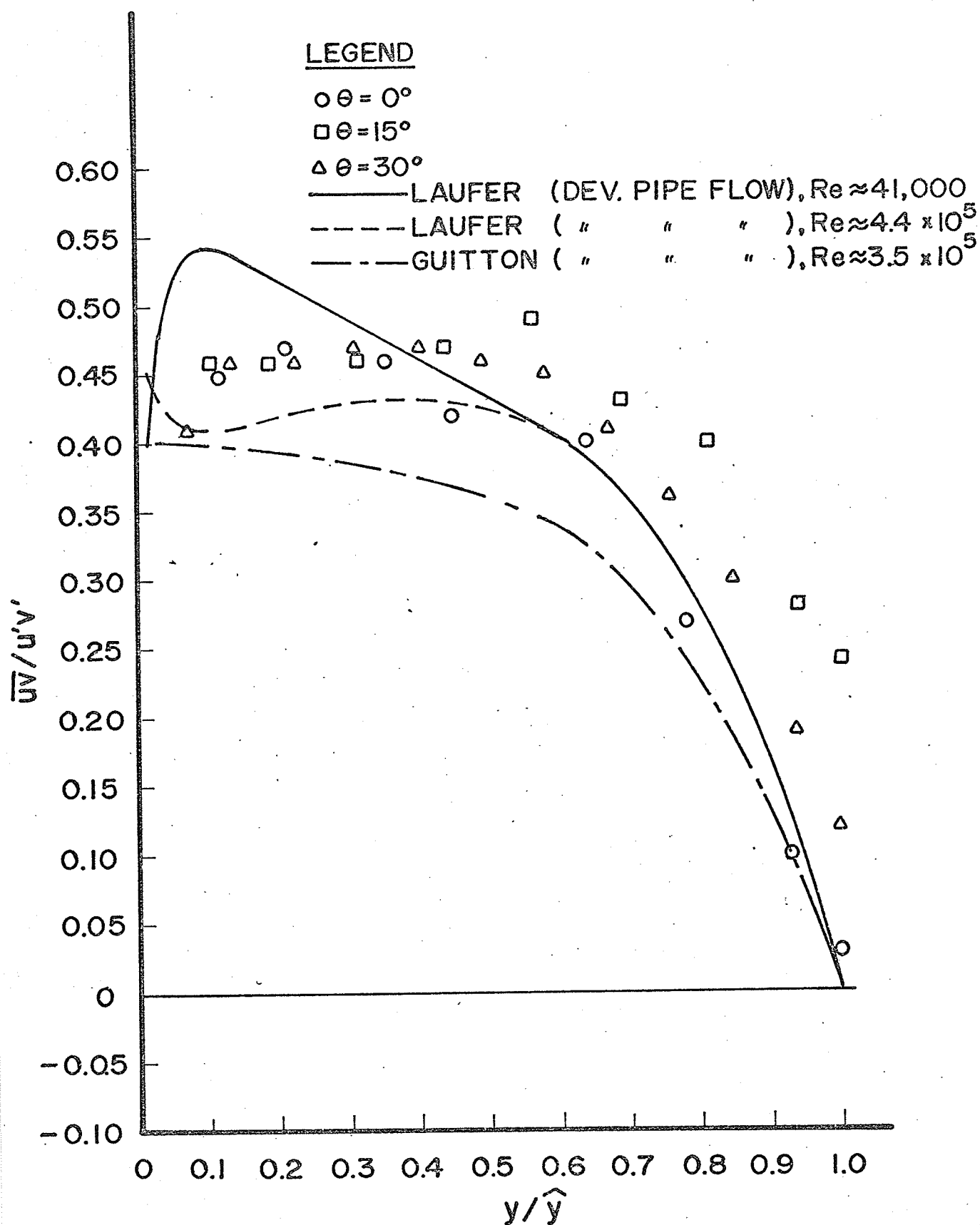
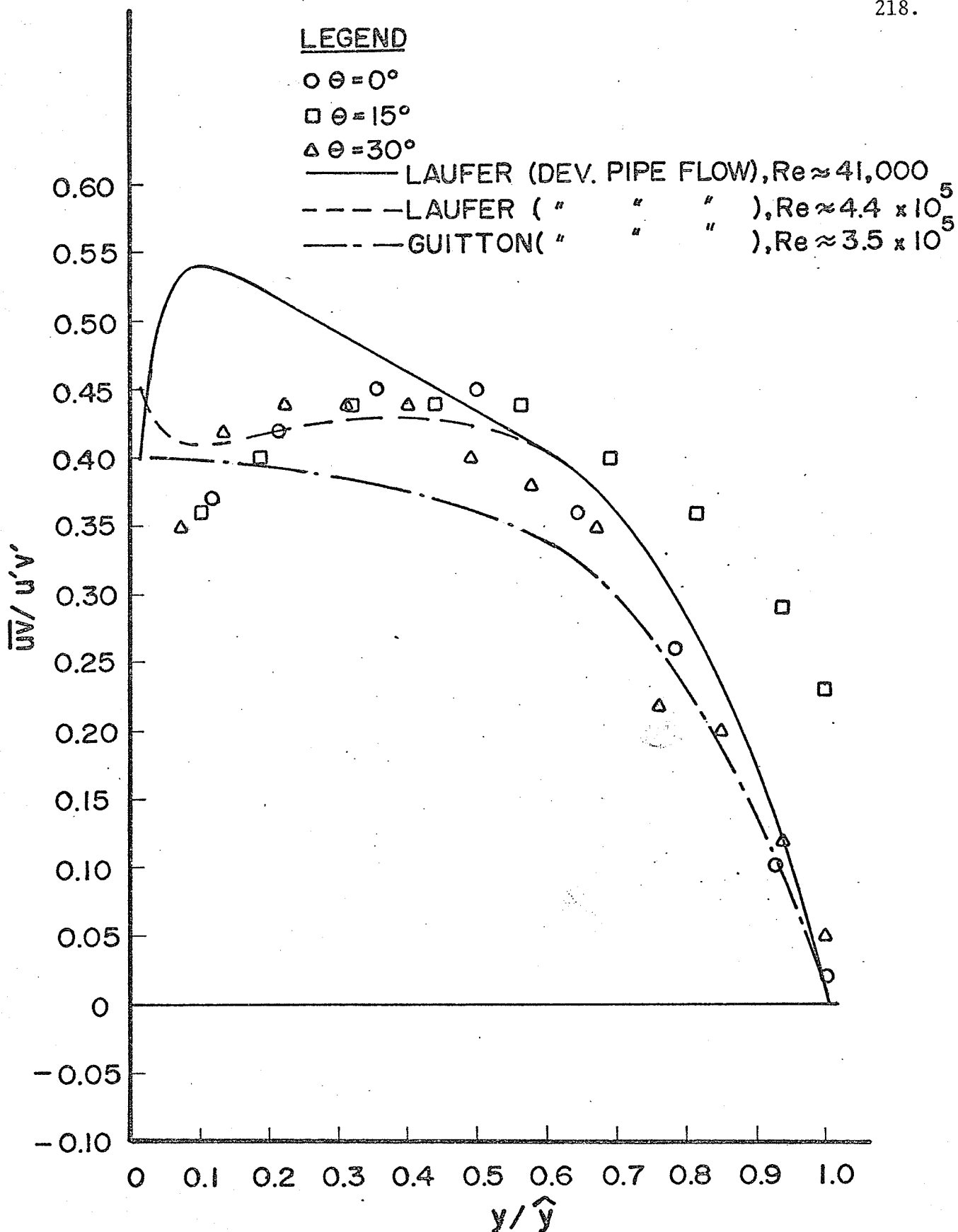


FIG.45c DISTRIBUTION of  $R_{uv}$   
Test 3,  $P/D=1.35$

FIG.45d DISTRIBUTION of  $R_{uv}$ Test 6,  $P/D=1.35$

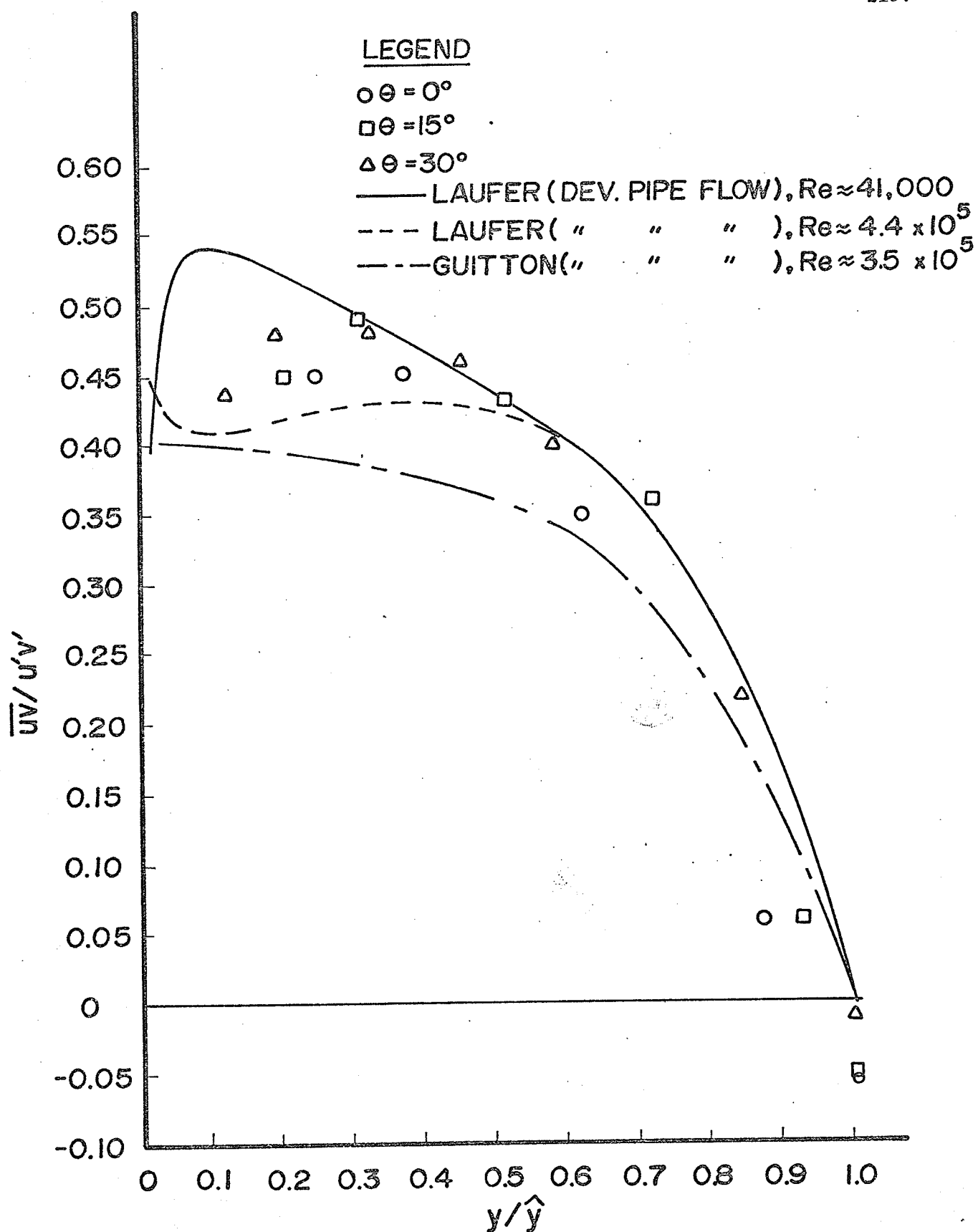


FIG45e DISTRIBUTION of  $R_{uv}$   
Test 4,  $P/D = 1.20$

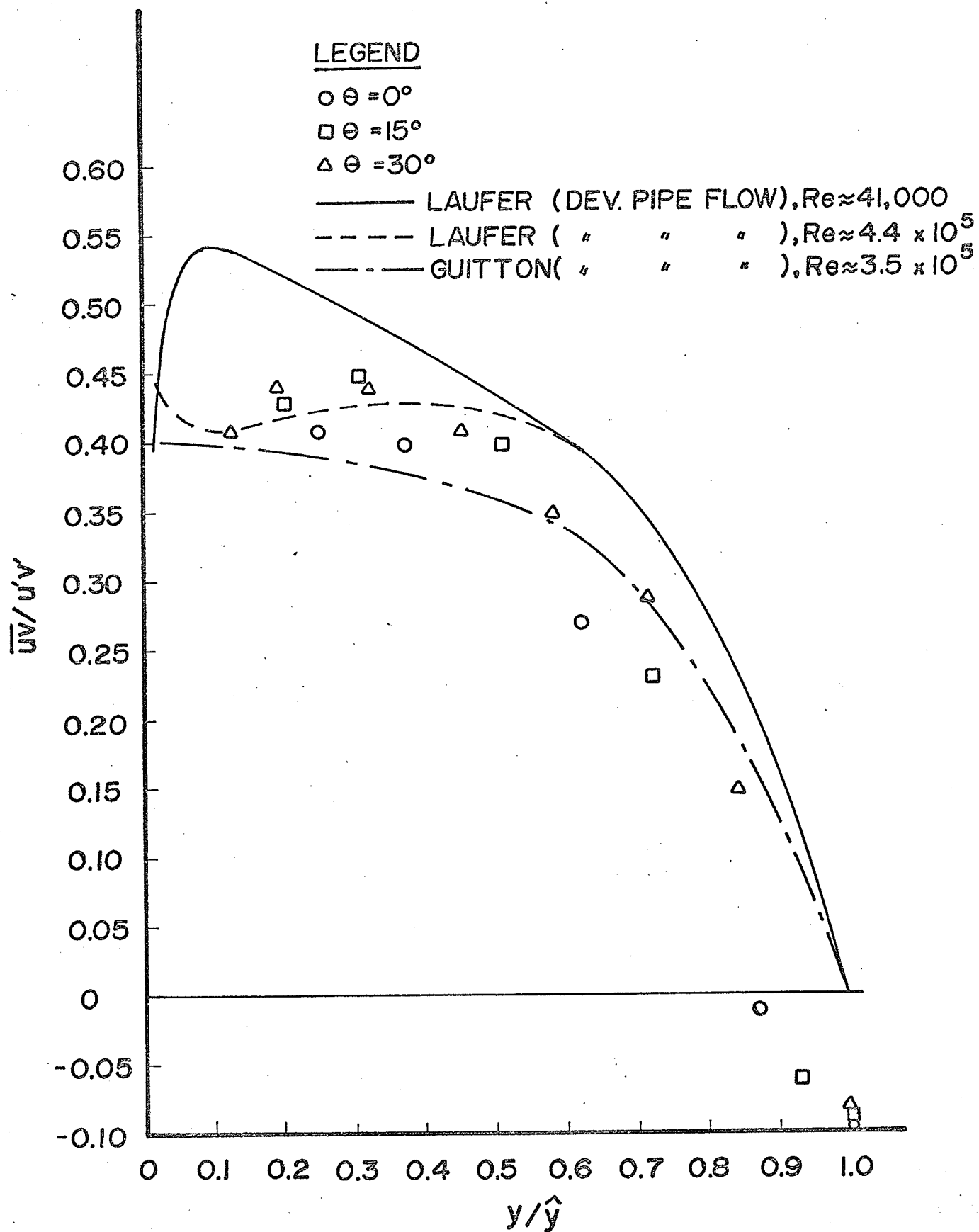


FIG.45 f DISTRIBUTION of  $R_{uv}$   
Test 6,  $P/D=1.20$

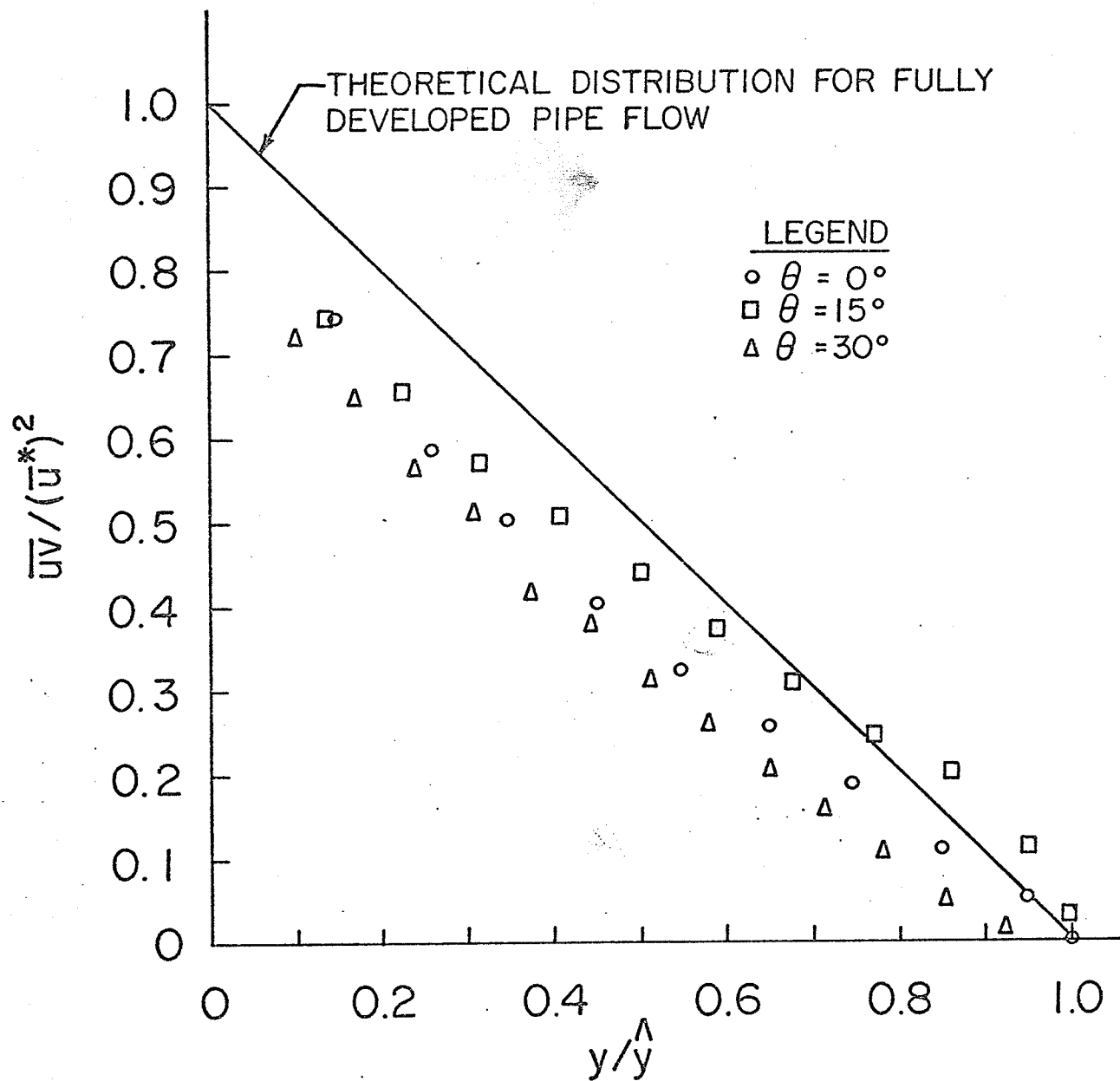


FIG.46a DISTRIBUTION OF REYNOLDS SHEAR STRESS  $\overline{uv}$  TEST 2,  $P/D = 1.50$



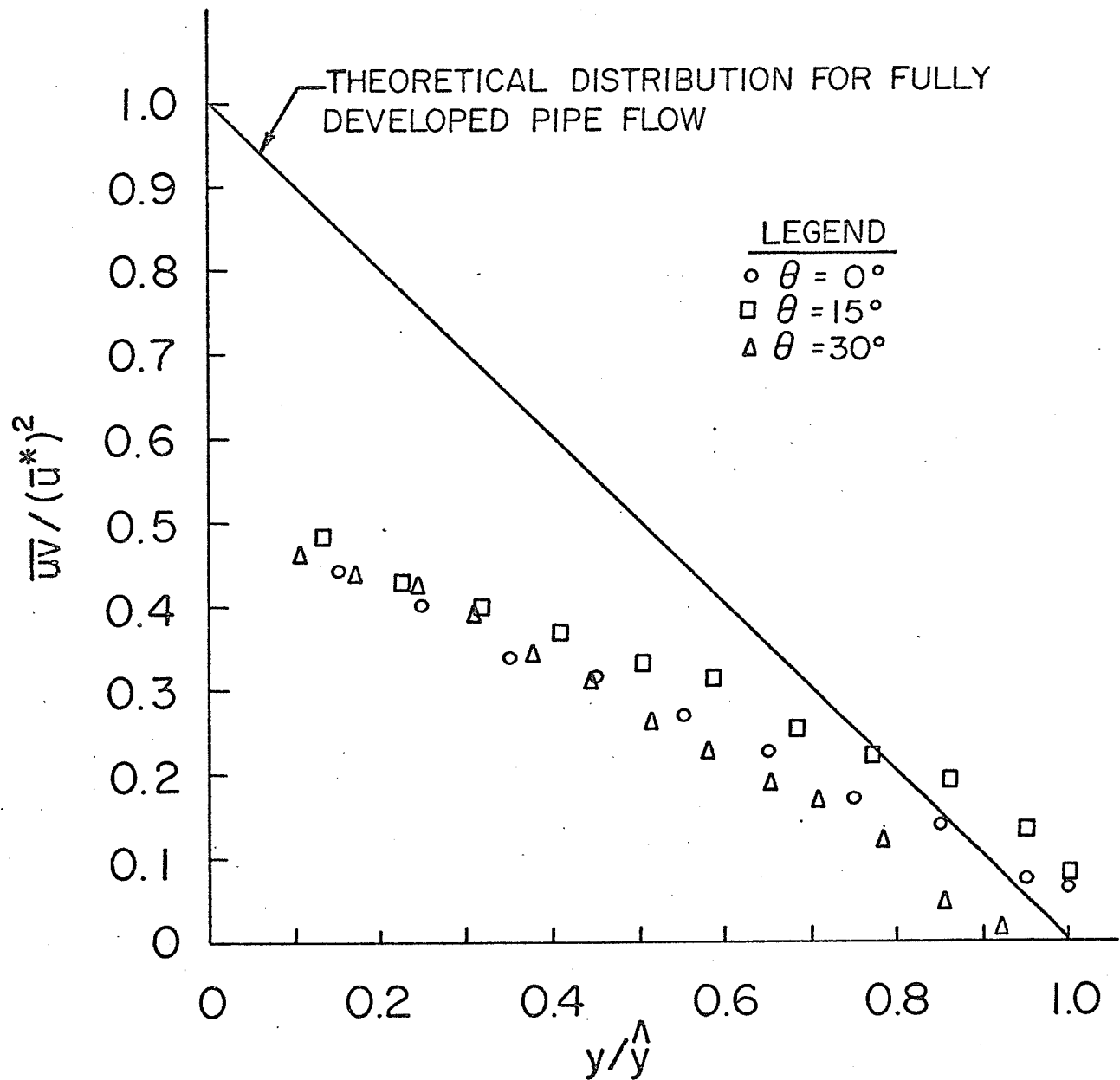


FIG.46b DISTRIBUTION OF REYNOLDS SHEAR STRESS  
 $\overline{uv}$  TEST 5 , P/D = 1.50

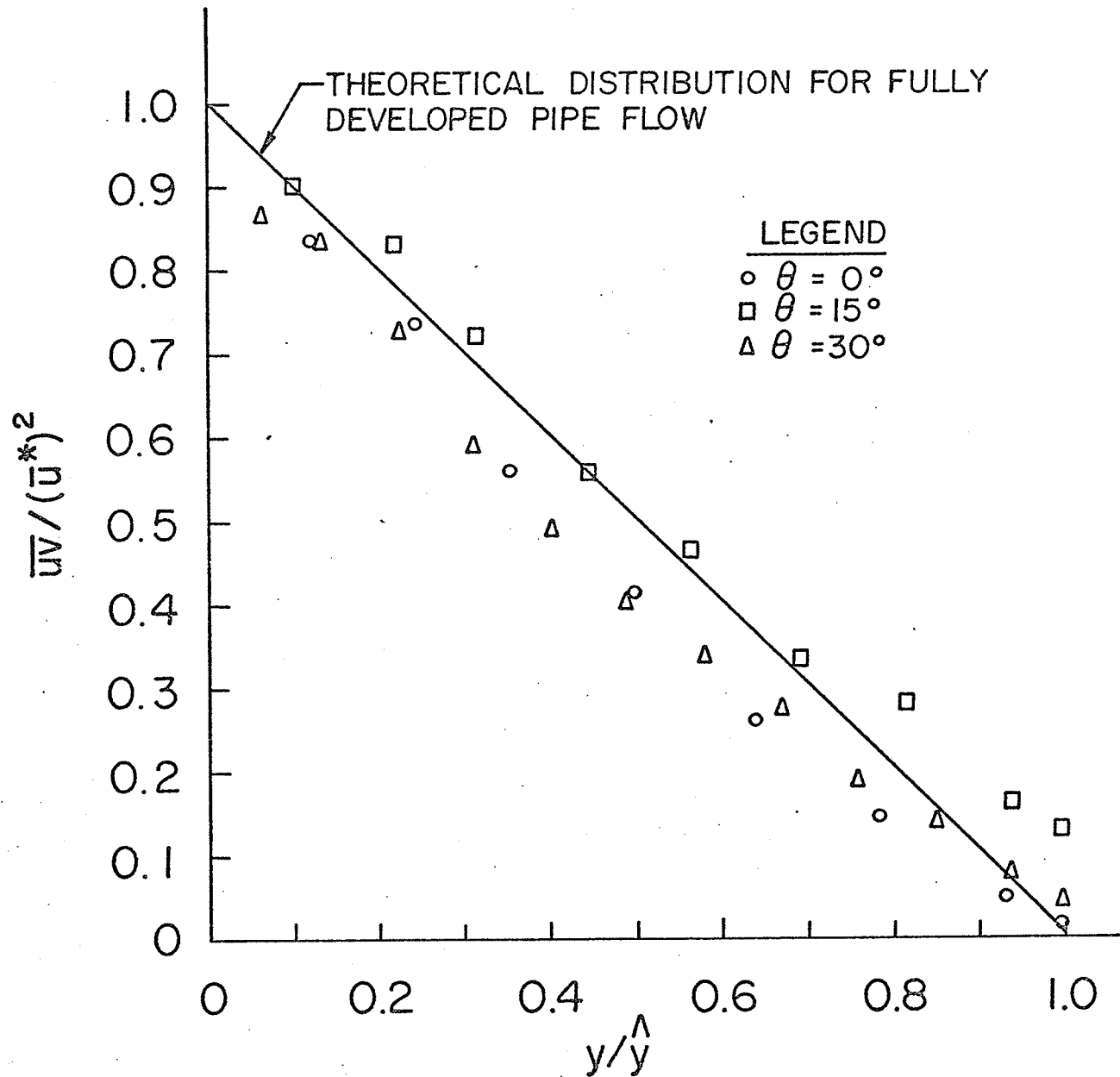


FIG.46c DISTRIBUTION OF REYNOLDS SHEAR STRESS  
 $\overline{uv}$  TEST 3 ,  $P/D = 1.35$

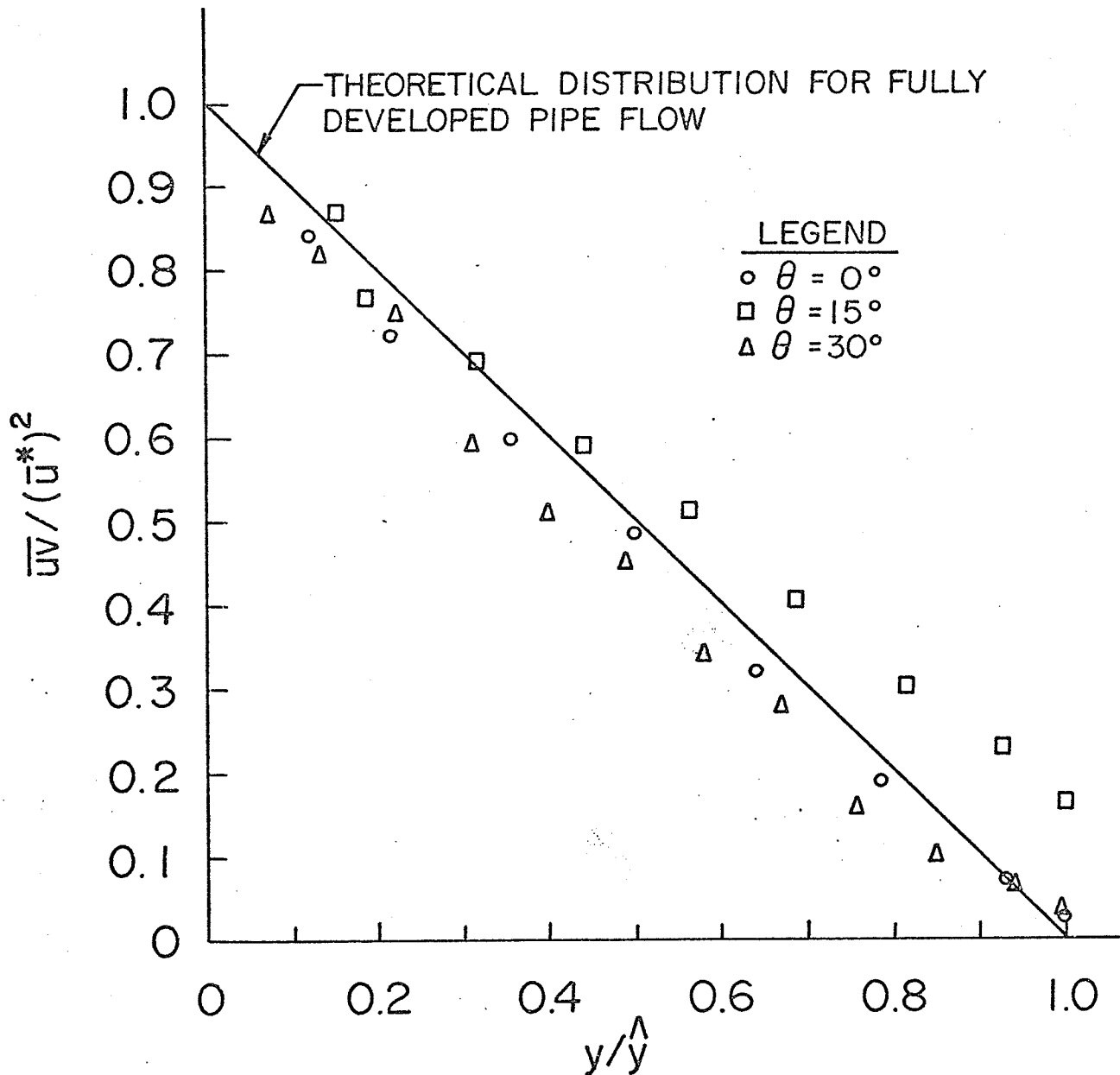


FIG.46d DISTRIBUTION OF REYNOLDS SHEAR STRESS  
 $\overline{uv}$  TEST 6 ,  $P/D = 1.35$

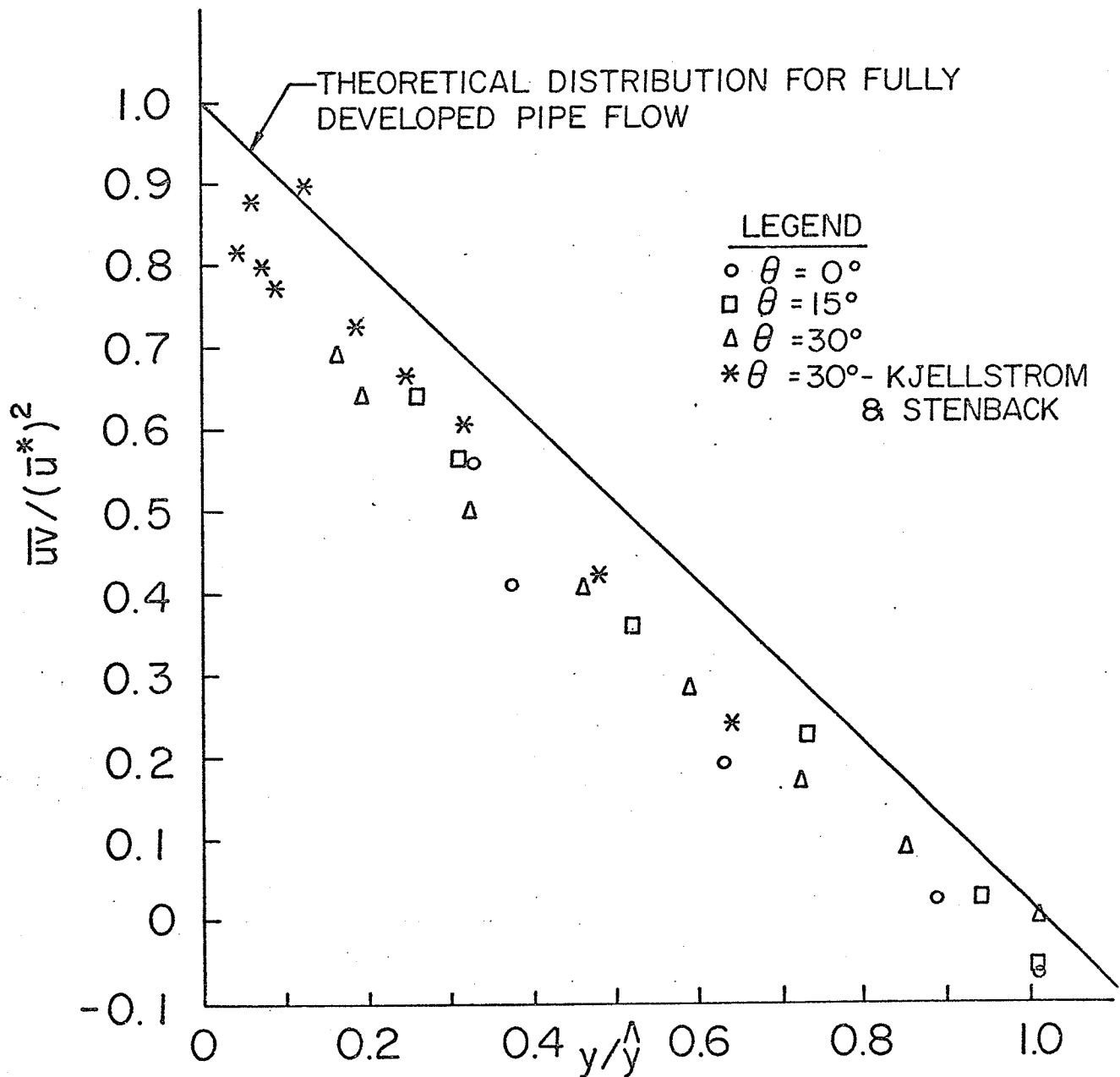


FIG.46e DISTRIBUTION OF REYNOLDS SHEAR STRESS  
 $\overline{uv}$  TEST 4 ,  $P/D = 1.20$

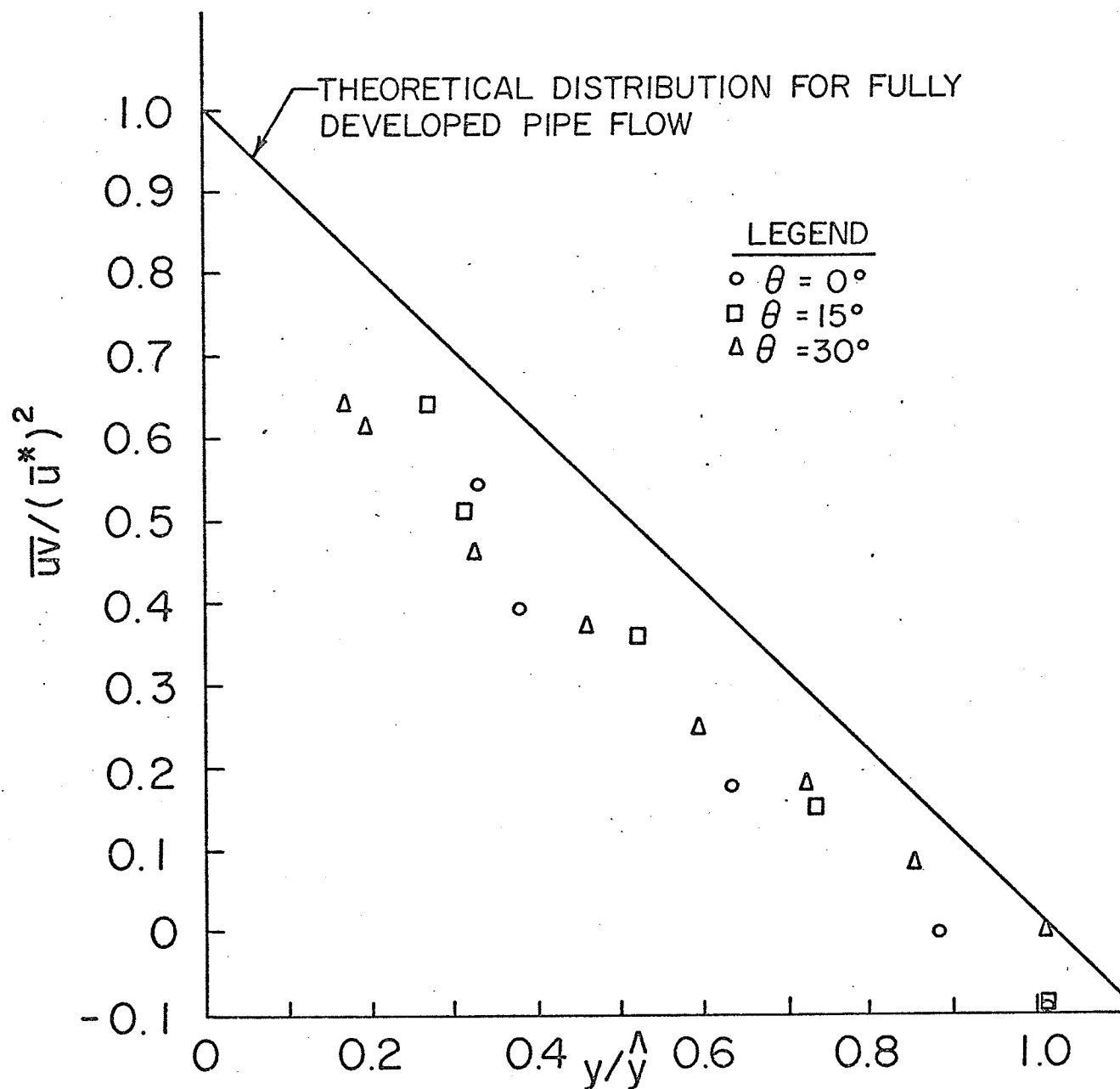


FIG.46f DISTRIBUTION OF REYNOLDS SHEAR STRESS  
 $\overline{uv}$  TEST 6 , P/D = 1.20

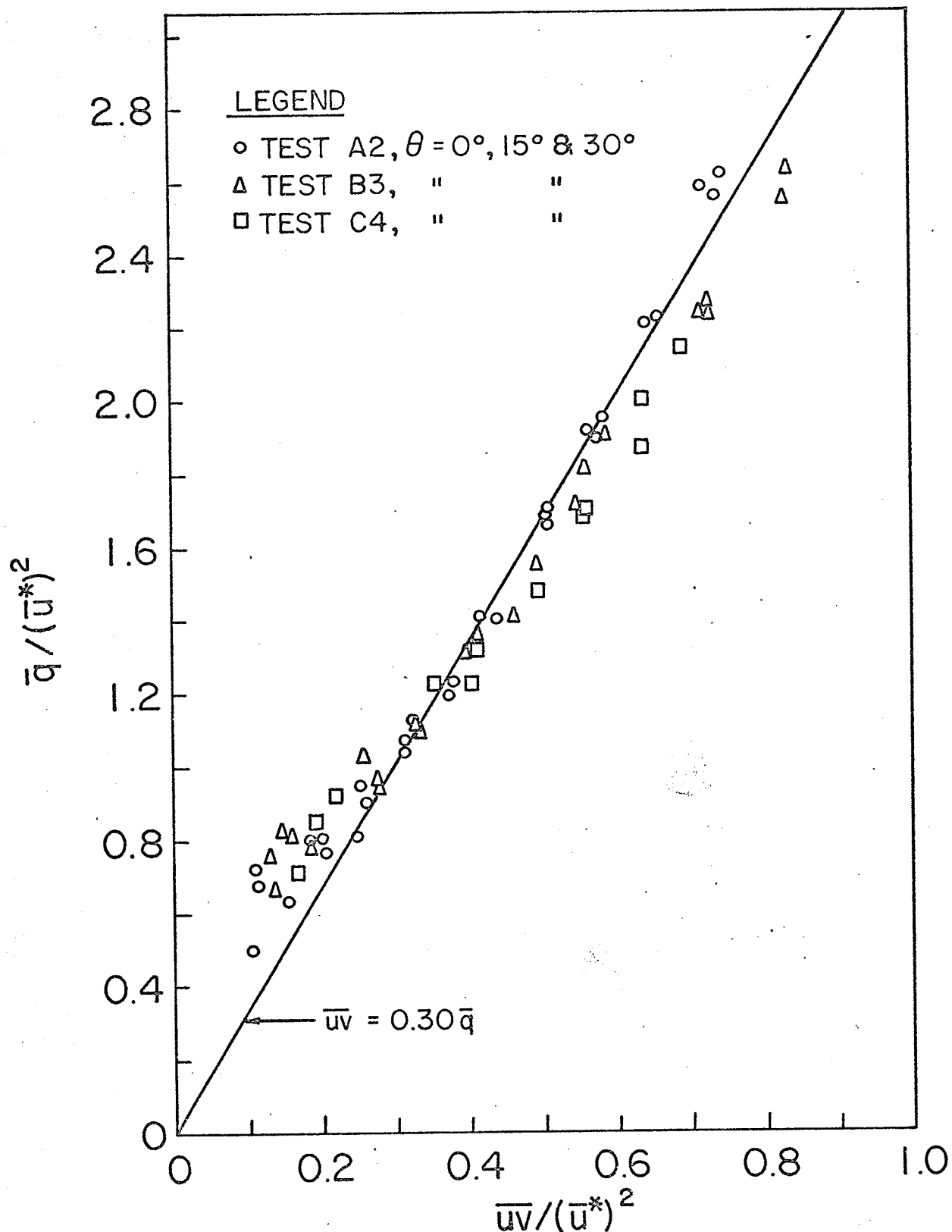


FIG. 47 CORRELATION BETWEEN TURBULENT SHEAR STRESS AND MEAN TURBULENT KINETIC ENERGY FOR ROD BUNDLE FLOWS

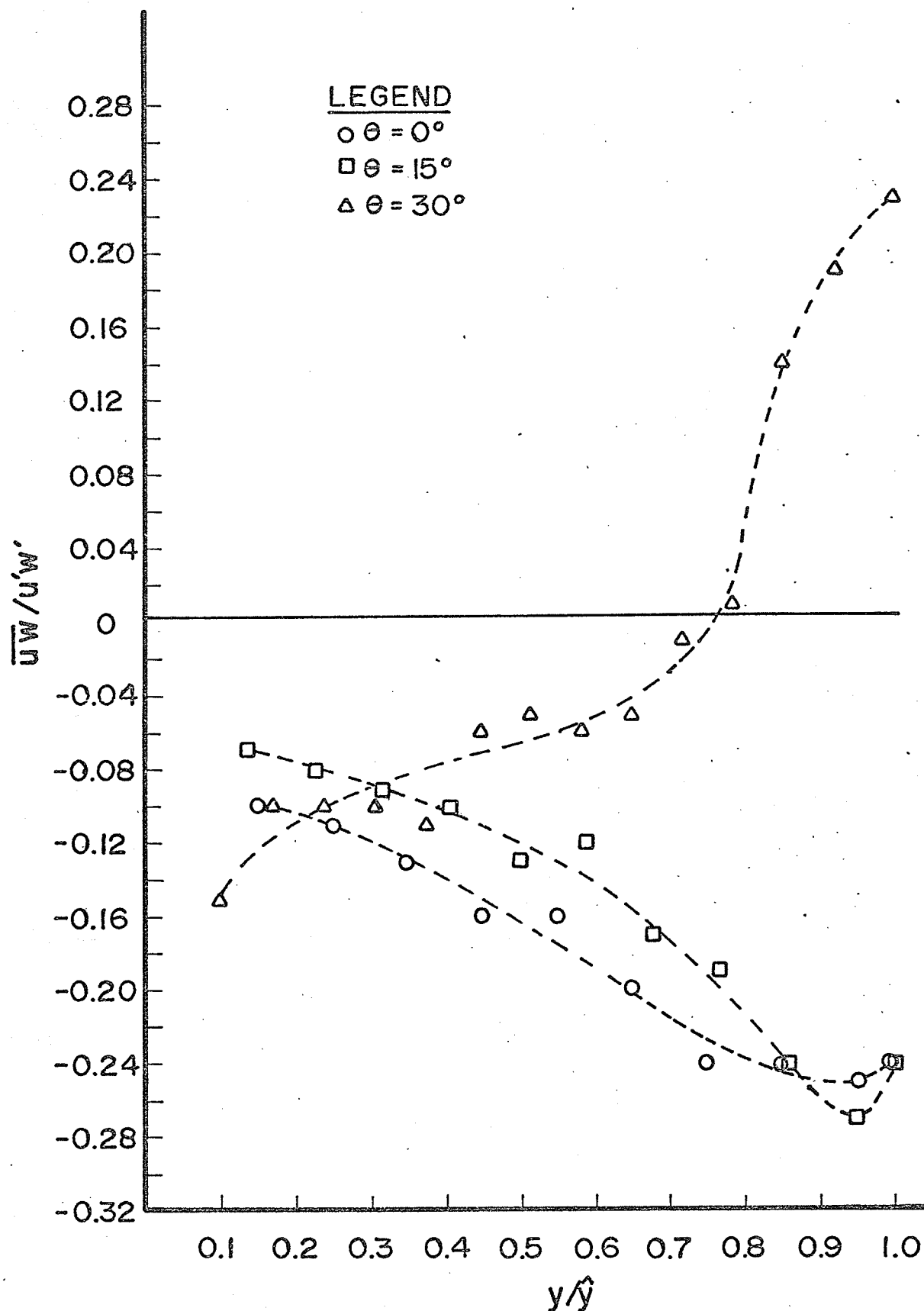


FIG.48a DISTRIBUTION of  $R_{uw}$   
Test 2,  $P/D=1.50$

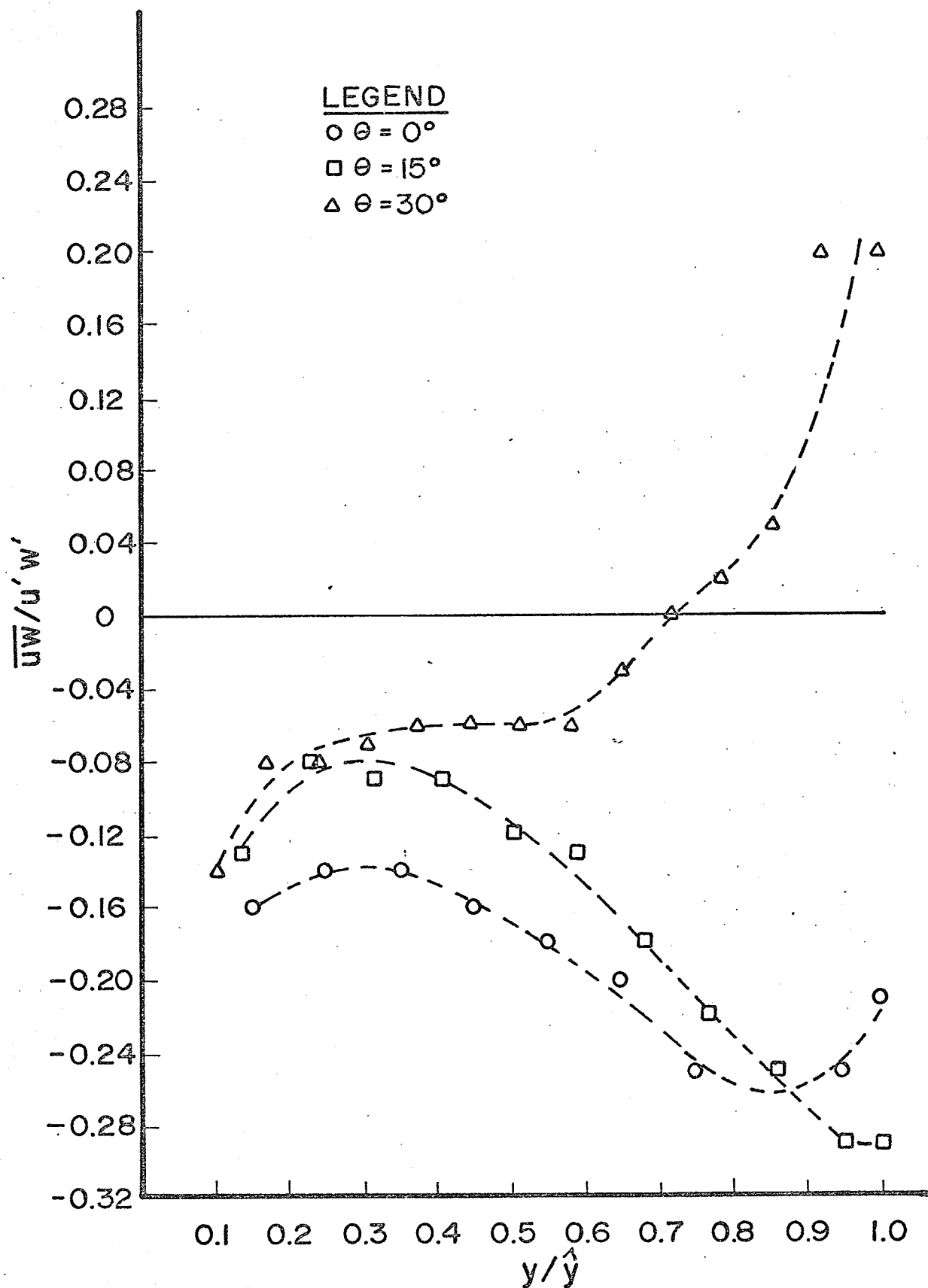


FIG. 48b DISTRIBUTION of  $R_{uw}$   
Test 5,  $P/D=1.50$



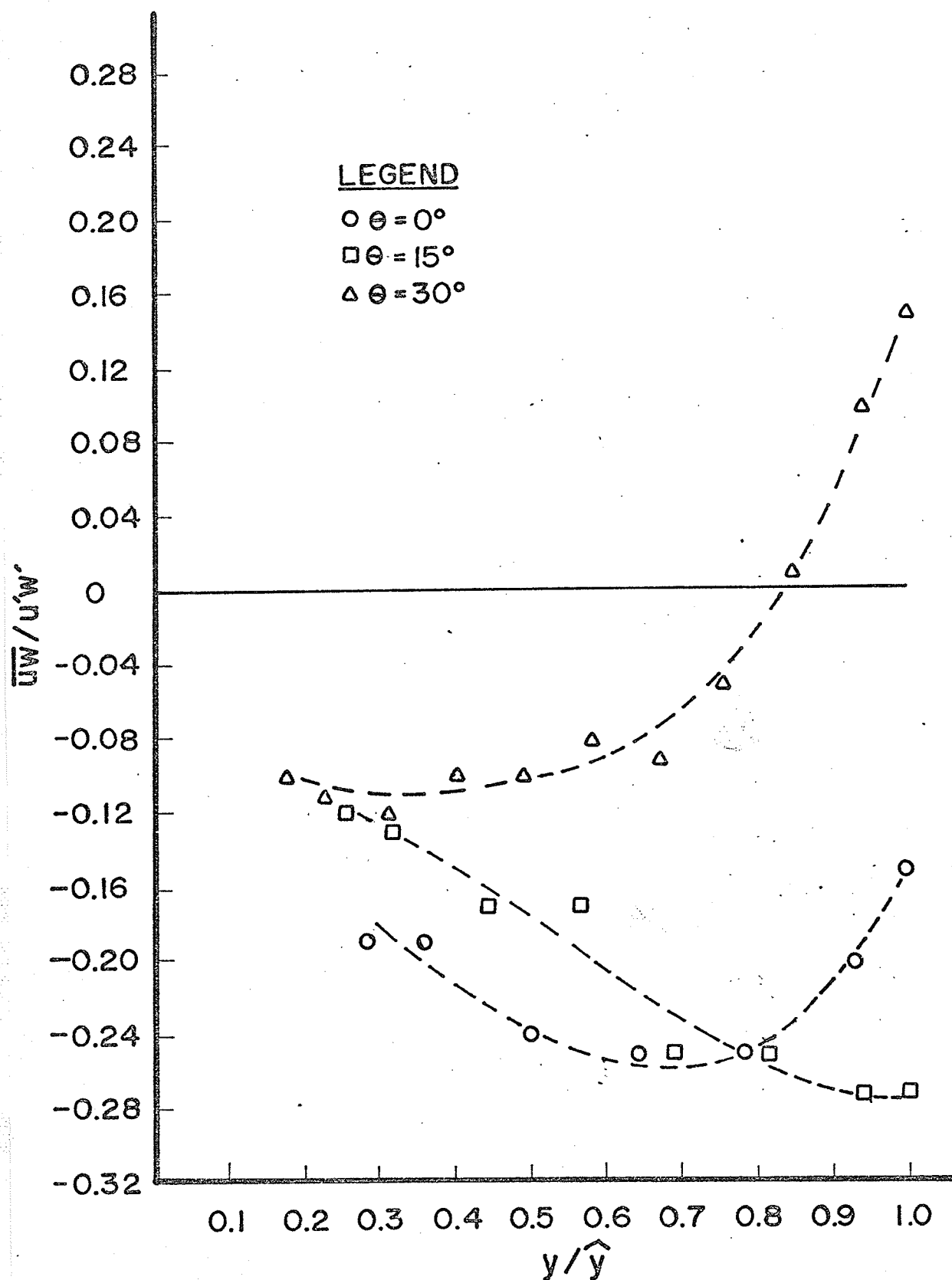


FIG.48c DISTRIBUTION of  $R_{uw}$   
Test 3,  $P/D=1.35$

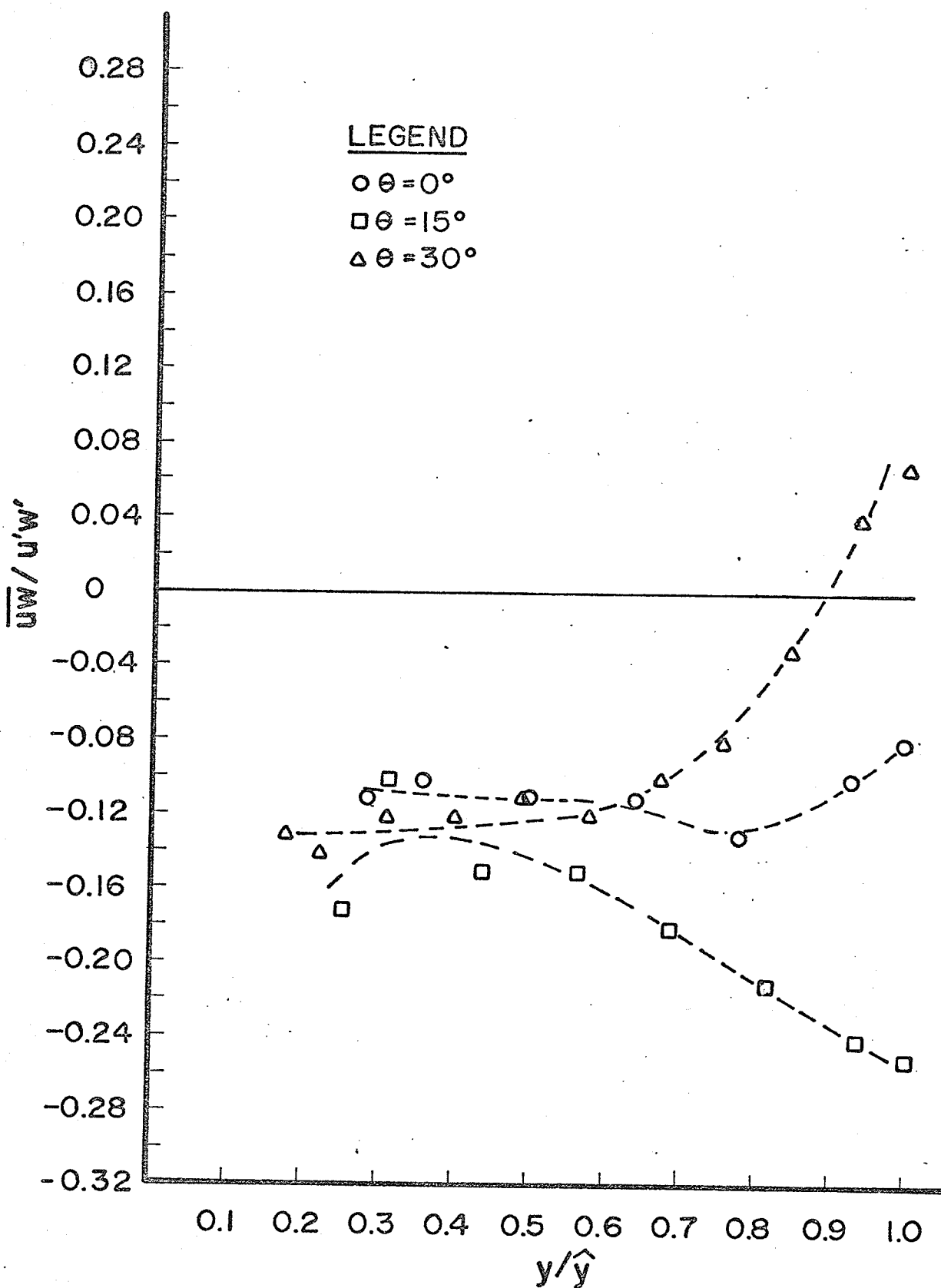


FIG. 48d DISTRIBUTION of  $R_{uw}$   
Test 6,  $P/D=1.35$

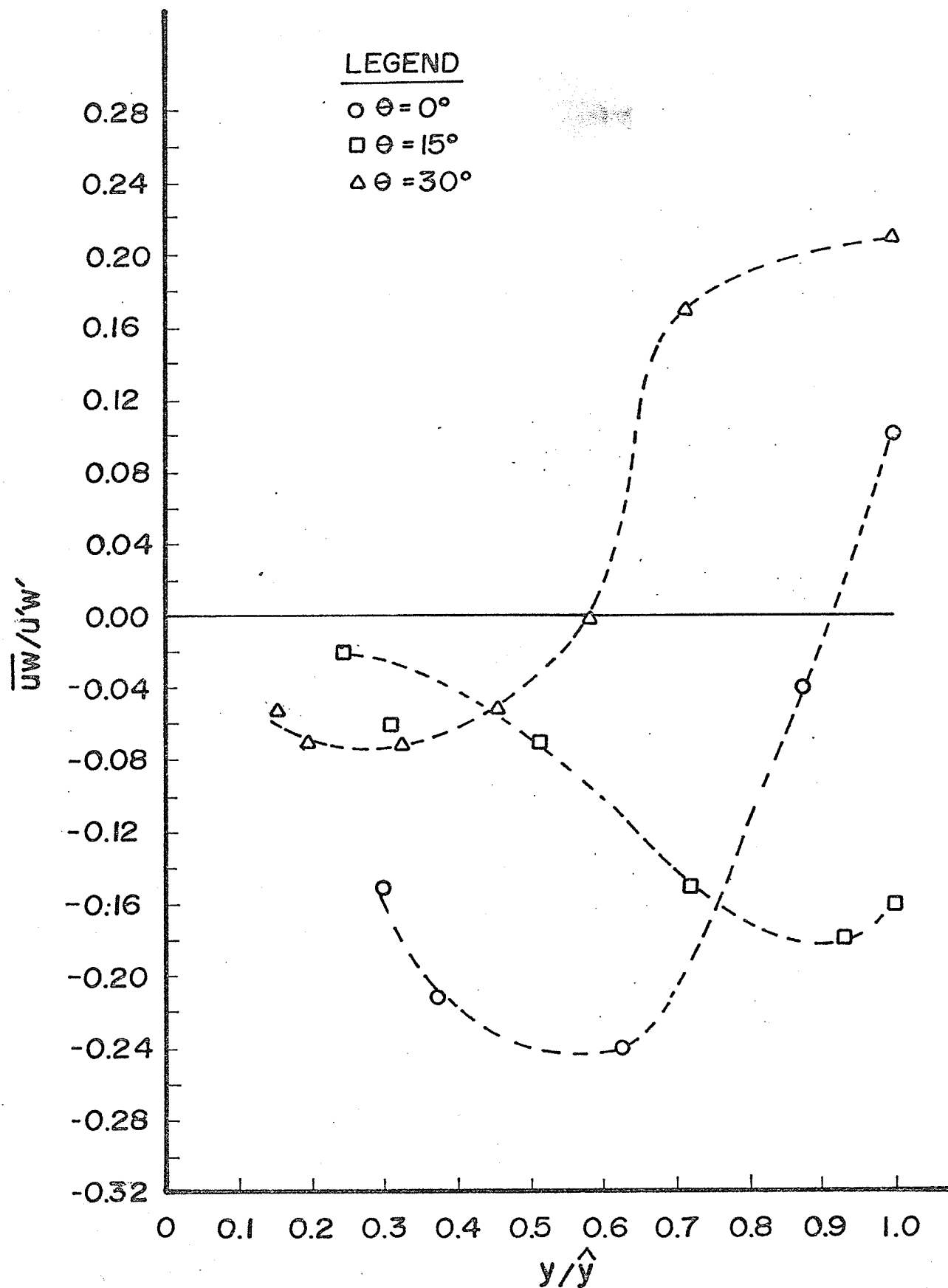
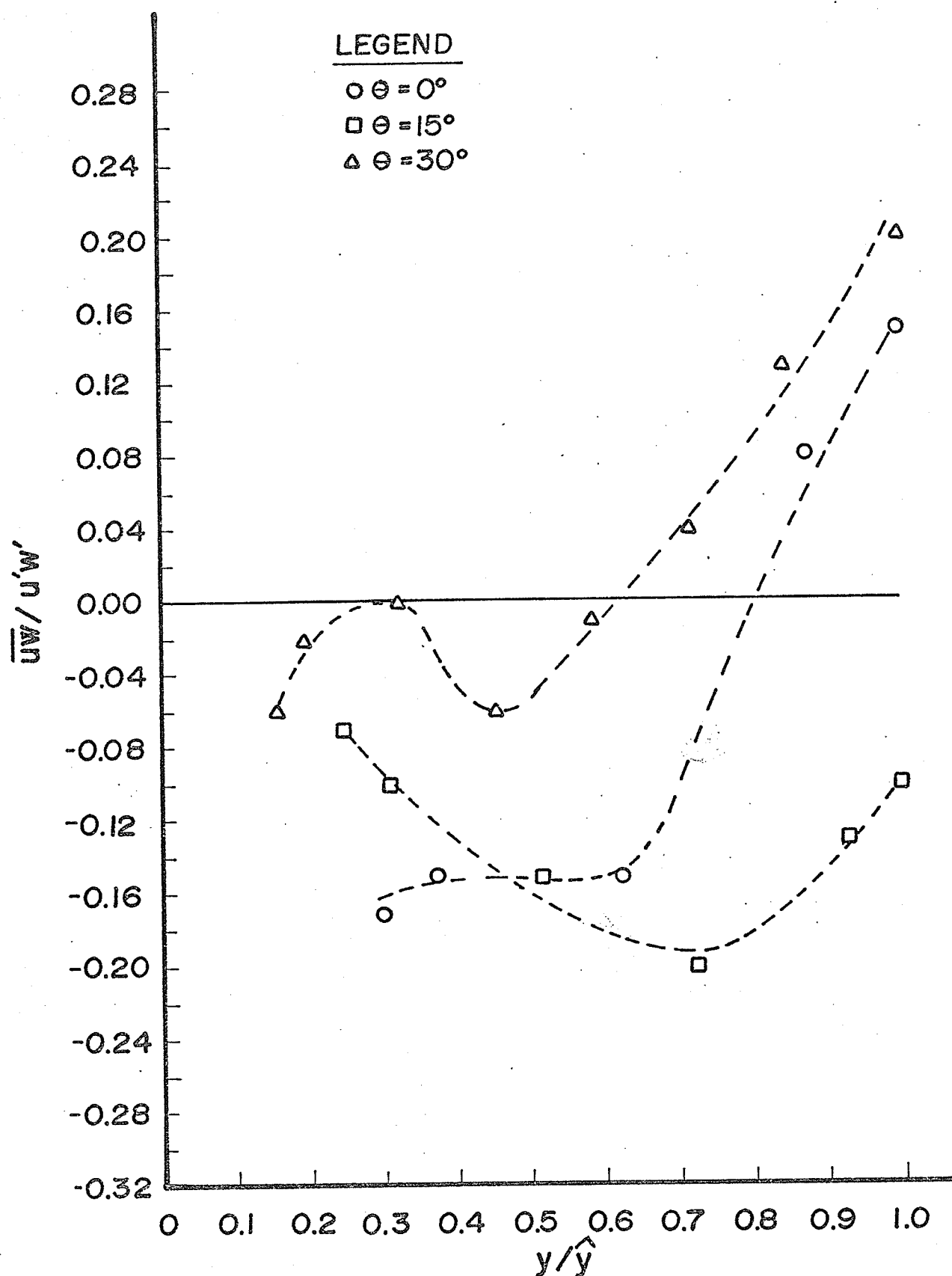


FIG.48e DISTRIBUTION of  $R_{uw}$   
Test 4,  $P/D=1.20$

FIG.48f DISTRIBUTION of  $R_{uw}$ Test 6,  $P/D = 1.20$

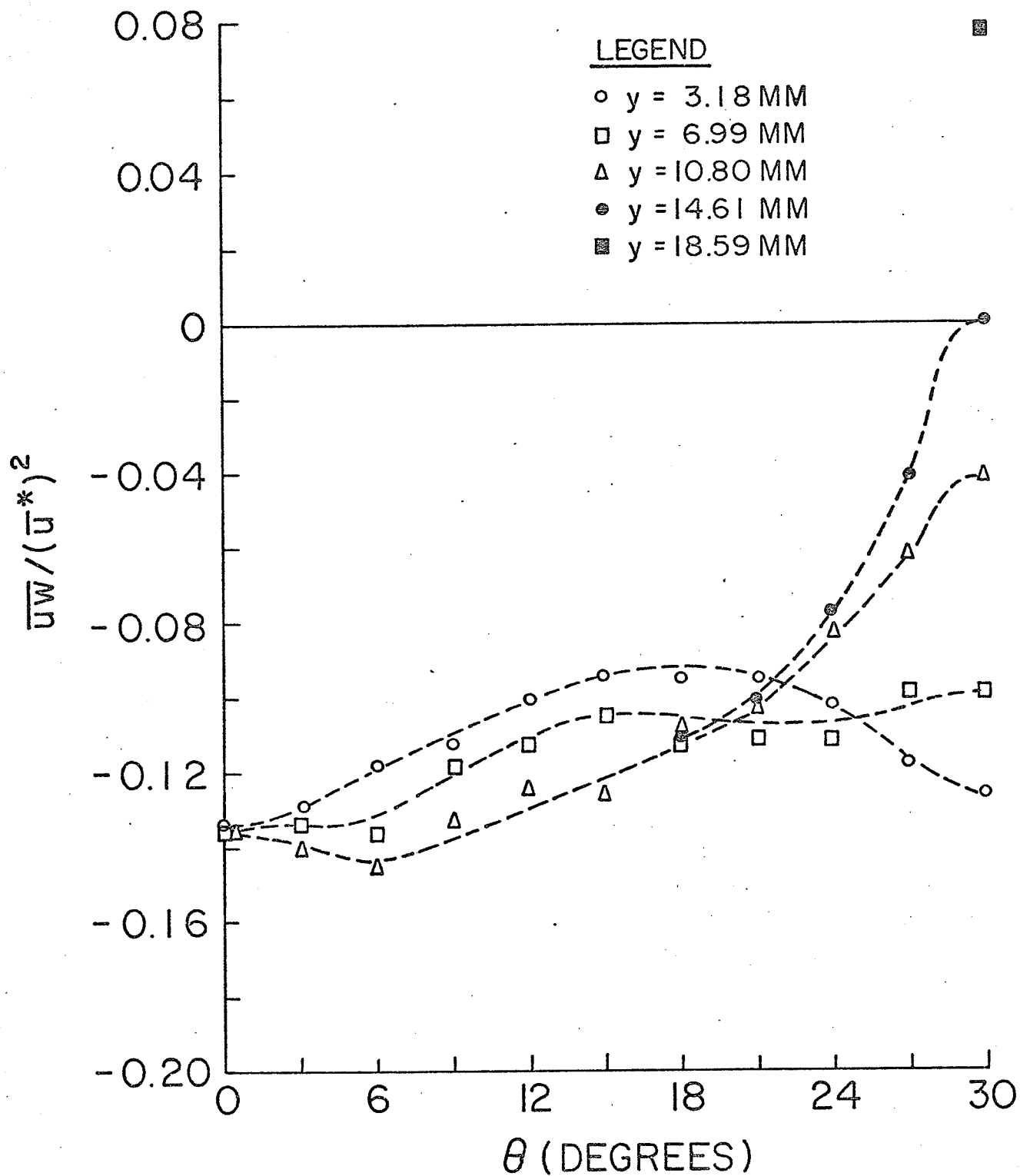


FIG.49a DISTRIBUTION OF REYNOLDS SHEAR STRESS  
 $\overline{uw}$  TEST 2,  $P/D = 1.50$

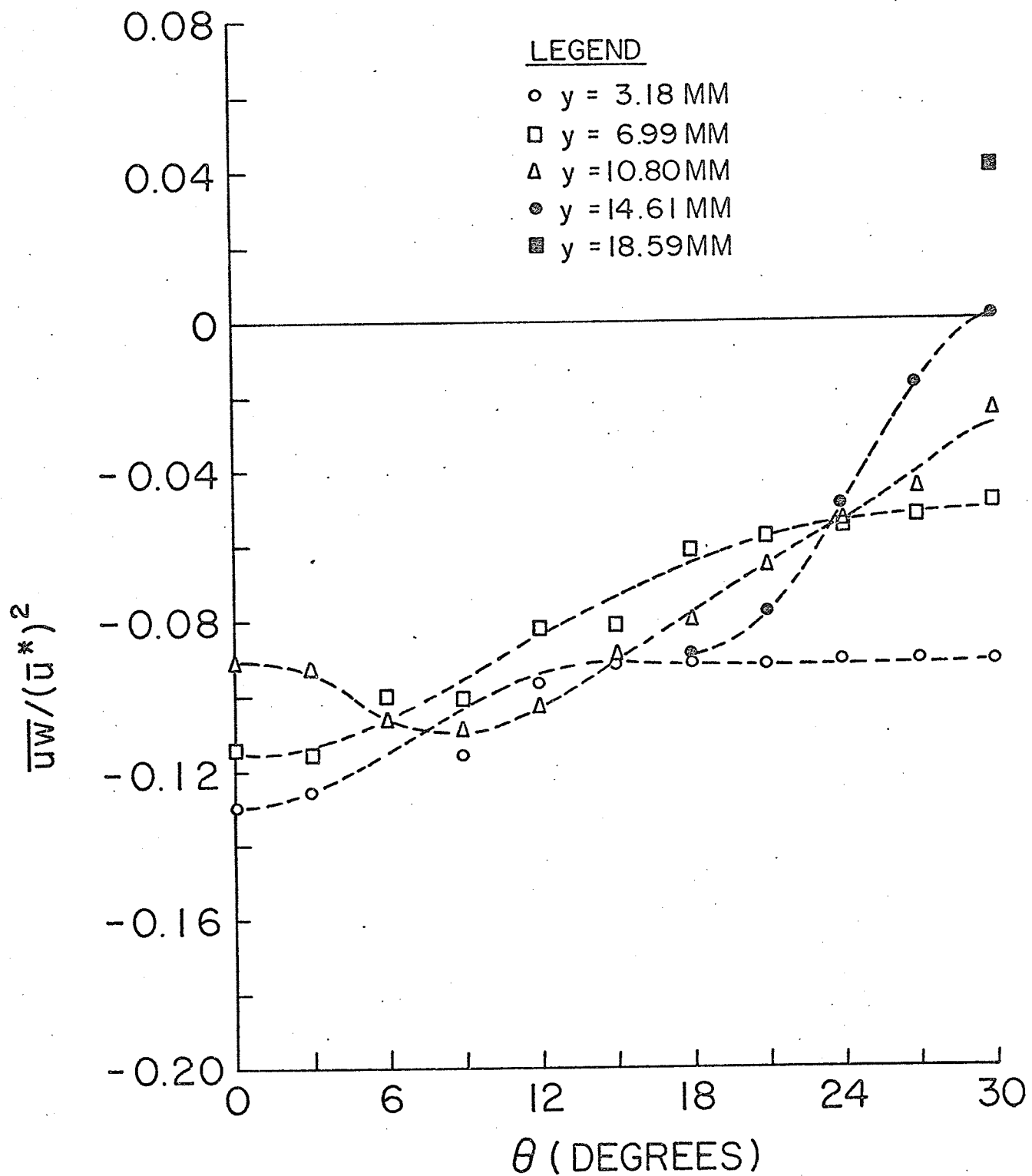


FIG.49b DISTRIBUTION OF REYNOLDS SHEAR STRESS  
 $\overline{uw}$  TEST 5 , P/D = 1.50

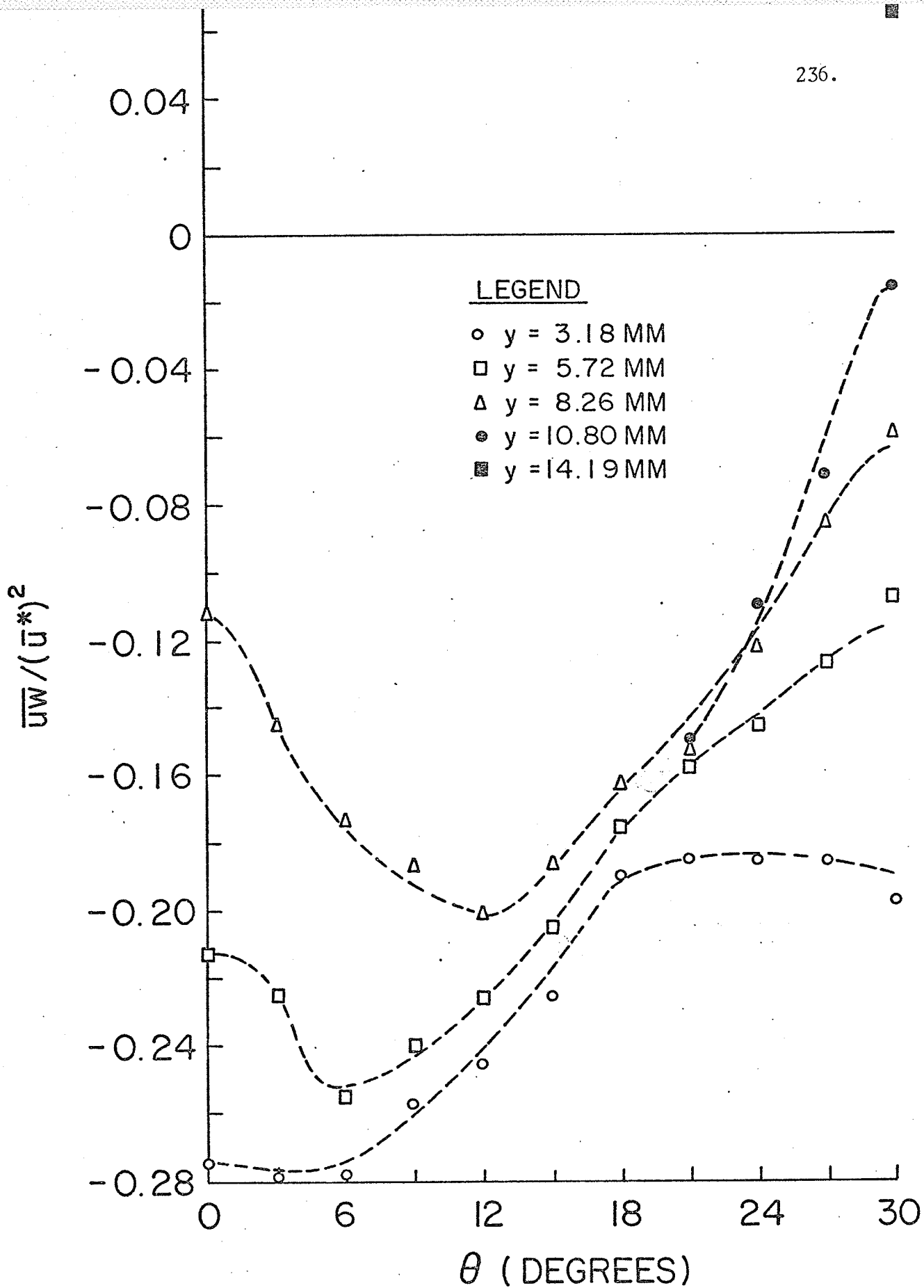


FIG.49c DISTRIBUTION OF REYNOLDS SHEAR STRESS,  $\overline{uw}$  TEST 3,  $P/D = 1.35$

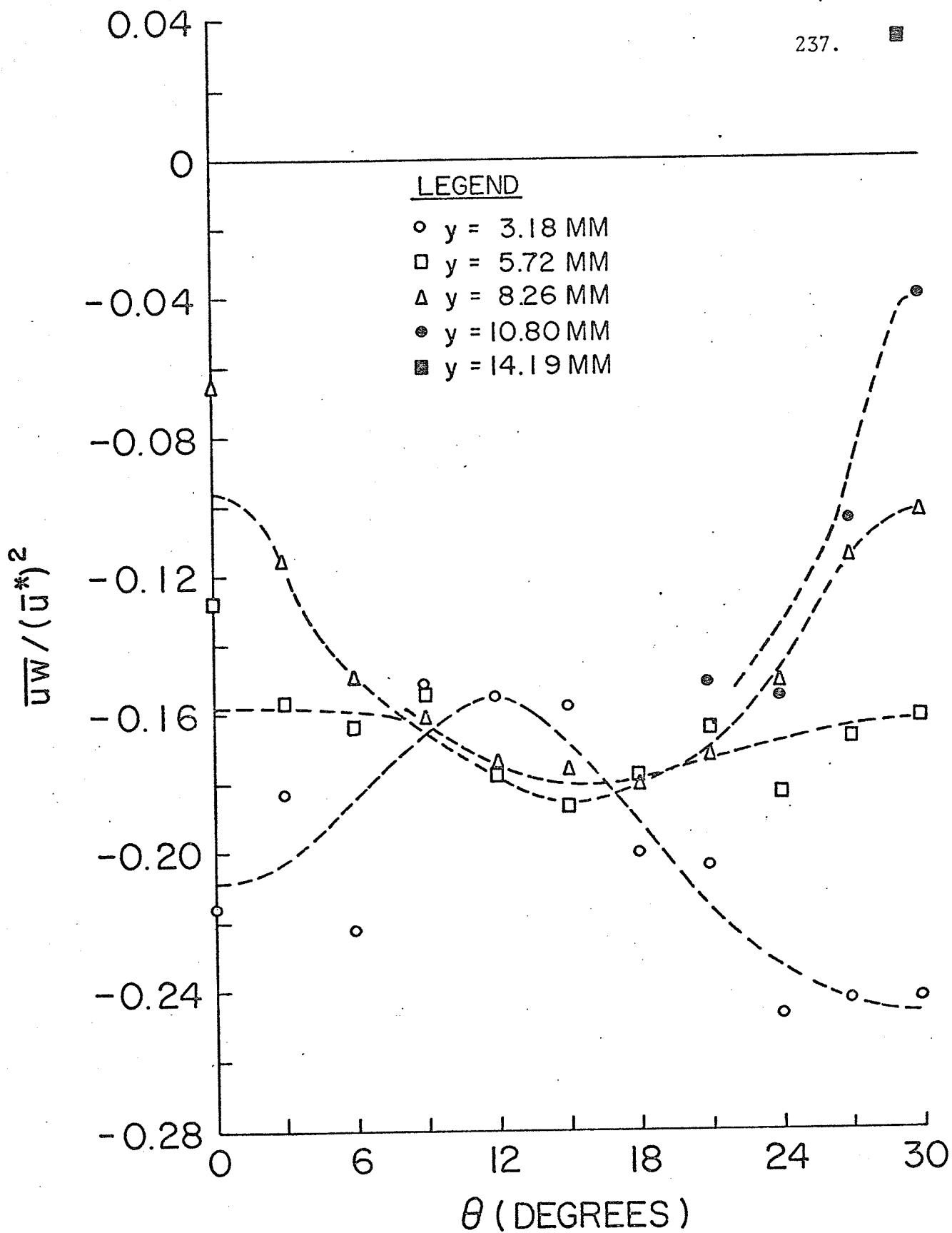


FIG.49d DISTRIBUTION OF REYNOLDS SHEAR STRESS  
 $\overline{u'w'}$  TEST 6 ,  $P/D = 1.35$



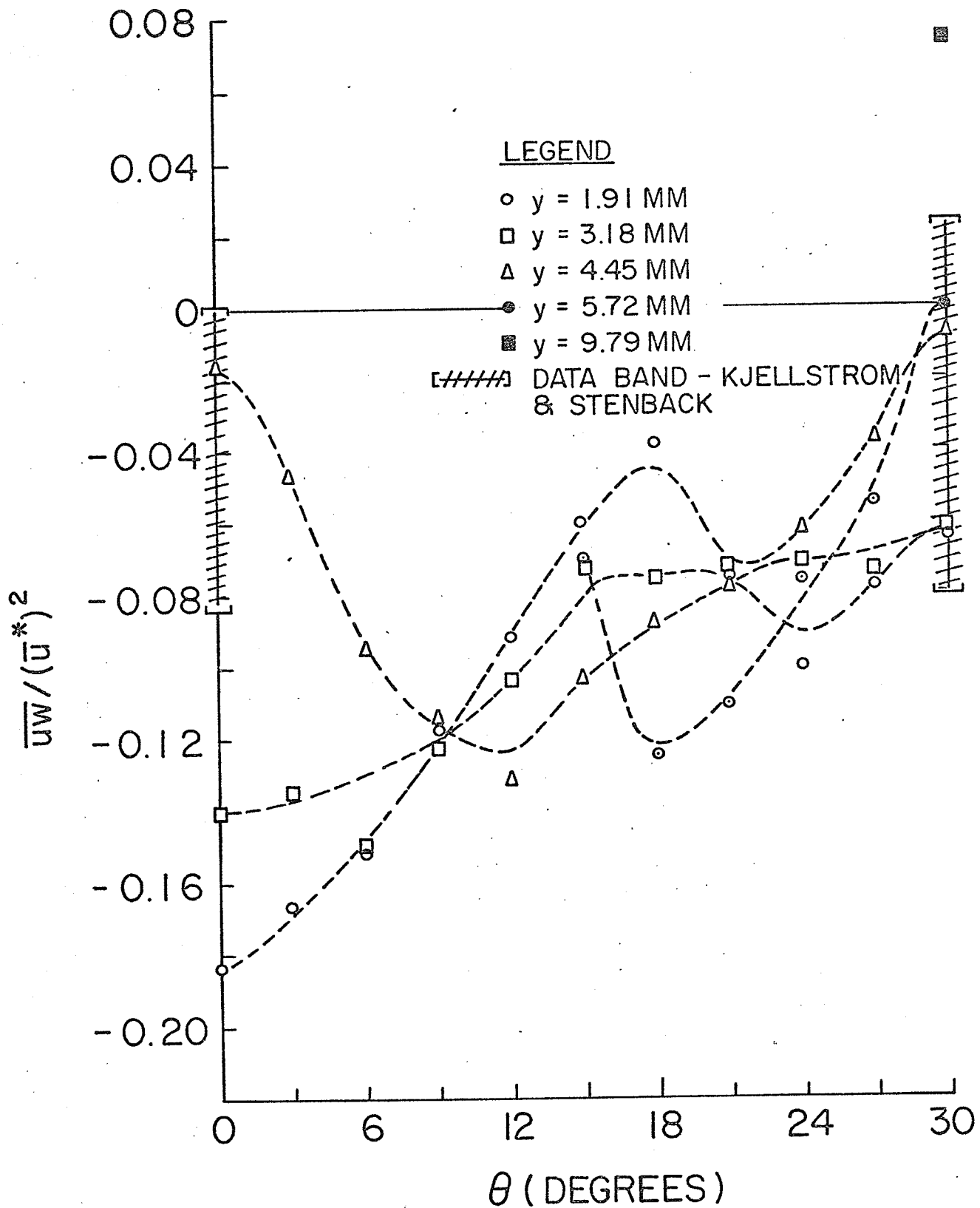


FIG.49e DISTRIBUTION OF REYNOLDS SHEAR STRESS  
 $\overline{uw}$  TEST 4, P/D = 1.20

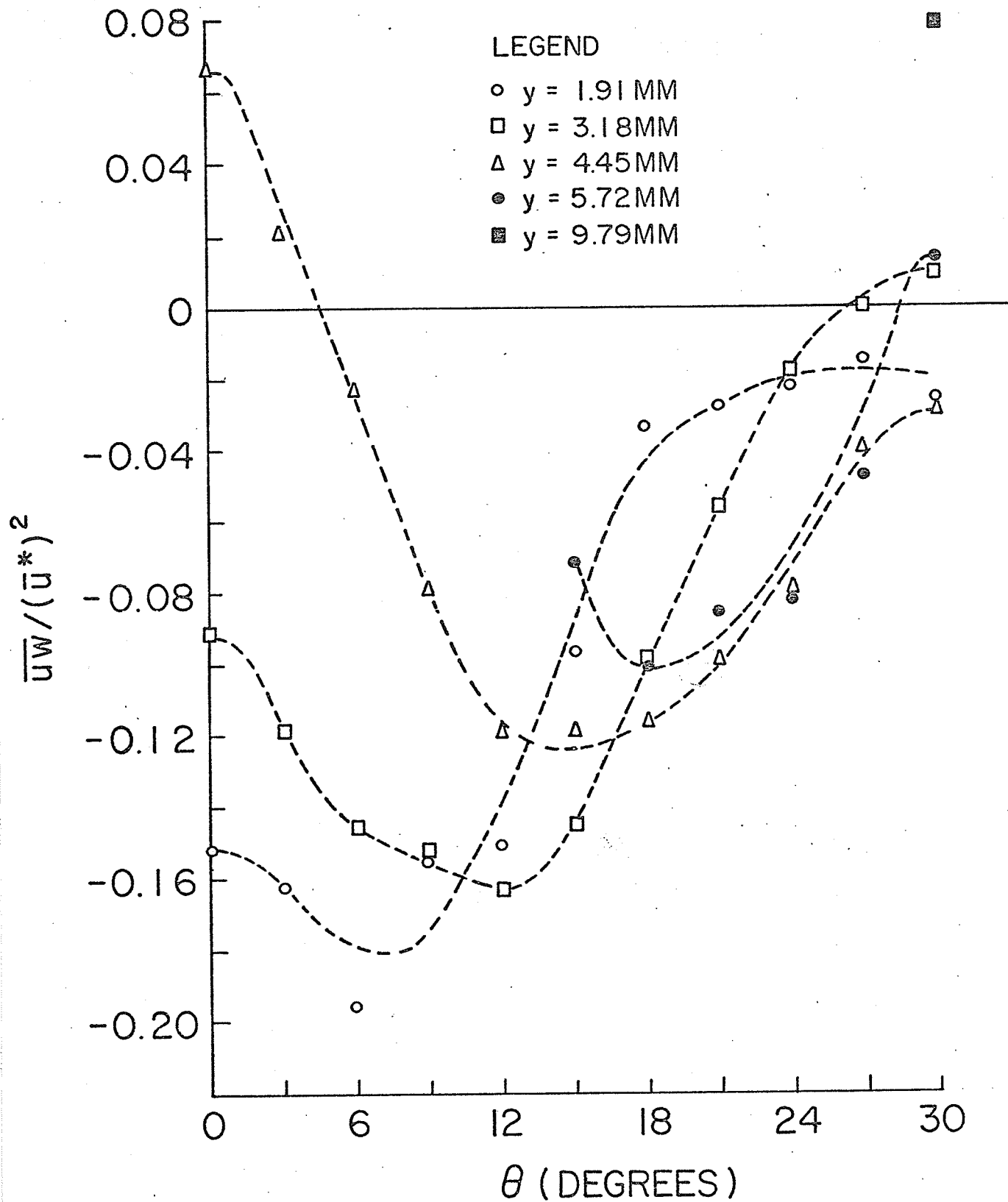


FIG.49f DISTRIBUTION OF REYNOLDS SHEAR STRESS,  
 $\overline{uw}$  TEST 6,  $P/D = 1.20$

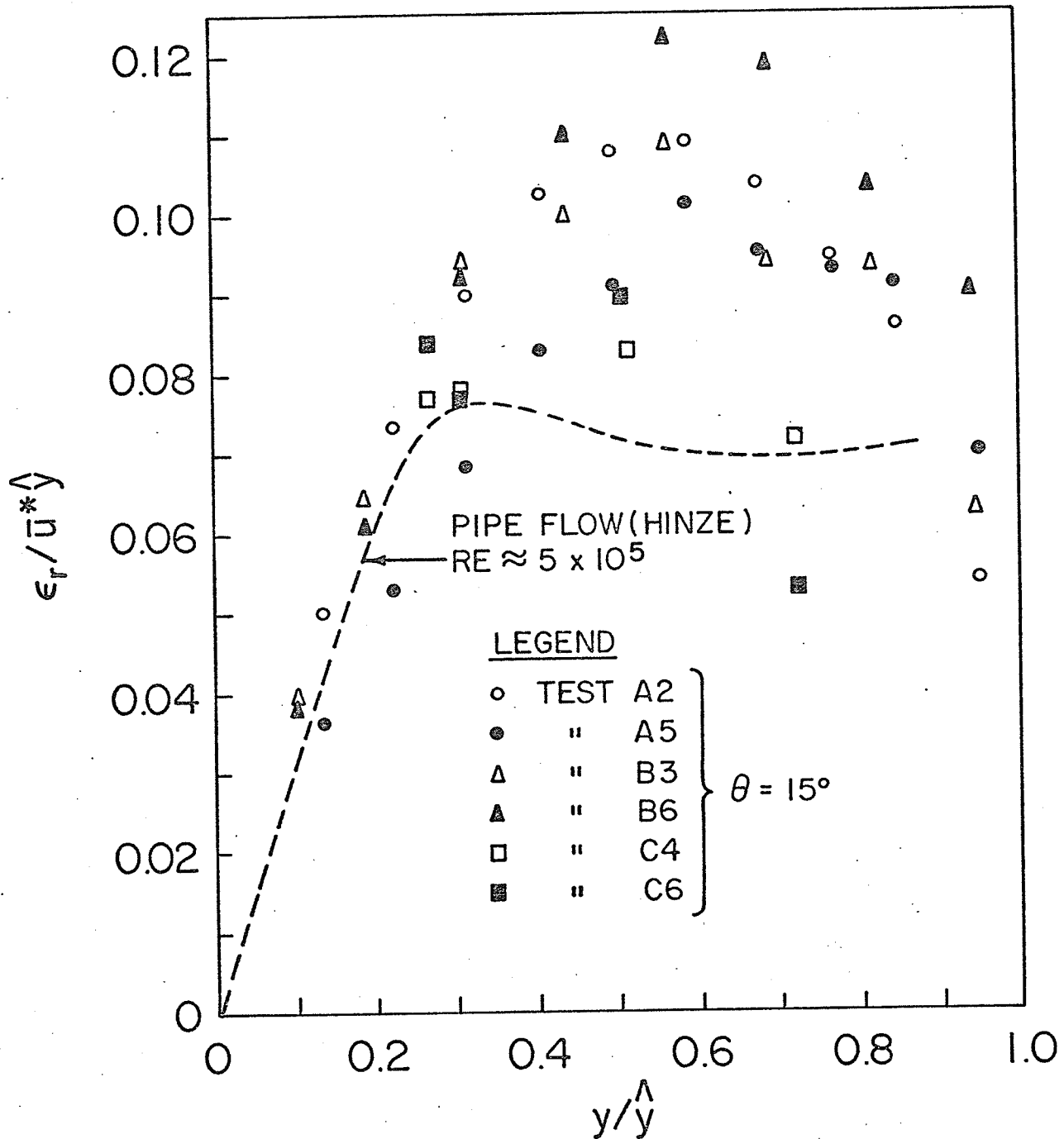


FIG.50 DISTRIBUTIONS OF EDDY DIFFUSIVITIES  
 IN THE RADIAL DIRECTION

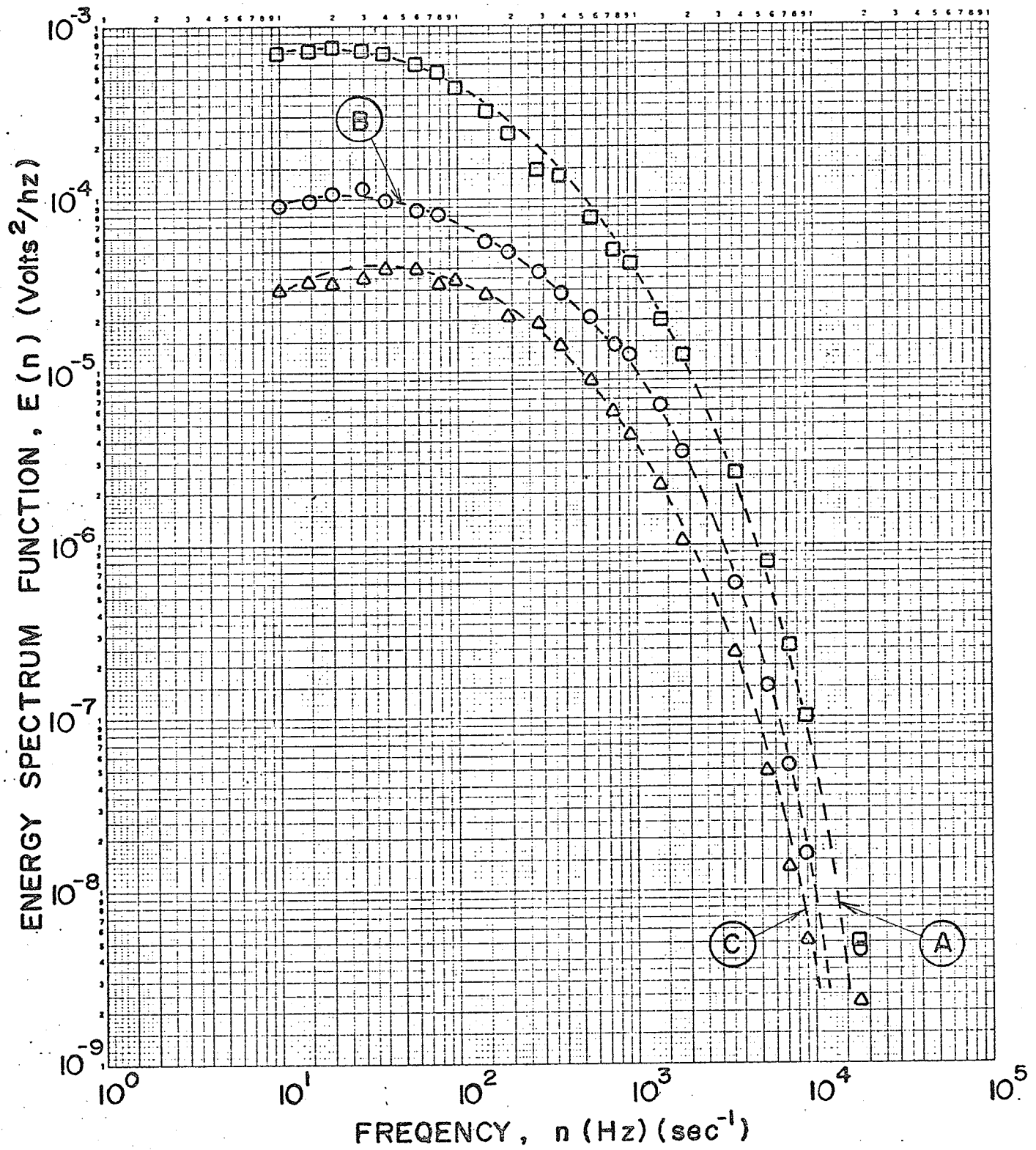


FIG.51a POWER SPECTRA of AXIAL TURBULENCE  
Test 2, P/D = 1.50

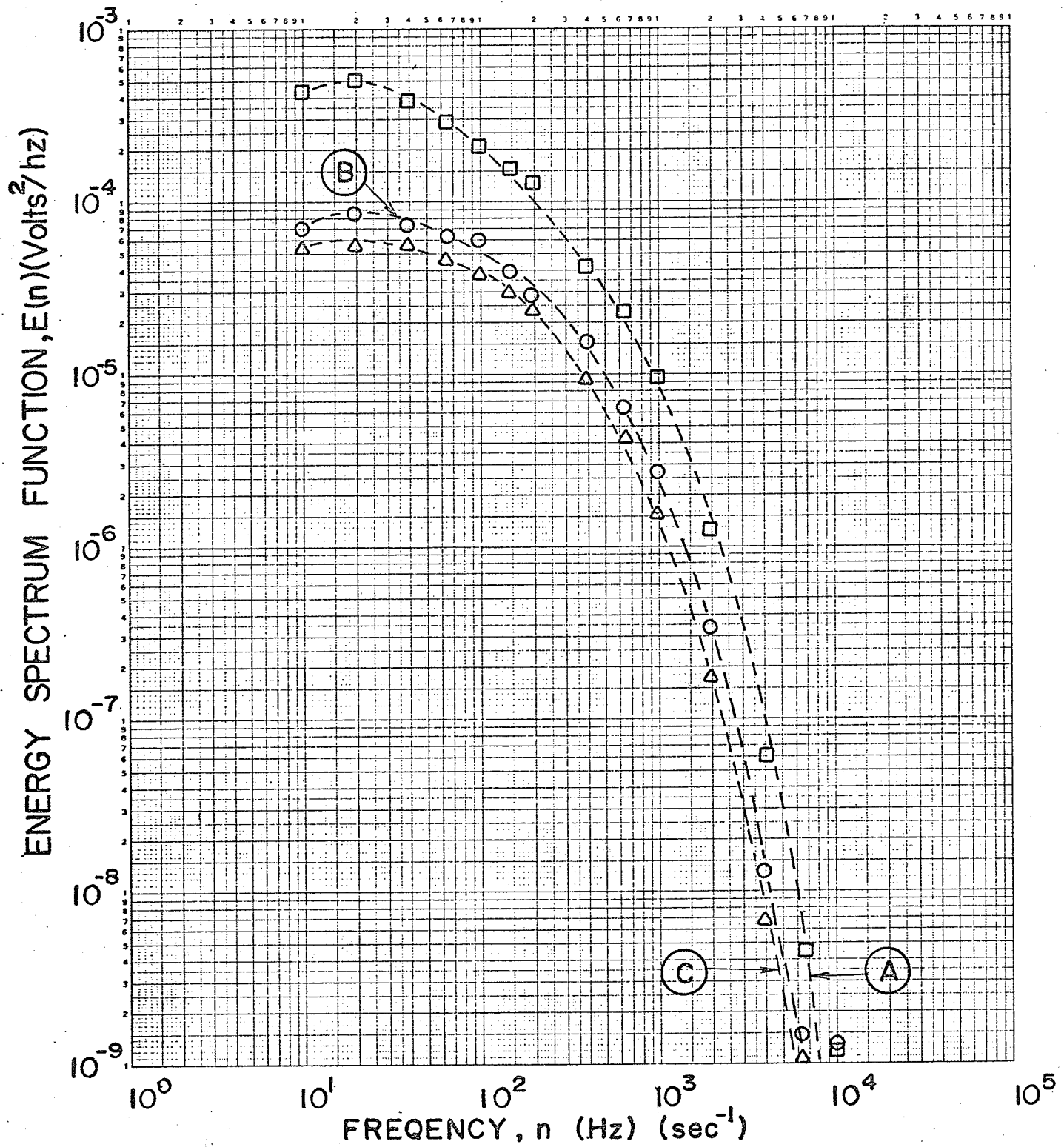


FIG.51b POWER SPECTRA of AXIAL TURBULENCE

Test 5,  $P/D = 1.50$

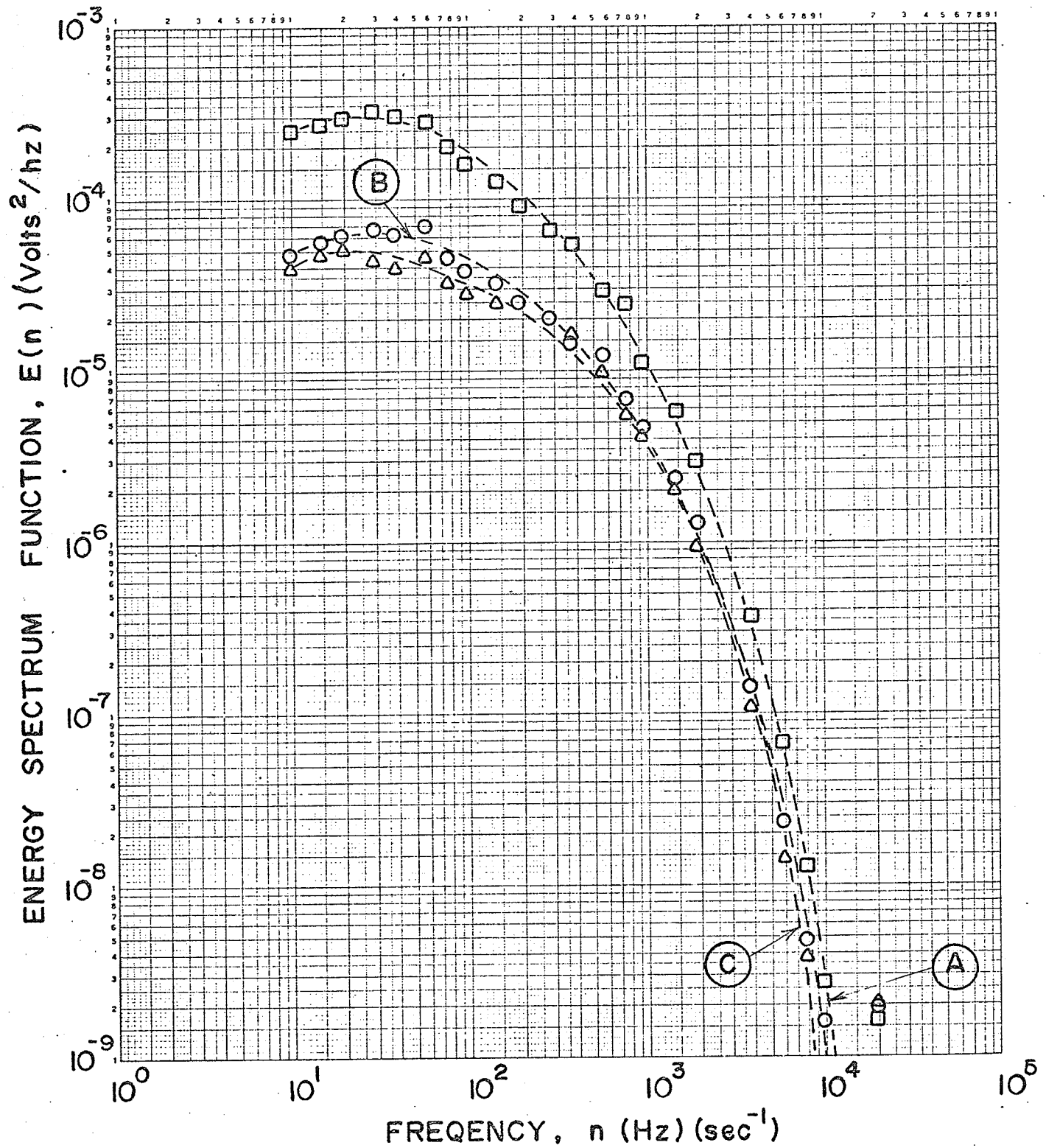


FIG.51c POWER SPECTRA of AXIAL TURBULENCE

Test 3,  $P/D=1.35$

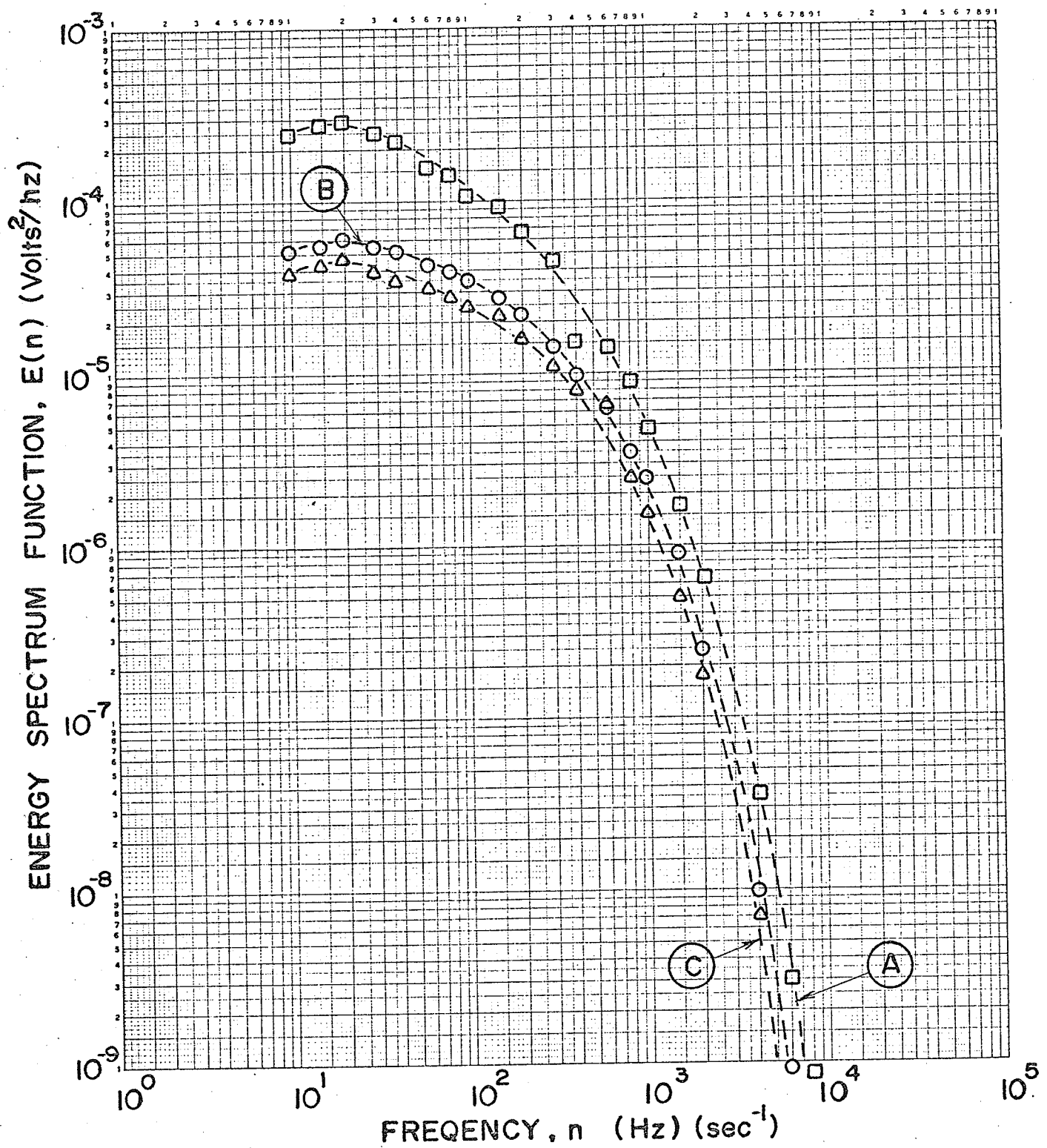


FIG.5Id POWER SPECTRA of AXIAL TURBULENCE  
Test 6,  $P/D=1.35$

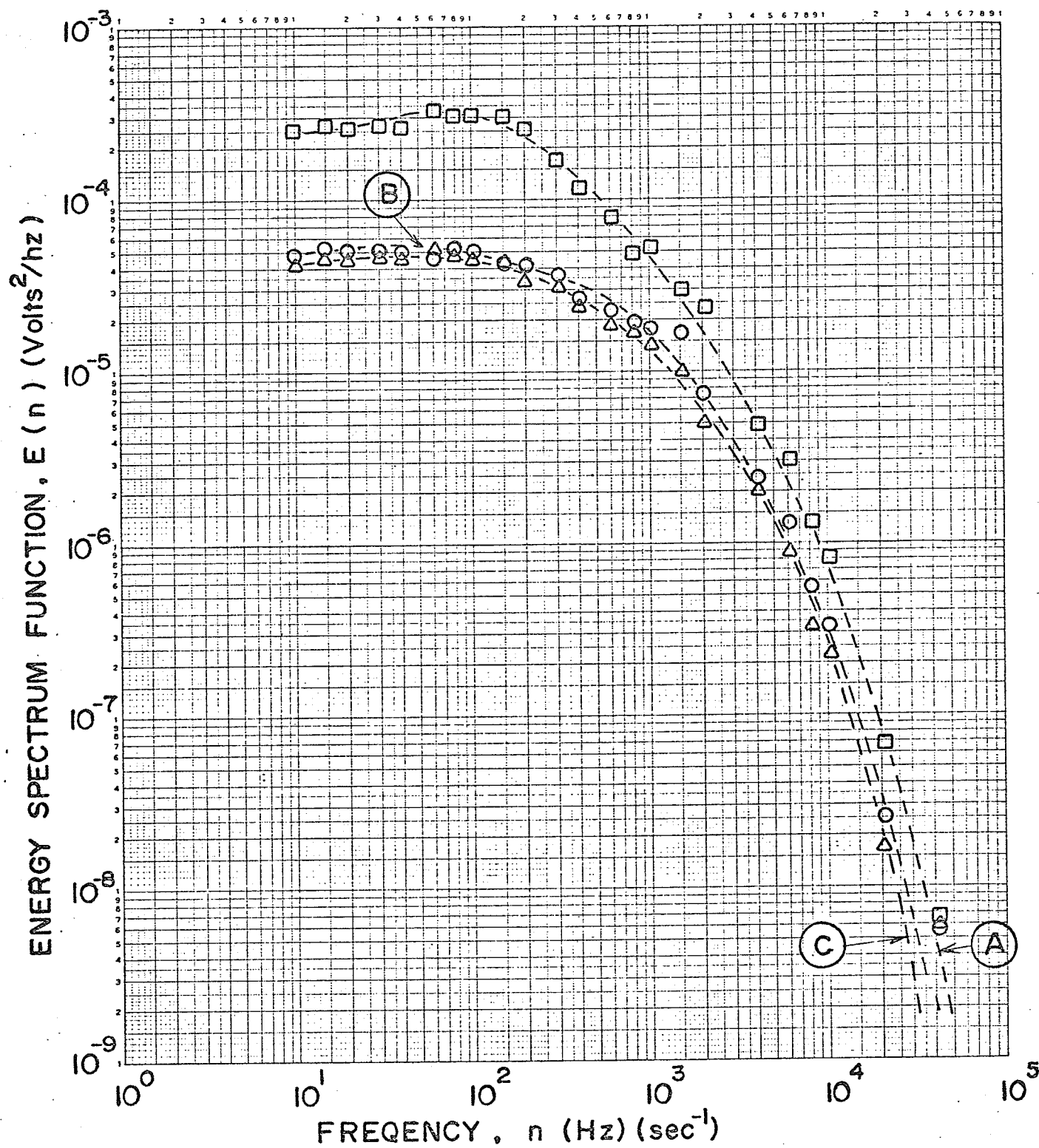


FIG.51e POWER SPECTRA of AXIAL TURBULENCE  
Test 4,  $P/D=1.20$



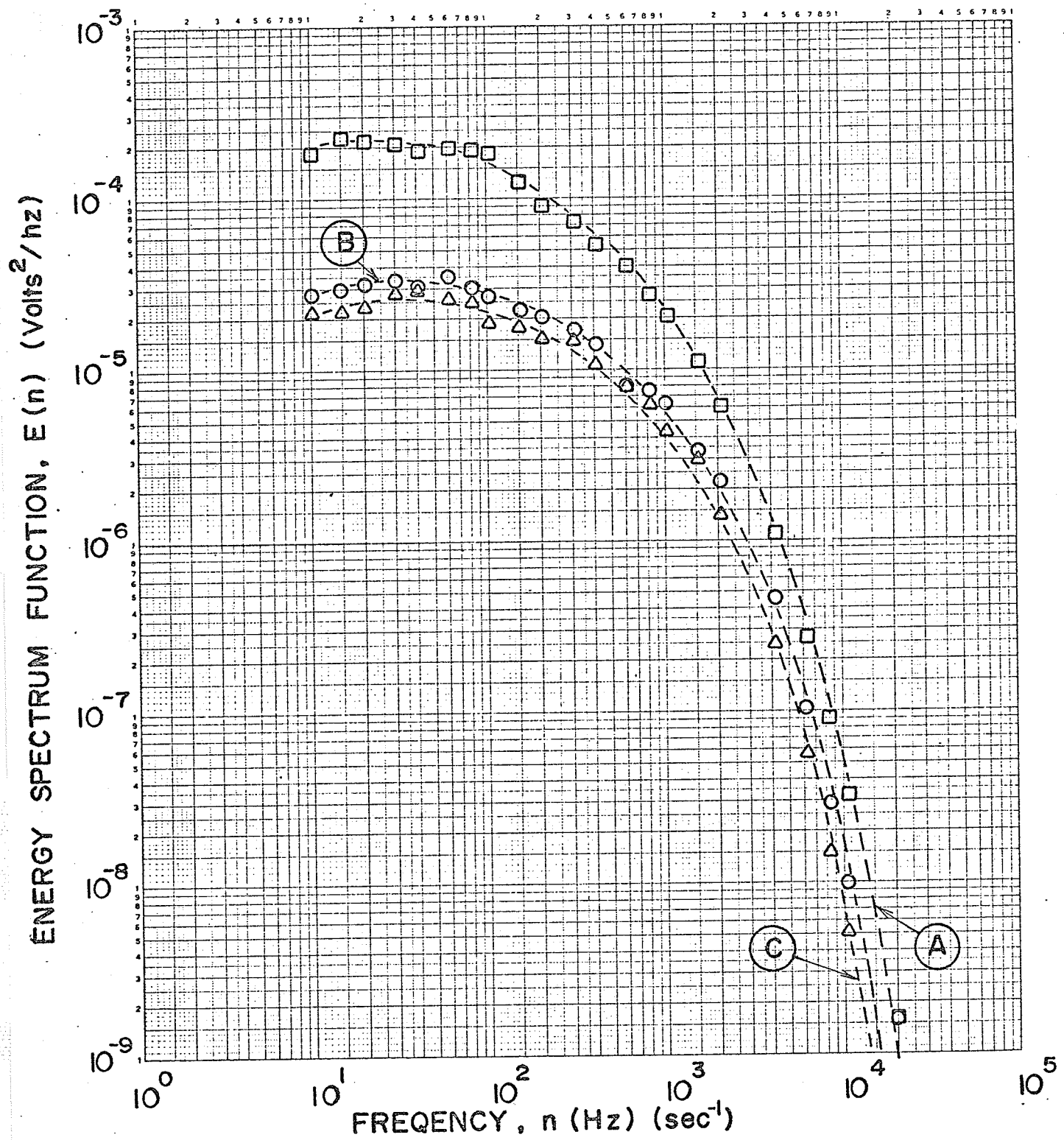


FIG.5 If POWER SPECTRA of AXIAL TURBULENCE

Test 6,  $P/D=1.20$

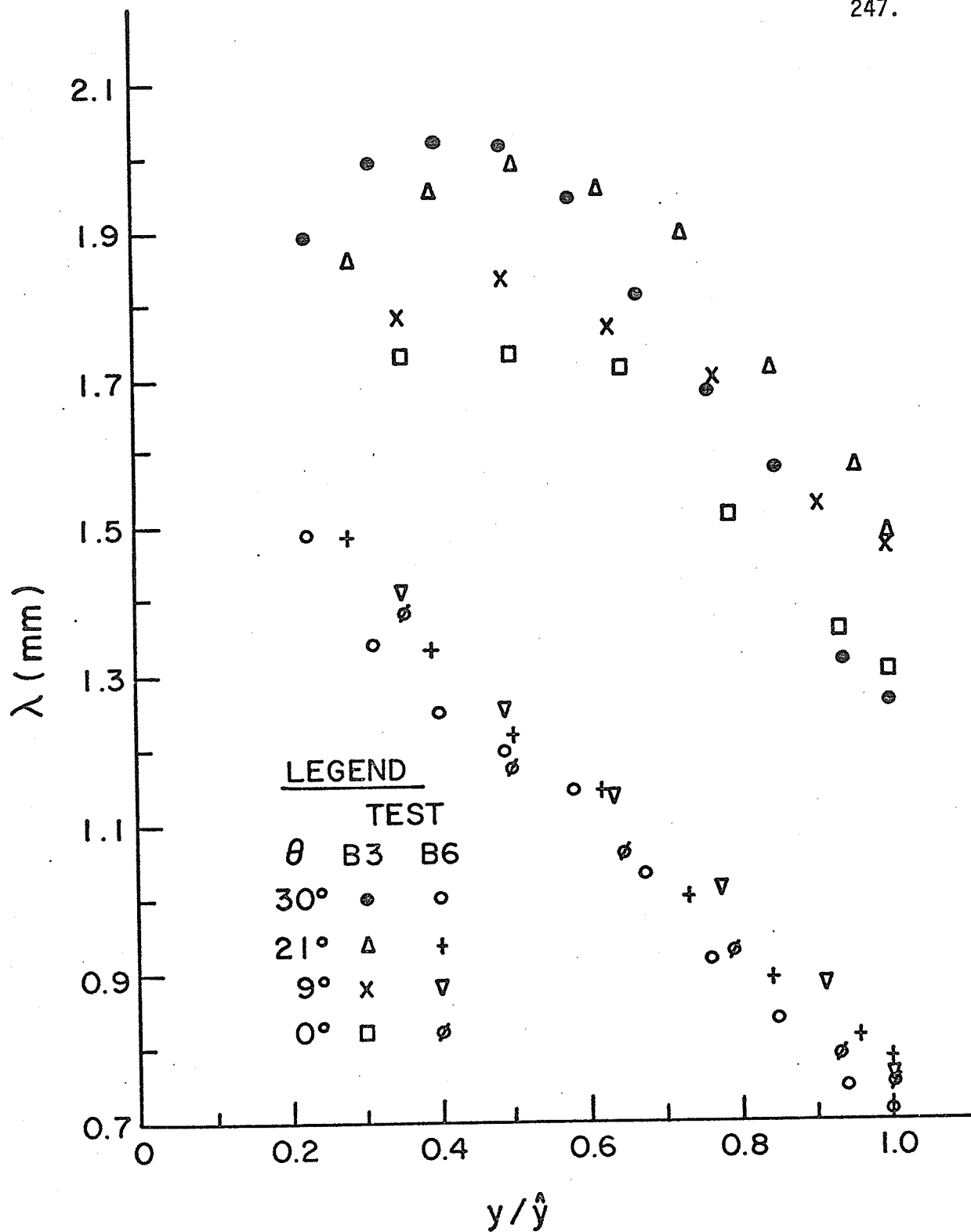


FIG. 52 MICRO-SCALE DISTRIBUTIONS-P/D = 1.35

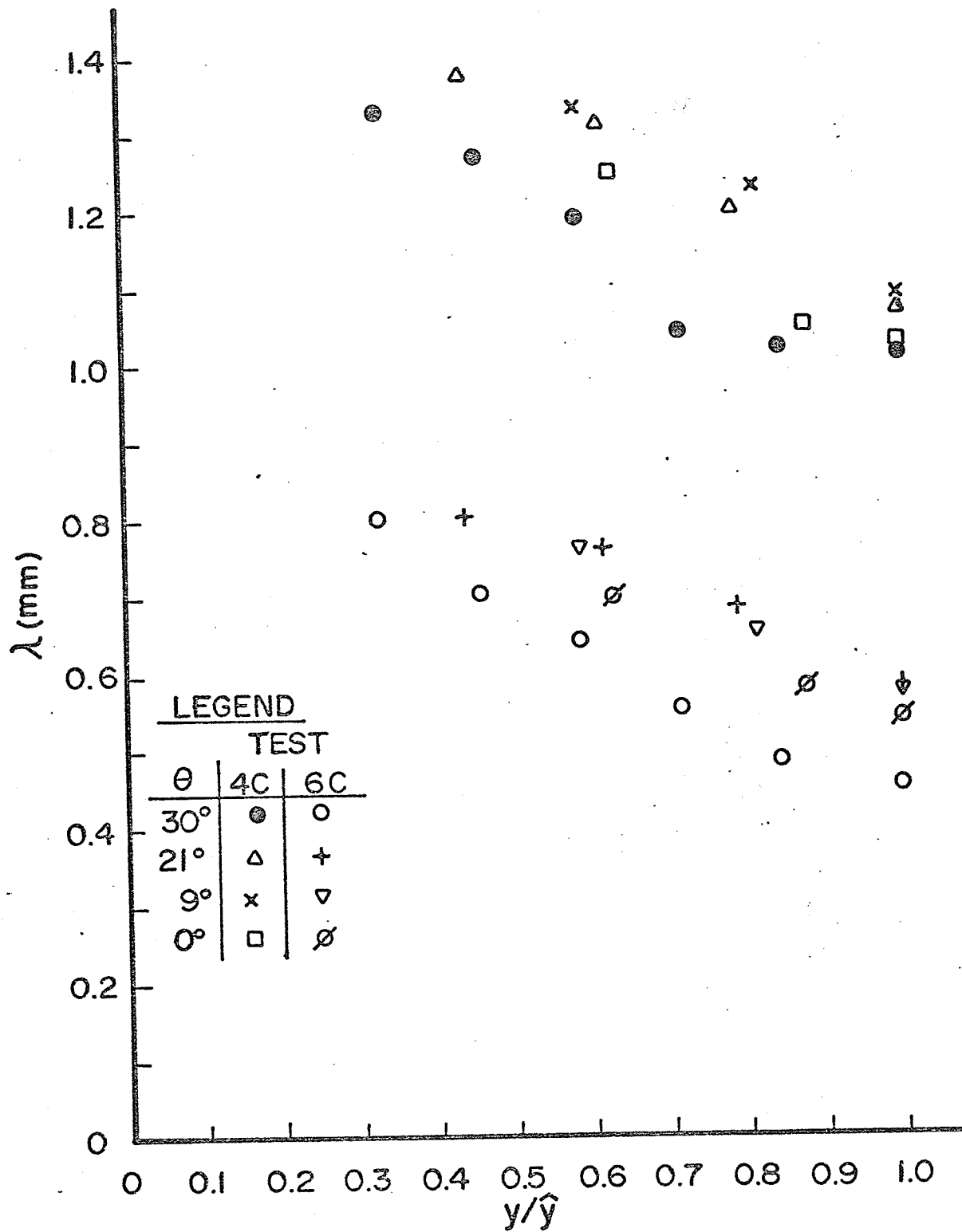
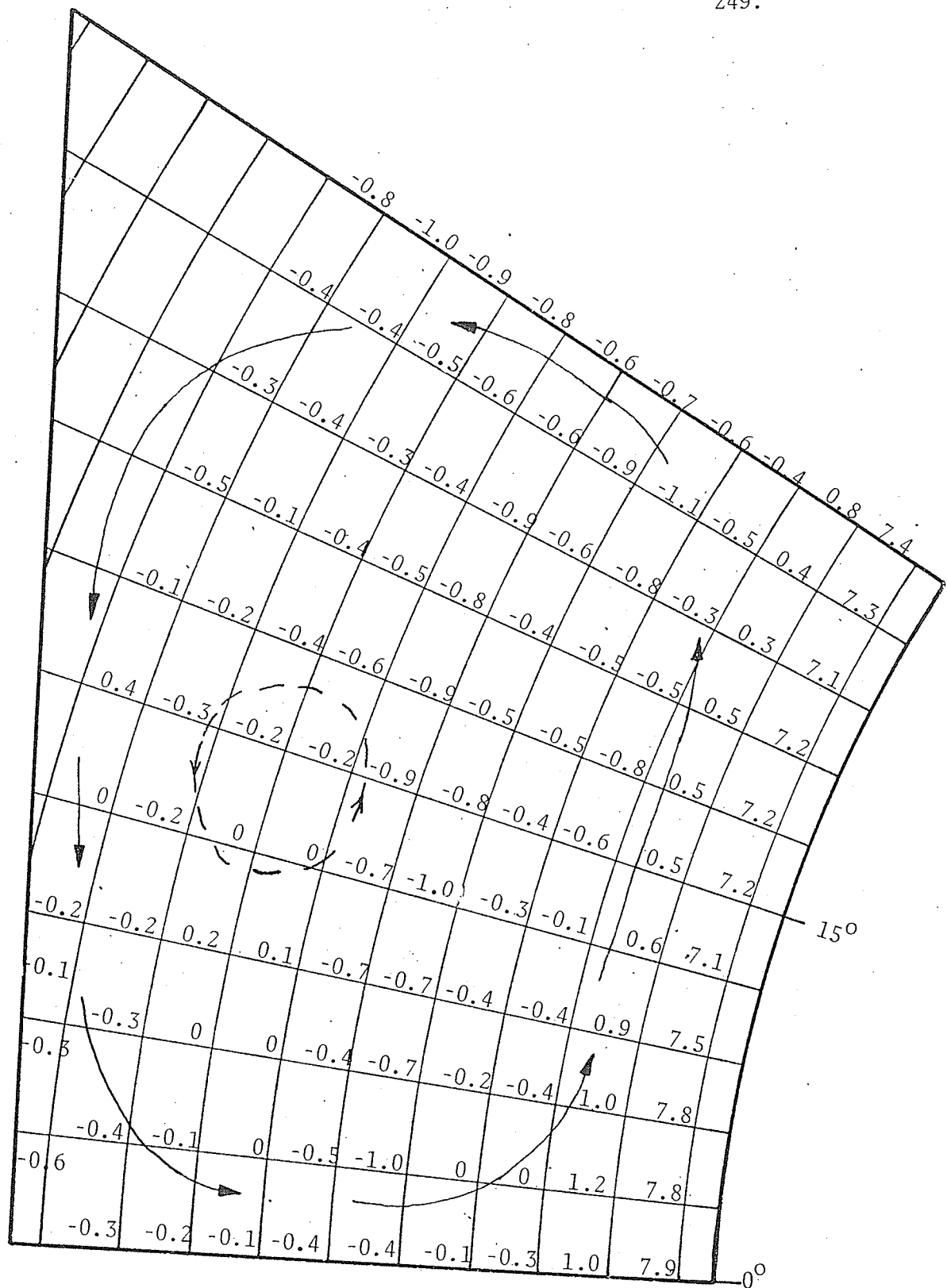
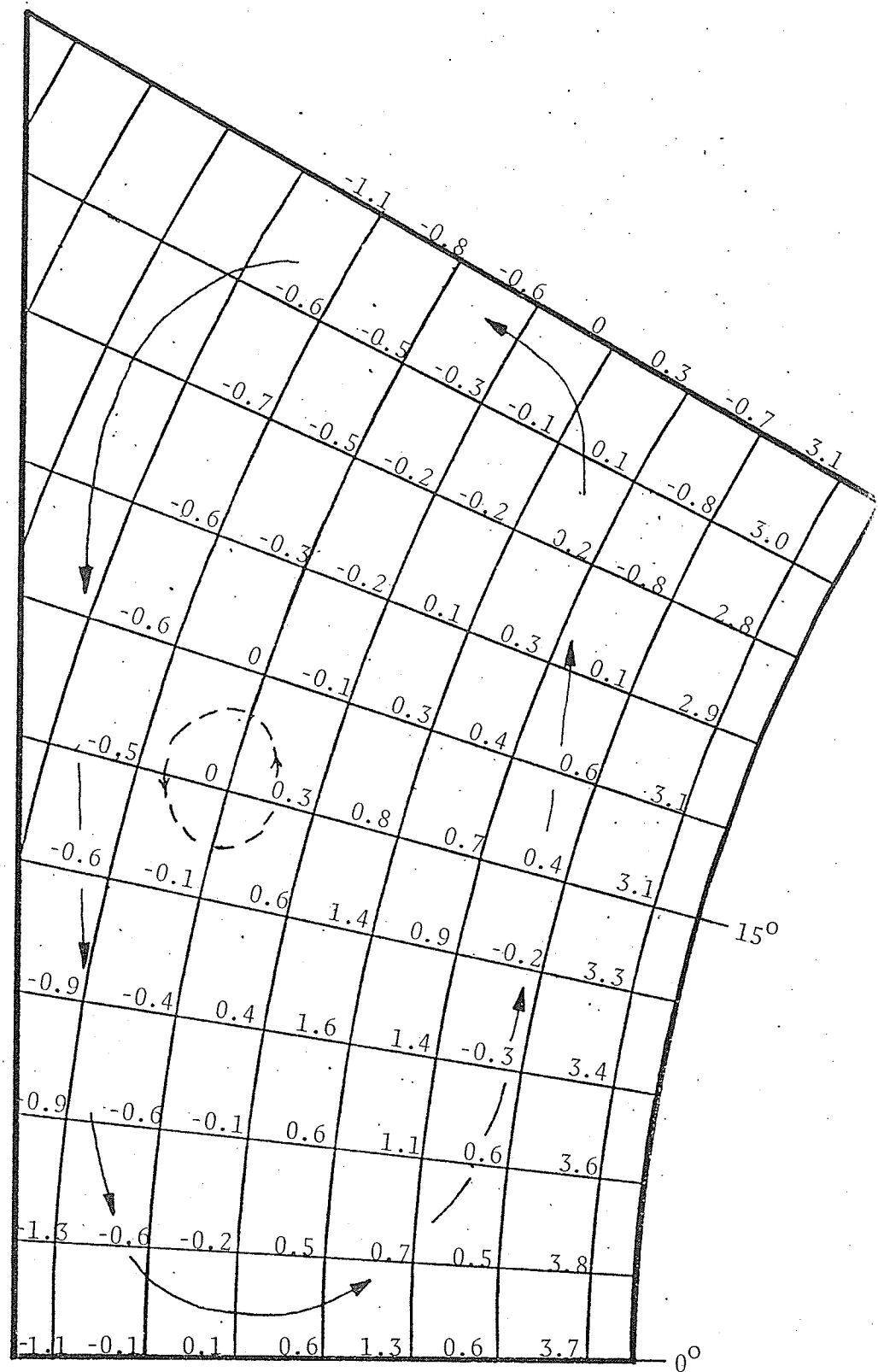


FIG.53 MICRO-SCALE DISTRIBUTIONS- P/D=1.20



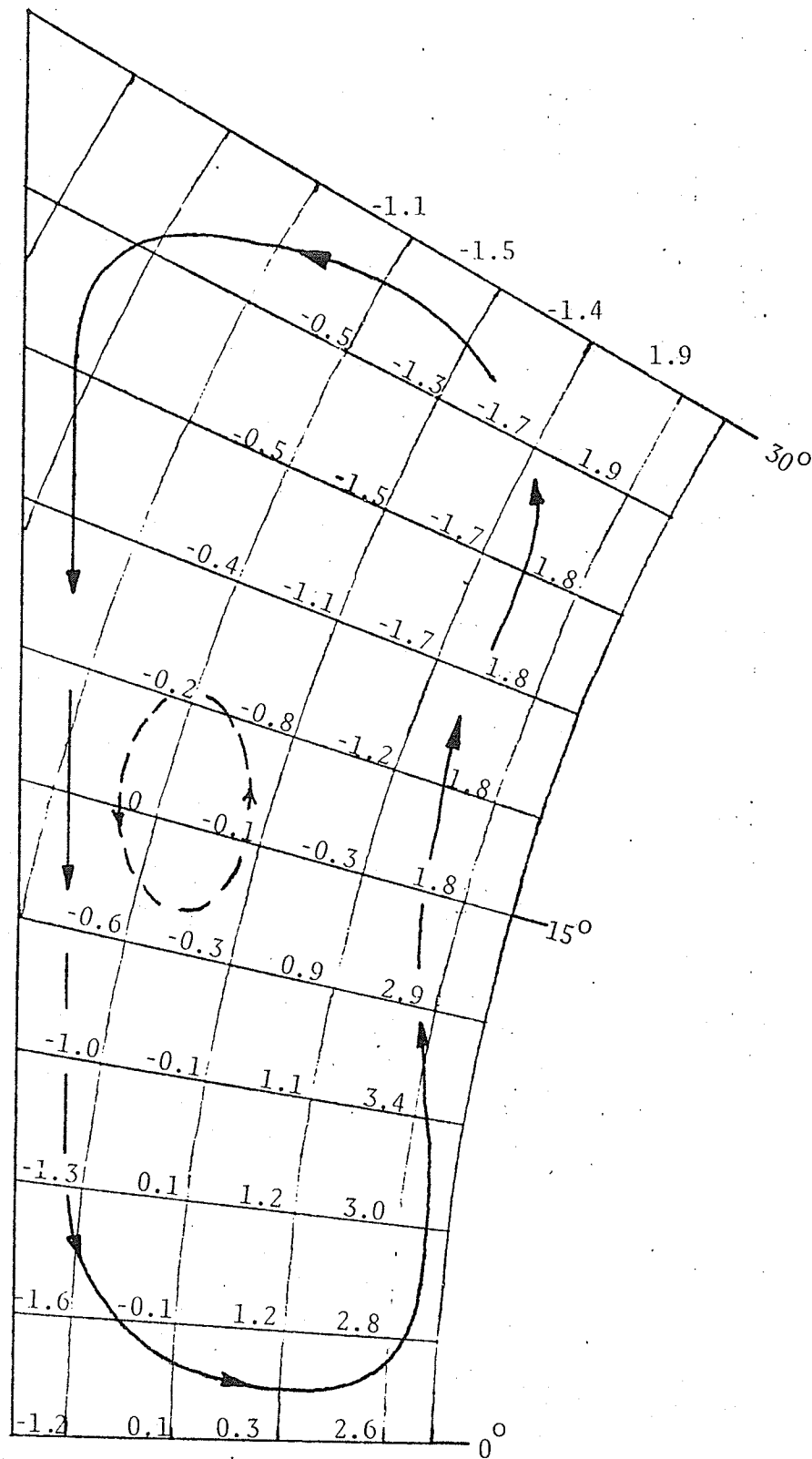
Test A3. Values shown are Term B  $\times 10^2$  and apply to node at lower right-see appendix D.

FIGURE 54: INFERRED SECONDARY FLOW PATTERN  $P/D = 1.50$



Test B3. Values shown are Term B x  $10^2$  and apply to node at lower right-see appendix D.

FIGURE 55: INFERRED SECONDARY FLOW PATTERN  $P/D = 1.35$



Test C3. Values shown are Term B x 10<sup>2</sup> and apply to node at lower right-see appendix D.

FIGURE 56: INFERRED SECONDARY FLOW PATTERN P/D = 1.20

## VITA

### ALLAN CHARLES TRUPP

- 1934 Born, December 16th, at Shellmouth, Manitoba, Canada.
- 1956 Graduated Diploma Course in Aeronautical Engineering, RCAF Stn Aylmer, Ontario.
- 1957 Graduated B.Sc. (Mech. Eng'g), University of Manitoba.
- 1957-60 Aeronautical Engineering Officer - Royal Canadian Air Force.
- 1960-62 Design Engineer - Atomic Energy of Canada Ltd., Chalk River, Ontario.
- 1962-64 M.Sc. student and demonstrator - University of Manitoba.
- 1964 Graduated M.Sc. (Heat Transfer and Fluid Mechanics), University of Manitoba.
- 1964-65 Lecturer - Mechanical Engineering, University of Manitoba.
- 1965-68 Research and Development Engineer - Atomic Energy of Canada Ltd., Pinawa, Manitoba.
- 1968-73 Lecturer and Ph.D. student - Mechanical Engineering, University of Manitoba.

## PUBLICATIONS

- A.C. Trupp: "Design Proposal for a NPD Single Bundle Shipping Flask", AECL Rep. ED-173, 1961.
- A.C. Trupp: "Methods of Solving Heat Conduction Problems with Particular Reference to Frozen Dams", M.Sc. Thesis, University of Manitoba, 1964.
- A.C. Trupp: "Preliminary Report on Heat and Mass Diffusion Calculations Associated with the Design of Hydrogen Sinks for a Nuclear Reactor Zircaloy Pressure Tube", University of Manitoba, Dept. of Mechanical Engineering, Rep. ER25.02, 1964, (Also issued as AECL Rep. WDI-27, 1965).

H.E. Thexton and A.C. Trupp: "WR-1 Finned Zr-4 Fuel Channel Specification, AECL Rep. EXP-WRI-90401, 1965,

H.E. Thexton, B.J.S. Wilkins, A.C. Trupp and A. Sawatzky: "Prospects for Zirconium Alloy Coolant Tubes in Organic Cooled Reactors", American Nuclear Society, Denver, Colorado, June, 1966.

A.C. Trupp: "The Numerical Finite-Difference Approach to Heat and Mass Diffusion Problems", First Western Canadian Heat Transfer Conference, Saskatoon, Saskatchewan, Sept., 1966.

K.D. Meek, A.C. Trupp, M.E. Cleary and H.E. Thexton: "Proposal to Irradiate in WR-1 a Zircaloy-4 Fuel Channel Incorporating Zircaloy-4 Fins as Hydrogen Sinks, AECL Rep. EXP-WRI-90403, 1967.

A.C. Trupp: "A review of Fluidization Relevant to a Liquid Fluidized Bed Nuclear Reactor", AECL Rep. AECL-2788, 1967.

A.C. Trupp: "Fluidized Particle-to-Liquid Heat Transfer--A Dynamicist's View", Second Western Canadian Heat Transfer Conference, Vancouver, B.C., May, 1968, (Also AECL Rep. AECL-3185, 1968).

A.C. Trupp, R. MacFarlane and R.K. Armstrong: "Expansion Characteristics of Liquid Fluidized Beds of Spheres", AECL Rep. AECL-3027, 1968.

A.C. Trupp, R. MacFarlane and R.K. Armstrong: "The Collapse Mechanism of Fluidized Beds Subjected to Sudden Loss of Liquid Flow", AECL Rep. AECL-3028, 1968.

A.C. Trupp, R. MacFarlane and R.K. Armstrong: "Porosity Fluctuations in Liquid Fluidized Beds of Spheres", AECL Rep. AECL-3029, 1968.

A.C. Trupp: "Dynamics of Liquid Fluidized Beds of Spheres", Tripartite Chemical Engineering Conference, Montreal, Quebec, Sept., 1968: I, Chem. E. Symposium Series No. 30 (1968: Inst Chem, Engrs., London), pp. 182-189.

A.C. Trupp, R.S. Azad, N.W. Wilson and P.A.C. Okwuobi: "Turbulence Characteristics in a Straight Conical Diffuser, Symposium on Internal Flows, University of Salford, England, Apr. 20-22, 1971, Paper No. 9.



N.W. Wilson, R.S. Azad and A.C. Trupp: "An Analysis of the Effect of Secondary Flows on the Longitudinal Velocity Distribution in Square Ducts", Symposium on Internal Flows, University of Salford, England, Apr. 20-22, 1971, Paper No. 11.

A.C. Trupp and R.S. Azad; "A Three-Wire Probe System for Turbulence Measurements", University of Manitoba, Dept. of Mechanical Engineering, Rep. ER25,18, 1972,